KIT
Karlsruher Institut für Technologie

Fakultät für Physik
Institut für Theorie der Kondensierten Materie

Dynamics of disordered and measured systems

Zur Erlangung des akademischen Grades eines
DOKTORS DER NATURWISSENSCHAFTEN (Dr. rer. nat.)

von der KIT-Fakultät für Physik
des Karlsruher Instituts für Technologie (KIT)
genehmigte
Dissertation

von

M. Sc. Paul Pöpperl
aus Karlsruhe

Introduction

> We may regard the present state of the universe as the effect of its past and the cause of its future. An intellect which at a certain moment would know all forces that set nature in motion, and all positions of all items of which nature is composed, if this intellect were also vast enough to submit these data to analysis, it would embrace in a single formula the movements of the greatest bodies of the universe and those of the tiniest atom; for such an intellect nothing would be uncertain and the future just like the past could be present before its eyes.
>
> —Pierre Simon Laplace, A Philosophical Essay on Probabilities [1].

In 1814, Pierre-Simon Laplace articulated the idea that, given the state of the universe at one instant in time, an entity with perfect knowledge of the laws of nature and sufficient computational power (referred to as Laplace's demon by other authors) could predict the state of the universe at any given past or future time [1]. In the following we focus on his statement about the future. Three immediate problems with Laplace's idea come to mind:

1. *The state*: Obtaining "the state of the universe" is impossible since the universe is very large and not entirely observable.

2. *The calculation*: The enormous size of the universe adds too many variables to its future, such that the calculation is impossible.

3. *Determinism*: The very idea of future events being completely determined by a past state is doubtful since the arrival of quantum mechanics.

While perfect knowledge of the state and sufficient computational power are obviously impossible premises which are taken for granted in the quote for the sake of the *Gedankenexperiment*, the third problem is less obvious and goes against its main statement. It manifests itself in the quantum mechanical description of a *measurement*: The state of the system can be thought of as attributing probabilities to the different measurement outcomes, instead of encoding a definitive result of a given measurement. As soon as the measurement is performed, the state changes according to its outcome (*backaction*), such that the course of the future is affected. In other words, if a measurement takes place during the time evolution of a state, different possible outcomes of this measurement correspond to different possible future states, and we generally do not know with certainty which of these *quantum trajectories* the state will follow. There are other interpretations of quantum mechanics, but an interpretation can by definition not overcome a "lack of predictive power" of the theory.

As a consequence, it is both practically as well as fundamentally impossible to accurately and completely determine the future, according to our present knowledge of the laws of nature.

Despite all of these problems, many physics research projects can be described as predictions of aspects of the future. In particular, *dynamics* is directly concerned with the time evolution of a system from a given initial state. Interestingly, even if the system of interest is just a tiny subsection of the universe, all three problems listed above still impact this task. In the following we relate them to the broader scope of this thesis.

Fortunately, a complete and exact description of the initial state is often not necessary to make strong predictions. Instead, particularly in large systems, it is often beneficial to employ a statistical point of view, deriving system properties from an assumed distribution of states or state properties. For instance, the assumption of *disorder* lays a basis for a generic description of a complicated state, giving rise to powerful predictions. As an example, consider a piece of metal. A lot of information about its state can be compressed by assuming that the constituent ions are arranged in a crystal lattice. By specifying a basis for the lattice, the underlying structure of the metal is described, no matter its size. However, this crystal structure is not sufficient to calculate, for example, the conductivity of the metal at low temperatures. Taking a closer look, one realizes that the dynamics of the electrons is actually crucially influenced by *impurities* of the metal [2]—spots, where the crystal structure is distorted and perturbed in some way. Such imperfections are in fact commonly present in solid objects [3]. Determining the position of each impurity is again impractical and in fact for many purposes not necessary. Instead, we can assume their positions to be *disordered*—described by a probability distribution. In this way, disorder enters the description of the state as an assumed "classical" source of randomness. This assumption allows one to correctly predict for example the Drude conductivity of the metal [2].

Regarding the computational aspect, great progress has been made since Laplace's time due to the establishment of the computer. Numerical methods allow us to perform brute-force physics simulations to confirm results from other methods. The probabilistic nature of quantum measurements and disorder make such simulations particularly useful. By repeating a simulation with random elements many times we can obtain information about the distribution of different values an observable can take. In particular, we can use simulations to follow individual quantum trajectories, by choosing random measurement outcomes according to the Born rule; thus performing a "numerical experiment" to get a grasp of the typical behavior of the system.

Lastly, studying the dynamics of a system, one clearly has to reconcile with quantum mechanics. The quantum mechanical time evolution of a state is governed by two different paradigms: *Unitary time evolution*, which is governed by the Schrödinger equation and deterministic, and *projective measurements*, which are associated with probabilistic outcomes and the collapse of the wave function to the measured state.

Relying on the first paradigm only, we can calculate the expectation values of different measurement outcomes after an interval of unitary time evolution, which in turn already provide a lot of information. However, when a measurement takes place, the system has to follow one particular quantum trajectory and the measurement thus influences the dynamics.

One of the striking implications of quantum mechanical measurements on the dynamics of a system was first formalized in Ref. [4]: If a system is measured repeatedly, with little time in between two measurements for unitary time evolution, there is a high probability that each measurement resets the system to the same eigenstate of the measured observable, thus effectively "freezing" its time evolution. This is called the *quantum Zeno effect*, alluding to Zeno's paradox of a flying arrow which supposedly can not actually move, since at every individual moment of observation it is at one precise location. In quantum mechanics, the Zeno effect is more than just a paradox or a thought experiment. Experimental observations are reported for example in Refs. [5–7].

In summary, overcoming the difficulties in calculating dynamical properties of a large system motivates the study of disorder and quantum measurements. Both of these "sources of randomness" lead to interesting dynamical phenomena, as we elaborate below.

Disorder, measurements, localization, and randomness

A seminal work that gave rise to the discovery of a whole class of dynamical phenomena in disordered systems was published by P. W. Anderson in 1958 [8]: If disorder of is added to a quantum lattice, the system can become *localized.* As an example, in non-interacting one and two dimensional lattices the introduction of disorder implies spatially exponential decay of every single eigenstate, provided a sufficiently large system [9, 10]. This prevents particles from propagating through the system and thus leads to the absence of diffusion (as put by Anderson) and to exponential suppression of transport quantities like the conductivity. Part of what makes localization fundamentally important is the implied absence of *thermalization*—familiar concepts of statistical mechanics are not applicable to localized systems, as equilibration between subsystems is inhibited [11].

While disordered one- and two-dimensional non-interacting systems are always strongly localized in above sense, localization in higher dimensional lattices depends on the *strength* of disorder [9, 10] which can be thought of as the standard deviation of the governing random distribution. Therefore, higher dimensional lattices feature a transition in their behavior as a function of the disorder strength [8, 10], which comes with its own intricacies. Other than in transport quantities, the *Anderson transition* also manifests itself in the scaling of the entanglement between different parts of the system as a function of the system size [12]. Roughly speaking, localization reduces the number of spatially overlapping single-particle wave functions, thus also reducing correlations and entanglement.
Below the critical disorder strength, disorder can lead to *weak localization*, reducing the conductivity and slowing down transport.

The generalization of Andersons ideas to interacting, disordered systems [13–15] is called *many-body localization* [11, 16–19] and is still an active field of research. As a function of disorder and interaction strength, a one-dimensional system can exhibit different phases that are either thermal or localized. These phases are separated by the *many-body localization transition*, which also present itself in the dynamics of transport observables as well as in the scaling of the entanglement entropy.

Disorder-induced localization offers up a parallel to the dynamics of measured systems and the quantum Zeno effect, which can also spatially localize a state. Intuitively, repeated projective measurements of spatially local quantities can prevent the spatial spreading of entanglement. The interest in measurement-influenced dynamics has spiked recently due to the conceptualization of *measurement induced transitions* [20–39], where the system-size-scaling of the entanglement entropy exhibits a transition as a function of characteristics of the measurements (for example the measurement frequency [22]). On this basis it was argued, that measurement-induced transitions and many-body localization transitions are fundamentally linked [40]. In Refs. [38, 41] a connection between measurement induced transitions in $D > 1$ dimensional systems of free fermions and Anderson transitions in $D + 1$ dimensions was established based on the mathematical descriptions of these transitions.

Measurements however can not only hinder the spreading of entanglement. Choosing appropriate measurement operators, measurements can create entanglement as well [30, 42]. Most generally, the backaction of specifically designed measurements may be used to control and *steer* a system to a specific target state. This interesting direction for measured dynamics is called *measurement induced steering* [43–45]. It is relevant for both theory and experiment: While the design of measurement protocols that allow for efficient steering is an interesting theoretical task, the advantages of being able to set up the initial state of an experiment at will is clear. Also for quantum computing it is desirable to be able to steer the state as a means to encode data for a computation.
The versatility of measurements offers another reason to consider measurements and disorder in the same context. If they are brought together in the same system, their interplay may lead to the

destruction of localization, or to the emergence of novel phases, depending on the character of the measurements [46, 47]. Measurements may serve as a controllable source of noise, to induce transport in an otherwise localized system [48]; elaborate measurement protocols may even induce correlations into non-interacting systems to mimic interaction- and disorder effects.

Both disorder as well as measurements can be regarded as sources of randomness. While measurements add an inherent, quantum mechanical element of randomness to the dynamics of a system, disorder (in the context of this thesis) is a classical source of randomness, written into the Hamiltonian in the form of random numbers that follow a given distribution. For this reason, some of the tools to analyze disordered and measured systems are similar. To make general statements about systems with random elements, distributions of possible outcomes should be considered. This suggests taking averages over random quantities, investigating the possibility of deducing properties of the system from "typical" realizations.

An interesting parallel between all of our projects presented below is the emergence of classical random walk descriptions for aspects of the dynamics, which inherit from the underlying quantum nature. Such descriptions can come about due to measurement-induced state changes on a lattice [49, 50], different paths for quantum mechanical propagation in a disordered system [51] or the interplay between Hamiltonian time evolution and measurements [52, 53].

For above reasons, the dynamics of measured and disordered systems is an important subject of study. Both measurements and disorder separately are associated with interesting dynamical phenomena. There are reasons to believe that it is beneficial to think about them on similar grounds. Moreover, their interplay can give rise to additional puzzles.

In the following we introduce the three projects that are presented in this thesis, explaining motivation and goals, and relating them to the research topics outlined above. The chapters are arranged to build on each other conceptually.

Measurements on an Anderson chain   Chapter 1 is based on Ref. [53].

The setup for this project is a single particle on a one-dimensional, disordered *Anderson chain*. As all eigenfunctions of such a chain are localized [8–10], if the particle is placed on one of the chain sites, the probability to find it in the vicinity of this site after arbitrary times is still large. On the individual sites of the chain, projective measurements are performed in regular time intervals. Each measurement can have one out of just two different results—the particle is at the measured site or it is not there. Each of these outcomes implies the corresponding collapse of the wave function, manifesting in the dynamics of the particle.

We investigate two general directions: The impact of measurements at random locations on the dynamics of the system, and the possibility of measurement induced spatial steering of the particle, choosing the measurement locations deliberately.

The first issue addresses the generic interplay of localization and measurements, and possible implications for the dynamics. Specifically, we ask about the fate of localization in the presence of measurements, with respect to the exponential shape of the wave function as well as with respect to transport. The possibility of measurement-induced transitions in disordered systems was investigated in non-interacting [46] and interacting [47] systems of multiple fermions. Considering just a single particle, we do not discuss entanglement. However, as it turns out, measurements of arbitrary frequency indeed induce diffusive transport via a click-outcome governed random walk. In this sense, the introduction of measurements does imply a dynamical transition. At the same time, the exponential shape of the wave functions is preserved, such that the distribution of wave function spreads (related

to the "local" localization length in a small window around the center site) enters the random walk waiting time, controlling the diffusion constant. We demonstrate, that the tail of the resulting waiting time distribution falls off fast, such that diffusion is indeed the generic result.

Regarding the second issue, we find that we can use the measurement induced random walk to steer the particle over a distance of L sites within $\mathcal{O}(L^3)$ measurements, without having access to the detector readout anywhere but on the target site. If all readouts are available, ballistic steering can be achieved.

Regarding the models, the following two chapters branch into slightly different directions, Chapter 2 being concerned with general properties of a disordered system (without measurements); and Chapter 3 addressing an interacting system-detector model (without disorder).

Memory effects in the imbalance in delocalized disordered systems   Chapter 2 is based on Ref. [54].

In this chapter, we investigate disorder effects in the absence of strong localization. In particular, we calculate how an initial state characterized by spatial variation at a short length scale decays in the presence of disorder. This decay is captured by the *density imbalance* between even and odd sites of a lattice, which is subject to many experimental and numerical studies of many-body localization [55–58] due to its sensibility to localization: Initially, a state of maximal imbalance is set up, alternating between occupied and empty sites. If the system is strongly localized, the imbalance of this state does not completely decay, but keeps an "infinite memory" (and a finite imbalance) of its initial state. However, localization can be inhibited by interaction effects [59, 60] or the dimensionality of the system [9]. If this happens, one could think that strongly imbalanced initial states decay exponentially quickly, because particles only have to travel a short distance to even out the imbalance. This expectation contradicts the observation of power-laws in the imbalance on the delocalized side of the many-body localization transition [57, 59–61]. These power-laws were proposed to emerge from a mechanism related to scattering paths returning to their starting points after diffusive motion ("return processes") by the authors of Ref. [57]. Such a mechanism is known to contribute long-time tails in disordered systems to other observables [62, 63].

Using the diagrammatic technique for disorder averaging, we calculate corrections from return processes to the imbalance, confirming the origin of the imbalance long-time tails in these processes. Due to the relation with the return probability, the power-law exponent depends on the dimension of the system. We obtain a universal relation between imbalance- and mean-square exponents, which was predicted in Ref. [59]. We discuss weak-localization corrections to our results.

Employing a phenomenological modification of the diffusion propagator, we generalize our results to the subdiffusive phase on the ergodic side of the many-body localization transition.

Our calculation is supported by numerical simulations of non-interacting two-dimensional systems. In two dimensions, there is a parameter regime where $l \ll \xi \ll L$, where l is the mean free path, ξ is the localization length, and L is the system size [64]. Even though all states are localized in two dimensions at arbitrarily weak disorder in the thermodynamic limit, this regime allows us to confirm our predictions without having to go to the large Hilbert space of an interacting system.

Ancilla measurements on a two-level system   Chapter 3 was written in parallel with Ref. [65].

In this project, we look into the dynamics of a two-site "chain" under *ancilla measurements*: One particle is placed on the chain. The two-level ancilla "detector"—initially prepared in a specific, known state—interacts with the density on one of the chain sites during a fixed interval of time evolution (the

total density on the chain is conserved). The detector is then projectively measured, and afterwards reset to its initial state. These steps are repeated many times.

The outcome of the projective measurement on the detector can give information about the state of the chain. The amount of information obtained by a single measurement depends on the system parameters. Our setup comprises one of the simplest non-trivial models of ancilla measurements. As such, it is well suited to investigate principal differences between projective- and more general measurements that emerge from joined system-detector unitary dynamics [66].

The authors of Ref. [67] demonstrated, that a similar model in the continuous measurement limit shows generalized quantum-Zeno phenomenology, with a "cascade of transitions in the system dynamics". As it turns out, considering arbitrary parameters in our model, a complicated structure of different dynamical phases emerges.

Main object of our investigation is the distribution of states of the chain immediately after the measurements, averaged over time and different measurement outcomes, which turns out to live on a one-dimensional circle for most parameter sets. The exponential branching of possible quantum trajectories due to different measurement outcomes leads to complex behavior of this distribution of states. It exhibits transitions between different types of behavior as a function of the system parameters, that manifest themselves also in the average of individual wave functions over time instances after the measurements.

Discretizing the state manifold, we obtain a random walk on a graph structure, which can reduce to a one-dimensional random walk in a special case. At finite discretization, the random walk on the graph exhibits a transition between ergodic- and non-ergodic phases as a function of the time interval between measurements, and the strength of the chain-detector coupling. We show that the non-ergodic phase is a true feature of the continuous process, and argue, that this process indeed also possesses an ergodic phase. The distributions on the circle can be either sharply peaked around few angles, or broadly distributed—reminiscent of the Anderson transition between localized- and delocalized phases as a function of disorder [10]. The connection to the Anderson transition is established by calculating a quantity similar to the typical value of the local density of states, which is used as an indicator of the Anderson transition [10, 68].

Interestingly, our distribution curves can also exhibit a fractional box-counting dimension, reminiscent of multi-fractality of wave functions across the Anderson transition [10].

A connection between measurement-induced transitions and Anderson transitions emerges from an analogy in their field-theoretical descriptions as was recently established in Refs. [38, 41, 69–71].

Developing physical intuition for this simple system helps to understand more complex situations, for example a more elaborate detector, or a larger measured system, or a "crystal" of measured sites with ancillas, which is expected to feature a measurement induced transition [39].

Structure

Measurements on an Anderson chain   After the introduction of Chapter 1 in Sec. 1.1, we begin with some fundamentals. Localization is introduced from a phenomenological point of view, in terms of localized wave functions in Sec. 1.2.1. Measurements in quantum mechanics are recapitulated on the example at hand (density measurements on the Anderson chain), and compared to unitary time evolution in Sec. 1.2.2. We also introduce random walks, as well as diffusion and subdiffusion in the random walk framework 1.2.3.

In Sec. 1.3 we introduce the model and the time evolution protocol, and in Sec. 1.4 we motivate

the characterization of quantum trajectories by the moments of the wave function. In Sec. 1.5, we investigate the fate of localization in the presence of measurements in terms of these moments. Our setup provides a natural platform for spatial steering, which we concentrate on in Sec 1.6. Finally, we formalize the connection to the random walk in Sec. 1.7. We conclude in Sec. 1.8.

Memory effects in the imbalance in delocalized disordered systems   Chapter 2 is introduced in Sec. 2.1. We introduce the diagrammatic technique for disorder averaging [2, 64] in Sec. 2.2.1. In Sec. 2.2.2 we outline, how diffusion and weak localization can be understood in the diagrammatic framework. To get a better intuition of these mechanisms and to understand how localization can be inhibited by interactions ("dephasing") [2, 64] we briefly outline the interference interpretation of localization in Sec. 2.2.3. In Sec. 2.3, we show how the imbalance is related to the density-density response function, which we then analyze with the diagrammatic technique. In Sec. 2.4 we explain how power-law tails of the relaxation of a density perturbation are related to the return probability of a random walk and calculate the resulting long-time relaxation tails of the imbalance in one- and two dimensions. Using a phenomenological approach to subdiffusion, we extend our arguments to the slow-relaxation phase near the many-body localization transition in one dimension. Our numerical approach 2.5 is based on properties of localization specific to two-dimensional systems. To confirm the validity of our numerics, we explore these properties further in Appendix A.1. We conclude in Sec. 2.6.

Ancilla measurements on a two-level system   Chapter 3 is introduced in Sec. 3.1. We then present the definition and some basic properties of our system-detector model and an intuitive physical discussion for the ancilla measurements in Sec. 3.2. In Sec. 3.3 we show that the dynamics of our model can be characterized by a distribution on a circle on the Bloch-sphere. After presenting two special cases for which the distribution can be obtained analytically in Sec. 3.4, we demonstrate that it can often be calculated from a time average of a single quantum trajectory or as the stationary state of a Master-equation (Sec. 3.5). In Sec. 3.6, we present examples of distributions in the generic case, obtained from numerical methods. In Sec. 3.7, we characterize such distributions for a range of parameters in terms of different observables. We conclude in Sec. 3.8.

Contents

1 Chapter 1
Measurements on an Anderson chain

In this chapter, we study the interplay between disorder and measurements on the dynamics of a single particle in a one dimensional system. In quantum mechanics, there are two very different paradigms of time evolution: Usually, time evolution is governed by a unitary operator, which is constructed from the Hamiltonian of the system. However, if a measurement is performed, the state of the system is projected into an eigenstate of the measured operator. This process is generally not reversible, and does not correspond to a unitary operation. Therefore, time evolution protocols encompassing unitary evolution as well as measurements can lead to unique dynamical effects. In the presence of disorder, a non-interacting one-dimensional system becomes Anderson localized: The eigenstates of the system decay exponentially in real space. In this chapter, we ask whether localization is affected if measurements are performed on such a system, and about the particular effects of combining localization and measurements. We find that the application of measurements at random localization leads to delocalization of the ensemble of quantum trajectories across the system. At the same time, typical quantum trajectories still correspond to localized wave functions. The measurement induced random motion of a trajectory is found to be diffusive, by a comparison to a random walk. We find, that coordinated measurements can be used to induce transport in a predetermined way, and to steer the particle towards a designated location.

The contents of this chapter are based on Ref. [53]. Large passages of Secs. 1.1, 1.4, 1.5, 1.6, 1.7, and 1.8 are direct quotes, and the Figures in these sections are adapted from this publication[1]. The results were developed and discussed together with my coauthors.

1.1 Introduction

In quantum mechanics, a measurement on the state of the system leads to the collapse of the wave function to an eigenstate of the measured observable. This behavior is drastically different from unitary time evolution governed by the system Hamiltonian. The interplay between unitary time evolution and measurements of varying strength and frequency in different systems is a recently very active subject of research [21–37]. Examples for emergent dynamical effects are transitions in the asymptotics of the entanglement entropy in quantum circuit models [27] and Hamiltonian systems [28–33], as well as statistical properties of measurement outcomes in quantum lattices [49, 50]. Similar observations are made in related systems with noise or dissipation instead of measurements [72–74].

---

[1]Reprinted excerpts / figures with permission from [Paul Pöpperl, Igor V. Gornyi, and Yuval Gefen, Phys. Rev. B 107, 174203 Published 9 May 2023]

If disorder is introduced into a one-dimensional non-interacting chain, the system becomes Anderson-localized [8, 9, 75]. All eigenstates decay exponentially, and transport from one end of the chain to the other is exponentially suppressed with the size of the system. Because of this special property of the eigenstates, it is natural to ask about measurements in this context. In particular, one may wonder whether the introduction of measurements could destroy localization and establish transport. A related issue of noise-induced dynamics in a localized system was discussed in Ref. [48].

In the present chapter, we consider local projective measurements of the site occupation. If such a measurement occurs within the localization length of a localized particle, the particle is often detected at the measured site. In these cases, the center of the wave function shifts to the measured site as a consequence of the projection, and the wave function starts spreading around this site. This spreading may be influenced by the localization volume, by the next detection of the particle, or by some putative mechanism introduced by the measurement backaction after a no-click event that may impact the localization properties of the system. Repeated measurements are therefore expected to induce transport in the system. With this idea in mind, we follow two general directions: On the one hand, we choose measurement locations at random and investigate the consequent dynamics. On the other hand, we try to manipulate the state of the system in a controlled way, by designing "measurement protocols" that aim for spatial steering of the particle through a chosen sequence of measured sites. The engineering and manipulation of quantum states through measurements was explored in Refs. [43, 76–78]. Based on the fact that a projective measurement collapses the particle's wave function to the measured site when occupation one is measured, there are different intuitive expectations that one may have for the average behavior of the particle position. On the one hand, in the limit of very frequent measurements, the particle is confined to its initial site as a consequence of the quantum Zeno effect [4, 79–81]. On the other hand, if the time between two measurements is sufficiently large for the time evolution to spread the wave function to its exponential envelope, diffusion would be a natural expectation for the spread of an ensemble of particle positions. The latter case of large time intervals between two measurements is investigated in this chapter.

While diffusion may first come to mind, thinking about a click-driven "classical random walk" of the localized wave function, the distribution of the spread of the wave functions may spoil this behavior. In fact, the site with the largest probability to host a click event is typically the center of the wave function, where the previous click has occurred. Depending on the probability of long successions of click events on the same site, "waiting" of the particle in rare regions of small wave function spread may potentially lead to subdiffusion. Indeed, it was shown in Ref. [48] that rare regions can provide bottlenecks for the dynamics in the related case of a disordered system with temporal noise, leading to subdiffusion on intermediate, parametrically large, time scales. Another issue is related to the impact of no-click events on the wave function. A no-click event, measuring zero occupation on the site, produces a "hole" at the measured position, where the particle is then known to not be. The total probability to find the particle is consequently redistributed by the normalization among all other sites. A priori, it is not clear whether this procedure of making a hole and renormalizing the wave function favors localization or delocalization. Localization may be favored, because no-click events are more likely to occur in the tail of the wave function, removing weight from the tail and shifting it towards the center via normalization, such that the probability of a subsequent click event within the localization volume would increase. Delocalization may be favored, because holes close to the center have a larger impact on the wave function, as a larger portion of the wave function is redistributed—also into the tails. Overall, the no-click events could then enhance the probability of large wave function spread such that long jumps due to click events become more likely.

In this chapter, we formalize and investigate these questions about the fate of localization of the

wave function, as well as transport in the ensemble of particle positions, under sequences of repeated projective measurements. We follow individual quantum trajectories (sequences of measurement outcomes for given sequences of measurement positions in a fixed disorder realization) to acquire statistics that allows us to obtain averaged observables.

In the case of random measurement locations, our key observation is that while the particle position is randomized over the entire system, the wave function typically remains exponentially localized around its center site. Considering averages over measurement outcomes, measurement locations, as well as over disorder realizations, we investigate the spread of the ensemble of wave-packet centers throughout the system and modifications to the wave function spread due to the measurements. Supported by a connection to a classical random walk, we argue that the particle trajectories of different random realizations spread diffusively in the long-time limit. The idea of measurement-induced random walks was addressed in Ref. [82]. In Ref. [52], the authors used a mapping to a classical random walk to model dynamical properties of quantum systems subject to measurements and disorder. The authors of Ref. [46] investigate a measured and disordered non-interacting fermionic Anderson chain (as we do), but their system features multiple particles, and instead of projective measurements, they perform continuous monitoring of the chain. Their work focusses on the possibility of a measurement-induced transition.

Regarding steering, we analyze and compare different kinds of protocols, either using the detector readout only at a designated target site, or at every measurement location. Having access to all readouts allows us to induce ballistic transport. In this sense, both types of steering, passive [43] and active [76], are considered. Diffusion due to random measurements allows for polynomial steering times, even if only reading out the target site.

The chapter is structured as follows. In Sec. 1.2 we introduce the basic concepts of Anderson localization, quantum mechanical time evolution, and random walks. We introduce our time evolution protocol for random measurements in Sec. 1.3 and describe the resulting dynamics qualitatively, motivating the discussion of particle trajectories and corresponding observables in Sec. 1.4. With these observables, we investigate "delocalization" due to measurements in Sec. 1.5. We present the numerical results on steering by non-random measurements in Sec. 1.6. Finally, in Sec. 1.7, the relation to a classical random walk is formalized, and, based on that, our numerical results are further discussed. We conclude in Sec. 1.8.

1.2 Fundamentals

To set the stage for the following discussion of the interplay of Anderson-localization and measurements, we give a brief introduction to Anderson localization from a phenomenological point of view in Sec. 1.2.1. In Sec. 1.2.2, we recapitulate projective measurements and compare them to unitary time evolution. Classical random walks and the concept of diffusion are introduced in Sec. 1.2.3.

1.2.1 Disorder and localization

If disorder is introduced to a non-interacting one-dimensional chain, the system becomes *localized* [8–10]. This means, that each one-particle eigenfunction $|\epsilon\rangle$ in the space of the chain sites $|i\rangle$, $i \in \{1, \dots, L\}$ can be characterized by a center position j_0 and a *localization length* ξ such that [10, 83, 84]

$$\langle i|\epsilon\rangle \propto \mathrm{e}^{-|i-j_0|/\xi}, \tag{1.1}$$
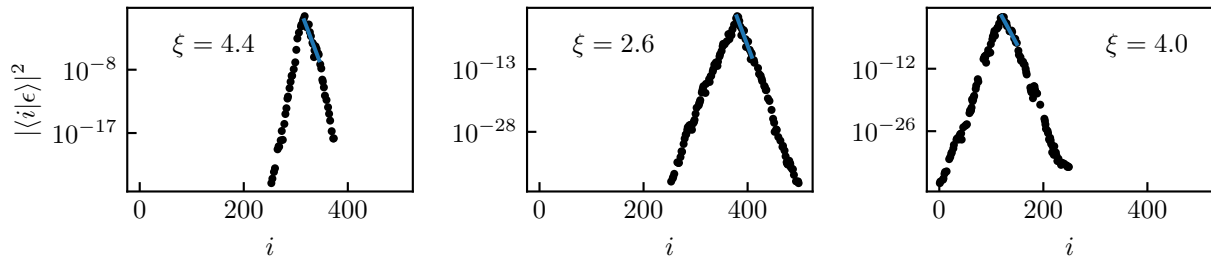
Figure 1.1: Examples for localized eigenfunctions of the Anderson Hamiltonian: Three eigenfunctions of a Hamiltonian of the form (1.2) with disorder strength $W = 5$, at system size $L = 500$. The blue lines are exponential fits in ranges $\Delta i = 30$ to estimate the localization lengths.
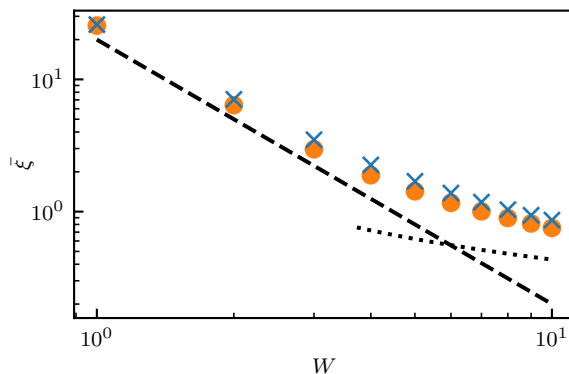
Figure 1.2: Average localization lengths $\bar{\xi}(W)$ of the Anderson Hamiltonian (1.2), in the center of the band. Orange disks: Uniform disorder, $\varepsilon_i \in [-W, W]$. Blue crosses: Gaussian disorder, the ε_i are drawn from a normal distribution of standard deviation $\sigma_W = W/\sqrt{3}$. The dashed line shows the weak disorder asymptotics $\bar{\xi} \propto W^{-2}$ as a guide for the eye. The dotted line shows the strong disorder asymptotics $\bar{\xi} \propto 1/\log(W)$ as a guide for the eye.

in the limit $L \to \infty$. As an example, consider an *Anderson Hamiltonian* of the form

$$H = \sum_{i,j=1}^{L} \left[J\delta_{\langle i,j \rangle} + \varepsilon_i \delta_{i,j} \right] |i\rangle \langle j|, \tag{1.2}$$

$$\delta_{\langle i,j \rangle} := \begin{cases} 1 & i, \ j \text{ nearest neighbors} \\ 0 & \text{else}, \end{cases} \tag{1.3}$$

with nearest neighbor hopping of amplitude $J \equiv 1$, and an onsite disorder potential, defined by random numbers $\{\varepsilon\}$. Let us draw these random numbers from a uniform distribution $\varepsilon_i \in [-W, W]$. W (controlling the standard deviation of these random numbers) is called the *disorder strength*.

In Fig. 1.1 we show probability amplitudes $|\langle i|\epsilon \rangle|^2$ of three different eigenfunctions of such a Hamiltonian with $W = 5$. Indeed, these eigenfunctions decay exponentially with respect to different center positions. Fitting the exponential slope in windows $|j_0 - i| \in [0, 30]$, we obtain localization lengths

$\xi \in [2.6, 4.4]$. As the localization lengths depend on the given *disorder realization* (the configuration of random numbers $\{\varepsilon\}$), they are random quantities themselves. However, the localization lengths are *self-averaging*: The variance of the distribution of localization lengths obtained from different wave functions decreases with increasing size of the considered window $\Delta i = |j_0 - i|$ [85]. As $\Delta i \to \infty$, the tail of almost every wave function is characterized by the same *average localization length* $\bar{\xi}$ which only depends on the disorder strength and energy.

The average localization length can also be obtained by averaging the approximate localization lengths from small windows Δi from many different eigenfunctions [85]. If the disorder strength increases, the average localization length decreases. At weak disorder $W \ll 1$, the average localization length scales as $\bar{\xi}(W) \propto W^{-2}$. At strong disorder $W \ll 1$, the average localization length scales as $\bar{\xi}(W) \propto 1/\log(W)$. By restricting the eigenenergies of the considered eigenfunctions, the average localization length can be energy resolved. Localization lengths are largest in the band center, and decrease towards the band edges.

In Fig. 1.2 we show average localization lengths for Hamiltonian (1.2) calculated in the band center, for $W \in [1, 10]$. Orange disks correspond to uniform disorder, blue crosses correspond to a normal distribution with a standard deviation $\sigma_W = W/\sqrt{3}$ (same standard deviation as a uniform distribution at the same W). The black dashed (dotted) line serves as a guide for the eye and shows the $W \ll 1$ ($W \gg 1$) limit $\xi \propto W^{-2}$ ($\xi \propto 1/\log(W)$). In the considered disorder range, we have average localization lengths between 0.5 and 30 sites.

The localized nature of the eigenfunctions has implications for the time evolution of a localized system. If an eigenstate of the chain $|i_0\rangle$ is prepared as an initial state, this state shares significant overlap only with a small number of eigenfunctions that have their center position within few localization lengths of i_0 (overlap with other eigenfunctions being suppressed exponentially). The overlap between two sites due to time evolution up to arbitrary times is thus suppressed exponentially as well:

$$\left| \langle j | U(t) | i_0 \rangle \right| := \left| \langle j | e^{-iHt} | i_0 \rangle \right| \tag{1.4}$$

$$= \left| \sum_\alpha e^{-i\varepsilon_\alpha t} \langle j | \varepsilon_\alpha \rangle \langle \varepsilon_\alpha | i_0 \rangle \right| \tag{1.5}$$

$$\sim \left| \sum_\alpha \frac{e^{2/\xi_\alpha} + 1}{e^{2/\xi_\alpha} - 1} e^{-i\varepsilon_\alpha t} e^{-|j - i_\alpha|/\xi_\alpha} e^{-|i_0 - i_\alpha|/\xi_\alpha} \right| \tag{1.6}$$

$$\lesssim \sum_\alpha \frac{e^{2/\xi_\alpha} + 1}{e^{2/\xi_\alpha} - 1} \min\left(e^{-|j - i_\alpha|/\xi_\alpha}, e^{-|i_0 - i_\alpha|/\xi_\alpha} \right) \tag{1.7}$$

$$\sim \frac{1 + e^{1/\bar{\xi}}}{\cosh\left(1/\bar{\xi}\right)} e^{-\frac{|j - i_0|}{2\bar{\xi}}}. \tag{1.8}$$

As a consequence, transmission through the system and any kind of transport is suppressed exponentially with the system size. In Fig. 1.3 we show the time evolution of the probability density from an initial state $|50\rangle$, $\varrho_i(t) = |\langle i | U(t) | 50 \rangle|^2$, for $t \in [0, 200]$ at $W = 2$. Up to $t \approx 10$, the wave function spreads into an exponential envelope (note the logarithmic colorscale). After this initial phase, the wave function does not spread further but remains localized.
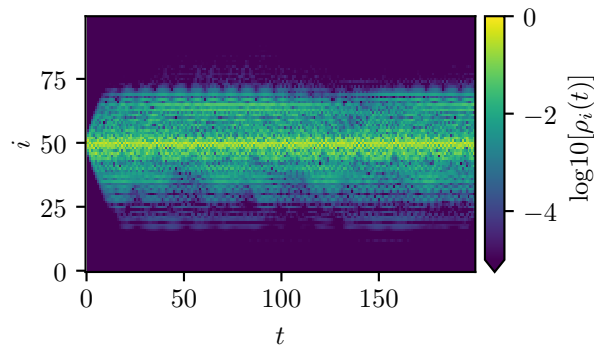
Figure 1.3: Example: Unitary time evolution according to time evolution operator $U(t) = \mathrm{e}^{-\mathrm{i}Ht}$ with a Hamiltonian of the form (1.2) with disorder strength $W = 2$, at system size $L = 100$; starting from initial state $|50\rangle$.
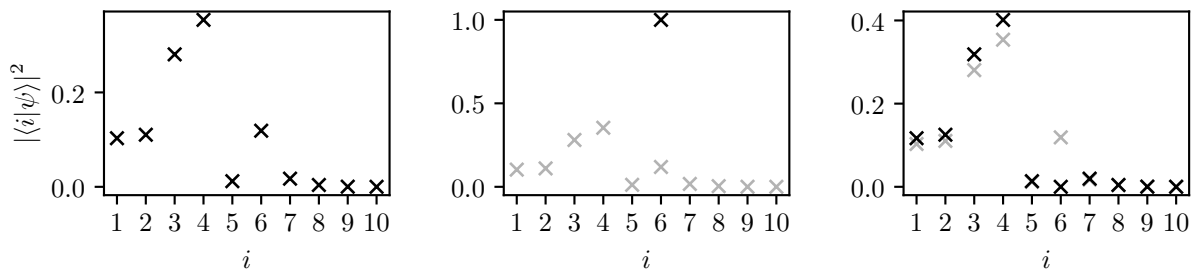
Figure 1.4: Example of the possible outcomes of a measurement with operator $n_6 = |6\rangle\langle 6|$. *Left panel*: On-site probabilities $|\langle i|\psi\rangle|^2$ for some example state $|\psi\rangle$, before the measurement is applied. *Middle panel*: Black marker: Click outcome. The state is projected to the measured site. Grey markers: Non-measured wave function for comparison. *Left panel*: Black markers: No-click outcome. The state is projected away from the measured site and renormalized. Grey markers: Non-measured wave function for comparison.

1.2.2 Time evolution and projective measurements

In quantum mechanics, there are two different paradigms of time evolution. Usually, time evolution is governed by the Schrödinger equation, or equivalently, a unitary time evolution operator [86], which reads for a time interval t and the simplest case of a time-independent Hamiltonian H

$$U(t) = \exp(-\mathrm{i}tH). \tag{1.9}$$

As $U(t)$ is a unitary operator, its effect on a system can be reverted by applying the inverse operator $U^{-1}(t)$. As long as the time evolution of a system is governed by unitary time evolution, the initial state can be reconstructed at any point. This situation changes as soon as a *projective measurement* is performed to determine some property of the system. In quantum mechanics, a measurement typically changes the state of the system [86], thus constituting a form of time evolution that takes place in

the time instant the measurement is performed. The effect of the measurement on the state is called *backaction.*

A *projective measurement* is formulated as follows [66]: Any measurement is associated with an observable $M = \sum_m m P_m$, where P_m projects onto the eigenspace of M with eigenvalue m. The P_m form a complete set of orthogonal projectors,

$$\sum_m P_m = \mathbb{1} \tag{1.10}$$

$$P_m P'_m = \delta_{m,m'} P_m. \tag{1.11}$$

The measurement has $\sum_m$ different possible outcomes, corresponding to the different projectors. Given the state of the system $|\psi\rangle$ before the measurement, there is a probability

$$p_m = \langle\psi| P_m |\psi\rangle \tag{1.12}$$

that the measurement projects the system into the corresponding eigenstate of the operator

$$|\psi\rangle \to \frac{P_m |\psi\rangle}{\sqrt{p_m}}. \tag{1.13}$$

Eq. (1.12) is called the *Born rule.* Due to the completeness of the projectors, the probabilities of all different outcomes sum to one; some outcome is always realized.
Using this, we formulate the on-site measurements that we want to apply to the chain: Consider our lattice spanned by a number of sites $i \in \{1, \ldots, L\}$. The wave function is

$$|\psi\rangle = \sum_{i=1}^{L} c_i |i\rangle, \tag{1.14}$$

where $|c_i|^2$ is the probability to find the particle on site $i \in [1, L]$ of a one-dimensional lattice. In this system, let us consider the set of observables $\{n_j := |j\rangle\langle j|\}$, $j \in \{1, \ldots, L\}$. For each of these observables, we can define projectors

$$P_{\mathrm{c}}^{(j)} := |j\rangle\langle j| \tag{1.15}$$

$$P_{\mathrm{nc}}^{(j)} := (\mathbb{1} - |j\rangle\langle j|). \tag{1.16}$$

Measuring n_j tells us, whether or not the particle is located at a given site j. There are two possible outcomes to this measurement, corresponding to the projector decomposition of the observable: With probability $p_{\mathrm{c}} = |\langle j|\psi\rangle|^2 = |c_i|^2$, the particle is, in fact, found at site j by the measurement (an imaginary measurement apparatus *clicks*), the wave function after the measurement is given by

$$|\psi_{\mathrm{c}}\rangle = |j\rangle \tag{1.17}$$

$$\propto |j\rangle\langle j|\psi\rangle. \tag{1.18}$$

With probability $p_{\mathrm{nc}} = \langle\psi| [\mathbb{1} - n_j] |\psi\rangle = 1 - |\langle j|\psi\rangle|^2 = 1 - p_{\mathrm{c}}$ the particle is not found at the given

site (*no-click event*), the state after the measurement is determined from the second projector

$$|\psi_{\mathrm{nc}}\rangle = \frac{\sum_{i\neq j} c_i \, |i\rangle}{\sqrt{1-p_{\mathrm{c}}}} \tag{1.19}$$

$$\propto \left[\mathbb{1} - |j\rangle \langle j|\right] |\psi\rangle. \tag{1.20}$$

Sometimes, we refer to the outcome of the measurement as the *detector readout*, again alluding to an imaginary measuring device. As an example, see Fig. 1.4: The site-space density $|\langle i|\psi\rangle|^2$ of an example wave function $|\psi\rangle$ before a measurement is displayed in the left panel. This wave function is measured on site 6. Grey crosses indicate the wave function before the measurement for comparison in the other panels. The result of a click outcome (projection to site 6) is displayed in the middle panel. This outcome occurs with a probability of $|\langle 6|\psi\rangle|^2 \approx 0.12$, according to the Born rule. The result of a no-click outcome is displayed in the right panel: The wave function component on site 6 is set to zero, and the wave function is renormalized. The probability of this outcome is $p = 1 - |\langle 6|\psi\rangle|^2 \approx 0.88$.

A projection corresponding to a click event immediately destroys information about the state of the system prior to the measurement. Clearly, after a click-event, there is no way to reconstruct the wave function from before the measurement: Any wave function with a finite component on the click-site is a possible candidate for the pre-measurement state. In this way, measurements render time evolution irreversible.

At every time instance a measurement takes place, there is a branching of possible states corresponding to different outcomes of the measurement. Repeated measurements can therefore lead to an exponentially large number of different wave functions that may all result from the same time evolution protocol at the same time instance. In this context, a single time dependent wave function (corresponding to one particular sequence of measurement outcomes) is referred to as a *quantum trajectory* [87]. The existence of possibly exponentially many different quantum trajectories poses complications for the analysis of a measured system, because:

1. Different quantum trajectories can behave completely differently from each other. Instead of analyzing "the wave function" we have to describe a collection of different wave functions in some meaningful way.

2. Analyzing all quantum trajectories becomes unfeasible after few measurements, if their number grows exponentially.

In this chapter, we describe the ensemble of different quantum trajectories statistically, for example by averaging observables over different quantum trajectories. Instead of performing a complete average over all trajectories, we often use *Monte-Carlo simulations* to obtain an average over a much smaller number N_{it} of trajectories. For this, the time evolution protocol is repeatedly applied to the same initial state. If a measurement occurs, the outcome is chosen at random, with the probability of click- and no-click event dictated by the Born rule (1.12), and the state is updated with Eq. (1.13) according to the outcome.[2] Importantly, one instance of the simulation always follows one random quantum trajectory (a pure state). N_{it} is chosen such that the value of the considered observable converges to

---

[2]As an example, consider a density measurement on site i. Let the amplitude of the wave function on site i at the time of the measurement be $|\langle i|\psi\rangle|^2 =: p$. In our simulation, we generate a random number q, drawn from a uniform random distribution in the interval $[0, 1]$. If $q \leq p$, the measurement outcome is taken to be a click (the particle is detected) and the wave function is updated accordingly. Otherwise, the wave function is updated according to the no-click outcome.

sufficient accuracy. This works, if the ensemble average of the trajectory is dominated by "typical" trajectories (that do not correspond to comparably unlikely sequences of measurement outcomes).

A simple and prominent example for the drastic impact that measurements can have on the time evolution of a state is the *quantum Zeno effect* [4]. The idea is to apply measurements in rapid succession, with very short periods of unitary time evolution in between. Short means here, that the unitary time evolution operator is close to a unity, in the sense of barely affecting the state the system was projected into by the measurement. Therefore, the probability to find the system in exactly the same state again is almost one at the instant of the next measurement. In this way, frequent measurements can "freeze" the state of a system, by resetting it to the same measurement eigenstate over and over again: In a quantum system, repeatedly looking at the arrow actually slows it down [4].

Numerical implementation of projective measurements and unitary time evolution

To simulate a quantum trajectory starting from a given initial state $|\Psi\rangle$, we can perform unitary time evolution and projective measurements numerically. For a single particle on a lattice of L sites, this is straightforwardly done in the basis of lattice sites $\{|1\rangle, \ldots, |L\rangle\}$ as follows:

- Unitary time evolution for a time interval Δt: Calculate the matrix exponential $U_{i,j}(\Delta t) := [\mathrm{e}^{-\mathrm{i}\Delta t[H]}]_{i,j}$ where $[H]$ is the Hamiltonian in site space with elements $[H]_{i,j} = \langle i| H |j\rangle$ (computational complexity of order $\mathcal{O}(L^3)$). Calculate the evolved state as $\langle i|\Psi(\Delta t)\rangle =: \Psi_i(\Delta t) = \sum_{j=1}^{L} U_{i,j}(\Delta t)\Psi_j$. (Computational complexity of order $\mathcal{O}(L^2)$).

- Calculating the probability of a click-event at site a: $p_a = |\Psi_a|^2$ (complexity of order $\mathcal{O}(1)$).

- Updating the state after a click-outcome on site a: Replace the wave function by $\Psi_j = \delta_{a,j}$ (complexity of order $\mathcal{O}(1)$).

- Updating the state after a no-click outcome on site a: Set $\Psi_a = 0$ and renormalize the wave function (complexity of order $\mathcal{O}(L)$).

If a time evolution protocol involving unitary evolution and a projective density measurement at every step is iterated for N_t steps, the complexity is accordingly of order $\mathcal{O}(L^3 N_t)$ for variable Δt, and $\mathcal{O}(L^3 + L^2 N_t)$ for fixed Δt (the matrix exponential is calculated only once).

The computational cost can be reduced by performing the calculation in the basis where H is diagonal. Say, the corresponding basis transformation from site space is described by a matrix $[V]$ with elements $[V]_{i,\alpha} := \langle i|\epsilon_\alpha\rangle$ such that

$$[[V^\dagger][U(\Delta t)][V]]_{\alpha,\beta} = \delta_{\alpha,\beta}\mathrm{e}^{-\mathrm{i}\Delta t\epsilon_\alpha} \quad \alpha, \beta \in \{1, \ldots, L\} \tag{1.21}$$

where the ϵ_α are the eigenenergies of the Hamiltonian. To calculate the click probability on site a, the corresponding site-component of the wave function is restored within $\mathcal{O}(L)$ operations:

$$\Psi_a = \sum_{\alpha=1}^{L} V_{a,\alpha} \langle \epsilon_\alpha|\Psi\rangle \tag{1.22}$$

The components of the state after a click event on site a are obtained as

$$\langle \epsilon_\alpha|i\rangle = V_{\alpha,i}^\dagger \tag{1.23}$$

and after a no-click event on site a the corresponding on-site component is removed according to

$$\langle \epsilon_\alpha | \Psi \rangle - \langle \epsilon_\alpha | a \rangle \langle a | \Psi \rangle = \langle \epsilon_\alpha | \Psi \rangle - \left[\sum_{\beta=1}^{L} V_{a,\beta} \left\langle \epsilon_\beta \middle| \Psi \right\rangle \right] V_{\alpha,a}^\dagger; \qquad (1.24)$$

afterwards, the state is renormalized.

All of these state updates can be performed within $\mathcal{O}(L)$ operations. Therefore, time evolution of the state can be performed in $\mathcal{O}(L^3 + LN_t)$ operations, by

- Diagonalizing the Hamiltonian to obtain the eigenenergies $\{\epsilon_\alpha\}$ and the matrices $[V]$ and $[V^\dagger]$ ($\mathcal{O}(L^3)$ operations). This determines the time evolution operator $U_{\alpha,\beta}(\Delta t)$ for any Δt.

- Performing unitary time evolution according to $\left\langle \epsilon_\alpha \middle| \Psi(\Delta t) \right\rangle = U_{\alpha,\alpha}(\Delta t) \langle \epsilon_\alpha | \Psi \rangle$ within $\mathcal{O}(L)$ operations.

- Calculating the probability of measurement outcomes and updating the state according to Eqs. (1.22), (1.23) and (1.24) within $\mathcal{O}(L)$ operations.

Calculating observables can require rotating back into site space ($\mathcal{O}(L^2)$ operations).

Projective measurements on several non-interacting fermions

Our example of projective density measurements on a lattice with sites $i \in \{1, \dots, L\}$ can be generalized to a many-body situation with several particles on the lattice. In this section we discuss the example of non-interacting spinless fermions, which is convenient from a numerical point of view [88].

If we consider a fixed number of N spinless fermions on a lattice of L sites, the Hilbert space is spanned by $\binom{L}{N}$ states. A possible basis is given by all different "bit-strings" with N 1s and $L - N$ 0s, where a one (zero) designates an occupied (empty) site. For example, if $N = 2$ and $L = 4$, these basis states are

$$|0011\rangle, |0101\rangle, |0110\rangle, |1001\rangle, |1010\rangle, |1100\rangle \qquad (1.25)$$

or in terms of creation and annihilation operators

$$a_3^\dagger a_4^\dagger |0\rangle, a_2^\dagger a_4^\dagger |0\rangle, a_2^\dagger a_3^\dagger |0\rangle, a_1^\dagger a_4^\dagger |0\rangle, a_1^\dagger a_3^\dagger |0\rangle, a_1^\dagger a_2^\dagger |0\rangle. \qquad (1.26)$$

where $a_i^\dagger$ creates a particle on site i. Importantly, the size of the basis is for an extensive number of particles $N \propto L$ exponential in the number of sites L (instead of linear as for a single particle). Choosing for example half-filling $N = L/2$, the number of basis states is

$$\binom{L}{L/2} \sim 2^L / \sqrt{L\pi/2}. \qquad (1.27)$$

As a consequence, only small systems $L \in \mathcal{O}(10)$ are accessible to numerical methods without further approximations, if the entire Hilbert space is relevant for the calculation.

In second quantization, density measurements can be described in analogy to the single particle case

using the projectors

$$P_{\mathrm{c}}^{(j)} := n_j, \tag{1.28}$$

$$P_{\mathrm{nc}}^{(j)} := \mathbb{1} - n_j, \tag{1.29}$$

where $n_j = a_j^\dagger a_j$ is the density operator with creation and annihilation operators on site j, $a_j^\dagger$ and a_j.

Again, immediately after a click outcome, the density on the measured site is one; after a no-click outcome it is zero. The Born rule probabilities and the wave functions after the measurements can be constructed from the projectors as before. Note however, that the correspondence between the measured density profile and the wave function is not as intuitive as in the single particle case—density one on a single site does not completely specify the wave function.

An important tool for the numerical (measured) time-evolution of a non-interacting fermionic system are *fermionic Gaussian states* (in the following just "Gaussian states") [28, 38, 46, 88]. A Gaussian state $|\Psi\rangle$ is by definition[3] completely characterized by two-point correlation functions [88]

$$\langle\Psi| a_j^\dagger a_i |\Psi\rangle := D_{i,j} \tag{1.30}$$

(in general we also need correlators with two creation or annihilation operators, but we limit ourselves in the following to cases where those vanish).

In our example of a lattice with L sites, there are L^2 such correlators. If the time evolution of a many-body system takes place in the subspace of Gaussian states, this means that we can represent the state much more compactly by those correlators, than by all the projections on different Hilbert state basis vectors. Indeed, unitary time evolution with a quadratic Hamiltonian preserves Gaussianity [88]. Importantly, projective density measurements as described above do so as well. This means if we initialize the system in a Gaussian state its time evolution due to a non-interacting Hamiltonian and projective density measurements takes place entirely in the space of Gaussian states, allowing for an efficient representation with just L^2 numbers. This technique is commonly used to analyze non-interacting measured fermionic systems numerically [28, 38, 46].

This is for example done as follows [28, 46, 88]: Let us consider a pure Gaussian state of the form

$$|\Psi\rangle = \prod_{k=1}^{N} \left(\sum_{j=1}^{L} M_j^k a_j^\dagger \right) |0\rangle \tag{1.31}$$

$$= \prod_{k=1}^{N} c_k^\dagger |0\rangle \quad c_k^\dagger := \sum_{j=1}^{L} M_j^k a_k^\dagger \tag{1.32}$$

---

[3]its density operator can be written as an exponential of a "Hamiltonian" quadratic in creation- and annihilation operators [88]

where the numbers M_j^k describe N orthonormal single-particle states on the lattice:

$$\delta_{k,k'} = \langle 0 | c_k c_{k'}^\dagger | 0 \rangle \tag{1.33}$$

$$= \sum_{j,j'=1}^{L} (M^*)_j^k M_{j'}^{k'} \langle 0 | a_j a_{j'}^\dagger | 0 \rangle \tag{1.34}$$

$$= \sum_{j=1}^{L} (M^*)_j^k M_j^{k'}. \tag{1.35}$$

The state can be described by an $L \times N$ matrix $[M]$ with elements $[M]_{j,k} := M_j^k$. The orthonormality condition in terms of this matrix reads $[M^\dagger][M] = \mathbb{1}_N$. The $c_k^\dagger$, c_k are fermionic creation- and annihilation operators fulfilling anticommutation relations

$$\{c_k, c_{k'}\} = \{c_k^\dagger, c_{k'}^\dagger\} = 0, \tag{1.36}$$

$$\{c_k^\dagger, c_k\} = \sum_{j,j'=1}^{L} (M^*)_j^k M_{j'}^{k'} \delta_{j,j'} = \delta_{k,k'}, \tag{1.37}$$

$$\{c_k, a_i^\dagger\} = (M^*)_i^k. \tag{1.38}$$

The correlation matrix of the Gaussian state can be calculated using Wick's theorem

$$D_{i,j} = \langle \Psi | a_j^\dagger a_i | \Psi \rangle = \langle 0 | c_N c_{N-1} \ldots c_1 a_j^\dagger a_i c_1^\dagger \ldots c_N^\dagger | 0 \rangle \tag{1.39}$$

$$= \sum_{k=1}^{L} (M^*)_j^k M_i^k = ([M][M^\dagger])_{i,j}. \tag{1.40}$$

Here, we used Eq. (1.38) for contractions between a and c operators. $i = j$ is a necessary condition for a non-zero contraction, since otherwise the remaining operators contract to zero. From Eq. (1.40) it can be seen that the matrix M (and thus the wave-function) can be reconstructed from the correlation matrix using eigendecomposition.

The time-evolution (unitary, and projective density measurements) can be entirely described in terms of the correlation matrix. Consider first unitary time evolution with an operator $U(t) = \mathrm{e}^{-itH}$ where $H = \sum_{i,j=1}^{L} [H]_{i,j} a_i^\dagger a_j$:

$$D_{i,j}(t) = \langle \Psi | U^\dagger(t) a_j^\dagger a_i U(t) | \Psi \rangle = \langle \Psi | a_j^\dagger(t) a_i(t) | \Psi \rangle \tag{1.41}$$

$$= \sum_{l,l'=1}^{L} [U(t)]_{i,l} [U^\dagger(t)]_{l',j} D_{l,l'} \tag{1.42}$$

$$\Rightarrow [D(t)] = [U^\dagger(t)][D][U(t)] \tag{1.43}$$

using

$$\frac{\partial a_l(t)}{\partial t} = \mathrm{i}[H, a_l](t) = \mathrm{i} \sum_{i,j=1}^{L} [H]_{i,j} [a_i^\dagger a_j, a_l](t) = -\mathrm{i} \sum_{j=1}^{L} [H]_{l,j} a_j(t) \tag{1.44}$$

$$\Rightarrow a_l(t) = \sum_{j=1}^{L} [U(t)]_{l,j} a_j. \tag{1.45}$$

Next we consider a click event on site i, described by the operator n_i. Taking into account normalization of the state, the components $D'_{j,k}$ of the correlation matrix after the click are related to the components $D_{j,k}$ before the click as

$$D'_{j,k} D_{i,i} = \langle \Psi | n_i a_k^\dagger a_j n_i | \Psi \rangle = \langle \Psi | a_i^\dagger a_k^\dagger a_j a_i | \Psi \rangle + \delta_{i,j} \delta_{i,k} D_{i,i} \tag{1.46}$$

$$= \sum_{l,l'=1}^{N} (1 - \delta_{l,l'}) M_i^{*l} M_k^{*l'} \left[-M_j^l M_i^{l'} + M_j^{l'} M_i^l \right] + \delta_{i,j} \delta_{i,k} D_{i,i} \tag{1.47}$$

$$= -D_{i,j} D_{k,i} + D_{i,i} D_{j,k} + \delta_{i,j} \delta_{i,k} D_{i,i} \tag{1.48}$$

where we again used Wick's theorem to calculate the expectation value. The resulting click transformation can be summarized as

$$D'_{j,k} = \delta_{i,j} \delta_{i,k} + D_{j,k} - \frac{D_{i,k} D_{j,i}}{D_{i,i}} = \begin{cases} D_{j,k} - \frac{D_{i,k} D_{j,i}}{D_{i,i}} & i \neq j \text{ and } i \neq k \\ 1 & i = j \text{ and } i = k \\ 0 & (i = j \text{ and } i \neq k) \text{ or } (i = k \text{ and } i \neq j). \end{cases} \tag{1.49}$$

With an analogous calculation the correlation matrix after a no-click event on site i can be expressed as

$$D'_{j,k} = D_{j,k} + \frac{D_{j,i} D_{i,k}}{1 - D_{i,i}} + \frac{\delta_{i,j} \delta_{i,k} D_{i,i} - \delta_{i,j} D_{i,k} - \delta_{i,k} D_{j,i}}{1 - D_{i,i}} \tag{1.50}$$

$$= \begin{cases} D_{j,k} + \frac{D_{j,i} D_{i,k}}{1 - D_{i,i}} & i \neq j \text{ and } i \neq k \\ 0 & \text{else.} \end{cases} \tag{1.51}$$

Using Eqs. (1.42), (1.49), and (1.51) time-evolution of a random quantum trajectory with a measurement protocol combining unitary time evolution and a projective density measurement in one time step can be performed in $\mathcal{O}(L^3 N_t)$ computational complexity, where N_t is the number of time steps:

- Calculating the matrix exponential $U(t)$ in the single-particle basis costs $\mathcal{O}(L^3)$ operations.

- Unitary time evolution according to Eq. (1.42) costs $\mathcal{O}(L^3)$ operations for every time step, as it can be written as two matrix multiplications[4].

- The click- and no-click transformations (1.49) and (1.51) cost $\mathcal{O}(L^2)$ operations each, since L^2 components have to be calculated and each component requires $\mathcal{O}(1)$ operation (note that i is fixed, it is the measured site).

---

[4]We assume the basic matrix multiplication algorithm.

If a large number of time steps is considered, it is again beneficial to consider the time evolution in the eigenbasis of the single-particle Hamiltonian $[H]_{i,j}$ where the operator $[U(t)]_{i,j}$ is diagonal—as in the single particle case. Let the corresponding basis transformation be denoted by a matrix $[V]$,

$$[V]^{\dagger}[U][V] := [\tilde{U}] = \mathrm{diag}(\dots), \tag{1.52}$$

$$\tilde{D} = [V^{\dagger}][D][V] \tag{1.53}$$

Clearly, unitary time evolution in this basis costs only $\mathcal{O}(L^2)$ operations[5],

$$[\tilde{D}(t)] = [\tilde{U}^{\dagger}(t)][\tilde{D}][\tilde{U}(t)] \tag{1.54}$$

$$\tilde{D}_{i,j}(t) = \tilde{U}_i^{\dagger}(t)\tilde{D}_{i,j}\tilde{U}_j(t) \quad \tilde{U}_i(t) := U_{i,i}(t). \tag{1.55}$$

But what about the measurement transformations? The probability to find a particle at site i is

$$p_i = D_{i,i} = ([V][\tilde{D}][V^{\dagger}])_{i,i} = \sum_{j,k=1}^{L} V_{i,j}\tilde{D}_{j,k}V_{k,i}^{\dagger}, \tag{1.56}$$

and can thus be calculated within $\mathcal{O}(L^2)$ operations ("matrix-vector multiplications"). It can be seen that click- and no-click measurements can be expressed as

$$\tilde{D}'_{j,k} = \begin{cases} V_{j,i}^{\dagger}V_{i,k} + \tilde{D}_{j,k} - \frac{1}{p_i}\left[\sum_{i_1=1}^{L} V_{i,i_1}\tilde{D}_{i_1,k}\right]\left[\sum_{i_2=1}^{L} \tilde{D}_{j,i_2}V_{i_2,i}^{\dagger}\right] & \text{click} \\ \tilde{D}_{j,k} + \frac{1}{1-p_i}\left[\sum_{i_1=1}^{L} V_{i,i_1}\tilde{D}_{i_1,k}\right]\left[\sum_{i_2=1}^{L} \tilde{D}_{j,i_2}V_{i_2,i}^{\dagger}\right] + \frac{V_{j,i}^{\dagger}V_{i,k}p_i - V_{j,i}^{\dagger}V_{i,i_1}\tilde{D}_{i_1,k} - \tilde{D}_{j,i'}V_{i',i}^{\dagger}V_{i,k}}{1-p_i} & \text{no-click} \end{cases} \tag{1.57}$$

and both transformations still cost $\mathcal{O}(L^2)$ operations (note that the sums in above expression do not have to be calculated for each component but only once).

As a result, time-evolution in the eigenbasis of $[H]$ can be performed in $\mathcal{O}(L^3 + N_t L^2)$ operations:

- Diagonalization of the Hamiltonian costs $\mathcal{O}(L^3)$ operations. The eigenvalues are used to construct the time evolution operator in its diagonal basis in $\mathcal{O}(L)$ operations. $[\tilde{D}] = [V^{\dagger}][D][V]$ is calculated within $\mathcal{O}(L^3)$ operations.

- Each step of the time evolution protocol can involve constructing a time evolution operator given the time interval of unitary time evolution, performing the time evolution according to this operator, and performing a density measurement at a total cost of $\mathcal{O}(L^2)$ operations.

To calculate observables, rotating back to the original basis can be necessary (at a cost of $\mathcal{O}(L^3)$ operations). However, if the observable is not needed at every time step, employing the basis transformation is still beneficial.

Measurement-induced transitions

The following discussion is based on Ref. [38].

---

[5]There is no summation, each of the L^2 components is calculated within $\mathcal{O}(1)$ operations.

Let us put the numerical method described in the previous section to use, to illustrate the quantum Zeno effect and the idea of measurement-induced transitions. Consider a simple time-evolution protocol consisting of repeating the steps

- Unitary time evolution with Hamiltonian $H = -J \sum_{i=1}^{L}(a_i^\dagger a_{i+1} + \text{hc.})$

- Projective density measurement on a randomly chosen site i

until time $t_{\max}$ is reached. The durations of the time intervals of unitary time evolution are drawn from a random exponential distribution such that the rate of measurements per site and unit time $1/J$ is Γ.

To demonstrate the dynamics governed by this protocol, we show the time evolution of density profiles corresponding to four different measurement rates $\Gamma \in \{0.01, 0.1, 0.5, 2\}$ in Fig. 1.5. The profiles were obtained by initializing a state with $N = 100$ particles at random sites in a system of size $L = 200$, and performing time evolution according to above protocol up to $t_{\max}J = 200$, following a single random quantum trajectory. Increasing the rate gradually, we can observe how the measurements alter the density profile. At a small rate $\Gamma = 0.01$ (upper left panel) few measurements take place per unit time and unitary time evolution distributes the density evenly over the system. Click (no-click) outcomes are visible as yellow (blue) spots in the density profile, forcing an occupied (empty) site. As the measurement rate is increased, many projections lead to a noise-like density profile (upper right panel). At an even higher measurement rate, streaks of the same outcome begin to form as the unitary time intervals between two projections become comparably short (lower left panel). This is a manifestation of the quantum Zeno effect. At the highest displayed measurement rate, the density profile consists of long streaks of occupation one and zero as the rapid succession of measurements freezes the density eigenstates over long time intervals (lower right panel).

Changing the measurement rate clearly leads to qualitative changes in the system dynamics as observed in the density profile—from uniform spreading of the density, to freezing of the initial state. It is natural to ask whether these changes can be associated with a transition in the thermodynamic limit.

Usually, to identify a measurement induced transition, the *entanglement entropy* is considered [22]. The entanglement entropy measures how strongly different parts of a system in a pure state are entangled with each other. Unitary time evolution is associated with increasing entanglement, while a local projective measurement disentangles the measured site from the system. The idea is that a critical measurement rate distinguishes between qualitatively different behavior of the outcome-averaged entanglement entropy in the thermodynamic limit [22].

The entanglement entropy is calculated by partitioning the system into two complementary parts, say A and $\bar{A}$. In our example, $A \subset \{1, 2, \ldots, L\}$ and $\bar{A} = \{1, 2, \ldots, L\}\backslash A$. A *reduced density matrix* ρ_A of subsystem A is defined by tracing the density matrix of the system ρ over the basis of $\bar{A}$:

$$\rho_A := \text{tr}_{\bar{A}}(\rho). \tag{1.58}$$

The entanglement entropy $\mathcal{S}_A$ is defined as the von Neumann entropy of the reduced density matrix

$$\mathcal{S}_A := -\text{tr}(\rho_A \ln \rho_A). \tag{1.59}$$

If there is no entanglement between A and $\bar{A}$, ρ_A corresponds to a pure state and $\mathcal{S}_A = 0$. Otherwise, ρ_A corresponds to a mixed state and $\mathcal{S}_A > 0$.
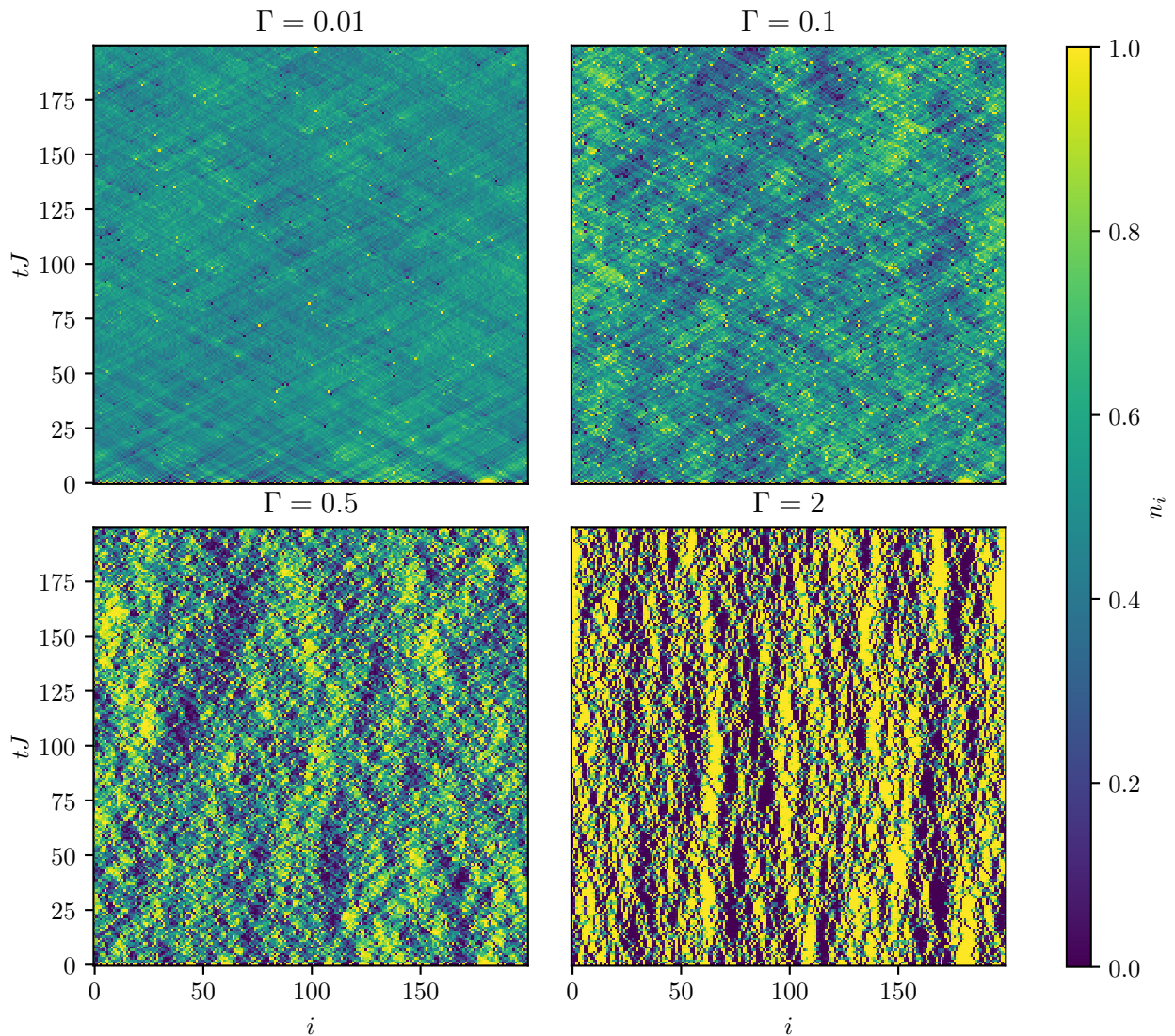
Figure 1.5: Figure adapted from Ref. [38]. Time evolution of density profiles for individual quantum trajectories according to the measurement protocol described in Sec. 1.2.2. The system is initialized by randomly occupying $L/2$ sites. Unitary time evolution is governed by nearest neighbor hopping. Projective measurements are performed at random sites and and random times, such that the expected rate of measurements per site is Γ. A small rate corresponds to few measurements per time interval; unitary time evolution distributes the density evenly over the system (*upper left panel*). Yellow (blue) spots are visible where click (no-click) outcomes force an occupied (empty) site. At a high measurement rate, a fast succession of measurements on the same site can freeze the occupation of that site due to the quantum Zeno effect, thus leading to long traces of the same occupation eigenstate (*lower right panel*).

As a simple example, consider the entanglement entropy between the first site and the rest of the system $\mathcal{S}_{\{1\}}$ for $L = 3$ sites with $N = 2$ particles. If the first site is not entangled with the rest of the system, the reduced density matrix corresponds to a pure state and the entanglement gives zero. For example, if the system is in a state $|\Psi_1\rangle = |1, 1, 0\rangle$ or $|\Psi_2\rangle = 2^{-1/2}(|1, 1, 0\rangle + |1, 0, 1\rangle)$, the reduced density matrix in the basis $|0\rangle, |1\rangle$ reads

$$\rho_{\{1\}} = \begin{pmatrix} 0 & 0 \\ 0 & 1 \end{pmatrix} \tag{1.60}$$

and thus[6] $S_{\{1\}} = 0$. On the other hand, if the first site is entangled with the rest of the system, say $|\Psi\rangle = 2^{-1/2}(|1, 0, 1\rangle + |0, 1, 1\rangle)$, we obtain a density matrix corresponding to a mixed state, here

$$\rho_{\{1\}} = \frac{1}{2} \begin{pmatrix} 1 & 0 \\ 0 & 1 \end{pmatrix} \tag{1.61}$$

and $\mathcal{S}_{\{1\}} = 2\ln(2) > 0$.

In terms of the entanglement entropy, a measurement induced transition is diagnosed by determining the scaling of its average with the size of the subsystem $|A|$ in the thermodynamic limit $|A| \to \infty$. For this purpose, the entanglement entropy is averaged over different quantum trajectories (weighed by their Born-rule probabilities). Possible regimes are for example *volume-law* scaling (the averaged entanglement entropy is proportional to $|A|$ or $|L|$) or *area-law* scaling (the averaged entanglement entropy is proportional to the size of the boundary between A and $\bar{A}$). A third possibility is sub-linear scaling of the entanglement entropy with the sub-system size, for example logarithmically (*critical phase*). Volume-law scaling is associated for example with typical thermal many-body states [89]. A measurement induced transition manifests in a transition between two qualitatively different types of scaling in the entanglement entropy, for example at a critical measurement rate, in the thermodynamic limit. For example, interacting many-body systems with measurements and unitary time evolution have been reported to feature a transition from volume-law to area-law [90–92].

For one-dimensional, non-interacting fermionic systems as the one described above, the existence of a measurement-induced transition at a finite transition parameter has been under debate. Transitions from critical to area-law phase were reported in Refs. [28, 29, 46]. On the other hand, Refs. [32, 93] suggest that measurements always lead to an area-law in such systems.

For above model it was found in Ref. [38] that the entangelement entropy is always characterized by area-law scaling, without a transition. However, to observe the area law, one has to consider subsystem sizes above a correlation length l_{corr} that grows exponentially with the inverse measurement rate [38]. Below l_{corr} a transient regime with critical scaling is predicted. Due to the fast growth of the correlation length with Γ^{-1} the growing extension of the transient phase can easily be mistaken for a measurement induced transition in a numerical study, because a slight decrease of Γ can push the sub-system size required to observe the area-law far beyond the considered system size.

The mathematical derivation of these findings establishes a connection between the measured system in d spatial dimensions and a disordered system in $d + 1$ spatial dimension [38, 41]. Indeed, in two-dimensional disordered systems, the localization length grows exponentially as a function of the mean-free path [64]. On this basis, measurement induced transitions of free fermions in higher spatial dimensions $d > 1$ were predicted, in analogy to Anderson transition in disordered systems with $d >$

---

[6]Understanding the term $0\ln(0)$ as $\lim_{\varepsilon \to 0} \varepsilon \ln(\varepsilon) = 0$.

2 [38, 41] where the system transitions between delocalization and localization as a function of the disorder strength [10].

1.2.3 Classical random walk and diffusion

In many instances, it is helpful to consider a (possibly simplified) picture of the dynamics in a system in the form of a *classical random walk*[7]. A random walk is a stochastic process, which can be described as "successive summation of independent, identically distributed random variables" [96]. As a simple example, consider the discrete position $i \in [1, L]$ of a *random walker* on a one-dimensional chain, with one step of the process defined as a step of the random walker either to the left, or to the right, both with probability $1/2$. Equivalently, this could be formulated as randomly summing values ± 1. This is a memoryless *Markov-process* (the future state only depends on the present state [97]) on the state space of chain sites, described by a transition matrix

$$M_{i,j} := \frac{1}{2} \delta_{\langle i,j \rangle} \tag{1.62}$$

$$\delta_{\langle i,j \rangle} = \left(\delta_{i,j+1} + \delta_{i,j-1} \right) \tag{1.63}$$

where $M_{i,j}$ describes the probability for a random walker to transition from site j to site i. The probability W_i to find the random walker after N_t time steps on some chain site i is then given by

$$[W_{N_t}]_i = \sum_{j=1}^{N} [[M]^{N_t}]_{i,j} [W_0]_j, \tag{1.64}$$

where $[M]$ is the matrix with elements $\{M_{i,j}\}$, $i, j \in \{1, \ldots, L\}$ and the $[W_0]_i$ comprise the initial probability distribution of the random walker over the chain.
The time evolution simplifies in a basis where M_N is diagonal:

$$[D]\mathbf{W}_{N_t} = [D][M]^{N_t}[D^{-1}][D]\mathbf{W}_0 \tag{1.65}$$

$$D_{k,i} := \mathrm{e}^{iik} \tag{1.66}$$

$$\Rightarrow [W_{N_t}]_i = \sum_k \sum_j \mathrm{e}^{-iik} \cos^{N_t}(k) \mathrm{e}^{ikj} [W_0]_j \tag{1.67}$$

$$= \begin{cases} \left(\frac{1}{2}\right)^{N_t} \sum_{j|j-i \text{ even}} \begin{pmatrix} N_t \\ \frac{j-i-N_t}{2} \end{pmatrix} [W_0]_j & N_t \text{ even} \\[2em] \left(\frac{1}{2}\right)^{N_t} \sum_{j|j-i \text{ odd}} \begin{pmatrix} N_t \\ \frac{j-i-N_t}{2} \end{pmatrix} [W_0]_j & N_t \text{ odd} \end{cases} \tag{1.68}$$

---

[7]In this thesis, by random walk, we always mean a "classical random walk" governed by a Master equation with transition probabilities. This should be contrasted with a "quantum walk" [94, 95], governed by the Schrödinger equation and generated by the matrix elements of the Hamiltonian.

(Ignoring boundary effects.) If the random walker is initially at site j_0, W_{N_t} is described by a binomial distribution. For example, for even j_0, i and N_t

$$[W_{N_t}]_i = \left(\frac{1}{2}\right)^{N_t} \begin{pmatrix} N_t \\ \frac{j_0 - i - N_t}{2} \end{pmatrix}.$$ (1.69)

If $N_t \gg 1$ and $(j_0 - i - N_t)/2 \gg 1$, this distribution is well approximated by a Gaussian

$$[W_{N_t}]_i \approx \frac{1}{\sigma\sqrt{2\pi}} \exp\left(-\frac{1}{2}\left(\frac{(N_t - i - j_0)/2 - \mu}{\sigma}\right)^2\right)$$ (1.70)

$$\mu = N_t/2 \quad \sigma = \sqrt{N_t/4}.$$ (1.71)

A closely related process can be formulated in continuous time and space [96]:

$$[W_{N_t+1}]_i - [W_{N_t}]_i = \sum_j (M_{i,j} - \delta_{i,j})[W_{N_t}]_j$$ (1.72)

$$\Rightarrow [W_{N_t+1}]_i - [W_{N_t}]_i = \frac{1}{2}\left([W_{N_t}]_{i+1} + [W_{N_t}]_{i-1} - 2[W_{N_t}]_i\right)$$ (1.73)

$$\rightarrow \frac{\partial}{\partial t}\mathcal{W}(t,x) = D\frac{\partial^2}{\partial x^2}\mathcal{W}(t,x)$$ (1.74)

In the last step we introduced continuous coordinates $x = \Delta x \cdot i$, $t = \Delta t \cdot N_t$, took the limits $\Delta t, a \rightarrow 0$ and defined the *diffusion coefficient* $D := \Delta x^2/(2\Delta t)$. The diffusion equation (1.74) with a localized initial condition is solved by a Gaussian distribution.

Using this result, we can compute the time dependence of the spreading of an ensemble of random walkers over the chain. This can be measured by the mean-square displacement

$$r_2(t) := \int \mathrm{d}x\, \mathcal{W}(x,t)x^2.$$ (1.75)

If $\mathcal{W}(x,t)$ is given by a Gaussian, we can see, that the mean-square displacement asymptotically behaves as $r_2(t) \propto t^{\gamma_{\mathrm{diff}}}$ with the diffusive exponent $\gamma_{\mathrm{diff}} = 1$.

We just discussed one specific model of a random walk, limiting ourselves to one dimension, and symmetric transition probabilities to neighboring sites. Generalization to higher dimensions is straightforward (the diffusive exponent $\gamma_{\mathrm{diff}} = 1$ stays the same in d dimensions), and regarding the transitions, the diffusion law holds true on a much more general basis [96]. This can be understood from the interpretation of a random walk as a summation of random variables, due to the central limit theorem [96]. The central limit theorem states that a sum of independent, identically distributed random numbers is Gaussian distributed, as long as the probability distribution of the random numbers has finite mean and variance. The aforementioned process can thus be generalized for example by introducing a randomly distributed *waiting time* between two transitions, or a more complex distribution of transition distances (*jump distribution*) [98], while the diffusion law still holds true.

However, the diffusion law can in fact break down in a random walk, for example if above assumptions about the waiting time or the jump distance are not fulfilled: If these distributions feature long power-law tails, such that mean or variance diverges, the central limit theorem does not hold true [98]. In some cases, conclusions on the asymptotics of the process can still be drawn, but the characteristics of
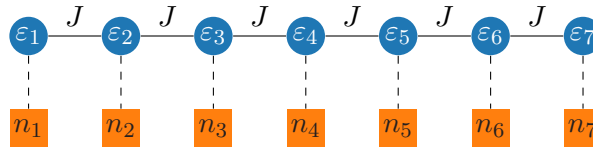
Figure 1.6: Picture of the model. Blue disks are sites of a one-dimensional lattice. According to Hamiltonian (1.2), each site i has an onsite energy ε_i which is drawn from a random distribution. Each site is coupled to its two nearest neighbors via tunneling $J \equiv 1$. We perform projective measurements of the observables $\{n_i\}$ that indicate whether or not site i is occupied.

the diffusive process are violated (*anomalous diffusion*). In particular, if the mean square displacement scales as

$$r_2(t) \propto t^\alpha \tag{1.76}$$

the process is called *subdiffusive*, if $\alpha \in (0, 1)$ and *superdiffusive* if $\alpha > 1$ [99].

1.3 Model

Having introduced the basic concepts for this chapter, we move on to introduce the model and time evolution protocol to be discussed in the following, which combines unitary evolution and projective measurements. In the remainder of this chapter we consider of single particle quantum trajectories.

We consider a one-dimensional Anderson chain, described by the Hamiltonian (1.2), again with $J \equiv 1$. The random onsite energies $\{\varepsilon_i\}$ are are drawn from a Gaussian distribution with zero mean and standard deviation $\sigma_W = W/\sqrt{3}$. ("Disorder strength W" often refers to a uniform distribution of width $2W$ in the literature. Such a distribution has standard deviation $W/\sqrt{3}$. By choosing the standard deviation of our Gaussian distribution accordingly, we get comparable localization lengths etc. at equal disorder strengths, see Fig. 1.2.) The chain is initially prepared in a one-site state $|i_0\rangle$, and subsequently time evolved by iterating N times the two-step protocol

1. Unitary time evolution with $U = \exp\left(-\mathrm{i}H\Delta t\right)$.

2. With probability p, projective measurement of a randomly chosen site.

The time interval Δt is chosen sufficiently large for the wave function to spread within its exponential envelope, $\Delta t \geq \bar{\xi}$. The measured sites $i_{\Delta t \cdot m}$, $m \in [1, N]$ define the *measurement path i_t*. Fig. 1.6 shows a sketch of the model.

Several sources of randomness are contained within the model. One quantum trajectory is defined by the disorder realization $\{\varepsilon_i\}$, the measurement path i_t, as well as the set of all measurement outcomes (click or no click) $n_t \in \{0, 1\}$.

These different sources of randomness give rise to different kinds of averages which can be performed on observables in the system. In the following, we use the notation

$$\langle O \rangle_\psi := \langle \psi | O | \psi \rangle \tag{1.77}$$
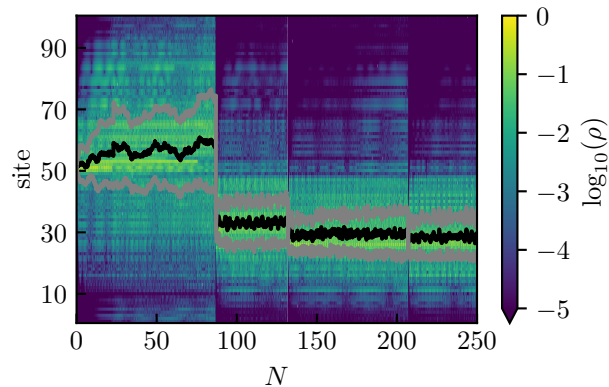
Figure 1.7: Figure adapted from Ref. [53]. Example probability density obtained from a single quantum trajectory at parameters $W = 2$ $p = 1$, $\Delta t = 10$. The black line shows the particle trajectory $r_1(t)$ (cf. Eq. (1.78)). The grey lines show $r_1(t) \pm \xi^{\mathrm{eff}}(t)$ with the effective localization length (1.81).

for the quantum mechanical average with the wave function $|\psi\rangle$, and subscripts o (outcomes), p (measurement paths) and d (disorder realization) to indicate averaging over Monte-Carlo simulations with the subscripted quantities chosen at random between different runs. For example, $\langle O \rangle_{\mathrm{o,p}}$ denotes that observable O is calculated from separate runs with randomly chosen outcomes and measurement paths[8] The outcome average is necessarily always a part of any average, because the outcome probabilities must be governed by the Born rule to get a physically sensible result. It would not make sense to fix the outcomes and average over disorder realizations for example, since this would lead to atypical quantum trajectories where the outcomes would on average not correspond to the Born rule probabilities.

1.4 Particle trajectories and observables

In order to get a feeling for some general aspects of the time evolution protocol, we show the probability density obtained from a single quantum trajectory with disorder strength $W = 2$, $p = 1$, and $\Delta t = 10$ in Fig. 1.7. In this example, several important aspects of the dynamics are represented: Initially, the system is prepared in state $|51\rangle$. Due to localization, the wave function remains localized in a region of size $\mathcal{O}(\bar{\xi})$ around this initial site during time evolution with the Anderson Hamiltonian. Similarly after measurements 87, 132, and 207 at sites 31, 29 and 28 which feature click outcomes, projecting the wave function on the respective site. The first click outcome leads to a large jump over 20 sites, which has a low probability due to the spatially exponential decay of the wave function. All other click

---

[8]If we only average over different measurement outcomes (keeping the disorder realization and the measurement path fixed) the *complete* outcome average can be performed in $\mathcal{O}(N^2)$ operations: The n-th measurement has two different outcomes. If a click event takes place, the state is projected to the measured site, regardless the previous state. So the click outcomes from all existing quantum trajectories can be tracked by adding the corresponding click probabilities weighted by the probability of the quantum trajectory, and attaching the result to one new trajectory (the new one-site state) that is added to the list of time evolved trajectories. All previously existing trajectories are modified according to a no-click outcome. Thus, the number of kept trajectories increases by one at every measurement time step, which gives rise to a computational effort of $\mathcal{O}\left(\sum_{n=1}^{N} n\right) \in \mathcal{O}(N^2)$ operations. We can use this to verify the Monte-Carlo averaging up to $N \sim 10^4$ evolution steps.

events are "typical", taking place close to the center site, where the probability density is high. The probability to have a click outcome for any measurement is $p_{\text{click}} = \frac{1}{N}\sum_{i=1}^{N}\rho_i = 1/N$, therefore the expected number of clicks during $N \in [1, 250]$ is 2.5.

All other measurements result in no-click events, which correspond to black pixels at the respective time and position. Since $\bar{\xi} \ll L$, most no-clicks have only a small renormalization effect on the wave function, as the redistributed amount of weight is exponentially small. As a result, the wave function remains well localized, even throughout long sequences of no-click events.

This should be compared to the non-measured time evolution, Fig. 1.3: Without any measurements, the wave function remains localized indefinitely in the vicinity of the initial position. The occurrence of click events allows shifts of the wave function center by projection to a different region of the chain. No-click measurements lead to slight broadening of the wave function—note how the tail of the wave function grows between $N = 140$ and $N = 200$ in Fig. 1.7.

The observation, that a typical quantum trajectory corresponds to a well localized wave function, performing occasional click-induced jumps motivates a simplified description in terms of moments of the probability density

$$r_q(t) := \sum_{i=1}^{L} \rho_i(t)i^q. \tag{1.78}$$

In particular, we refer to the first moment $r_1(t)$ as the *particle trajectory*, which tracks the path of the localized wave function through the system. The black line in Fig. 1.7 shows the particle trajectory corresponding to the probability density example. In the left panel of Fig. 1.8, an ensemble of 10 such particle trajectories is shown, obtained for parameters $W = 2$, $p = 1$, and $\Delta t = 100$, from a single disorder realization and measurement path; starting at $i_0 = 51$. As a result of random measurement outcomes, the ensemble spreads with time over the system in reminiscence of a jump-facilitated random walk. In the right panel of Fig. 1.7, we summarize the particle trajectories corresponding to all possible measurement outcomes of a fixed random disorder realization and measurement path with the quantity

$$\Pi_i(t) := \frac{1}{N_{\text{o}}} \sum_{\text{o}} \delta_{[r_1^{(\text{o})}(t)],i} \tag{1.79}$$

where $r_1^{(\text{o})}$ is the expected position of the wave function for outcome sequence o rounded to the nearest integer, and N_{o} is the number of sequences. In this quantity, every measurement at a position which did not appear previously in the measurement creates a new line of non-zero probability, which is continued by no-click outcomes. This is best observed at early times $N \in [1, 10]$, where measurements take place far from i_0, leading to dark lines representing a low probability. Over time, the line corresponding to the initial site darkens and evolves into a wider region of moderate probability, as the ensemble of particle trajectories spreads over the system due to click events. Eventually, at times $t \gtrsim 10^3$, the ensemble spreads over a large fraction of the system. Based on two main observations—"delocalization" of the ensemble of particle trajectories over the system, while individual wave functions remain localized—we introduce two observables to further investigate this behavior: The spread of the ensemble of wave functions is described by the displacement

$$\Delta_\mu(t) = [\langle r_2(t)\rangle_\mu - \langle r_1(t)\rangle_\mu^2]^{1/2}. \tag{1.80}$$

Here and in the following, μ denotes the different averages which were taken. Sensible averages are
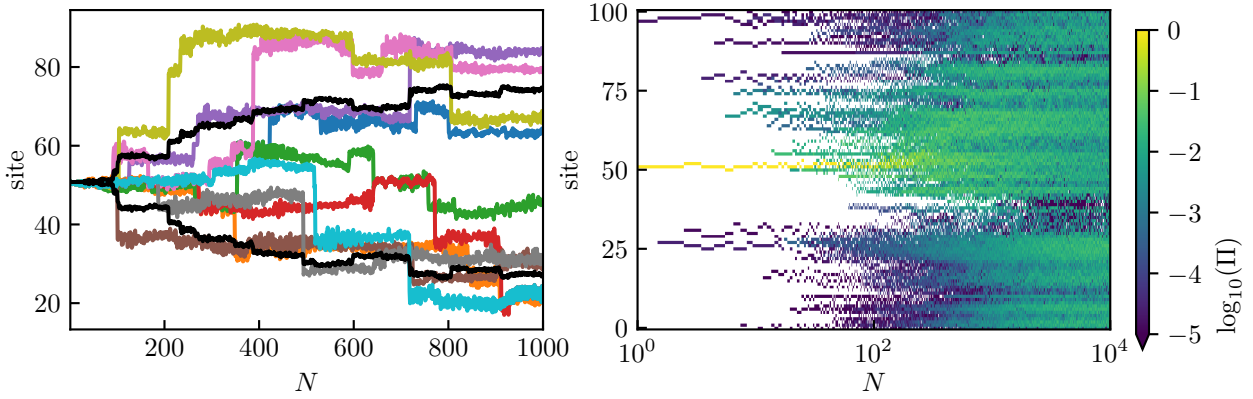
Figure 1.8: Figure adapted from Ref. [53]. *Left panel*: Colorful lines: Ensemble of 10 particle trajectories from random outcome sequences at fixed random disorder realization and measurement path. Black line: $i_0 \pm \Delta_{\mathrm{o}}^{\mathrm{class}}(t)$ averaged over the displayed particle trajectories, see Eq. (1.82). *Right panel*: Time evolution of the position histogram of all possible particle trajectories at fixed random disorder realization and measurement path. The parameters for both plots are $W = 2$, $p = 1$, $\Delta t = 10^2$, and $i_0 = 51$.

(see also the explanation in the beginning of this section):

- No average over realizations at all (no index μ).

- Average over outcomes ($\mu = \mathrm{o}$).

- Average over outcomes and measurement path ($\mu = \mathrm{o}, \mathrm{p}$).

- Average over outcomes and disorder realization ($\mu = \mathrm{o}, \mathrm{d}$).

- Average over outcomes, disorder realization, and measurement path ($\mu = \mathrm{o}, \mathrm{d}, \mathrm{p}$).

In Sec. 1.5 we discuss and compare the effects of different averages. The observable also carries an average index μ, since it may give different results for different averages. To highlight that a result does not depend on the type of average, we use the index μ without specification.

The displacement captures contributions from the spreading of individual wave functions, as well as the spreading of the ensemble of particle trajectories. If strongly localized trajectories spread equally over the entire chain, the spread is given by $\Delta_\mu(t) = L/\sqrt{12}$ if $L \gg 1$.

In order to capture the localized nature of individual quantum trajectories, we introduce the "effective localization length" [100]

$$\xi_\mu^{\mathrm{eff}}(t) = \sqrt{\left\langle \left\langle \left[\hat{x} - r_1(t) \right]^2 \right\rangle_{\psi(t)} \right\rangle_\mu}, \tag{1.81}$$

which serves as a dynamical definition of the "local" localization length, sensitive to changes in the shape of the wave function due to the interplay of localization and measurements. Importantly, the effective localization length quantifies by definition the *spread* of a wave function with respect to its

center site. As opposed to the "true" localization length ξ the spread is determined by the wave function coefficients close to the center site and not by its long exponential tail. For this reason, the effective localization length is not self-averaging. Instead, the variance of its distribution is independent of the system size[9] [85, 100, 101]. For our purposes, the "spread" ξ_μ^{eff} and not the self-averaging ξ is relevant as becomes clear in the following. The average spread is related to the average localization length.

Averaging over an ensemble of point-like densities, $\xi_\mu^{\mathrm{eff}} = 0$. For a wave function exactly of the form (1.1) (without any fluctuations of the exponent ξ) $\xi_\mu^{\mathrm{eff}} = \xi/\sqrt{2}$ if $L \gg \xi$ and $\xi \gtrsim 1$—therefore, the average localization length is related to the average effective localization length.

In Fig. 1.7 we show the effective localization length (grey lines) relative to the particle trajectory $r_1(t)$, confirming our observation by eye of a localized wave function despite measurements.

If we do not perform any kind of average over measurement runs, $\xi^{\mathrm{eff}}(t) = \Delta(t)$. In general, it holds

$$\sqrt{\Delta_\mu^2(t) - [\xi_\mu^{\mathrm{eff}}(t)]^2} = \sqrt{\langle r_1^2(t)\rangle_\mu - \langle r_1(t)\rangle_\mu^2}$$
$$=: \Delta_\mu^{\mathrm{class}}(t) \in \mathbb{R}. \tag{1.82}$$

where $\Delta_\mu^{\mathrm{class}}$ is the classical spread of the ensemble of particle trajectories. In Fig. 1.8 we show $\Delta_o^{\mathrm{class}}$ relative to the initial position i_0 (black lines). As we can see, $\Delta_o^{\mathrm{class}}$ captures the spread of different particle trajectories over the system. The spread Δ_μ captures the spread of particle trajectories as well as the spread of individual wave functions, such that delocalization in either quantity leads to an increase in Δ_μ. In summary, we have three observables that capture the spread of different things:

- ξ_μ^{eff}: Average spread of a wave function with respect to its center site. In the non-measured system related to the average localization length $\bar{\xi}$. For a single wave function, ξ^{eff} describes the spread of that wave function with repect to its center site (a "local" localization length near the center of the wave function).

- $\Delta_\mu^{\mathrm{class}}$: Spread of the ensemble of particle trajectories r_1. For a single wave function $\Delta^{\mathrm{class}} = 0$. If the particle trajectories are spread out evenly over the system, $\Delta_\mu^{\mathrm{class}} = L/\sqrt{12}$.

- Δ_μ: Spread of the ensemble of wave functions. For a single wave function $\Delta = \xi^{\mathrm{eff}}$. If the particle trajectories or the individual wave functions are spread out evenly over the system, $\Delta_\mu = L/\sqrt{12}$.

All observables are calculated immediately before measurements. This is important to capture the effect of the localization length: The system is given enough time to spread to its envelope after the possible occurrence of a projection.

1.5 Measurement induced delocalization

In the previous section, we introduced the observables $\Delta_\mu(t)$—quantifying the spread of the particle trajectories—and the effective localization length $\xi_\mu^{\mathrm{eff}}(t)$. In the absence of measurements, these observables assume their final values within $\mathcal{O}(\bar{\xi})$ hopping times, as a consequence of the eigenfunction's localization in the Anderson chain. In this case, both observables measure the usual disorder localization length in a small window, as the particle remains confined to its initial position. In the following,

---

[9]In this regard the "effective localization length" is more similar to the participation ratio $\sum_i |\psi_i|^4$ than to the actual localization length ξ.
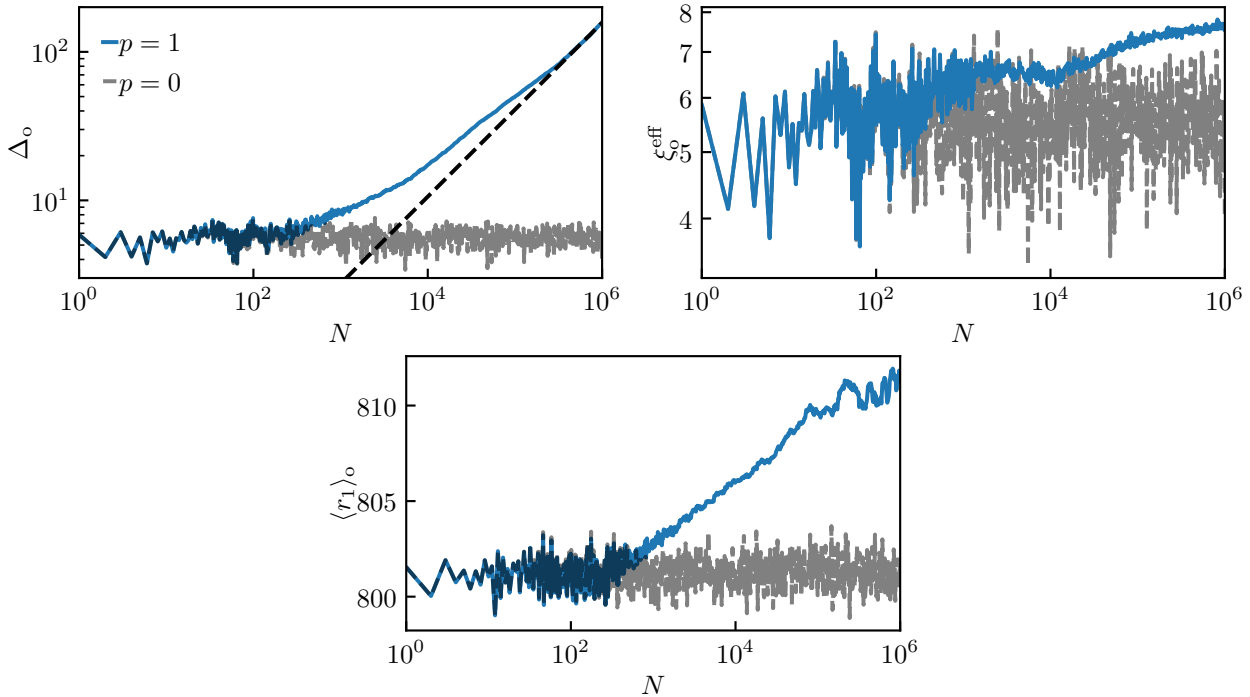
Figure 1.9: Figure adapted from Ref. [53]. *Upper panels*: Displacement (*left*) and effective local-
ization length (*right*) for a system of $L = 1600$ sites, with fixed disorder realization
($\bar{\xi} \approx 7$), $\Delta t = 100$ and fixed random measurement path and initial site $i_0 = 801$.
Time is measured in units of Δt; $t = N\Delta t$. The data is averaged over $4 \cdot 10^3$ mea-
surement outcome sequences. The dashed line in the left panel corresponds to a
power-law with $\Delta_{\mathrm{o}}(t) \propto t^{0.59}$. *Lower panel*: Position expectation value in the same
system. In all panels grey (blue) lines represent $p = 0$ ($p = 1$).

we quantify the impact of uniformly distributed measurements on the dynamics of the system through
these observables.

1.5.1 Different averages

Figure 1.9 shows the observables Δ_{o}, $\xi_{\mathrm{o}}^{\mathrm{eff}}$ and $\langle r_1 \rangle_{\mathrm{o}}$ obtained from an outcome average over $4 \cdot 10^3$ runs
in a system of $L = 1600$ sites, with a fixed disorder realization for $W = 2$ corresponding to $\bar{\xi} \approx 7$
and fixed random measurement path with $p = 1$ (blue lines) and $\Delta t = 100$. Grey, dashed lines show
the same observables in the non-measured case $p = 0$ for comparison. Throughout section 1.5, we use
periodic boundary conditions.

Let us first consider the outcome-averaged position expectation value: At $p = 0$ this value fluctuates
by $\mathcal{O}(\bar{\xi})$ sites around the initial position. These fluctuations are due to the unitary time evolution,
mediating between $|i_0\rangle$ and $\mathcal{O}(\bar{\xi})$ neighboring sites through the localized eigenfunctions. In contrast,
at $p = 1$, the fluctuations are less pronounced, as they average out over different quantum trajectories.
At $N \sim L = 1600$, however, the average position starts to slowly drift away from the initial position,
reaching $i \approx 810$ at $N \approx 10^5$. The drift velocity is very small $v \approx 1/10^4 \ll 1$. At $N \geq 10^5$ the average
drift continues even more slowly, while fluctuations of magnitude $\mathcal{O}(1)$ emerge.

Since $p = 0$ corresponds to a single quantum trajectory, only the spread of the wave function contributes to the displacement Δ. Accordingly, ξ^{eff} and Δ are equal in this case, and $\Delta = \xi^{\text{eff}} \sim \bar{\xi}$. This is similar for the measured case up to $N \ll L/p = 1600$, where again both quantities behave similarly (not shown), since all quantum trajectories away from the initial position are very unlikely— few click events occur up to this point and there are also few impactful no-click events up to $N \sim L/(p\xi) \approx 250$. In consequence, there is no classical contribution to Δ_{o} from the displacement of the wave function center, and the shape of the wave function is largely determined by the unitary time evolution. At $N \sim L$, however, $\xi_{\text{o}}^{\text{eff}}$ at $p = 1$ is increased compared to non-measured ξ^{eff}, while Δ_{o} continues to grow as an approximate power law $\propto t^{\gamma}$ with $\gamma \approx 0.59$ (close to the diffusive exponent $\gamma_{\text{diff}} = 1/2$).

At $N = L$ for $p = 1$, we expect $\mathcal{O}(1)$ click-events for each trajectory, shifting the positions of the wave functions; and no-click events close to the center of the wave functions, redistributing the weight which is projected away from the measured site. Importantly, however, $\xi_{\text{o}}^{\text{eff}} \ll L$, validating the picture of an effective localization length that is still defined in the presence of measurements. Considering the entire time interval, we notice slow fluctuations in the local power law exponent of Δ_{o}; $\xi_{\text{o}}^{\text{eff}}$ reaches a local minimum at $t \sim 10^4$ and slightly increases at later times.

If we redraw the measurement path between runs, in addition to considering random outcome sequences for every run, the features of the plots are largely similar to the exclusively outcome averaged case (not shown). This is expected even for $N \gg L$, when measurements play an important role. The outcome-average alone spatially separates the particle trajectories over time, and at this point different trajectories experience independent measurement locations in their vicinities anyway. There may be subtle differences at intermediate time scales, where many trajectories are still overlapping. However, we are mostly interested in the long-time behavior.

Finally, we consider the observables $\Delta_{\text{o,p,d}}$ $\xi_{\text{o,p,d}}^{\text{eff}}$, $\langle r_1 \rangle_{\text{o,p,d}}$ and $\Delta_{\text{o,p,d}}^{\text{class}}$ with averages over outcomes, paths and disorder at the same parameters $W = 2$, $L = 1600$, $p = 1$, $\Delta t = 100$ (Fig. 1.10). In addition, $\Delta_{\text{o,p,d}}$ and $\xi_{\text{o,p,d}}^{\text{eff}}$ are plotted together in the lower right panel, to demonstrate the difference between $\Delta_{\text{o,p,d}}^{\text{class}}(t)$ (1.82) and $\Delta_{\text{o,p,d}}(t)$. Averaging over disorder realizations and paths, we remove all spatial inhomogeneities from the averaged quantities. As a result, $\langle r_1 \rangle_{\text{o,p,d}}$ is constant up to finite sample fluctuations, also in the measured case. The remaining fluctuations can be explained as follows by the finite sample average: $\Delta_{\text{o,p,d}}^{\text{class}}(t)$ growing with time means that the mean position r_1 of a given trajectory can be considered a random number sampled from an increasingly broad distribution (see Sec. 1.7 for details). Thus, we estimate the magnitude of the finite-sample fluctuations as a function of time by calculating the variance σ^2 in a large sample of averages of $4 \cdot 10^3$ random numbers per sample from a Gaussian distribution of standard deviation $\Delta_{\text{o,p,d}}^{\text{class}}(t)$. We observe, that $\langle r_1(t) \rangle_{\text{o,p,d}}$ is always within $\pm 2\sigma$ (blue shaded area) from zero.

The obtained exponent for the spread $\gamma = 0.49$ is very close to the diffusive value. Contrary to the previous cases, $\xi_{\text{o,p,d}}^{\text{eff}}$ saturates after $\mathcal{O}(10^3)$ measurements to a value that does not further change with time. This is because the introduction of an average over disorder realizations removes, right from the outset, correlations between different runs of the simulation. The converged value of $\xi_{\text{o,p,d}}^{\text{eff}}$ is slightly larger in the measured case $p = 1$ than in the non-measured case $p = 0$. This is discussed in more detail in Sec. 1.5.3.

Regarding the classical displacement, we note that $\Delta_{\text{o,p,d}}^{\text{class}} \approx 1 > 0$ for $p = 0$ as well as $p = 1$ (with $N \lesssim 10^2$). This is due to the spread of the initial wave function across $\mathcal{O}(1)$ sites around $i_0 = 801$. In different disorder realizations, the center position r_1 slightly varies, reflecting in a finite value of $\Delta_{\text{o,p,d}}^{\text{class}}$. At later times, the $p = 0$ curve remains at this initial value, while the $p = 1$ curve grows according to
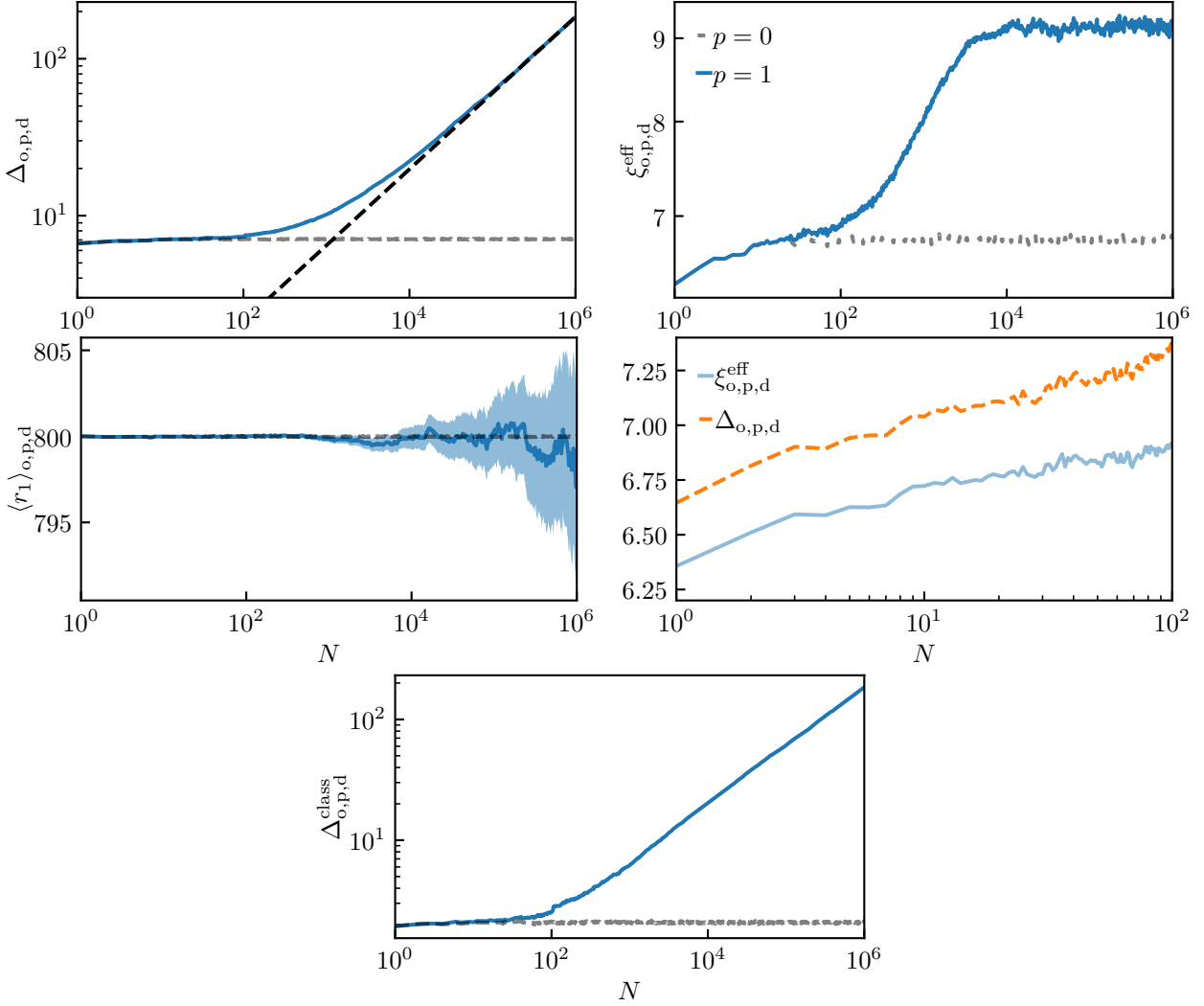
Figure 1.10: Figure adapted from Ref. [53]. *Upper panel*: Displacement (*left*) and effective localization length (*right*) for a system of $L = 1600$ sites, with $\bar{\xi} \approx 7$ and $\Delta t = 100$. The data is averaged over $4 \cdot 10^3$ runs, with random measurement outcomes, paths, and disorder realizations and initial site $i_0 = 801$. The black dashed line in the left panel corresponds to a power-law with $\Delta_{\mathrm{o,p,d}}(t) \propto t^{0.49}$. Blue and grey lines correspond to $p = 1$ and $p = 0$ respectively in all panels. The increased effective localization length in the presence of measurements (blue line in the upper right panel) is discussed in Sec. 1.5.3. *Middle panel*: Position expectation value in the same system with two-sigma finite sample size error estimation from a bootstrap procedure (shaded region) (*left*). Comparison between displacement and effective localization length during the initial evolution (*right*). *Lower panel*: Classical displacement (1.82).

the measurement induced spread of the particle trajectories. Fitting $\Delta_{\mathrm{o,p,d}}^{\mathrm{class}}$ at $N \geq 5 \cdot 10^5$ to a power law, we obtain again $\gamma = 0.49$. Importantly, the classical contribution to $\Delta_{\mathrm{o,p,d}}$ determines its behavior
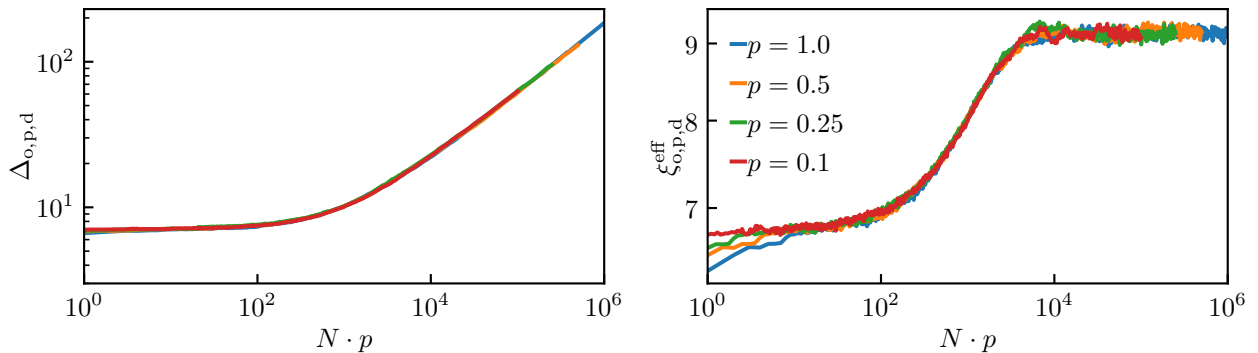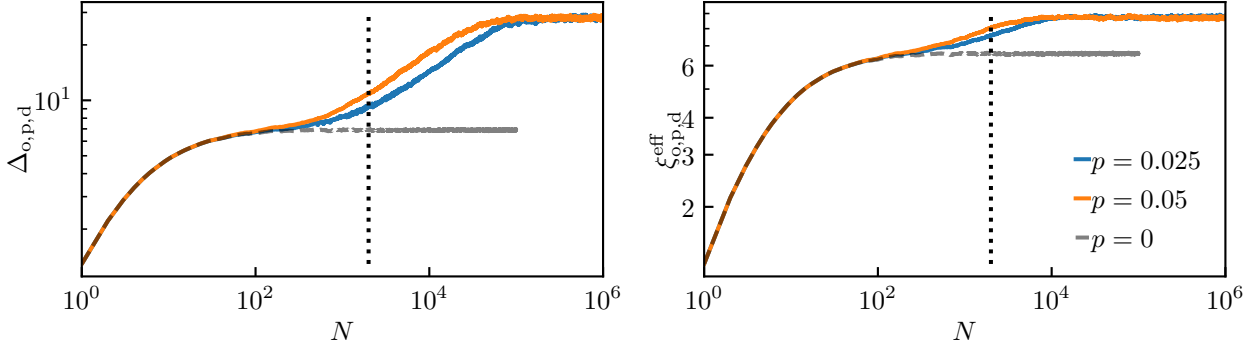
Figure 1.11: Figure adapted from Ref. [53]. Displacement (*left*) and effective localization length (*right*) for a system of $L = 1600$ sites, at $\bar{\xi} \approx 7$ and $\Delta t = 100$ for different measurement probabilities. Each curve is averaged over $4 \cdot 10^3$ runs, with random measurement outcomes, paths, and disorder realizations. The data is plotted over the expected number of measurements $N \cdot p$.

in the long time limit, since the effective localization length converges to a system size independent value, while the trajectories spread over the entire system.

The average number of measurements required to displace the wave function center from a specific site is determined by the spreads of the eigenfunctions peaked close to this site, which are, in turn, determined by the disorder realization. If disorder is not averaged over, a region of small spreads ("traps") slows down all trajectories passing through that region. Such traps can lead to drifting of $\langle r_1 \rangle_{\mathrm{o,p}}(t)$ (partially blocking transport on one side of the system), as well as to fluctuations in $\Delta_{\mathrm{o,p}}(t)$ (traps slow down the average spread) and $\xi_{\mathrm{o,p}}^{\mathrm{eff}}(t)$ (the trap corresponds to small ξ and, thus, small ξ^{eff}). On the other hand, regions of large ξ can speed up the spread and lead to upwards fluctuations in $\xi_{\mathrm{o,p}}^{\mathrm{eff}}$. In the thermodynamic limit $L, N \to \infty$, we expect these effects to vanish, even if the observables are only averaged over outcomes, as the trajectories become increasingly spatially distributed and thus less correlated. This suggests, that the diffusive power law exponent obtained by performing all averages should also be seen at long times, if only an average over outcomes is performed. However, our numerics do not probe the corresponding time scales. Upon disorder averaging, there is an immediate average over different ξ at every point in time, since the observables are averaged with wave functions from different disorder realizations, leading to $\gamma \approx 1/2$ for a sufficiently large sample average. In contrast, if no average over disorder realizations is performed, it takes much longer to reach the diffusive limit. Due to traps, deviating exponents are observed for different disorder realizations on intermediate time scales.

Based on the approximation that the trajectories spread diffusively due to click-events, we can estimate the number of measurements required to achieve a sufficient effective average over different effective localization lengths without performing the disorder average. From Fig. 1.10, we conclude that ~ 1000 independent sites are sufficient for the effect of traps to be averaged out. Therefore, having $\Delta_{\mathrm{o,p}} \sim 10^3 \bar{\xi}$ without disorder averaging should facilitate a similar average. This corresponds to $t' \sim 10^6$, where $t' = Np/L$ is the expected number of click events. We find $N \sim 10^6 L/p$, where we have to set $L \gtrsim 10^3 \bar{\xi}$ to avoid finite-size effects. We find $N \sim 10^9 \bar{\xi}/p$ with an additional numerical $\bar{\xi}$-dependent factor taking into account zero-distance jumps. From this estimate, it is clear that we would have to go to much larger numbers of measurements to find diffusive behavior without averaging over disorder realizations.
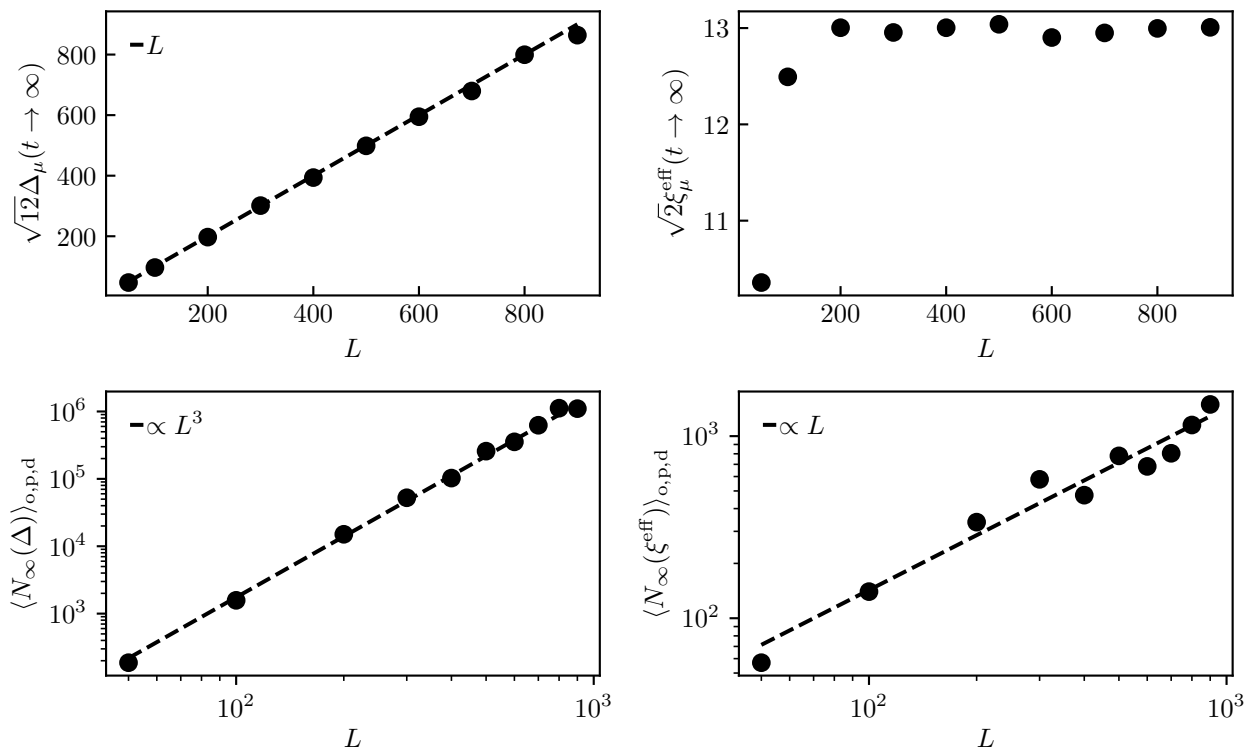
Figure 1.12: Figure adapted from Ref. [53]. Displacement (*left*) and effective localization length (*right*) in a system with $\bar{\xi} \approx 7$ and $L = 100$. The data is averaged over $4 \cdot 10^3$ runs, with random outcomes, disorder realizations and measurement paths ($\Delta t = 1$ here). The vertical dotted lines mark one expected click event, $N_{1c} = L/p$ for $p = 0.05$.

In Fig. 1.11, we compare $\Delta_{\mathrm{o,p,d}}$ and $\xi_{\mathrm{o,p,d}}^{\mathrm{eff}}$ at different measurement probabilities in order to demonstrate that the measurement frequency only rescales the time axis and has no impact on the diffusive exponent, as long as $\Delta t \gg \bar{\xi}$. For this purpose, we plot each quantity as a function of the expected number of measurements $N \cdot p$ on top of each other. Indeed, after an initial phase corresponding to few measurements, the curves lie on top of each other.

1.5.2 Length and time scales

In order to separate the influence of measurements on the average quantities from the non-measured time evolution, we consider small measurement probabilities $p \in \{0.025, 0.05\}$ in a system with $L = 100$ and $\bar{\xi} \approx 7$ ($p = 0$ is shown for reference), averaging over $\mathcal{O}(10^3)$ runs, see Fig. 1.12. We choose $\Delta t = 1$, which does not come with the Zeno effect, since $\Delta t/p \gg \bar{\xi}$. In order to avoid the related intermediate-scale effects, we average not only over outcomes and measurement paths, but also over disorder realizations. Because of the small measurement probability, it takes many steps of the time evolution protocol for the measurements to show a pronounced effect on the system, leading to a separation of the initial time scale, where the observables basically behave as in the absence of measurements (gray, dashed lines), from the time scale, where the effect of measurements sets in. Specifically, for these parameters of the protocol, $N = L/(\bar{\xi}p) \sim 300$ steps are required until one measurement within the localization radius has taken place on average, and about $N = L/p \sim 2000$ steps (black dotted lines) until one click is encountered. Consequently, a difference between the $p = 0$ and $p = 1$ curves becomes apparent between these time steps.

As we observed before, $\xi_{\mathrm{o,p,d}}^{\mathrm{eff}}(t)$ increases to its saturated value $\xi_{\mu}^{\mathrm{eff}}(t \to \infty) > \bar{\xi}$ which is much smaller than the system size, $\xi_{\mu}^{\mathrm{eff}} \ll L$. At the same time $\Delta_{\mathrm{o,p,d}}(t)$ grows according to a power law. The spread of the trajectories is limited by the system size, which shows as a second plateau with $\Delta_{\mathrm{o,p,d}} \approx L/\sqrt{12} \approx 30$—corresponding to uniform spreading over the system. Assuming diffusive spreading of trajectories, driven by click events, the corresponding scale can be estimated as $t'^{1/2} \sim L/\bar{\xi}$, where the time is counted in expected clicks $t' = Np/L$, giving $N \sim L^3/(p\bar{\xi})^2 \sim 6 \cdot 10^5$, in agreement with the actual time of saturation to the second plateau. Since $\xi_{\mu}^{\mathrm{eff}}(t \to \infty)$ is related to no-click events, the corresponding plateau sets in when there is averaging over contributions of all relevant numbers of successive no-click events. As a rough estimate, the probability of a sequence of exclusively no-click
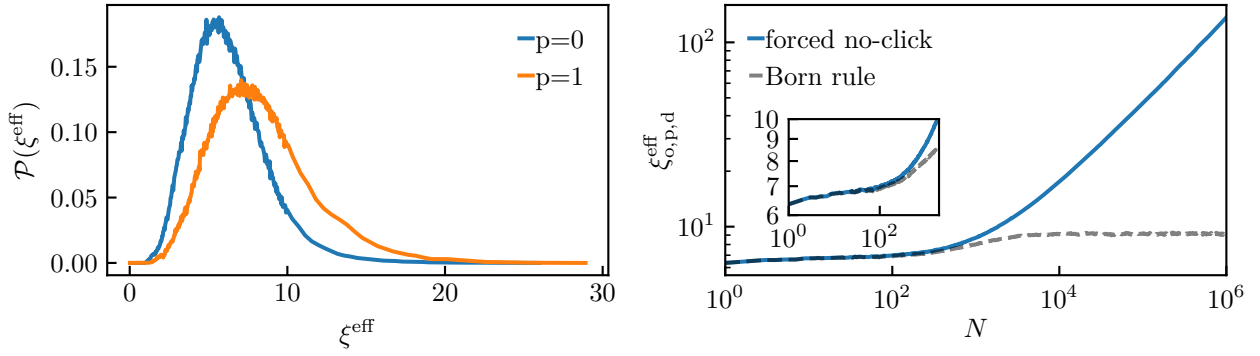
Figure 1.13: Figure adapted from Ref. [53]. *Upper panels*: System size scaling of the time converged values $\sqrt{12}\Delta_\mu(t\to\infty)$ (left) and $\sqrt{2}\xi_\mu^{\text{eff}}(t\to\infty)$ (right) at $\bar{\xi}\approx 7$, $p=1$ and $\Delta t = 100$. *Lower panels*: Required number of measurements to reach 90% of the plateau value for $\Delta_{\text{o,p,d}}$ (left) and $\xi_{\text{o,p,d}}^{\text{eff}}$ (right) in the same system.

events decreases exponentially with the length of this sequence. We thus estimate $N \sim L/(p\bar{\xi}) \sim 300$ with the numerical factor depending on the details of effective localization length's origin.

In the upper panel of Fig. 1.13, we demonstrate the scaling of $\Delta_\mu(t\to\infty)$ (left) and $\xi_\mu^{\text{eff}}(t\to\infty)$ (right) with the size of the system for parameters $p=1$, $W=2$, $\Delta t = 100$. In agreement with uniform spread over the entire system, we find $\sqrt{12}\Delta_\mu(t\to\infty)(L) \approx L$ (lower left, dashed line). On the contrary, $\xi_\mu^{\text{eff}}(t\to\infty,L)$ (lower right) saturates to $\sqrt{2}\xi_\mu^{\text{eff}}(t\to\infty,L\to\infty) \approx 13$ for $L \gtrsim 250$. This further validates that there are still localized wave functions in the presence of measurements, despite the spread of trajectories. In the lower panels, we plot the number of measurements required to reach the plateaus in $\Delta_{\text{o,p,d}}$ (left) and $\xi_{\text{o,p,d}}^{\text{eff}}$ (right); confirming the cubic (linear) dependence on the system size.

1.5.3 Effective localization lengths

The average value of $\xi_\mu^{\text{eff}}(t\to\infty)$ depends non-trivially on W, p, Δt and L. In particular, W determines $\bar{\xi}$ and, thus, the average value of $\xi_\mu^{\text{eff}}(t\to\infty)(p=0)$. We already observed that finite p leads to an increase in $\xi_\mu^{\text{eff}}(t\to\infty)$ in the limit $\Delta t/p \gg \bar{\xi}$. We do not consider the Zeno limit $\Delta t/p \to 0$, where $\xi_\mu^{\text{eff}}(t\to\infty) \to 0$; however this limit implies that $\xi_\mu^{\text{eff}}(t\to\infty)(\Delta t/p)$ has a maximum at finite $\Delta t/p$. In the upper right panel of Fig. 1.13, we see the effect of L acting as an upper cutoff on $\xi_\mu^{\text{eff}}(t\to\infty)$.

Figure 1.14: Figure adapted from Ref. [53]. *Left panel*: Probability distribution of effective localization lengths in measured ($p = 1$) and non measured ($p = 0$) system for $\bar{\xi} \approx 7$, $L = 300$, and $\Delta t = 100$. These effective localization lengths were obtained in the time window $[2900, 3000]$ (where the effective localization length is converged for these parameters, see Fig. 1.13) and histrogrammized from $4 \cdot 10^3$ runs with different disorder realizations and measurement paths and random measurement outcomes. *Right panel*: Comparison of $\xi_{\mathrm{o,p,d}}^{\mathrm{eff}}$ with forced no-click only outcomes to usual time evolution according to our protocol, both at parameters $L = 1600$, $W = 2$, $\Delta t = 100$. The inset shows a close-up of the time interval $[1, 2 \cdot 10^3]$.

Concerning the effect of measurements on the effective localization length, we know that every click outcome resets $\xi^{\mathrm{eff}} \to \xi^{\mathrm{eff}}(\Delta t)$—recall that observables are calculated immediately before the measurement, thus after the interval of unitary time evolution. Because $\Delta t/p \gg \bar{\xi}$, the wave function is given enough time to spread into its exponential envelope. A no-click outcome outside of the effective localization length has an exponentially small effect. A no-click event within the effective localization length can lead to enhancement of the wave function tails and, thus, to a slight growth in ξ^{eff}, resulting in $\xi_\mu^{\mathrm{eff}}(t \to \infty) > \bar{\xi}$. To further illustrate the effect of measurements on the localization length, we compare in the left panel of Fig. 1.14 the distributions of effective localization lengths in the measured and non-measured case for $\bar{\xi} \approx 7$, $\Delta t = 100$, $L = 300$. In this figure, we histogrammize effective localization lengths obtained from $4 \cdot 10^3$ random disorder realizations time evolved with our protocol, at $p = 0$ and $p = 1$ respectively, with random measurement paths and -outcomes. For every instance, we calculate ξ^{eff} at 100 successive time steps, between $2.9 \cdot 10^3$ and $3 \cdot 10^3$.

The $p = 0$ distribution captures the stochasticity of effective localization lengths (the spread of the wave functions with respect to their center sites) in the non-measured system between different disorder realizations, which was investigated for bulk eigenfunctions in Ref. [100]. As expected, the measurements enhance the distribution towards larger effective localization lengths. Importantly however, the overall shape of the distribution is qualitatively preserved. While the distribution of inverse effective localization lengths of eigenstates at fixed energy is known to be Gaussian [75, 100, 101] this only approximately describes the distributions shown in Fig. 1.14 since our wave functions are given by linear combinations of a few eigenstates, and states of all energies are taken into account. Prominent features are a maximum (typical ξ^{eff}) between quick decay towards small effective localization lengths and a long tail towards large localization lengths. Since in the fully averaged case the effective localization length is still larger than in the free system, we conclude that the increase of average $\xi_\mu^{\mathrm{eff}}(t \to \infty)$ in

the presence of measurements has to be connected to no-click events, since clicks reset the contribution of a wave function to the non-measured value.

To show this more explicitly, consider the right panel of Fig. 1.14: The grey dashed line shows the already established result for $\xi_{\text{o,p,d}}^{\text{eff}}$ at parameters $L = 1600$, $\Delta t = 100$, $W = 2$, which converges to $\xi_\mu^{\text{eff}}(t \to \infty) \approx 9$. The blue solid line is obtained by forcing a no-click outcome at every measured site. The inset shows a close-up of the time interval $[1, 2 \cdot 10^3]$ to demonstrate that the curves coincide in the initial phase, where the expected number of click events is low. In the forced no-click case, in contrast to the Born rule simulation, $\xi_{\text{o,p,d}}^{\text{eff}}$ does not show a plateau, but continues to increase throughout the observed time window. This demonstrates again the delocalizing effect of no-click events. Without occasional click events, the wave functions would eventually completely delocalize and spread across the entire system. Note that this delocalization process could take much longer if we simply post-selected trajectories with no-clicks only. In such a trajectory the measurements would typically take place in the tail of the wave function, where the impact on the wave function is smaller. Forcing no-click outcomes, the measurement position is equally distributed along the chain. This procedure bears a certain similarity to "forced measurements" discussed in Ref. [102], but in that paper all quantum trajectories (also involving click outcomes) were forced to be equally likely. In our case, we have "forced measurements with no-click postselection". When the Born rule is employed, delocalization induced by no-click outcomes is stopped by a single click event; as a result, the true effective localization length saturates.

To summarize the above, we have found that randomly distributed measurements lead to delocalization of particle trajectories. Each projective measurement transfers the particle to the measured site. Following this process for a sufficient time span, the probability to find a particle at a particular site is equal for all sites. At long times, the spread of particle trajectories due to this process is described by a diffusive power law $\Delta_\mu(t) \propto t^{1/2}$ independent of the performed averages. During this process, the wave functions are still well described by an effective localization length, as opposed to spreading over the size of the system, despite the delocalizing impact of no-click events.

1.6 Steering with measurements

In the preceding section, we concluded that random measurements all over the system lead to delocalization of quantum trajectories, while almost all individual trajectories correspond to localized particles. This raises the question, if the well-defined location of the particle can be efficiently manipulated, inducing controlled transport in a "localized" system by performing measurements according to an appropriate steering protocol.

The concept of having localized trajectories with the location governed by click events can be applied to steer the particle from its initial site to a specified target, with the goal of having a click at the target. The average number of measurements required to achieve this goal defines efficiency of the measurement protocol, which dictates the measurement path. In a localized system, where only the target site is measured, the expected number of measurements would increase exponentially with the system size. Contrarily, if the wavefunction is completely delocalized, the expected number of measurements would scale linearly with system size, when measuring again only the target site. In our localized system, where all sites may be measured, we expect to find efficient (sub-exponential), non-trivial measuring strategies, since, on the one hand, quantum trajectories seem to spread over the system on a non-exponential time scale, while, on the other hand, still corresponding to localized

wavefunctions.

In order to investigate spatial steering, we consider the following setup. In a system of L sites we initialize the particle at site $i_0 = 1$ and specify a target site $i_{\text{target}} = L$ (using open boundary conditions). Again, we consider large times between two measurements $\Delta t \gtrsim \bar{\xi}(W)$, in order to avoid confining or repelling the particle through the Zeno effect. The goal is to design a measurement protocol that leads to a click outcome at the target site after as few measurements as possible. The time of arrival in a quantum lattice was also studied in Refs. [49, 103]. Hereby, we differentiate between two types of protocols: *Adaptive protocols*, which may use the readouts from every performed measurement in determining the position of the successive measurements; and *blind protocols*, which may only use the readout at the target site.

The simplest protocol one may think of is to just repeatedly measure the target site, until the particle is detected. Since this protocol requires readout only at the target site, it is a *blind* protocol with the termination policy employed. Based on the localized nature of the system, this protocol typically terminates after an exponentially large number of measurements $N \in \mathcal{O}(\exp(L/\bar{\xi}))$, upon averaging over disorder realizations. As this protocol scales exponentially with the system size, it becomes impractical (also for numerical simulations), if L is of the order of a couple of localization lengths.

At the same time, there is a simple adaptive protocol, which is optimal in the sense that $\langle N \rangle_{\text{o,d}} \propto L$. This protocol works as follows:

1. Place the detector at $i_1 = i_0 + 1$.

2. Measure this site, until the particle is detected.

3. Shift the detector by one site towards the target.

4. Repeat steps 2 - 4.

Given that the expected number of measurements until the next click is finite, the total number of measurements scales linearly with the system size. For numerical simulations, we use a slightly improved version of this protocol: Instead of always measuring at a distance 1 from the site where the last click event took place, we randomly measure sites within one localization length of this site in the direction of the target site. This has two benefits: Local dips of the wave function as well as effects of preceding no-click events are avoided. Indeed, the left panel of Fig. 1.15 demonstrates that the simulated expected number of measurements for this protocol (blue dots) scales approximately linearly with the system size (black fit line). In this sense, ballistic transport is realized by this protocol.

Evidently, efficient steering is possible, if the readout is always accessible. In an experiment, however, this may not be the case. Therefore, we try to find a blind protocol with an expected number of measurements that behaves polynomially with the system size. As an attempt to improve the runtime of the blind protocol, we perform blind measurements along the chain at random locations until the particle is detected at the target site. As we already observed, this leads to approximately diffusive spread of the trajectories and is thus much more efficient than only measuring the target site. In simulations, we are able to steer the particle to a target site at a distance of several hundred localization lengths, see the right panel of Fig. 1.15. The simulation values for $\langle N \rangle_{\text{d,p,o}}$ (blue dots) scale approximately with $f(L) \sim L^3$ (black dashed line), as expected in a diffusive system.

We thus demonstrated a possibility of efficiently manipulating (dragging) a particle subject to a random potential in a one-dimensional chain by means of measurement-induced steering, using both
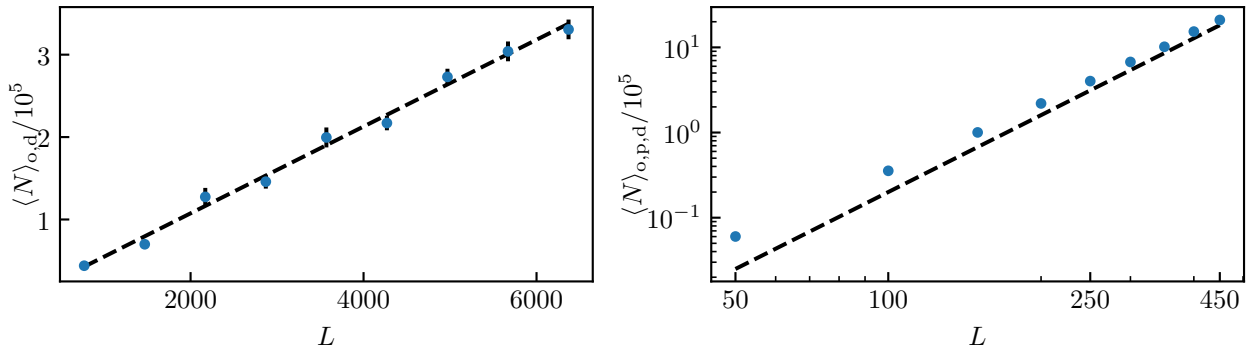
Figure 1.15: Figure adapted from Ref. [53]. Scaling of adaptive readout protocol (*left panel*) and random blind protocol (*right panel*) as a function of system size, for $W = 2$, $\Delta t = 100$. The dashed lines show a linear fit (*left panel*) and the function $f(L) \sim L^3$ (*right panel*) as a guide for the eye.

passive (blind) and active (adaptive) protocols. This type of steering can be further generalized to more sophisticated scenarios, as compared to simply moving the particle through the chain from one end to the other. In particular, one may envision manipulating several particles in the disordered background (not necessarily in a one-dimensional system) to exchange their positions and braid them by measurements.

1.7 Relation to a classical random walk

In this section, we describe how the dynamics of the spread of particle trajectories in our measured system is related to a classical random walk model. The random walk picture is useful for several reasons. For a wide variety of random walks, asymptotic properties are known, allowing us to explain the long-time behavior of our system. The random walk language offers a simplified description of the dynamical features of the ensemble of particle trajectories, which are much more difficult to calculate analytically when taking its full quantum nature into account. Our main question is about the asymptotic behavior of the spread $\Delta_\mu(t)$ (or, equivalently, the asymptotic behavior of $\Delta_\mu^{\mathrm{class}}(t)$). In Sec. 1.5 we argued, that the particle trajectories spread diffusively in the long time limit, and in the following we use the random walk picture to back up this statement analytically.

On the level of particle trajectories, the measurement-induced dynamics bears immediate similarity to a classical random walk. Consider a set of states $\{i\}$ with $i \in [1, L]$, representing the sites of the system. Approximating the position of a trajectory by the nearest site and limiting our consideration to the discrete set of time points immediately after a measurement, every particle trajectory is described by transitions $i \to j$ with $i, j \in [1, L]$. A natural approach is to describe the ensemble of different particle trajectories in terms of transition matrices $M(n)$ with $n \in [1, N]$, acting on a state ϱ with $\varrho_i(n)$ corresponding to the probability to find a particle on site i at time step n, and

$$\varrho_i(n+1) = \sum_{j=1}^{L} M_{i,j}(n)\varrho_j(n). \tag{1.83}$$

We assume that the transitions are mediated by click events, with the transition probabilities deter-

mined by the wave functions immediately before the measurement. Indeed, we showed in Sec. 1.5 that the effect of no-click events can essentially be viewed as a correction to the localization length. Since on average every L-th measurement produces a click, one time step in Eq. (1.83) thus implies L steps of the measurement protocol.

At this point, we need to specify properties of the $M_{i,j}(n)$, incorporating localization into the classical picture through the statistics of these matrix elements. Localization implies that the transition probability decreases exponentially with the distance. Therefore, we keep only transitions over distances one and zero (distance one representing unit distance $\mathcal{O}(\bar{\xi})$ jumps) and consider a symmetrical nearest-neighbor transition matrix

$$M_{i,j}(n) = \delta_{i,j}p_i(n) + \delta_{(i+1),j}\frac{\bar{p}_j(n)}{2} + \delta_{(i-1),j}\frac{\bar{p}_j(n)}{2}; \tag{1.84}$$

$$\bar{p}_i = 1 - p_i \qquad i,j \in [1,L], \tag{1.85}$$

where respective boundary conditions should be taken into account.

In this model, at every time step n, the particle either remains on a given site i with *waiting probability* $p_i(n)$, or jumps with equal probabilities $\bar{p}_i(n)/2$ to one of the two adjacent sites. The waiting probabilities are assumed to be time independent, $p_i(n) =: p_i \quad \forall n$ (we comment later on this assumption). They are drawn from a probability distribution $\mathcal{P}_p(p)$ which is related to localization and determined in the following.

The key insight is, that the asymptotic behavior of the spread $\Delta_\mu(t)$ crucially depends on the probability of zero distance jumps, corresponding to successive click events at the same site (*waiting* on that site). If zero distance jumps never occurred ($p_i = 0 \quad \forall i$), the corresponding random walk would necessarily give diffusion.

If there was however a long tail in the distribution $\mathcal{P}_p(p)$ towards large waiting probabilities $p \to 1$, rare regions with atypically large waiting probabilities could slow down the jump-facilitated transport (inducing many distance zero jumps), resulting in subdiffusion. The distribution of waiting probabilities $\mathcal{P}_p(p)$ is related to the distribution of inverse effective localization lengths $y = 1/\xi^{\text{eff}}$, since the probability for the particle to "wait" on a site $|j_0\rangle$ is determined by the peak weight of the wave function $\langle i|j_0(t)\rangle$[10]. We thus make the connection to the localized wave functions, by choosing the distribution of the waiting probabilities $\mathcal{P}_p(p)$ according to the distribution of inverse effective localization lengths $\mathcal{P}_y(y)$—see Fig. 1.16 for an illustration.

The probability distribution of the inverse effective localization length $y := 1/\xi^{\text{eff}}$ of eigenfunctions at a given energy E and disorder strenth W is given by a Gaussian [75, 100, 101],

$$\mathcal{P}_y^E(y) = \mathcal{N}_1 \exp\left[-\frac{1}{2}\left(\frac{y - \mu(W,E)}{\sigma(W,E)}\right)^2\right] \qquad y \in [0,\infty), \tag{1.86}$$

with normalization constant $\mathcal{N}_1$, variance σ^2, and mean μ. For the toy model, we approximate the probability to have a zero distance jump p_i to be given by the center-site maximum of the localized

---

[10]The waiting probability is determined by the spread of the wave function (quantified by ξ^{eff}), not by the localization length ξ. As the wave function decays exponentially, only a small region around the center site is accessible for measurement-induced jumps. For this reason there is a distribution of waiting probabilities in the first place, instead of a constant waiting probability given by the self-averaging localization length.
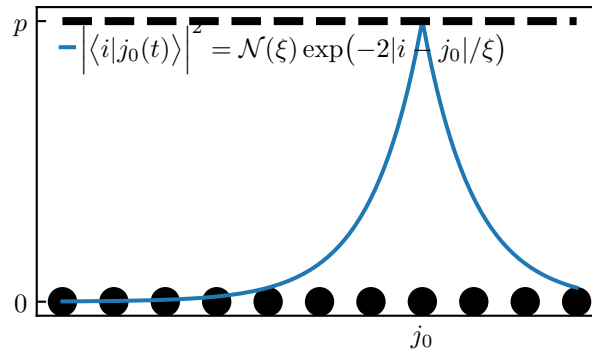
Figure 1.16: Figure adapted from Ref. [53]. Illustration of the relation between localization length ξ and waiting probability p: After a click event on site j_0 and successive time evolution over period t (without further click events), the density $|\langle i|j_0(t)\rangle|^2$ with localization length ξ establishes. The waiting probability p to have another click event at j_0 (distance zero jump) is connected to the localization length via the density on the center site $p = |\langle j_0|j_0(t)\rangle|^2 = \mathcal{N}(\xi)$.

probability density at time t after the click event

$$|\langle i|j_0(t)\rangle|^2 = \mathcal{N}(\xi) \exp\left(-2|i - j_0|/\xi\right) \tag{1.87}$$

$$\mathcal{N}(\xi) = \frac{\exp\left(2/\xi\right) - 1}{\exp\left(2/\xi\right) + 1} \qquad L \gg 1, \tag{1.88}$$

where ξ is obtained from the effective localization length ξ^{eff}. This approximation provides a mapping between the random variables p (representing a waiting probability) and y (representing an inverse effective localization length). After a click on an arbitrary site j_0 the waiting probability is given by

$$p = |\langle j_0|j_0(t)\rangle|^2 \tag{1.89}$$

And since the probability on the center site is given by $p = \mathcal{N}(\xi^{\text{eff}}(y)) \sim \mathcal{N}(1/y)$ (neglecting a constant factor between localization length and effective localization length), we get

$$p(y) = \frac{\exp(2y) - 1}{\exp(2y) + 1}. \tag{1.90}$$

We use this mapping for the change of variables $y \to p$ in $\mathcal{P}_y(y)$. From $y \in [0, \infty)$, it follows that waiting probabilities between 1 and 0 can be found: $p \in [0, 1)$. The probability distribution for the p_i

at a given energy takes the form

$$\mathcal{P}_p^E(p) = \frac{\mathcal{N}_1}{1-p^2} \exp\left\{-\frac{\left[\log\left(\frac{1+p}{1-p}\right) - 2\mu\right]^2}{8\sigma^2}\right\}. \tag{1.91}$$

where the energy dependence is encoded in μ, σ, and $\mathcal{N}_1$—see Eq. (1.86).

Since our time evolution protocol includes all eigenstates, we average over the band to obtain the waiting probability distribution

$$\mathcal{P}_p(p) = \int dE \nu(E) \mathcal{P}_p^E(p) \tag{1.92}$$

with the density of states ν. The correspondence between $\mathcal{P}_p(p)$ and $\mathcal{P}_y(y)$ is only approximate, since the wave function in our time evolution protocol is actually a superposition of eigenfunctions. Due to the exponential decay of the eigenfunctions we can however reasonably replace this superposition by the dominantly contributing eigenfunction (this becomes exact in the strong disorder limit $\xi \to 0$).

Using the random-walk picture, we can now address the question of diffusion in $\Delta_\mu(t)$ at asymptotic times. As mentioned before the asymptotic behavior of the random walk is governed by the behavior of $\mathcal{P}_p$ for $p \to 1$, because sites with a waiting probability of almost one provide bottlenecks for the dynamics in the system. Sites with large waiting probabilities correspond to wave functions with small localization lengths. It is known that spatial randomness in a potential can lead to anomalous transport via long tails towards waiting probability one [104]. It was shown in Ref. [105], that a random walk as specified above behaves diffusively, if the distribution of $\tau(p) := 2/(1-p)$ has a finite mean value. For our distribution, this mean value exists as it can be easily calculated for distribution (1.91).

Thus, we find $\Delta_\mu(t) \propto N^{1/2} \propto t^{1/2}$ in the asymptotic limit.

As explained in Sec. 1.5, this expectation is independent of the performed averages (provided that *any* average is performed) and holds thus true even if only the average over outcomes is taken. In this case however, on intermediate time scales which are not described by the toy model ($N \gg L$, $\Delta_o \sim \bar{\xi}$), few sites have a large impact on the dynamics. This can lead to apparent sub- or even superdiffusive dynamics on these time scales. If a fraction of trajectories reaches a site with $\xi^{\text{eff}} > \bar{\xi}$ ($\xi^{\text{eff}} < \bar{\xi}$), there is an increase (decrease) with time in the effective localization length (see Fig. 1.9 for an example). In the random-walk picture, this may be understood as a time-dependent jump distance distribution, which can raise or lower the local exponent of the power law in Δ_o.

As a last remark on the model, we reconsider the assumption of time independent p_i. In contrast, in our system, the probabilities p_i change due to no-click events altering the shape of the wave function, and oscillating contributions of different eigenfunctions to the wave function. However, since we found diffusion including "memory effects", we would find the same result if the $p_i(n)$ were taken to be completely uncorrelated in time while drawn from the same distribution.

Below, we give a brief summary of the other simplifications in the toy model

- We approximate all jumps distances greater than zero by a unit-distance. This is justified because the probability to jump over a distance x decreases exponentially with x/ξ.

- The model is based on the statistics of the eigenstates of the Anderson Hamiltonian. However, the actual wave functions result from time evolution of one-site states. The approximation is

justified by the exponential decay of the eigenstates, which implies that only $\mathcal{O}(\bar{\xi})$ sites overlap significantly with the original site.

- The effect of no-click events on the shape of the wave function is not explicitly taken into account. However, we showed that no-click events can be viewed as a correction to the effective localization length. We can incorporate corrections to this simplification on a phenomenological level through a modification of the localization length.

In summary, by introducing a classical random walk toy model of the particle trajectory ensemble, we are able to confirm that the spread of the ensemble behaves diffusively in the long time limit, thus supporting our findings from Sec. 1.5. In the random walk picture, click events facilitate jumps on the lattice, with the average localization length setting the typical jump distance. Since the wave functions fall off exponentially around a center site, jumps of distance zero are most likely. However, analyzing the distribution of localization lengths, we showed that such waiting events do not lead to subdiffusion.

With the insights from the random walk, we take another look at our measurement steering protocols. Turning first to the blind protocol with random measurements, we can identify the average runtime of the protocol with the maximum expected hitting time of a random walk on a connected graph [106]. This is the number of steps which the random walker needs to take on average, to first arrive on the most distant site, and it scales as L^2 for a simple chain [106]. Since we need $\propto L$ measurements to induce one step, we find $\langle N \rangle \propto L^3$, as seen in the numerics. For the adaptive protocol, the asymptotic behavior of the waiting probability distribution confirms a linear relation between the system size and the expected number of measurements, since the moments of the waiting times on a site do not diverge. This also implies that there is a Gaussian probability distribution of the steering times for sufficiently large system sizes, in accordance with the central limit theorem.

1.8 Summary

In this chapter, we investigated the dynamics of a single particle in a one-dimensional Anderson chain, subject to projective on-site measurements (the model was introduced in Sec. 1.3). Combining disorder-induced localization and measurements, the question arises whether measurements can introduce transport and whether localization is affected by the measurements. Interestingly, we found that while the measurements indeed lead to transport (and in this sense to delocalization), the wave functions of different quantum trajectories are still typically localized. This motivated us to investigate functions of moments of the wave functions, averaged over different quantum trajectories (corresponding to different sequences of outcomes), which where introduced in Sec. 1.4. The exponential localization of the wave function gives a meaning to the time dependent first moment (the position expectation value), which we refer to as a particle trajectory. Performing measurements at random locations, we found that particle trajectories, driven by click events, spread asymptotically diffusively over the system, independent of the considered ensemble (different outcomes, disorder realizations, or sequences of measurement locations). At the same time, the wave functions remain localized along individual quantum trajectories, but with a modified effective localization length (see Sec. 1.5) which we calculated as the spread of the wave function with respect to its first moment. The spread of the mean square displacement of the particle trajectories from these ensembles can be understood in terms of a classical random walk with random waiting times (or probabilities), which are inherited from the distribution of effective localization lengths via the probability on the center site of the localize wave function (the probability to perform a distance zero jump). This distribution falls off rapidly towards

long waiting probabilities, thus confirming the diffusive asymptotics of the spread. This argument was formulated in Sec. 1.7.

Above findings suggest that efficient steering protocols can be formulated, performing deliberate measurements to move the particle through the system to a predefined target site within a number of measurements, which is polynomial in the system size. We demonstrated this in Sec. 1.6: Given access to the readout of every measurement, ballistic steering is possible, reaching the target site with a number of measurements linear in its distance to the initial site. The idea is to repeatedly measure a location close to the last known position of the particle towards the target, thus "dragging" it towards the target. Even without having access to the detector readouts besides at the target (blind steering), a click-measurement at the target can be achieved within a cubic number of measurements, by just measuring random locations—making use of the diffusion law.

Our model is an intuitive platform to understand the concepts of Anderson localization and projective measurements, and to gain some intuition for aspects of the interplay between them. Introducing measurements at random positions to a localized system immediately changed its dynamics, transitioning from exponentially localized to diffusive transport. In this way, the measurements give rise to a classical picture of a moving ensemble of particle trajectories, which is influenced by the quantum localized nature of the wave functions.

Some questions remain open that could be investigated within our model. As an example, it may be interesting to observe the onset of the quantum Zeno effect by going from the considered regime of large time intervals of unitary evolution $\Delta t \gg \xi$ to smaller time intervals. If the time of unitary evolution is made a random quantity, this could lead to anomalous transport. In this case, the localization length would serve as a cut-off for the jump distribution. Due to its non-monotonic behavior, it would also be worthwhile to take a closer look on the average effective localization length as a function of the measurement probability.

Furthermore, there are many possible generalizations to this model, that could be interesting. Some of them have already been investigated in the literature. Clearly, the introduction of more particles or even interactions complicates the situation not only numerically but also conceptually. An Anderson chain with multiple fermions under continuous monitoring was investigated in Ref. [46], with a focus on a measurement-induced entanglement transition. Systems of measured interacting disordered fermions were considered in Ref. [47]. If several particles are present, the meaning of localized wave functions is less clear and it becomes more difficult to separate transport and localization in above sense [46]. Also, the interpretation of the wave function after a projective measurement is less obvious[11].

At the same time, in the presence of several particles, more elaborate steering may be attempted to introduce designed correlations into the system, possibly mimicking the behavior of an interacting system. Interactions on the other hand can lead to dynamical transitions in a disordered system themselves, adding to the interest of their interplay with measurements [47].

---

[11]For a single particle a click leads to a one-site localized state, a no-click to a hole. How does this generalize to two-particles? Of course this can be calculated from the projection operators, but the result is less intuitive.

2 Chapter 2
Memory effects in the imbalance in delocalized disordered systems

In this chapter, we study on a general basis the decay of short-scale excitations in disordered systems without strong localization. Non-interacting, one-dimensional systems are completely localized in the presence of disorder, no matter how weak. As a consequence, spatial correlations decay exponentially and transport is exponentially suppressed. However, in the presence of interactions or in higher dimensions, strong Anderson localization breaks down and is reduced to a transport correction. If this happens, we would naturally expect diffusive transport over distances much larger than the mean free path, due to many scattering events on the random disordered potential. The situation is less clear considering the response of the system to a short-scale density modulation (corresponding to a large wave vector): If the particles can remove the modulation by traveling only a short distance of the order of the lattice constant, we may expect exponentially fast equilibration (or "memory loss") of the initial state. In the following, we demonstrate that this intuition is false, as is also known from numerical studies. Instead, the relaxation of such large wave vector excitations is governed by power-law tails, keeping memory of the initial state for a long time. As we find out, this is the generic behavior for disordered systems without strong Anderson-localization. In particular, this discussion is relevant on the ergodic side of the many-body localization transition which is studied numerically and experimentally by monitoring the long-time decay of the density imbalance between even and odd numbered lattice sites after setting up a strongly imbalanced state initially. Our approach correctly reproduces the imbalance exponent observed far from the transition. Using a phenomenological approach to subdiffusion, we are able to relate the decay exponent to the exponent of the mean-square displacement. Our analytical results are confirmed by numerical simulations in non-interaction two-dimensional systems, in an intermediate weak-localization regime where the localization length is much larger than the system size.

The contents of this chapter are based on Ref. [54]. Large passages of Secs. 2.1, 2.3, 2.4, 2.5, and Sec. 2.6 are direct quotes and most Figures are adapted from this publication[1]. The results were developed and discussed together with my coauthors. The initial ideas and steps of this project are contained in my master thesis, but all main results [2] where established only afterwards.

---

[1] Reprinted excerpts / figures with permission from [Paul Pöpperl, Igor V. Gornyi, and Alexander D. Mirlin, Phys. Rev. B 106, 094201 Published 6 September 2022]

[2] In particular, the calculation at finite temperature, the justification of the lowest-order (in crossing lines) calculation, the phenomenological generalization to subdiffusion, the discussion of weak localization corrections, and all of the numerical results and approaches.

2.1 Introduction

Without interactions, random disorder leads to Anderson-localization. While all states are exponentially localized at finite disorder and infinite system size in one- and two-dimensional systems, localization in higher dimensions requires a minimum critical disorder strength [8–10].

Many-body localization (MBL) [11, 14–19] is the generalization of the concept of Anderson localization to interacting disordered systems. Similar to Anderson-localization MBL is characterized by the absence of transport in the thermodynamic limit. A consequence of the absence of transport is the inability of a system to *thermalize*: Generic quantum mechanical systems thermalize in the sense that matrix elements of local observables can be calculated from a thermal ensemble average after waiting for a sufficient amount of time after imposing an initial state. Thermalization implies that these observables "loose their memory" of the initial state, as they can be calculated from ensembles that do not contain any information about it. This may be surprising due to unitary time evolution keeping a perfect memory of the initial state. As explained in Ref. [19], this can be understood intuitively by picturing subparts of the system being immersed in a thermal bath provided by the much larger surrounding environment. Stationary states are then described by quantum statistical mechanics [107, 108]—similarly to ergodicity [3] in classical systems. As in classical physics, thermalization is the generic behavior of large quantum mechanical systems, and it is thus interesting to explore special situations where this basic physical concept is not applicable. As disordered systems exhibit localization in the absence of interactions, it is natural to expect, that disorder provides such special circumstances.

As of now, it is widely accepted, that in randomly disordered one-dimensional systems with short-range potentials and interactions there exists even in the thermodynamic limit a finite *critical disorder strength* above which the system fails to thermalize and thus becomes many-body localized [11, 14–19, 109], even though the critical disorder in the commonly investigated Heisenberg chain model has moved from $W_c \sim 3$ in earlier works [110] to larger values $W_c \sim 5$ [57] due to advances in numerical methods. Arguments in favor of an estimate as high as $W_c \sim 18$ were put forward recently [109]—the critical disorder is still debated from numerical and analytical perspectives.

The two phases separated by the critical disorder are called *thermal* (or *ergodic*) and *many-body localized* phase. As the many-body localized phase is approached, the onset of the transition manifests itself in slow, *subdiffusive transport* (sometimes distinguished as a third "prethermal" phase) [59–61, 111, 112]. The latter ergodic phase is of interest for us in this chapter, as we are investigating disorder effects in the absence of localization. In this regime, spatial correlations decay as power-laws with exponents slower than the diffusion law. If the disorder strength is sufficiently low, the system behaves diffusively [60]. Intuitively, this can be understood in terms of a finite coherence length introduced by the interactions: Interactions serve as a cut-off for the length of interfering forward- and backward paths in the weak-localization picture.

As an indicator to distinguish beetween MBL- and thermal behavior, the *density imbalance* is commonly used in experimental, as well as numerical studies [55–58]. For this, an initial state with a strong imbalance between densities of neighboring (even- and odd) sites is set up, and is monitored as a function of time. In a localized system, the suppression of transport prohibits equilibration of the state, and the imbalance remains finite even after arbitrary times. Without localization, the density imbalance is expected to quickly decay to zero. In this chapter, we investigate this imbalance decay for $t \to \infty$.

Naively, one may expect the density imbalance between neighboring sites to decay almost instantly in

---

[3]Adopting the language of Ref. [19], we use the word *ergodic* synonymously to thermalizing

the absence of localization: In a classical picture, each particle only has to travel to its neighboring site to establish equilibrium from such a large wave-vector initial state. Indeed, the diffusion propagator at large momenta decays exponentially with time [113, 114], and this result is also expected from the Boltzmann equation [57]. This should be contrasted with the decay of an initial state corresponding to a small wave vector—for example a step-distribution of the density in one dimension. In such a situation, the particles have to travel over long distances, possibly scattering on many impurities to smoothen out the initial state, and the diffusion propagator decays slowly according to the diffusion law.

Interestingly, the expectation of an exponential imbalance decay on the ergodic side of the MBL transition is disproven by numerical studies, which indicate a power-law decay of the imbalance in the delocalized phase [57, 58, 115–118]—this means that the imbalance as a function of time features a "long tail", instead of decaying within few mean free times. As we show in the following, this property of the imbalance is actually generic for disordered systems in the absence of localization. We demonstrate, that such long-time tails arise from "memory effects" beyond the diffusion approximation. The physical origin of this memory are scattering paths that correspond to large momentum exchange on a single impurity followed by diffusive motion and finally return and again large momentum exchange on the same impurity. In this way, the diffusion propagator aquires a small momentum and decays slowly.

From above reasoning it is clear that the resulting correction to the imbalance is related to the return probability (the probability for a random walker to eventually return to the initial region after some time t). The importance of similar return effects for transport in a disordered system has been recognised already in Refs. [119, 120]. Their effects on magnetoresistance and the *ac*-conductivity where investigated in Refs. [62] and [63].

In this chapter, we formalize above argument about the cooperation of the "fast mode"—taking away the large momentum in a single scattering event—and the "slow mode"—governing diffusive motion at low momentum, together leading to a slow decay of large-q initial states. The relevance of this "mode coupling"[4] mechanism for the imbalance decay was predicted in Ref. [57]. Calculating the corresponding contribution to the imbalance using the diagrammatic disorder averaging technique, we find the imbalance in a diffusive system to decay as $I(t) \propto t^{-d/2}$, where d is the number of spatial dimensions. The dependence on the spatial dimension (in contrast to the diffusion exponent) can be understood from the relation of the process to the return probability.

We generalize our argument to subdiffusion in interacting systems, by assuming an effective (momentum dependant) diffusion constant [122] $D \propto q^\beta$, obtaining $I(t) \propto t^{-d/(2+\beta)}$. Our theory, which substantiates earlier proposals [57, 117, 123] for the role of long-time tails, thus provides a relation between the exponents characterizing the mean square displacement and the imbalance decay that was observed in numerical simulations [59, 117].

To support our analytical results and to demonstrate that in a disordered system mode coupling generically leads to the power-law decay of the imbalance specified above, we performed numerical simulations of a non-interacting two-dimensional (2D) system.

As in 1D systems, all eigenfunctions decay exponentially as a function of distance, according to their localization lengths in 2D. However, there is an essential difference to the 1D case: While the average localization length in 1D is proportional to the mean free path, the relation between localization length and mean free path in 2D is given by $\xi = le^{\pi k_{\mathrm{F}} l/2}$ at the Fermi level [51, 64]. As a consequence, there is a parameter regime (in terms of disorder strength and system size) in 2D, where $l \ll L \ll \xi$. A particle can travel over a distance of several mean free paths without experiencing localization. This diffusive

---

[4]The application of this term in the context of Anderson localization seems to date back quite a while [121].

regime is important for our numerical approach: Instead of considering an interacting system, where localization effects are suppressed due to interactions, we can test the validity of our results in a 2D system in this transient regime. The numerical time evolution of non-interacting systems initialized in a product state is of polynomial complexity $\mathcal{O}(L^2)$ due to the time evolution taking place in the subspace of single slater determinants. This should be compared to the exponential complexity of performing time evolution in the N-particle Hilbertspace of an interacting system. In this way, we can access the exact long-time dynamics in a big system (up to 200×200 sites). The numerical results confirm the analytically predicted power-law decay of the imbalance, $I(t) \propto t^{-\gamma_I}$, governed by the memory effects, with the exponent γ_I somewhat below unity due to weak multifractality [5].

The structure of the remaining chapter is as follows. In Sec. 2.2, we introduce some of the fundamentals specific to the following sections. In Sec. 2.3, we define the imbalance $I(t)$ and derive a relation between the long-time asymptotics of the imbalance and the density response function. In Sec. 2.4, the diagrammatic calculation of the long-time tail in the imbalance resulting from memory effects is performed. Supporting numerical results are presented in Sec. 2.5. Our findings are summarized in Sec. 2.6.

2.2 Fundamentals

In this section we briefly introduce some theoretical concepts that are relevant for this chapter. This overview is mainly based on Refs. [2, 64]. We also give some references to the primary and secondary literature.

Sec. 2.2.1 provides an overview over the diagrammatic technique for disorder averaging. In Sec. 2.2.2, diffusion and weak localization corrections to the density correlator are discussed in the diagrammatic framework. Sec. 2.2.3 introduces the interference picture of weak localization.

2.2.1 Diagrammatic treatment of a disordered system

In the preceding chapter, we considered disordered systems from a numerical point of view, by explicitly diagonalizing a Hamiltonian, given a disorder realization on the lattice. In order to obtain analytical results for correlation functions, we use in this chapter the diagrammatic approach, utilizing the central limit theorem to average Green's function over disorder [64, 126].

Consider the exact retarded electronic Green's function of a disordered, non-interacting lattice

$$\mathcal{G}^{\mathrm{R}}_{i,j}(\varepsilon) = \left(\varepsilon \delta_{i,j} - [H_0]_{i,j} - U_i \delta_{i,j} + \mathrm{i}0 \right)^{-1} \tag{2.1}$$

in site space $i, j \in \{1, \dots, L\}$. $[H_0]_{i,j}$ is the hopping term, which we approximate by a parabolic dispersion in the continuum limit. Disorder is introduced through the disorder potential U_i. Here, we model disorder by assuming a spatial distribution of *impurities* at independent random positions

---

[5]Multifractality of the wave function (self-similarity in real space, that can not be described by a single fractal exponent) generically occurs in a critical disordered system, close to an Anderson transition (for example delocalized to localized in 3D) [10]. In 2D, there is no Anderson transition; all wave functions are localized in the thermodynamic limit. However, since the localization length is exponentially large, there is a regime, where a finitely sized system "looks critical" approaching the disorder strength driven crossover to localization lengths below the system size while the change of localization length with disorder strength is very slow [9]. This is a known mechanism for the emergence of intermediate-scale multifractality [101, 124, 125].

$$\{j_1, \ldots, j_{N_{\text{imp}}}\}$$

$$U_i := \sum_{k=1}^{N_{\text{imp}}} [V_0]_{i-j_k}, \tag{2.2}$$

where each impurity is described by the same potential $[V_0]_i$. In the following we assume $\sum_{i=1}^{L} [V_0]_i = 0$ for convenience. This assumption can be lifted by adding a constant energy shift.

Due to the spatial randomness, we can think of the $[V_0]_{i-j}$ as random vectors on the lattice, which are independent and identically distributed. According to the (multidimensional) central limit theorem, the probability distribution of their sum is thus described by a normal distribution in the limit $N_{\text{imp}}/V, N_{\text{imp}} \to \infty$. At fixed system volume, the variance of this distribution is proportional to $\sqrt{N_{\text{imp}}/V} =: \sqrt{n_{\text{imp}}}$. Thus, we scale the amplitude of each impurity as $V_0 \sim n_{\text{imp}}^{-1/2}$ to consider the limit $N_{\text{imp}}, n_{\text{imp}} \to \infty$ at fixed disorder strength. We obtain the distribution

$$\mathcal{P}(\{U_i\}) \propto \exp\left(-\frac{1}{2} \sum_{i,j=1}^{L} U_i K_{i,j} U_j\right) \tag{2.3}$$

$$\to \mathcal{P}[U] \propto \exp\left(-\frac{1}{2} \int d^d r_1 \, d^d r_2 \, U(\mathbf{r}_1) K(\mathbf{r}_1, \mathbf{r}_2) U(\mathbf{r}_2)\right) \tag{2.4}$$

in the limit $n_{\text{imp}} := \frac{N_{\text{imp}}}{V} \to \infty$, where the $K_{i,j}$ are the components of the covariance matrix which can be calculated explicitly with the central limit theorem. In the second line we take the continuum limit $i \to \mathbf{r}$ for convenience. Applying continuum results to the lattice is fine, as long as the ultraviolet cut-off due to the lattice constant does not affect the calculation.

Assuming a Gaussian distribution (2.4) of disorder configurations is called *Gaussian approximation* [64, 126]. It is convenient, because an average of a product of random potentials over disorder configurations fulfills a Wick's theorem in this approximation, decomposing into a sum of all pairwise expectation values. (Terms with an odd number of potentials vanish, because we assumed zero mean of the potential.) After performing a disorder average, the potential is thus fully characterized by the pair correlator

$$\langle U(\mathbf{r}_1) U(\mathbf{r}_2) \rangle := \int \mathcal{D}\{\mathbf{r}\} \mathcal{P}[U] U(\mathbf{r}_1) U(\mathbf{r}_2) =: W(\mathbf{r}_1 - \mathbf{r}_2). \tag{2.5}$$

This is used to construct diagrammatic rules for dealing with Green's functions of the disordered system.

As an example, consider the disorder average of a single exact Green's function (2.1). Expansion in powers of the disorder potential yields

$$\langle \mathcal{G}^{\text{R}} \rangle = \langle G_0^{\text{R}} \rangle + \langle G_0^{\text{R}} U G_0^{\text{R}} \rangle + \langle G_0^{\text{R}} U G_0^{\text{R}} U G_0^{\text{R}} \rangle + \langle G_0^{\text{R}} U G_0^{\text{R}} U G_0^{\text{R}} U G_0^{\text{R}} \rangle + \langle G_0^{\text{R}} U G_0^{\text{R}} U G_0^{\text{R}} U G_0^{\text{R}} U G_0^{\text{R}} \rangle + \ldots, \tag{2.6}$$

where we denoted the disorder average with angular brackets. In terms of diagrams, this reads

In the first line, we denoted each disorder potential by a dashed line with a cross. In the second line, we performed the disorder average using Wick's theorem: Diagrams with odd numbers of disorder lines drop out; in diagrams with even numbers of disorder lines we form all combinations of pairwise connections of the disorder lines. Each disorder "arc" corresponds to a pair correlator (2.5).

The disorder averaged perturbative expansion is equivalent to forming a sum of free Green's functions dressed with all possible pairwise connections of disorder lines; or, analogously, all possible combinations of arcs.

The lowest order correction to the self energy is given by a diagram with a single arc,

corresponding to the expression

$$\Sigma^{\mathrm{R}}(\mathbf{p}, \varepsilon) = \int \mathrm{d}^d p_1 \, \frac{W(\mathbf{p} - \mathbf{p}_1)}{\varepsilon - p_1^2/(2m) + \mathrm{i}0}. \tag{2.7}$$

To evaluate this expression, we have to assume some form of the correlator $W(\mathbf{r}_1, \mathbf{r}_2)$. We specify *white noise disorder*

$$W(\mathbf{r}_1, \mathbf{r}_2) := \Gamma \delta(\mathbf{r}_1 - \mathbf{r}_2), \tag{2.8}$$

where $\Gamma = (2\pi\nu\tau)^{-1}$ controls the strength of the disorder potential. τ is the elastic scattering time, and ν is the density of states at the Fermi level. White noise disorder corresponds to the limit of extremely short-ranged impurities. It is convenient because of the particularly simple form the expressions take. Our physical results do not depend on the exact form of the impurity potential.

With (2.8), we obtain for the imaginary part of the self-energy

$$\mathrm{Im}\,\Sigma^{\mathrm{R}}(\mathbf{p}, \varepsilon) = -\pi\nu(\varepsilon)\Gamma \tag{2.9}$$

$$:= -\frac{1}{2\tau} \tag{2.10}$$

where $\nu(\varepsilon)$ is the density of states, which we approximated by its value at the Fermi energy.

The Green's function thus obtains a finite lifetime τ due to the disorder,

$$\langle \mathcal{G}^{\mathrm{R}}\rangle(\mathbf{p}, \varepsilon) \simeq \frac{1}{\varepsilon - \frac{p^2}{2m} + \frac{\mathrm{i}}{2\tau}} =: G^{\mathrm{R}}(\mathbf{p}, \varepsilon). \tag{2.11}$$

In the following, single solid lines with an arrow denote G^{R} in the Feynman diagrams.

The length scale $l = v_{\mathrm{F}}\tau$ with Fermi velocity v_{F} is called the *mean free path*. Approximating the

Green's function using the lowest order self-energy contribution is valid in the limit of weak disorder $k_{\mathrm{F}} l \gg 1$.

The disorder average restores the translational invariance of the Green's function—the non-averaged Green's function being not translational invariant due to the spatially random potential.

2.2.2 Diffusion and weak localization

With the help of diagrams, transport is usually analyzed by calculating the linear response of the system to an external perturbation. The *Kubo formula* establishes a simple relation between the linear response of an observable O to the perturbation H' [2]:

$$\delta \langle O \rangle (t) := \langle O \rangle (t) - \langle O \rangle_0 = \int_{t_0}^{\infty} \mathrm{d}t' \, C_{OH'}^{\mathrm{R}}(t, t') \tag{2.12}$$

$$C_{OH'}^{\mathrm{R}}(t, t') := -\mathrm{i}\theta(t - t') \left\langle \left[O(t), H'(t') \right] \right\rangle_0. \tag{2.13}$$

Here, $\langle \cdot \rangle_0$ describes an equilibrium average over the ensemble of the unperturbed system. C^{R} is called a retarded response function.

In this chapter, we mainly consider the response of the density to a density perturbation, which is characterized by the retarded *density-density correlation function* or *density-density response function* (or just density response function)

$$\chi(\mathbf{q}, t) = -\frac{\mathrm{i}\theta(t)}{V} \int \mathrm{d}^d(r_1 - r_2) \, \mathrm{e}^{-\mathrm{i}\mathbf{q}(\mathbf{r}_1 - \mathbf{r}_2)} \left\langle \left[n(\mathbf{r}_1, t), n(\mathbf{r}_2, 0) \right] \right\rangle, \tag{2.14}$$

with the Heaviside theta function $\theta(t)$ and the density operators $n(\mathbf{r}, t) = a_{\mathbf{r}}^{\dagger}(t) a_{\mathbf{r}}(t)$ ($a^{\dagger}$ and a are fermionic creation and annihilation operators). The disorder average establishes translational symmetry, such that the averaged correlator is diagonal in momentum space.

For example, in a system of charged particles, χ describes the induced charge distribution due to an external charge distribution (dielectric function) [2].

In terms of exact retarded and advanced Green's functions $\mathcal{G}^{\mathrm{R,A}}$, the density-density response function of a fermionic system reads in a given realization of disorder and at finite temperature [2]

$$\tilde{\chi}(\mathbf{q}, \omega) = -\int \frac{\mathrm{d}\varepsilon}{2\pi \mathrm{i}} \int \mathrm{d}^d(r_1 - r_2) \, \mathrm{e}^{-\mathrm{i}\mathbf{q}(\mathbf{r}_1 - \mathbf{r}_2)} n_{\mathrm{F}}(\varepsilon) \left\{ \left[\mathcal{G}^{\mathrm{R}}(\mathbf{r}_1, \mathbf{r}_2; \varepsilon) - \mathcal{G}^{\mathrm{A}}(\mathbf{r}_1, \mathbf{r}_2; \varepsilon) \right] \mathcal{G}^{\mathrm{A}}(\mathbf{r}_2, \mathbf{r}_1; \varepsilon - \omega) \right.$$
$$\left. + \mathcal{G}^{\mathrm{R}}(\mathbf{r}_1, \mathbf{r}_2; \varepsilon + \omega) \left[\mathcal{G}^{\mathrm{R}}(\mathbf{r}_2, \mathbf{r}_1, \varepsilon) - \mathcal{G}^{\mathrm{A}}(\mathbf{r}_2, \mathbf{r}_1; \varepsilon) \right] \right\}. \tag{2.15}$$

where $n_{\mathrm{F}}(\varepsilon)$ is the Fermi function. This general expression needs to be averaged over disorder realizations.

To perform the disorder average, we have to identify those terms in the sum of all possible contractions, that dominantly contribute to the density-response function in the considered regime. In the limit of long time, and for a low external momentum $\mathbf{q}$, this family of diagrams is given by the ladder series of disorder lines (the "diffuson" propagator). This series features a pole in the limit $\mathbf{q}, \omega \to 0$ which is responsible for the slow diffusive spreading of the mean-square displacement. The diffuson propagator is associated with diffusive motion through the system along classical trajectories.

Diagrammatically, it is expressed as

$$\left\langle \overset{\mathcal{G}^{\mathrm{R}}}{\underset{\mathcal{G}^{\mathrm{A}}}{\bigcirc}} \right\rangle \approx \quad + \quad + \quad + \dots \tag{2.16}$$

$$=: \tag{2.17}$$

where the orange box denotes the ladder sum of disorder lines (diffuson)

$$\boxed{\mathbf{q},\omega} \;=\; \vdots \;+\; \tag{2.18}$$

$$\xrightarrow{\mathbf{q},\omega\to 0} \frac{1}{2\pi\nu\tau^2}\frac{1}{Dq^2-\mathrm{i}\omega}. \tag{2.19}$$

$D = v^2\tau/d$ is the diffusion constant with the particle velocity v, transport scattering time τ, and spatial dimensionality d. The resulting *markovian* density-density correlator (at zero temperature) is given by the well-known diffusive formula

$$\tilde{\chi}(q,\omega) = -\nu\frac{Dq^2}{Dq^2-\mathrm{i}\omega}\,. \tag{2.20}$$

The retarded-retarded and advanced-advanced contribution from Eq. (2.15) to this result in the given limit is the density of states ν [127].

In addition to the *particle-hole* ladder series shown in above figure, there is a second series of diagrams that can produce a pole: It corresponds to the sum of maximally crossed diagrams (the *particle-particle* series)

$$+ \quad + \quad + \quad \dots \quad =:$$
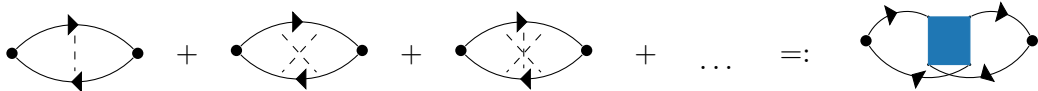
The associated ladder series
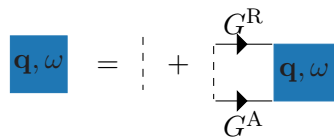
$$\mathbf{q}, \omega \quad = \quad \vdots \quad + \quad \mathbf{q}, \omega \tag{2.21}$$

$$\xrightarrow{\mathbf{q}, \omega \to 0} \frac{1}{2\pi\nu\tau^2} \frac{1}{Dq^2 - \mathrm{i}\omega}. \tag{2.22}$$

is commonly called a "cooperon".

As explained in the next section, these diagrams are associated with interference effects between time-reversed scattering paths.

It can be seen that this series of diagrams leads to a correction

$$\delta\tilde{\chi}(q, \omega) \propto \int \mathrm{d}^d q \, \frac{1}{Dq^2 - \mathrm{i}\omega} \tag{2.23}$$

to the density response function[6]. In $d \geq 2$ dimensions, this contribution diverges at its upper integration bound. The ultraviolet divergence at $q \to \infty$ is regularized by the mean free path $q \sim 1/l$ (as we are considering a small q expansion). The infrared divergence in $d \leq 2$ dimensions is controlled by the frequency ω. It results in a diverging contribution to the response function in the limit $\omega \to 0$, thus signalling the breakdown of the perturbation theory and the arrival of strong Anderson localization [2, 64, 127].

Physically, this contribution corresponds to interference between scattering events on different impurities [2]. Their contribution is therefore limited by the *coherence length* in the system (the length scale, on which a single particle description remains valid [2]) and the system size. It can thus be cut off by interaction effects and the system size, reducing it to a *weak localization correction* [2, 64].

2.2.3 Interference picture and relation to a random walk

The authors of Ref. [128] introduced an intuitive picture of classical and quantum mechanical contributions to the propagation probability of a particle in a disordered system between two given points [51, 128, 129]. The propagation amplitude corresponds to the retarded Green's function. In the language of path integrals, it is assembled by adding contributions from all possible paths between those points. The probability w is calculated from the modulus square of this sum of individual amplitudes A_i [128],

$$w \sim |\sum_i A_i|^2 \tag{2.24}$$

$$= \sum_i |A_i|^2 + \sum_{i \neq j} A_i A_j^*. \tag{2.25}$$

Evidently, this relates it to the retarded-advanced term in the density-response function.

The "classical" markovian description in terms of a Boltzmann equation is identified as the diagonal contribution $\sum_i |A_i|^2$. Each term in this sum is associated with a single classical trajectory [64]. In

---

[6]Similar contributions can be obtained by crossing the particle-hole ladder with a disorder line. However, it can be shown that such diagrams do not yield a divergence in the limit $\mathbf{q}, \omega \to 0$ [127]. Interestingly, as shown in this chapter, it is exactly this type of diagram that leads to memory effects in the density imbalance.

the classical picture, different trajectories do not interfere with each other.

Indeed, most non-classical, off-diagonal contributions can safely be neglected, because each such contribution has a different phase, leading to a vanishing average over terms with essentially random phases. This is not true however for pairs of amplitudes corresponding to the same path featuring a closed loop, which is traversed in opposite directions. The phases of such pairs of amplitudes cancel each other exactly, leading to an interference correction to, for example, the conductivity. This quantum correction is associated with weak Anderson localization and the crossing diagram series shown in the previous section [128, 129].

Interestingly, the spatial dimension naturally enters this consideration via the number of such loops that has to be considered in a given dimension [51]. Concretely, the contribution from closed loops is related to the *return probability*—the probability for a path to return to its origin, thus forming a closed loop, in the ensemble of all possible paths. Intuitively, the higher the spatial dimension, the more ways for the path to wander off in a different direction, away from the origin—thus the lower the return probability.

The cancellation between phases of different paths requires coherent propagation—if each path separately aquires a random phase, the phases do not cancel each other and the contribution vanishes again upon averaging. The phase coherence can be disturbed by interactions, which thus introduce an upper cut-off on the length of interfering paths [2]. In this way it can be understood, that interactions lift strong localization effects.

In a system of finite size, the system size provides a cut-off for the path length, which also serves as a cut-off for localization effects. This is important in 2D, where the localization length is exponential in the mean-free path, such that a parametric weak-localization regime $l \ll L \ll \xi$ exists in a finite-size system [51]. In one dimension, the mean-free path is proportional to the localization length, such that transport is either ballistic or strongly localized, but never quasi-diffusive (with weak localization corrections) [129].

Importantly, the diagonal contribution in (2.24) is unaffected by interaction induced dephasing, as it corresponds to the "self-interference" of a path.

2.3 Imbalance and its relation to the density response function

In this section, we define the imbalance and derive a relation between its tail at long times and the density response function. We consider first a 1D lattice; a generalization to 2D geometry (or a higher dimensionality) is straightforward and discussed in the end of the section.

We consider the time-dependent imbalance between the particle numbers $N_{\mathrm{even}}(t)$, $N_{\mathrm{odd}}(t)$ at even and odd lattice sites j normalized to the total number of sites N,

$$I(t) = \frac{\langle N_{\mathrm{even}}(t) - N_{\mathrm{odd}}(t) \rangle}{N} \tag{2.26}$$

$$= \frac{1}{N} \sum_{\mathrm{sites}\ j} \langle n_j(t) \rangle (-1)^j. \tag{2.27}$$

Here, the angular brackets denote the average over the quantum many-body state. Since we deal with disordered systems, the average $\langle \ldots \rangle$ below also includes the disorder average. We define the density

$n_j(t)$ and its continuum version $n(x,t)$, as well as the corresponding Fourier transform

$$\tilde{n}(q,t) = \sum_j e^{-iqaj} n_j(t) = \int dx\, e^{-iqx} n(x,t)\,, \qquad (2.28)$$

where a is the lattice spacing. The imbalance then reads:

$$I(t) = \frac{1}{n_0 V} \left\langle \tilde{n}\left(q = \frac{\pi}{a}, t\right) \right\rangle\,, \qquad (2.29)$$

where $n_0 = V^{-1}\langle \tilde{n}(q=0)\rangle$ is the conserved density and $V = Na$ is the system volume.

Experimentally and numerically, one explores the relaxation (or its absence) in the system by setting up a maximally imbalanced initial state at $t = 0$ that is then time-evolved with the Hamiltonian H of the system until long times t. In this chapter, we are interested in the long-time behavior of the imbalance in the delocalized phase where the system evolves towards an equilibrium state with a uniform density distribution, $I(t) \to 0$ at $t \to \infty$. To understand the form of this asymptotic tail, we can thus equivalently start from a state with only a small imbalance (i.e., that is close to equilibrium).

In this way, we can reformulate the problem under consideration in terms of a linear response near the equilibrium. Specifically, let us consider the system at $t \leq 0$ as an equilibrium state of the Hamiltonian $H_0 - H'$, where

$$H' = \frac{I_0}{\nu}\, \tilde{n}(q,t)\,. \qquad (2.30)$$

Here, q is the wave vector of the charge-density wave, $I_0 = (n_0 V)^{-1}\langle \tilde{n}(q, t=0)\rangle$ is the initial value of the imbalance, and ν is the density of states. H_0 is the sum of kinetic term and impurity potential. The term $-H'$ in the Hamiltonian describes a periodic potential that yields the initial imbalance I_0. Now, at time t we perform a quench by removing the term $-H'$, which is equivalent to adding a perturbation H' to the initial Hamiltonian. The system then starts relaxing towards the equilibrium state of the Hamiltonian H_0 with a uniform density; i.e., zero imbalance.

Applying the Kubo formula (2.13) to obtain the density response to the perturbation (2.30), we obtain

$$\langle \tilde{n}(q,t)\rangle = \langle \tilde{n}(q,0)\rangle \left[1 + \frac{1}{\nu}\int_0^t dt'\, \chi(q, t-t')\right]\,, \qquad (2.31)$$

where $\chi(q,t)$ is the retarded density-density correlation function (2.14). Note that, in the Kubo formula, we are supposed to average over the equilibrium state of the initial Hamiltonian, which is given by $H_0 + H'$. However, since the analysis is performed to linear order in the small perturbation H', we can discard H' here and average over the equilibrium state of H_0 towards which the system evolves.

Equations (2.29) and (2.31) establish the relation of the long-time tail of the imbalance with the density response function. An extension of this relation to higher-dimensional systems is straightforward. In particular, for a 2D square lattice one can consider the checkerboard imbalance corresponding to a charge density wave with the wave vector $\mathbf{q} = (\pi/a, \pi/a)$ or the columnar imbalance with the wave vector $\mathbf{q} = (\pi/a, 0)$. The formulas (2.29) and (2.31) remain valid with the replacement of q by the corresponding 2D wave vector $\mathbf{q}$. This relation is used below for the analytical study of the imbalance decay.

Considering the Markovian contribution (2.20) for sufficiently small values of the wave vector, $q \ll l^{-1}$, we obtain upon Fourier transformation to time-space

$$\chi(q,t) = -\nu D q^2 \exp\left(-Dq^2 t\right). \tag{2.32}$$

Substituting this into Eq. (2.31), we get

$$\langle \tilde{n}(q,t) \rangle = \langle \tilde{n}(q,t) \rangle \exp\left(-Dq^2 t\right), \tag{2.33}$$

and thus, according to Eq. (2.29), the exponential decay of the imbalance,

$$I(t) = I_0 \exp\left(-t/t_q\right), \tag{2.34}$$

with $t_q = 1/Dq^2$.

With increasing q, the decay time t_q becomes shorter, reaching a very short value $t \sim \tau$ at the ultraviolet border of the diffusive range of wave vectors, $q \sim l^{-1}$. For further increasing wave vectors, $q > l^{-1}$, the exponential decay $\exp\left(-t/t_q\right)$ with a short time $t_q \sim \tau$ remains valid in the quasiclassical contribution to the imbalance in the Markovian approximation. This is obvious physically (waves with a shorter wave lengths are expected to decay faster) and is easy to check by using an explicit form of the modified diffusion propagator in such ballistic range of wave vectors (see, e.g., Ref. [113] for 1D systems and Ref. [114] for 2D systems).

At large $q > l^{-1}$, this decay factor actually describes the envelope of the oscillatory quasiclassical Markovian imbalance. In particular, in the 1D case one gets: $I(t) \propto \exp\left(-t/2\tau\right)\sin(qvt)$. It should be noted that, on top of this quasiclassical contribution to $I(t)$, there is a purely quantum one (described by only retarded or only advanced Green's functions in the diagrammatic language, see Eq. (2.15)), which also decays exponentially in time. However, in contrast to the quasiclassical term, at the momentum $q = \pi/a$ at half filling (i.e., $q = 2k_{\mathrm{F}}$, where k_{F} is the Fermi momentum), this term yields a non-oscillatory contribution to $I(t)$. Its decay rate is given by the maximum of $1/\tau$ and temperature T (in our case $T\tau \gg 1$). This is similar to the decay of Friedel oscillations or magnetooscillations, which are also suppressed by both disorder and thermal averaging.

Thus, at the level of the Boltzmann equation (i.e., in the Markovian approximation), the imbalance decays exponentially, with a very short decay time. However, as we show in Sec. 2.4 by a diagrammatic analysis, there exists a contribution of memory effects, which is discarded by this approximation. Calculating this contribution, we demonstrate that the actual decay of the imbalance is of power-law form and determine the corresponding exponent.

2.4 Diagrammatic analysis

To calculate the long-time tail in the density response function (and thus in the imbalance in view of the relations (2.29) and (2.31)), we use the conventional diagrammatic technique for disordered systems, which is briefly introduced in 2.2.1. The calculation bears analogy with that of the zero-frequency anomaly of the conductivity in Ref. [63]. The starting point for the calculation is the formula (2.15) for the density response function.

Again, we have to select diagrams from the disorder average that govern the behavior of the density-response function in the long-time limit. In the conventional case of a low external momentum q, the

Figure 2.1: Figure adapted from Ref. [54]. *Left:* Example of a diagram contributing to the long-time tail of the density response function (and, thus, of the imbalance). The shaded box is the diffuson. It is crossed by one or several (two in the shown example) lines representing return events of a particle to the same scatterer(s) after moving diffusively for a long time t. *Right:* Another representation of the same diagram. The diffuson is shown here by a wavy line.

ladder sum of disorder lines features a pole and thus yields a diffuson, governing the long-time tail. The diffuson propagator describes the slow spread of the mean square displacement and is associated with the particle returns in arbitrary long times. At large external momentum, however, the situation is different: as pointed out in the previous section, the ladder sum in this case decays exponentially with time and thus does not describe a long-term memory.

The memory effects—that control the long-time tails that we are investigating—originate from the following type of processes. A particle is scattered by an impurity, then performs a diffusive motion during a long time t, which results in its return to the original position, where it is scattered again by the same impurity. By transferring the large external momentum via one or several impurity lines across the impurity ladder, the latter can again carry a small momentum, which results in a long-time tail.

Clearly, the contribution of such processes is related to the return probability as a function of time. Similar to the weak localization correction, the memory effect term depends on the number of return trajectories contributing to the correction of the density response function. In contrast to the weak localization correction however, the memory effect return processes correspond to diagonal terms in the path expansion of the propagation probability 2.24 and is thus insensitive to dephasing.

In a more general form, the scattering on a single impurity is replaced by scattering events on a few (two, three, ...) nearby impurities. An example of a corresponding diagram is shown in the left panel of Fig. 2.1. The orange box in this diagram is the diffuson (the ladder built out of impurity lines). Two dashed lines crossing the diffuson correspond to a repeated scattering of the particle on two nearby impurities after completing a closed diffusive path. The same diagram is shown, in a different way, in the right panel of the same figure, with the diffuson represented by a wavy line.

Every additional crossing line adds an additional smallness of the order $\mathcal{O}(1/(k_{\mathrm{F}}l))$. Disorder ladders can only be added in combination with more crossing lines, since inserting one as a vertex correction would lead to exponential suppression of the diagram at high external momentum in the long-time limit. For this reason it suffices in the long-time and large mean-free path limits to calculate the sum of diagrams with the least number of disorder- and diffuson lines, which does not vanish.

Let us start by considering the lowest-order processes describing repeated scattering on a single impurity. They are represented by diagrams with a diffuson crossed by a single impurity line. For weak disorder, these diagrams yield the dominant contribution to the memory effects. For not so weak disorder, diagrams with two or three crossing impurity lines may give a comparable contribution but this will only correct the overall numerical prefactor, without affecting the result in any essential way.

We analyze the density response function $\tilde{\chi}(\mathbf{q}, \omega)$ at low frequencies (which correspond to long times t). The sum of the diagrams with a diffuson and an impurity line inserted in all possible ways (corresponding to a rescattering on this impurity after executing the diffusive motion) can be written
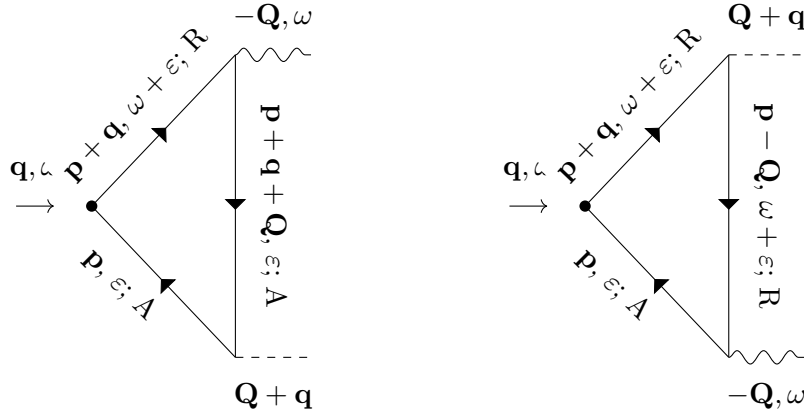
Figure 2.2: Figure adapted from Ref. [54]. Triangle vertices $V_1(\mathbf{q}, \mathbf{Q}, \varepsilon, \omega)$ and $V_2(\mathbf{q}, \mathbf{Q}, \varepsilon, \omega)$ entering Eq. (2.38). Here, $\mathbf{q}$ is the external momentum and $-\mathbf{Q}$ is the diffuson momentum. Disorder lines are dashed, diffuson lines are wavy. Retarded and advanced Green's functions are marked with R and A, respectively. The external vertices of the density response function are marked by thick dots.

as

$$\tilde{\chi}\left(\mathbf{q}, \omega\right) = -\mathrm{i}\,\omega B(\mathbf{q}) \int \frac{\mathrm{d}^d Q}{(2\pi)^d} \Lambda^{\mathrm{diff}}(\mathbf{Q}, \omega)\,, \tag{2.35}$$

where $\Lambda^{\mathrm{Diff}}(\mathbf{Q}, \omega)$ is the diffuson,

$$\Lambda^{\mathrm{Diff}}(\mathbf{Q}, \omega) = \frac{1}{2\pi\nu\tau^2} \frac{1}{DQ^2 - \mathrm{i}\omega}\,, \tag{2.36}$$

and the prefactor $B(\mathbf{q})$ is given by

$$B(\mathbf{q}) = \Gamma \int_{-\infty}^{\infty} \frac{\mathrm{d}\varepsilon}{2\pi} \left[-\frac{\partial n_{\mathrm{F}}(\varepsilon)}{\partial \varepsilon} \right] b(\mathbf{q}, \varepsilon) \tag{2.37}$$

with

$$b(\mathbf{q}, \varepsilon) = \lim_{\mathbf{Q} \to 0} \lim_{\omega \to 0} \left[V_1(\mathbf{q}, \mathbf{Q}, \varepsilon, \omega) + V_2(\mathbf{q}, \mathbf{Q}, \varepsilon, \omega) \right]^2. \tag{2.38}$$

Here, V_1 and V_2 are the vertex functions represented by the triangular diagrams shown in Fig. 2.2. In this Figure, $\mathbf{q}$ is the external momentum and $-\mathbf{Q}$ is the diffuson momentum, with the difference $\mathbf{q} + \mathbf{Q}$ carried by the impurity line crossing the diffuson (as discussed in the introduction). Since $-\mathbf{Q}$ and ω are the small momentum and frequency carried by the diffuson, we can discard them when calculating the vertices V_1 and V_2, as indicated in Eq. (2.38). The formulas (2.37) and (2.38) are obtained under the assumption that the vertex function $V_1 + V_2$ has a finite limit at $\mathbf{Q} \to 0$ and $\omega \to 0$. We show below by an explicit calculation that this is indeed generically the case.

The vertex functions $V_1(\mathbf{q}, \mathbf{Q}, \varepsilon, \omega)$ and $V_2(\mathbf{q}, \mathbf{Q}, \varepsilon, \omega)$ entering Eq. (2.38) are given by (see Fig. 2.2)

$$V_1(\mathbf{q}, \mathbf{Q}, \varepsilon, \omega) = \int \frac{\mathrm{d}^d p}{(2\pi)^d} G^{\mathrm{R}}(\mathbf{p} + \mathbf{q}, \omega + \varepsilon)$$
$$\times\, G^{\mathrm{A}}(\mathbf{p} + \mathbf{q} + \mathbf{Q}, \varepsilon)\, G^{\mathrm{A}}(\mathbf{p}, \varepsilon)\,, \tag{2.39}$$

$$V_2(\mathbf{q}, \mathbf{Q}, \varepsilon, \omega) = \int \frac{\mathrm{d}^d p}{(2\pi)^d} G^{\mathrm{R}}(\mathbf{p} + \mathbf{q}, \omega + \varepsilon)$$
$$\times\, G^{\mathrm{R}}(\mathbf{p} - \mathbf{Q}, \omega + \varepsilon)\, G^{\mathrm{A}}(\mathbf{p}, \varepsilon)\,, \tag{2.40}$$

where G^{R} and G^{A} are, respectively, the disorder averaged retarded and advanced Green's functions from Eq. (2.11),

$$G^{\mathrm{R}}(\mathbf{p}, \varepsilon) = \frac{1}{\varepsilon - \xi(\mathbf{p}) + \frac{\mathrm{i}}{2\tau}} = G^{\mathrm{A}*}(\mathbf{p}, \varepsilon)\,, \tag{2.41}$$

and $\xi(\mathbf{p})$ is the dispersion relation of the clean system.

Substituting Eq. (2.37) into Eq. (2.35) and performing the Fourier transformation from the frequency to the time domain, we get

$$\chi(\mathbf{q}, t) = \frac{B(\mathbf{q})}{2\pi\nu\tau^2} \frac{\partial}{\partial t} P(t)\,, \tag{2.42}$$

where $P(t)$ is the diffusive return probability,

$$P(t) = \int \frac{\mathrm{d}^d Q}{(2\pi)^d} \int \frac{\mathrm{d}\omega}{2\pi} \mathrm{e}^{-\mathrm{i}\omega t} \frac{1}{DQ^2 - \mathrm{i}\omega}$$
$$= \int \frac{\mathrm{d}^d Q}{(2\pi)^d}\, \mathrm{e}^{-DQ^2 t}\,, \tag{2.43}$$

equal to

$$P(t) = (4\pi D t)^{-d/2}\,. \tag{2.44}$$

By definition, $P(t)$ is the probability density for a diffusing particle that starts at a point $\mathbf{x_0}$ at time $t = 0$ to be found at the same point after time t. Substituting Eq. (2.42) into Eqs. (2.29) and (2.31), we get

$$\frac{I(t)}{I_0} = cP(t)\,, \tag{2.45}$$

where

$$c = \frac{B(\mathbf{q})}{2\pi\nu^2\tau^2}\,. \tag{2.46}$$

According to Eq. (2.45), the long-time tail of the imbalance is given (up to a coefficient) by the return probability $P(t)$.

Let us recall at this point that our main motivation is the physics on the ergodic side of the MBL transition. There, the interaction generates dephasing, thus destroying the localization. For this reason, we discard localization effects in the above diagrammatic analysis. This is especially important

in 1D geometry, where the diffusive regime does not exist in the absence of interaction since the localization length of a non-interacting system is of the order of the mean free path [64]. In the case of higher-dimensional systems, $d \geq 2$, our analysis applies also to non-interacting systems at not too strong disorder, such that the system is delocalized, i.e., the localization length is much larger than the system size.

We have obtained the formulas (2.42) and (2.45) that relate the long-time tails in the density response function to the return probability: $\chi(\mathbf{q}, t) \propto \partial P(t)/\partial t$ and $I(t) \propto P(t)$. While we have assumed conventional diffusive motion during the time t described by a simple diffuson (2.36), the effect is expected to remain valid in a more complex situation, when the particle executes a subdiffusion between the original scattering and the return to the same impurity. We will thus use these relations below in such, more general sense.

2.4.1 1D systems

We evaluate now the general formulas for the density response function and the imbalance for the case of a 1D system. To simplify the calculation, it is convenient to linearize the parabolic dispersion relation

$$\xi(p) \simeq \begin{cases} \xi_+(p) = (p - k_{\mathrm{F}})\, v, & p > 0\,, \\ \xi_-(p) = -(p + k_{\mathrm{F}})\, v, & p < 0\,, \end{cases} \tag{2.47}$$

where the branches ξ_+ and ξ_- correspond to right-moving and left-moving particles. The linearization does not affect the result in any essential way (up to an overall numerical prefactor of order unity). Upon linearization, we can easily carry out the integrations in Eqs. (2.39) and (2.40). We recall that we are interested in the limit $\omega \to 0$, $Q \to 0$. Further, we set the external momentum to be $q = \pi/a$. For this value of q, the particle always switches the branch at the external vertex. We denote the triangle vertices with $- \to +$ change of the branch at the external vertex (going along the arrow in Fig. 2.2, i.e., from G^{A} to G^{R}) by $V_1^{\mp}$, $V_2^{\mp}$ and those with the change $+ \to -$ by $V_1^{\pm}$ and $V_2^{\pm}$. The calculation of the vertices yields (see Ref. [54])

$$V_1^{\mp}(\varepsilon) + V_2^{\mp}(\varepsilon) = \frac{2\tau}{v}\, \frac{2k_{\mathrm{F}}v + 2\varepsilon - \pi v/a}{(2k_{\mathrm{F}}v + 2\varepsilon - \pi v/a)^2 + 1/\tau^2}\,, \tag{2.48}$$

and, similarly,

$$V_1^{\pm}(\varepsilon) + V_2^{\pm}(\varepsilon) = -\frac{2\tau}{v}\, \frac{2k_{\mathrm{F}}v - 2\varepsilon - \pi v/a}{(2k_{\mathrm{F}}v - 2\varepsilon - \pi v/a)^2 + 1/\tau^2}\,. \tag{2.49}$$

For definiteness, we assume half filling, $k_{\mathrm{F}} = \pi/2a$, in the following. (For a different density, the result remains the same, up to a prefactor.) We note in passing that, for half filling, the vertices (2.48) and (2.49) vanish exactly at $\varepsilon = 0$ (which is a manifestation of an extra symmetry related to Umklapp scattering), but are finite for any finite energy. Therefore, at nonzero temperatures, the vertex factor given by Eq. (2.38) is nonzero. Combining the contributions of the $- \to +$ and $+ \to -$ processes to the triangle vertices, we get for the prefactor $B(q = \pi/a)$ in Eq. (2.35)

$$B = \Gamma \left(\frac{8\tau}{v}\right)^2 \int_{-\infty}^{\infty} \frac{\mathrm{d}\varepsilon}{2\pi} \left[-\frac{\partial n_{\mathrm{F}}(\varepsilon)}{\partial \varepsilon}\right] \left(\frac{\varepsilon}{1/\tau^2 + 4\varepsilon^2}\right)^2\,. \tag{2.50}$$

Since the initial density-wave state is highly excited, it corresponds to a high temperature T, comparable to the band width J. We thus make an assumption $T\tau \gg 1$ to calculate the prefactor. The integral in Eq. (2.50) is then easily calculated, yielding $B = \tau^2/2\pi vT$. This gives for the prefactor in Eq. (2.42)

$$\frac{B}{2\pi\nu\tau^2} = \frac{1}{4\pi T} \,, \tag{2.51}$$

and thus $c = v/4T$ for the prefactor c in Eq. (2.46). This calculation of the prefactor (involving linearization of the spectrum) is controllable for $T \ll J$. For an estimate, we can, however, put here $T \sim J$, which yields $c \sim a$.

The above analysis, leading to the power-law decay of the imbalance,

$$I(t) \propto P(t) \propto t^{-1/2}, \tag{2.52}$$

applies to the diffusive regime of transport that takes place at a sufficiently weak disorder (well below the MBL transition) in interacting disordered systems [60]. At the same time, numerical studies show that a major part of the ergodic phase of such systems is characterized by subdiffusive transport [59–61, 111, 112]. In this chapter, we do not analyze a microscopic mechanism leading to subdiffusion in a particular model. Instead, we assume that the subdiffusive behavior holds and model it on a phenomenological level by introducing a modified diffusion propagator [122]:

$$\Lambda^{\text{diff}}(Q,\omega) \to \Lambda_\beta^{\text{subdiff}}(Q,\omega) \sim \frac{1}{\nu\tau^2}\frac{1}{D(Q)Q^2 - \mathrm{i}\omega} \,, \tag{2.53}$$

$$D(Q) = \tilde{D}|Q|^\beta \,. \tag{2.54}$$

Here $\beta > 0$ is the exponent controlling the subdiffusive character of the transport: $\beta = 0$ corresponds to normal diffusion, while $\beta \gg 1$ corresponds to the very slow transport as found near the MBL transition. The propagator (2.53) corresponds to the fractional diffusion equation [98]; the associated mean square displacement

$$r_2(t) = \left\langle \int \mathrm{d}x \, x^2 \bar{n}(x,t) \right\rangle \tag{2.55}$$

reads (see, e.g., Ref. [98]):

$$r_2(t) \sim (\tilde{D}t)^{\frac{2}{2+\beta}}. \tag{2.56}$$

Now, we analyze the long-time tail in the imbalance. As found above, it is proportional to the return probability $P(t)$ in the case of conventional diffusion. We argue that this result still holds true for subdiffusion. Indeed, this is expected because diffusive and subdiffusive processes are established at long times (long spatial scales), while the vertex functions at high external momentum $q \sim k_{\text{F}}$ are determined by large momenta, i.e., by short time (or spatial) scales. Therefore, microscopic details of the diffusive or subdiffusive process can plausibly be assumed to be irrelevant for the vertices. Using the anomalous-diffusion propagator (2.53), we get for the return probability

$$P(t) \sim (\tilde{D}t)^{-\frac{1}{2+\beta}}. \tag{2.57}$$

Substituting this into Eqs. (2.42) and (2.45), we obtain the asymptotics of the density response function,

$$\chi(q,t) = \frac{B(q)}{2\pi\nu\tau^2}\frac{\partial}{\partial t}P(t) \propto t^{-1-\frac{1}{2+\beta}} \, , \tag{2.58}$$

and of the imbalance,

$$\frac{I(t)}{I_0} = cP(t) \propto t^{-\frac{1}{2+\beta}} \, . \tag{2.59}$$

The slow power-law decay of the imbalance (2.59) is in agreement with numerical findings on the ergodic side of the MBL transition [57, 58, 115–118]. Comparing Eq. (2.56) and Eq. (2.59), we see a relation between the exponent γ_x characterizing the mean square displacement, $r_2(t) \propto t^{\gamma_x}$, and the exponent γ_I describing the imbalance decay, $I(t) \propto t^{-\gamma_I}$. Specifically, we obtain $\gamma_x = 2/(2+\beta)$ and $\gamma_I = 1/(2+\beta)$, with the ratio $\gamma_I/\gamma_x = 1/2$, independent of the subdiffusive exponent β. This exponent relation was proposed in Ref. [59] and is in reasonable agreement with numerical results on long-time dynamics in large systems obtained within the time-dependent Hartree-Fock approximation in Ref. [117].

In Fig. 2.3 we show an adaptation of a figure from Ref [117]. This figure was obtained on the ergodic side of the MBL transition $W < W_c$ in an interacting one-dimensional disordered system, using the time-dependent Hartree-Fock approximation [117]. The upper (lower) panel shows the imbalance (first moment with a domain wall initial state) and the respective time-dependent power law exponent. The exponent of the first moment of the domain wall is equivalent to the exponent of the mean-square displacement γ_x [117]. As both exponents are smaller than their diffusive values, the system is subdiffusive due to the proximity to the MBL transition. After an initial phase of time evolution, the respective exponents converge to constant values with slight finite-sample fluctuations. It can be seen, that the predicted relation between the exponents γ_I/γ_x is approximately fulfilled.

It should be emphasized, however, that the above derivation of the relation between the exponents is based on the assumption that the anomalous diffusion coefficient $D(q)$ in Eq. (2.53) depends on the momentum q and not on frequency ω. This leads to Eq. (2.57) for the return probability and, thus, to the scaling (2.59) of the imbalance. A more complex situation, with the anomalous diffusion constant $D(q,\omega)$ showing (at small ω and relatively large q) a scaling with both q and ω, corresponds to multifractality. In such a situation (that it is characteristic, in particular, to Anderson-transition critical points) the scaling of the return probability $P(t)$ is characterized by an exponent that is not directly determined by the exponent of the mean square displacement. We will return to this issue below.

2.4.2 2D systems

We extend now the analysis to 2D systems, $d = 2$. One natural extension of the imbalance to 2D systems on a square lattice is the checkerboard-imbalance

$$I_{\text{check}}(t) = \sum_{i,j}(-1)^{i+j}\frac{\langle n_{(i,j)}(t)\rangle}{N} \, . \tag{2.60}$$
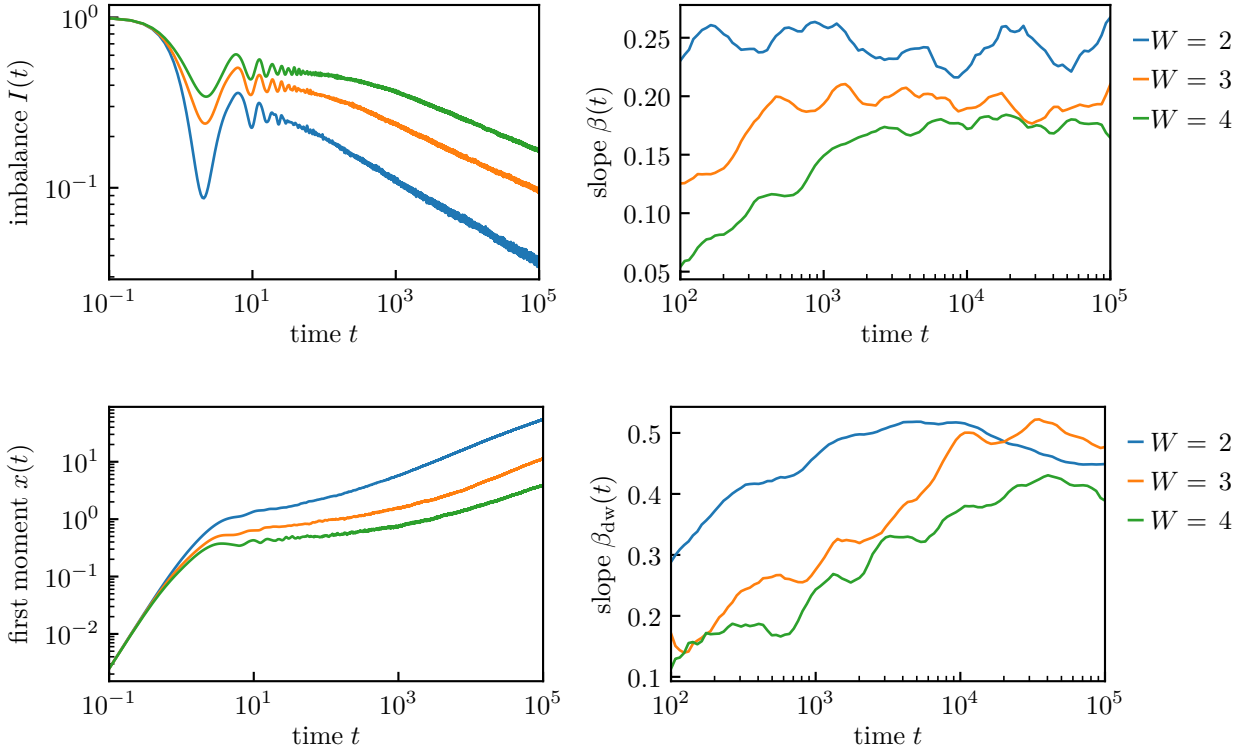
Figure 2.3: Figure adapted from Ref. [117]. The figure was obtained in a one-dimensional disordered interacting system with the time-dependent Hartree-Fock method and demonstrates subdiffusion which is expected on the ergodic side close to the MBL transition. *Upper panel:* Imbalance (left) and power-law exponent β as a function of the central region of the fit window (right). *Lower panel:* First moment of a domain wall (left) corresponding power-law exponent as a function of the central region of the fit window (right). It can be seen that the relation between the exponents $\gamma_I/\gamma_x = 1/2$ is fulfilled.

Here i and j enumerate the rows and columns of the system, respectively. Taking the continuum limit in analogy to the 1D case, we find, in analogy with Eq. (2.29),

$$I_{\text{check}}(t) = \frac{1}{n_0 V} \left\langle \tilde{n} \left(q_x = \frac{\pi}{a}, \, q_y = \frac{\pi}{a}, \, t \right) \right\rangle. \tag{2.61}$$

Alternatively, one can consider the columnar imbalance [58] $I_{\text{col}}(t)$ corresponding to the density wave with wave vector $q_x = \pi/a$ and $q_y = 0$. Our analytical treatment applies equally to both $I_{\text{check}}(t)$ and $I_{\text{col}}(t)$, so we use below the notation $I(t)$ to refer to any of them. For numerical calculations, we indicate which of the imbalances is shown.

Equations (2.42) and (2.45) give the tails of the density-response function and of the imbalance in terms of the return probability $P(t)$. In the case of normal diffusion, the return probability is given by Eq. (2.44). This yields the scaling

$$\chi(\mathbf{q}, t) \propto t^{-2}$$

for the density-response function and

$$I(t) \propto t^{-1} \tag{2.62}$$

for the imbalance. Estimating the coefficients, we get $B/2\pi\nu\tau^2 \sim 1/J$ for the coefficient in Eq. (2.42) and $c \sim a^2$ for the coefficient in Eq. (2.45).

For subdiffusive transport modelled by the anomalous diffusion propagator, Eqs. (2.53) and (2.54), we obtain the results analogous to Eqs. (2.57), (2.58), and (2.59), with a replacement of the exponent $1/(2+\beta)$ by $2/(2+\beta)$. For the ratio of the exponents, this yields $\gamma_I/\gamma_x = 1$. Clearly, a similar consideration in arbitrary spatial dimensionality would give

$$\gamma_I/\gamma_x = d/2.$$

As was already pointed out in Sec. 2.1, the 2D geometry allows us to consider a regime of (nearly) diffusive transport also in the absence of interaction. Indeed, even though the non-interacting system gets localized in the thermodynamic limit, the localization length ξ is much larger than the mean free path l when the disorder is sufficiently weak. The transport in the regime $l \ll L \ll \xi$ has then diffusive character (with weak-localization corrections for which the system size L serves as an infrared cut-off [83]), and the decay of imbalance can be investigated within the non-interacting picture. This problem is studied numerically below in Sec. 2.5. The non-interacting character of the model allows us to consider rather large system sizes (200×200) within exact diagonalization. We focus on times t much smaller than the time of diffusive spreading through the system. Before turning our attention to the numerical simulations, let us discuss the implications of the weak localization for the above analytical results.

Weak localization leads to a frequency-dependent logarithmic correction to the diffusion constant [64]:

$$D(\omega) \simeq D_0 \left(1 - \frac{1}{\pi k_F l} \ln \frac{1}{\omega\tau} \right) . \tag{2.63}$$

Note that the asymptotics of the mean square deviation $r_2(t)$ is controlled by the diffusion constant $D(q,\omega)$ at small ω and small q, with $Dq^2 \sim \omega$, so that we can put $q = 0$ in Eq. (2.63). In the regime of frequencies where the correction is relatively small, we can rewrite Eq. (2.63) as

$$D(\omega) \simeq D_0(\omega\tau)^{\frac{1}{2\pi g}} , \tag{2.64}$$

where we introduced the dimensionless conductance $g = k_F l/2$. This implies for the mean square deviation

$$r_2(t) \sim t^{1-\frac{1}{2\pi g}} , \tag{2.65}$$

i.e., a weak-localization correction to the exponent: $\gamma_x = 1 - 1/2\pi g$.

The tail of the return probability $P(t)$ is controlled by weak multifractality of 2D systems [101, 124, 125] (which is responsible for the behavior of the diffusion constant $D(q,\omega)$ at small ω and relatively large q). The corresponding multifractal exponent is [101, 130, 131] $d_2 = 2 - 2/\pi g$, yielding

$$P(t) \sim t^{-d_2/d} = t^{-1+\frac{1}{\pi g}} , \tag{2.66}$$

and thus $\gamma_I = 1 - 1/\pi g$. We see that the corrections to γ_x and γ_I are different (by factor of 2), and thus the exponents γ_x and γ_I deviate not only from unity but also from each other.

2.5 Numerical results

As discussed above, the numerics in this chapter is restricted to non-interacting 2D systems. We calculate the long-time asymptotics of both the checkerboard imbalance and the columnar imbalance starting from the corresponding maximum-imbalance states. In addition, we calculate the linear-response density response function $\chi(q_x, q_y, t)$, verifying thereby the relation (2.45) between the long-time tail of the imbalance and density response function. This also allows us to check that the power-law tail of the density response function has the same form for all momenta **q**.

We consider a square lattice of $N = L \times L$ sites described by the Hamiltonian

$$H = J \sum_{\mathbf{r},\mathbf{r}'} \delta_{\langle \mathbf{r},\mathbf{r}' \rangle} c_{\mathbf{r}}^{\dagger} c_{\mathbf{r}'} + \sum_{\mathbf{r}} \varepsilon_{\mathbf{r}} c_{\mathbf{r}}^{\dagger} c_{\mathbf{r}} \,, \tag{2.67}$$

where **r** and **r**′ label sites of the square lattice and

$$\delta_{\langle \mathbf{r},\mathbf{r}' \rangle} = \begin{cases} 1 \,, & \mathbf{r}, \mathbf{r}' \text{ nearest neighbors}, \\ 0 \,, & \text{else.} \end{cases} \tag{2.68}$$

We set $J = a = 1$. The onsite potential values $\varepsilon_{\mathbf{r}}$ are uncorrelated random numbers drawn from a random uniform distribution in the interval $[-W, W]$.

We analyze the numerical results based on the predictions for the density response function and the imbalance at long times,

$$\chi(q, t) = \chi_0 \exp\left(-t/t_q\right) + \frac{\chi_1}{t^{1+\gamma_I}} \,, \tag{2.69}$$

$$I(t) = I_0 \exp\left(-t/t_q\right) + \frac{I_1}{t^{\gamma_I}} \,. \tag{2.70}$$

The first terms in these formulas correspond to the exponentially decaying contribution from the Markovian approximation. Here, we keep these terms in addition to long-time tails, in order to be able to describe the case of sufficiently small values of q, such that the exponential decay is not yet strong at times addressed by numerical simulations. The second terms in Eqs. (2.69) and (2.70) are the long-time asymptotics governed by return processes. The exponent γ_I is slightly below unity, $\gamma_I = 1 - 1/\pi g$, as discussed in Sec. 2.4.2.

Since we are interested in the diffusive regime, we first need to identify an appropriate disorder strength. If the disorder is too weak, a density perturbation would spread ballistically; on the other hand, too strong disorder would lead to strong localization for considered system sizes. To identify the diffusive regime, we calculate the mean square displacement

$$r_2(t) = \left\langle \sum_{j=1}^{L} \sum_{i=1}^{L} R_{i,j} \left[n_{(i,j)}(t) - n_{(i,j)}(t=0) \right] \right\rangle \,, \tag{2.71}$$

$$R_{i,j} = [(i - i_0)^2 + (j - j_0)^2]. \tag{2.72}$$

Here, $n_{(i,j)}(t)$ is the particle density at site (i,j) at time t, with i and j labeling rows and columns, respectively, and angular braces denote an average over disorder configurations. The site (i_0, j_0) is the

original position of the density packet. Specifically, we initialize the system with

$$n_{(i,j)}(t=0) = \delta_{i,i_0}\delta_{j,j_0} \,. \tag{2.73}$$

In order to minimize finite-size effects, we choose the site (i_0, j_0) to be located in the center of the system.

The results for $r_2(t)$ for disorder strengths $W = 1.5$ and $W = 2$ are presented in the upper panel of Fig. 2.4: We find the asymptotic power-laws $r_2(t) \sim t^{0.88}$ for $W = 2$ and $r_2(t) \sim t^{0.98}$ for $W = 1.5$. The exponents are slightly below unity, in agreement with the expectation $\gamma_x = 1 - 1/2\pi g$. Therefore, these values of disorder correspond to the diffusive regime with weak-localization corrections. For stronger disorder ($W = 2$), the correction is more significant as expected. Using $r_2(t) = 4D_0 t$ and $D_0 = v^2\tau/2$ at time $t \approx 10$ at which the diffusion is fully established, we get an estimate for the mean free time: $\tau \approx 2$ for $W = 1.5$ and $\tau \approx 1$ for $W = 2$. The mean free time decreases with increasing W approximately as $1/W^2$, as expected for relatively weak disorder. We have also verified that if the initial state is chosen as a 1D domain wall and the corresponding 1D mean square displacement is calculated, the same results are obtained as for the disk mean square displacement (2.71).

The following comment is in order here. Since our initial condition contains single-particle states with different energies, our numerical procedure effectively involves the corresponding averaging. The dominant contribution comes from the broad central part of the band, where the dimensionless conductance g weakly depends on energy and where the majority of states is located. At the same time, one expects also a contribution of band tails, where g is smaller, so that the states have a localization length shorter than our system size. For the mean square displacement $r_2(t)$ this would only induce a small correction to the effective diffusion constant. At the same time, the contribution of localized states should lead to a saturation of the imbalance at long times, $t \to \infty$. Thus, by inspecting the behavior of the imbalance, one can numerically find out whether the localized states from the band tails are essential for the dynamics on a given time scale. We will see below that, within the time range of our numerics, $t = 10^2$, the role of band tails is negligible, even for our stronger disorder, $W = 2$. Therefore, within this time range, we essentially probe the physics associated with the majority of states in the central part of the band. This justifies our description, Eqs. (2.69) and (2.70). Indeed, we will see below that the predicted power laws for the imbalance and density response function are nicely observed in numerical simulations.
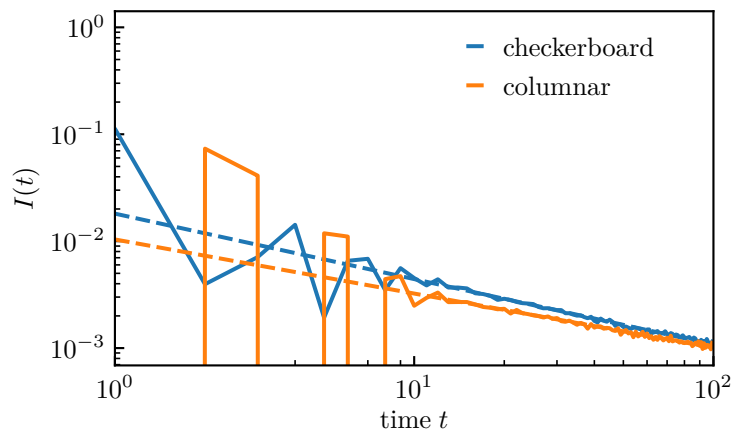
2.5.1 Imbalance

After having identified the diffusive regime by inspecting the mean square displacement, we turn to the numerical analysis of the imbalance. The checkerboard imbalance for $W = 1.5$ and $W = 2$ is shown in the lower panel of Fig. 2.4. A power-law decay of the imbalance is clearly observed. Fitting the imbalance tail to a power-law $\propto t^{-\gamma_I}$, we find $\gamma_I \approx 0.69$ for $W = 1.5$ and $\gamma_I \approx 0.61$ for $W = 2$. The values of the exponent γ_I are somewhat below unity, in agreement with the analytical prediction $\gamma_I = 1 - 1/\pi g$. The deviation of γ_I from unity is larger for larger disorder, as expected. Further, the deviations of γ_I from unity are larger than the respective deviations of γ_x, again in agreement with the analytical expectations.

As pointed out above, the imbalance does not exhibit any saturation within the considered time window (even though it drops down to a relatively small value $\sim 10^{-3}$). This shows that strongly localized states in the band tails do not play any essential role in this time range. In Appendix A.1, we explicitly check this statement by evaluating the fraction of strongly-localized states contributing
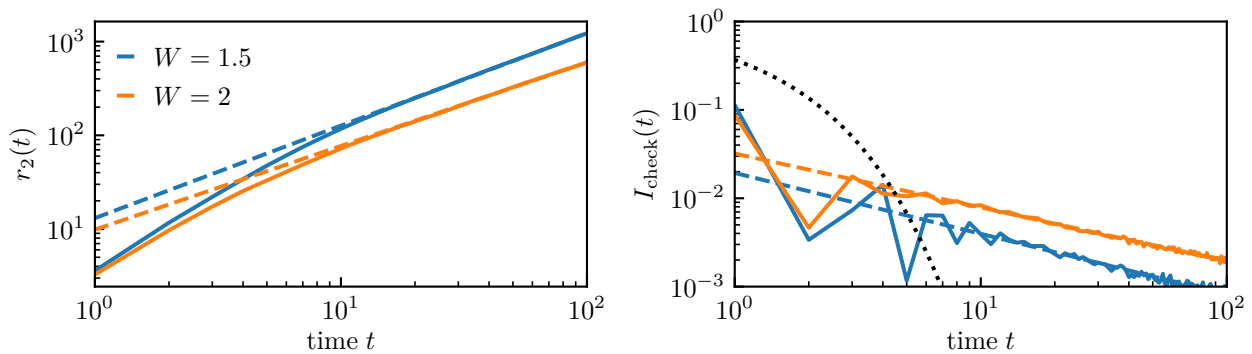
Figure 2.4: Figure adapted from Ref. [54]. Mean square displacement $r_2(t)$ (*left panel*) and checkerboard imbalance $I_{\text{check}}(t)$ (*right panel*) as functions of time for 2D systems with disorder strengths $W = 1.5$ and $W = 2$. Calculations were performed on a square lattice of 201×201 sites with open boundary conditions; averaging over 5 disorder configurations was done. The dashed lines in the upper panel are power-law fits, $r_2(t) \sim t^{\gamma_x}$, yielding $\gamma_x = 0.88$ for $W = 2$ and $\gamma_x = 0.98$ for $W = 1.5$. The dashed lines in the right panel are power-law fits $I_{\text{check}}(t) \sim t^{-\gamma_I}$, yielding $\gamma_I = 0.61$ for $W = 2$ and $\gamma_I = 0.69$ for $W = 1.5$. The black dotted line shows an exponential decay $\exp\left(-t/\tau\right)$ with $\tau = 1$ in units of the hopping time for comparison.

Figure 2.5: Figure adapted from Ref. [54]. Checkerboard and columnar imbalance as functions of time at disorder $W = 1.5$. Simulations were performed on square lattices of 101×101 and 100×100 sites, respectively, with open boundary conditions and with averaging over 60 disorder configurations. The dashed lines are power-law fits $I(t) \sim t^{-\gamma_I}$, yielding $\gamma_I = 0.61$ for the checkerboard imbalance and $\gamma_I = 0.51$ for the columnar imbalance.

to the imbalance dynamics in the transient time window $t \leq 100$. We also demonstrate there that the conductance in the band of extended states only slightly deviates from the value in the band center. As a result, the contributions of different energies to the imbalance produce, in our transient time

window, a function that is indistinguishable from a simple power law.

In order to emphasize the significance of the slow, power-law decay, we also show the Markovian result $\exp\left(-t/\tau\right)$ with $\tau = 1$ in the plot (black dotted line). On the scale of $t \approx 10$, this exponential contribution becomes negligible ($\sim 10^{-4}$). For our largest times, $t \approx 100$, it drops down to a value as small as $\sim 10^{-40}$. Our numerical results therefore clearly confirm an important role of classical memory effects in the imbalance of a disordered system. Furthermore, the predicted difference between the imbalance- and mean-square displacement exponents, γ_I and γ_x, is observed numerically.

As shown in Fig. 2.5, the behavior of the columnar imbalance is very similar to that of the checkerboard imbalance. Indeed, they are very close numerically and show almost the same power-law decay, with $\gamma_I \approx 0.51$ for the checkerboard imbalance and $\gamma_I \approx 0.61$ for the columnar imbalance. The system size in this figure is $N = 101 \times 101$, i.e., smaller than in Fig. 2.4 (where $N = 201 \times 201$). A slightly smaller value of γ_I for the checkerboard imbalance in comparison with Fig. 2.4 is thus attributed to finite-size effects.

2.5.2 Density response function

We have also performed numerical simulations of the density response function $\chi(q_x, q_y, t)$, which is predicted to decay at long times as $t^{-1-\gamma_I}$, see Eq. (2.69). Note that this prediction applies for any value of the momentum (q_x, q_y). To make a direct connection with the numerical analysis of the imbalance in Sec. 2.5.1, we carry out a linear-response calculation with respect to a thermal state with the chemical potential chosen in the center of the band, $\mu = 0$, and with a temperature of the order of the band width; see Appendix A.2 for details.

Instead of directly investigating the long-time tail of the correlator $\chi(q_x, q_y, t)$, we perform its numerical integration to obtain the long-time behaviour of the imbalance at the considered wave vector (see Eqs. (2.29), (2.31)):

$$I_{q_x, q_y}(t) \propto \int_0^t \mathrm{d}t' \, \chi(q_x, q_y, t') - \tilde{\chi}_0 \,. \tag{2.74}$$

Here the constant $\tilde{\chi}_0$ is equal to the zero-frequency limit of the density response function, $\tilde{\chi}_0 \equiv \tilde{\chi}(\omega = 0, q_x, q_y)$, which ensures $I_{q_x, q_y}(t) \to 0$ at $t \to \infty$. In order to characterize the long-time tails, we fit the integrated density response $\int_0^t \mathrm{d}t' \, \chi(q_x, q_y, t')$ in a late-time window $t \in [20, 100]$ to the function

$$f(t) = f_0 + f_1 t^{-\gamma_I} \tag{2.75}$$

with fitting parameters f_0, f_1, and γ_I. The constant f_0 corresponds to $\tilde{\chi}_0$ of Eq. (2.74) and is subtracted to get the imbalance. In this way, we obtain the imbalance $I_{q_x, q_y}(t)$ and the imbalance exponent γ_I for the whole range of momenta (q_x, q_y).

In Fig. 2.6, we show $I_q(t) \equiv I_{q_x=q, q_y=q}(t)$ at temperature $T = 3$ for a square system with $L = 80$ and disorder $W = 1.5$, for momenta $q = q_n = 2\pi n/L$ with $n = 2, 3, \ldots, 39$. For this plot the integrated density was rescaled by a factor determined from comparison of the large-q tails to the directly calculated imbalance. (Since the actual factor between imbalance and integrated response depends on the momentum, this can lead to the small-q curves exceeding unity at short times.) The values of momenta increase from top to bottom. For the lowest momenta, the power-law decay can barely be observed within the time window of the simulation, since the exponential contribution decays slowly. For larger momenta, the exponential contribution decays very quickly, so that $I_q(t)$ is governed by the power-law tail starting already from rather short times. We observe that, for sufficiently large
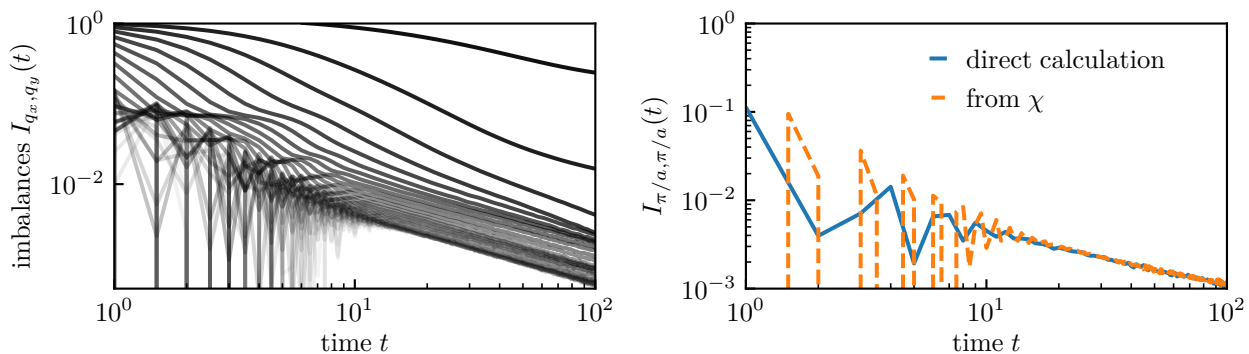
Figure 2.6: Figure adapted from Ref. [54]. *Left panel*: Numerical results for the imbalance $I_q(t) \equiv I_{q_x=q,q_y=q}(t)$ obtained according to Eq. (2.74) from the density response function for $W = 1.5$, $L = 80$, and temperature $T = 3$, with periodic boundary conditions. The data was averaged over about 500 disorder realizations. Imbalance $I_q(t)$ is calculated for momenta $q = q_n = 2\pi n/L$ with $n \in [2, 39]$. The numerical factor between imbalance and integrated density response function is obtained from a comparison of the long-time tail of the largest-q curve to the directly calculated imbalance result (cf. Fig. 2.5). *Right panel*: Comparison between the checkerboard imbalance directly calculated from the time evolution of a checkerboard state (with $L = 101$) and the checkerboard imbalance from the density response function. For this comparison, the shift constant and factor were determined by fitting the integrated density response function to a power-law with the same exponent as found for the checkerboard imbalance from the direct calculation.

q, all imbalance curves become parallel straight lines in the long-time limit, confirming the momentum independence of the exponent.

In Fig. 2.7, we show the values of the exponent $\gamma_I(n_x, n_y)$ corresponding to $I_{q_{n_x},q_{n_y}}(t)$. The left panel shows a color map of the exponent as a function of n_x and n_y for $n_x, n_y = 2, 3, \ldots, 39$. The right panel displays the diagonal exponents, $n_x = n_y = n$. As expected from the imbalance plots, the time window of our simulation does not suffice to find reliably the power-law exponents in the low momentum sector $n \lesssim 8$, as the exponential component decays too slowly. This region is therefore excluded in both panels. The error bars in the right panel show the range of exponents, for which the mean square error of the obtained fit deviates by up to five percent from the optimum fit. The numerical results are consistent with the analytical predictions that γ_I is independent of q and is somewhat below 1 (because of weak multifractality). Further, the numerical value $\gamma_I(q_{39}) \approx 0.8$, corresponding to the checkerboard imbalance, is in a good agreement with $\gamma_I \approx 0.7$ extracted from the direct checkerboard imbalance calculation in Sec. 2.5.1. This agreement is also demonstrated in the lower panel of Fig. 2.6 where the checkerboard imbalance obtained by direct simulations and from the density response function are compared. For this plot, the shift constant $\tilde{\chi}_0$ was obtained by fitting the integrated density response to a power-law with the exponent found for the directly calculated imbalance (slightly differing from the optimal-fit exponent for the integrated density); the overall scaling factor was fixed by comparing the tails.
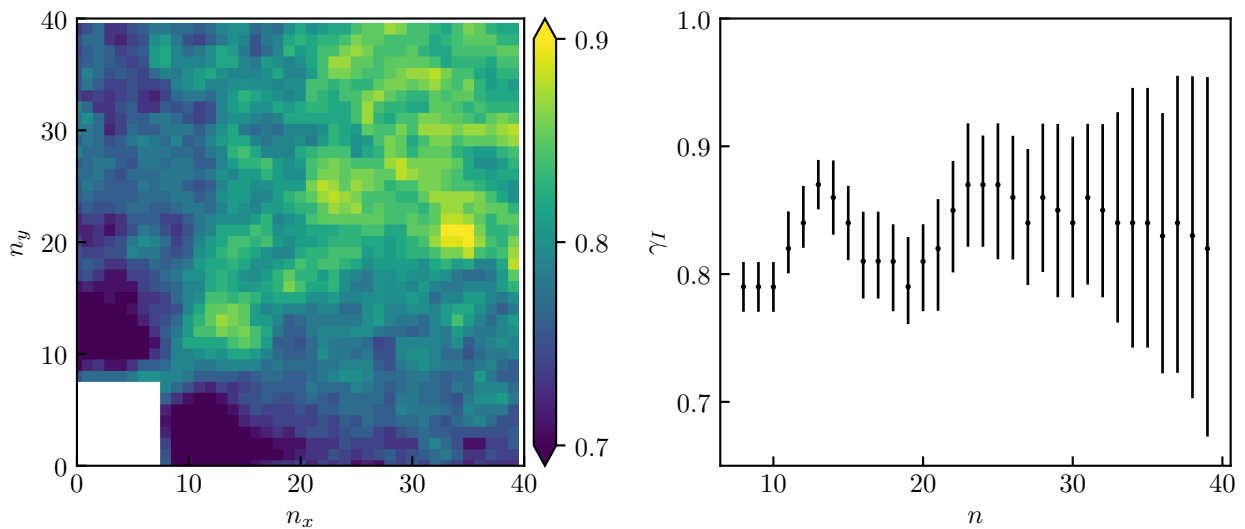
Figure 2.7: Figure adapted from Ref. [54]. *Left panel*: Tomography of power-law exponents $\gamma_I(q_x, q_y)$ for imbalance obtained according to Eq. (2.74) from the density response function. Exponents are obtained from fitting the long-time tail to a power-law in the time interval $t \in [20, 100]$. The range $(n_x < 8, n_y < 8)$ is excluded since the time window of the simulation does not allow us to extract reliably the power-law exponents at these momenta. *Right panel*: Exponents $\gamma_I(q_x = q_y = q)$ describing the power-law tails of the imbalance curves shown in Fig.2.6. The error bars are the intervals for which the mean square error of the corresponding fit is up to five percent larger than the mean square error of the optimal fit.

2.6 Summary

In this chapter we demonstrated that memory effects lead to a power-law asymptotic tail of the imbalance in disordered systems, $I(t) \propto t^{-\gamma_I}$. We derived a relation between the imbalance and the density response function and showed that $I(t) \propto P(t)$, where $P(t)$ is the probability for a particle to be found at the original point after a long time t ("return probability"). In the case of normal diffusive transport, the analysis based on classical memory effects related to diffusive returns yields $\gamma_I = d/2$, where d is the spatial dimensionality. Having in mind the ergodic side of the MBL transition, we have also considered the regime of subdiffusive transport. Specifically, we used its phenomenological modelling in terms of a momentum-dependent diffusion constant, $D(q) \propto q^\beta$, which yields the mean square deviation $r_2(t) \propto t^{\gamma_x}$ with $\gamma_x = 2/(2 + \beta)$. For the imbalance in this situation, we obtained a power-law decay with the exponent $\gamma_I = d/(2 + \beta)$, implying the ratio $\gamma_I/\gamma_x = d/2$, independent of the subdiffusive exponent β.

To complement the analytical results, we have performed numerical simulations for non-interacting disordered 2D systems. In these simulations, we have chosen a disorder range that ensures the diffusive character of transport for considered system sizes. More accurately, in view of weak-localization effects, the transport is "weakly subdiffusive", i.e., the exponent γ_x is slightly below unity. For such systems, we have demonstrated a crucial role of memory effects in the long-time behavior of the imbalance and found a power-law decay of the imbalance. The corresponding exponent γ_I shows a downward

deviation from unity, which is related to weak multifractality of eigenstates of 2D non-interacting disordered systems. This deviation leads to a weak violation of the relation $\gamma_I = \gamma_x$.

Our results explain the slow, power-law decay of the imbalance on the ergodic side of the MBL transition, as observed in numerical simulations of 1D disordered interacting systems [57, 58, 115–118]. The relation $\gamma_I = \gamma_x$ that we find by modelling the subdiffusive transport by a diffusion constant $D(q) \propto q^\beta$ is consistent with numerical observations [59, 117]. The subdiffusive transport in this class of systems is usually attributed to Griffiths effects related to rare strongly localized spots. Our analysis is, however, rather general and shows that, whatever the mechanism of the subdiffusion is, it will lead to the corresponding slow decay of the imbalance due to mode coupling induced by the memory effects.

A slow decay of the imbalance was also numerically observed on the ergodic side of the MBL transition in 2D systems [58, 117]. In this case, it was found that the corresponding effective exponent γ_I increases with time, saturating at the value $\gamma_I = 1$ at long times. This is consistent with the relation $\gamma_I = \gamma_x$, since in 2D geometry the Griffiths effects cannot suppress the conventional diffusion ($\gamma_x = 1$). An increase of γ_I towards unity at intermediate times is a transient effect attributed to trapping of particles at rare localized spots [117, 123].

A slow, power-law decay of the imbalance was numerically found also for 1D quasiperiodic systems. Specifically, it was observed [117] that the exponent γ_I increases with time, saturating at the value $\gamma_I = 1$. This is in consistency with the relation $\gamma_I = (d/2)\gamma_x$, in view of the ballistic character of transport ($\gamma_x = 2$) in quasiperiodic systems. It is worth pointing out, however, that our analysis in this chapter was performed for truly random systems, so that its application to quasiperiodic systems should be viewed as a conjecture. Further work in this direction is needed, especially in view of the importance of quasiperiodic systems for experimental investigations.

A weak violation of the relation $\gamma_I = (d/2)\gamma_x$ in 2D non-interacting disordered systems in the weak-localization regime poses the question as to whether the relation is exact on the ergodic side of the MBL transition. The mechanism related to quantum coherence of single-particle states, which is responsible for multifractality in 2D non-interacting systems, should not be relevant for the ergodic interacting systems at high temperature, in view of decoherence. This provides an expectation that the relation $\gamma_I = (d/2)\gamma_x$ strictly holds (for the exponents characterizing the limiting long-time behavior) in the ergodic phase of an interacting disordered system. In fact, Ref. [123] identified other power-law contributions related to trapping of particles by localized spots in 1D geometry. These contributions are, however, subleading (i.e., decaying faster) in comparison with that studied in the present chapter, and thus do not affect our derivation of the relation $\gamma_I = (d/2)\gamma_x$. Further computational and experimental work towards a systematic verification of the relation between the exponents γ_I and γ_x on the ergodic side of the MBL transition would be of much interest.

3

Ancilla measurements on a two-level system

In this chapter, we introduce and investigate a model of a two-level system ("chain") interacting with a two-level detector during fixed intervals of unitary time evolution. At the beginning of each time interval, the detector is initialized in the same eigenstate. At the end of each time interval, its state is projectively measured. This model presents a simple realization of system-detector evolution. In certain limiting cases, the protocol partly mimics strong measurements on the chain. However generally, despite the simplicity of the model, the dynamics is very complex. Main object of our investigation is the distribution of chain states immediately after the measurement, averaged over time and measurement outcomes. This distribution can be understood from a functional master equation in the state space. As a function of the interaction strength and the duration of the unitary time evolution interval, we identify different dynamical phases based on the properties of the distribution. The distribution functions can be attributed properties which are reminiscent of localization and delocalization in a disordered system. A connection to Anderson transitions is established via known indicators of Anderson localization, for which counterparts are defined based on the distribution of states. Furthermore, the distribution curves generically feature non-trivial fractal box-counting dimensions. Many qualitative features of the distributions and the phase diagram can be understood based on special cases, in which the shape of the distribution can be understood from analytical considerations. The results in the generic case are established using Monte-Carlo simulations and numerical solution of the discretized master equation Master-equation.

The results presented in this chapter were developed and discussed together with my collaborators Oleg M. Yevtushenko, Igor V. Gornyi, and David B. Saakian. The one-step solution of the model, as well as the special cases of freezing, shifting, and $\gamma = 0$ (presented in 3.2) where largely established by my collaborators before I joined the project. The presentation in the mentioned section is based on their notes. Ref. [65] was written in parallel to this chapter. This chapter contains literal excerpts from Ref [65].

3.1 Introduction

In the first chapter we encountered localization and measurements in their arguably most basic forms, with exponential localization of every wave function in a one dimensional system, and projective measurements. After turning to more nuanced disorder effects in weakly localized or delocalized

systems in the second chapter, we now focus on a more general notion of measurements, considering the dynamics of a two-level system under indirect measurements via an ancilla system serving as a detector.

The concept of measurements can be generalized from axiomatic quantum mechanical (projective) measurements, by introducing a "detector" or "ancilla", which interacts with the system to be measured during intervals of unitary time evolution. [66, 132, 133]. Here, the projective measurement is performed on the detector instead of the system itself so that there is only an indirect backaction of the measurement on the system [133]. This process of joined system-detector unitary evolution and projection of the detector can also be summarized in terms of generalized *measurement operators* [66]. Such indirect measurements are sometimes called "weak" because they do not necessarily allow to determine the state of the measured system with certainty without prior knowledge [132]. At the same time, the measurement does not necessarily perturb the system state as strongly as a projective measurement would.

Explicitly taking the detector into account in the time evolution is a natural idea from the point of view of reductionism. Like the system itself, the detector in an experiment should obey the laws of quantum mechanics, time evolve according to the Schrödinger equation, and couple to the system via some system-detector Hamiltonian. The properties of the detector can be important for the physical process of the measurement. Thus, we should investigate how its microscopic properties can influence this process. The concept is immediately relevant to laboratory experiments, as they may be not well described by "direct" projective measurements of the monitored observable [132].

Additional motivation to consider generalized measurements comes from the field of measurement induced transitions, where measurements drive a dynamical transition in the measured system [20–39]. Indeed, specifics of the detector model can introduce additional parameters [26], besides the measurement frequency which controls the transition in the presence of projective measurements. An example is the *strength* of each measurement, which is a function of the parameters determining the system-detector interaction and allows to control the backaction on the system and the amount of information provided by a measurement outcome [134].

In any case, one can ask a question about how much the induced dynamics actually depends on the employed measurement model.

In the literature, the time evolution of large systems with generalized and continuous[1] measurements has been investigated in the context of measurement-induced phase transitions [26, 30, 135]. The dynamics of a spinless fermion chain with ancilla measurements is investigated in Ref. [39]. In the appendix of Ref. [30], a single site with variable occupation is combined with a detector, to investigate the emergent stochastic dynamics in such a system.

Our setup is most similar to the model investigated in the continuous-measurement limit in Ref. [67]: We consider a "chain" of two sites with a single particle on it as the measured system. The "detector" is another two-level system (say, a spin) which interacts with the density on one of the sites during a time interval T. The strength of the interaction is called M. After each projective measurement, the detector is reset to the same eigenstate. In contrast to the model investigated in Ref. [67], there are no periods of free time evolution of the chain. Detector and chain are always coupled during unitary time evolution. Furthermore, we do not restrict ourselves to the continuous limit, but consider the entire $M - T$ plane.

---

[1]Continuous measurements are obtained by taking the measurement frequency to infinity while taking the strength of each measurement to zero. The fixed product of frequency and measurement strength gives a new effective measurement strength over a finite time interval [67, 134]. In our system the continuous limit is realized by taking the coupling $M/\gamma \to \infty$ and the unitary time evolution interval $T\gamma \to 0$, keeping $M^2 T/\gamma$ fixed [67].

Although this setup seems rather simplistic, the dynamics of the coupled system turns out to be complex, exhibiting dynamical transitions in the $M - T$ parameter plane. This is in agreement with the findings by the authors of Ref. [67] who demonstrate in a similar model dynamical transitions that generalize the quantum Zeno effect to several stages in the continuous limit.

As the accessible[2] Hilbert space of our system has just four states, the joined system-detector time evolution can easily be solved for single time steps. The solution consists of two possible mappings between the immediate post-measurement states of the chain, corresponding to two possible outcomes of the projective measurement on the detector. As the detector is reinitialized to the same state after every projection (removing its "memory" of the measurement outcome), the post-measurement states can be described as points on a Bloch-sphere: While the state of the detector is fixed, the chain state is generally not projected by the detector measurement, and can lie anywhere in the two-level Hilbert space. The number of different quantum trajectories grows exponentially with the number of measurements, thus complicating the situation.

It turns out that typical quantum trajectories—represented by the post-measurement states—converge to a one dimensional submanifold of the Bloch sphere which forms a circle through its poles. The poles of the Bloch sphere represent the density eigenstates of the chain site coupled to the detector[3].

We characterize a parameter point (M, T) by the distribution of states on this circle, averaged over time and measurement outcomes. These distributions are investigated via single time-averaged quantum trajectories (from Monte-Carlo simulation of the Born rule) and a Master-equation approach, that converts the post-measurement mappings into a Markov process on the circle (governed by an implicit equation similar to what was investigated in [136–138]). The Master equation is analyzed analytically along different special kinds of parameter lines, and numerically by discretization. The discretized dynamical process on the circle exhibits a transition between ergodic- and non-ergodic phase as a function of the parameters. This transition is argued to survive, if the limit to the continuous process is taken.

We also analyze the distributions with observables familiar from Anderson localization, using the participation ratio and support measures to describe "localization" and "delocalization" on the Bloch-sphere (similarly observed in distributions from random matrices in Ref. [139]). Localized and delocalized regions in (M, T) parameter space can approximately be described in terms of cases where the outcome average can be understood analytically. An important difference to the physics of Anderson localization is the absence of a controllable system size in our problem. Interestingly, our distributions also exhibit fractal properties (reminiscent of an Anderson transition), which we describe with a box-counting dimension. A connection to the Anderson transition is established by calculating a quantity closely related to the local density of states in a disordered system, which can serve as an indicator of the Anderson transition [10, 68]. This quantity recognizes the non-ergodic phase in our system (in analogy to a localized phase in an Anderson insulator) as well as the phase where we observe complete delocalization in terms of participation ratio and support (in analogy to a disordered metal). In between, it exhibits a transient behavior that does not have an analogue in the Anderson transition.

The occurrence of similarities to the Anderson transition in our measured system is interesting in light of recent field theoretical descriptions of measurement-induced transitions that suggest a relation to Anderson localization [38, 41, 69–71]. In particular, in Refs. [38, 41] measurement-induced transitions in free, $D > 1$-dimensional fermionic systems were related to Anderson transitions in $D+1$ dimensions.

The chapter is structured as follows: The model is introduced and solved for a single time step

---

[2]restricted to half-filling

[3]The exact plane of the circle can be gauged arbitrarily and hence does not have physical relevance.

in Sec. 3.2. We also demonstrate attraction of generic quantum trajectories to the one-dimensional manifold and discuss some basic physical intuition for the ancilla measurements. In Sec. 3.3 we define the state distribution on the one dimensional manifold, and explore the possibility of different averages in this definition, together with corresponding numerical approaches. In Sec. 3.4, we analytically derive some properties of the distribution for certain special cases. Our numerical approaches are tested and analyzed in Sec. 3.5. In Sec. 3.6, we show examples of distributions for generic parameters, which are analyzed systematically in a plane of parameters (M, T) in Sec. 3.7, in terms of ergodicity, localization, and fractality. We conclude in Sec. 3.8.

3.2 The model

In this section, we introduce the model, solve it for a single time step, and show, that typical post-measurement quantum trajectories are attracted to a one-dimensional sub-manifold of the Bloch-sphere. We discuss connections to the familiar case of projective measurements and the quantum Zeno effect.

3.2.1 Description

We consider a single particle which can tunnel between two sites s_1 and s_2 (the "chain") with amplitude $\gamma \in \mathbb{R}$. The particle density on site s_1 interacts with a two-level system D (the "detector"), with states $|+\rangle$, $|-\rangle$ through interaction strength $M > 0$. The detector enters the Hamiltonian only through its coupling to the site s_1, instead of being described by a separate kinetic term. A basis of the the joined chain-detector Hilbert space is given by the states

$$
\begin{aligned}
|b_1\rangle &= |1, 0\rangle \otimes |+\rangle \\
|b_2\rangle &= |1, 0\rangle \otimes |-\rangle \\
|b_3\rangle &= |0, 1\rangle \otimes |+\rangle \\
|b_4\rangle &= |0, 1\rangle \otimes |-\rangle.
\end{aligned}
\tag{3.1}
$$

The Hamiltonian governing the unitary time evolution of the system reads

$$
H = \gamma(a_1^\dagger a_2 + a_2^\dagger a_1) + M n_1 \sigma_x \quad n_1 := a_1^\dagger a_1
\tag{3.2}
$$

$$
= \gamma(|b_1\rangle \langle b_3| + |b_2\rangle \langle b_4|) + M |b_1\rangle \langle b_2| + \text{hc.},
\tag{3.3}
$$

$$
[H] = \begin{pmatrix} 0 & M & \gamma & 0 \\ M & 0 & 0 & \gamma \\ \gamma & 0 & 0 & 0 \\ 0 & \gamma & 0 & 0 \end{pmatrix},
\tag{3.4}
$$

where $a_i^\dagger$ and a_i are creation and annihilation operators on site $i \in \{1, 2\}$, and σ_x is the Pauli-x-matrix, acting on the Hilbert space of the detector. The first term (proportional to γ) describes the free evolution of the chain. In absence of detector coupling $M = 0$ the chain performs free oscillations between the two levels. Here and in the following, we denote the matrix representation of an operator with square brackets.
The time evolution of chain and detector is described by the following protocol:
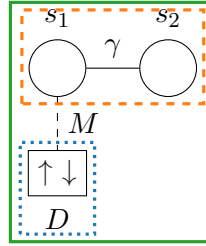
Figure 3.1: Sketch of the model. A single particle tunnels between sites s_1 and s_2 with tunnel amplitude γ. Site s_1 interacts with a two-level system D, which is measured projectively. D acts as a detector for the density on s_1. In the text we refer to the sites $s_{1,2}$ as "the chain" (orange dashed box), the two-level system D is called "the detector" (blue dotted box) and the entirety of chain and detector is refered to as "the system" (green solid box).

1. Prepare the system in state $|\Psi_0\rangle = \alpha_0 |b_2\rangle + \beta_0 |b_4\rangle$.

2. Perform unitary time evolution according to H for a time T.

3. Projectively measure the state of D (in the basis $|+\rangle$, $|-\rangle$).

4. Reset the state of D to $|-\rangle$.

5. Iterate steps 2 - 4 N_t times.

Determining the state of D can give information about the state of the chain, even without prior knowledge of this state. In this sense, D acts as a detector for the chain state (this is elaborated further in Sec. 3.2.5). Fig. 3.1 shows a picture of the model.

Without loss of generality, we can fix one of the three model parameters M, T, γ—this is merely a choice of units. In this sense, our model "lives" in a two-dimensional parameter *plane*. For all of our numerical results, we fix $\gamma = 1$.

3.2.2 Solving the model

Initially, our system is prepared in state $|\Psi_0\rangle = \alpha_0 |b_2\rangle + \beta_0 |b_4\rangle$. After every measurement, the detector D is reinitialized in state $|-\rangle$. Thus, the state at post-measurement time $t_i^+ := i \cdot T + 0$ (the *post-measurement state*) is again of the form

$$|\Psi_i\rangle := \left|\Psi(t = t_i^+)\right\rangle := \alpha_i |b_2\rangle + \beta_i |b_4\rangle. \tag{3.5}$$

We solve a single time step of the model, by expressing α_i and β_i in terms of the previous coefficients α_{i-1} and β_{i-1}. To obtain this mapping, the first step is to perform unitary time evolution on $\left|\Psi_{i-1}\right\rangle$.

The matrix exponential of H can be calculated explicitly, and we obtain

$$e^{-iTH} \left| \Psi_{i-1} \right\rangle = \alpha_i^{(+)} \left| b_1 \right\rangle + \beta_i^{(+)} \left| b_2 \right\rangle + \alpha_i^{(-)} \left| b_3 \right\rangle + \beta_i^{(-)} \left| b_4 \right\rangle \tag{3.6}$$

$$\alpha_i^{(+)} := \alpha_{i-1} a_{10}^{(+)} + \beta_{i-1} b_{10}^{(+)}, \quad \beta_i^{(+)} := \alpha_{i-1} a_{01}^{(+)} + \beta_{i-1} b_{01}^{(+)} \tag{3.7}$$

$$\alpha_i^{(-)} := \alpha_{i-1} a_{10}^{(-)} + \beta_{i-1} b_{10}^{(-)} \quad \beta_i^{(-)} := \alpha_{i-1} a_{01}^{(-)} + \beta_{i-1} b_{01}^{(-)} \tag{3.8}$$

$$a_{10}^{(+)} = -i \left(\sin[MT/2] \cos[YT/2] + \frac{M}{Y} \cos[MT/2] \sin[YT/2] \right), \tag{3.9}$$

$$a_{10}^{(-)} = \cos[MT/2] \cos[YT/2] - \frac{M}{Y} \sin[MT/2] \sin[YT/2], \tag{3.10}$$

$$a_{01}^{(+)} = -\frac{2\gamma}{Y} \sin[MT/2] \sin[YT/2], \tag{3.11}$$

$$a_{01}^{(-)} = -i\frac{2\gamma}{Y} \cos[MT/2] \sin[YT/2], \tag{3.12}$$

$$b_{10}^{(\pm)} = a_{01}^{(\pm)}, \quad b_{01}^{(\pm)} = a_{10}^{(\pm)} - \frac{M}{\gamma} a_{01}^{(\mp)}; \tag{3.13}$$

where we introduced $Y := \sqrt{4\gamma^2 + M^2}$. The next step is to calculate the backaction on the chain of the projective measurement on D. Depending on the outcome of this measurement, the system ends up in a different state. We refer to the measurement outcome as a click event $(+)$, if the detector is found in the $|+\rangle$ state, and as a no-click event $(-)$ otherwise. These two outcomes correspond to the projectors

$$\mathcal{P}^{(\pm)} := |\pm\rangle \langle\pm| \mathbb{1}_{s_1,s_2}. \tag{3.14}$$

The measurement outcome is random, with the probabilities $P^\pm$ of each outcome determined by the coefficients of the respective states:

$$P^\pm = \|\mathcal{P}^{(\pm)} e^{-iTH} \left| \Psi_{i-1} \right\rangle\| \tag{3.15}$$

Taking into account reinitialization of the detector (step (4) of the protocol) we can express the post-measurement states using the projectors:

$$\left| \Psi_i^{(\pm)} \right\rangle = \frac{\langle\pm| \mathcal{P}^{(\pm)} e^{-iTH} \left| \Psi_{i-1} \right\rangle}{\sqrt{P^\pm}} |-\rangle. \tag{3.16}$$

With the factor $\sqrt{P^\pm}^{-1}$ normalizing the state. Without this factor, the state is generally not normalized, since the measurement on the detector projects out a component of the state.

Considering only post-measurement states, we can conveniently summarize the time evolution as a

mapping between post-measurement states after $(i-1)$-th and i-th measurement:

$$\begin{pmatrix} \alpha_i^{(\pm)} \\ \beta_i^{(\pm)} \end{pmatrix} = \frac{1}{\sqrt{P_{i-1}^{\pm}}} [M^{\pm}] \begin{pmatrix} \alpha_{i-1} \\ \beta_{i-1} \end{pmatrix}, \tag{3.17}$$

$$[M^{\pm}] = \begin{pmatrix} a_{(10)}^{(\pm)} & b_{(10)}^{(\pm)} \\ a_{(01)}^{(\pm)} & b_{(01)}^{(\pm)} \end{pmatrix}, \tag{3.18}$$

where the probabilities are given by

$$P^{\pm} = \begin{pmatrix} \alpha^* & \beta^* \end{pmatrix} [M^{\pm}]^{\dagger} [M^{\pm}] \begin{pmatrix} \alpha \\ \beta \end{pmatrix} \tag{3.19}$$

Because we use them later, we also give the explicit forms of the matrices $[M^{\pm}]$:

$$[M^-] = \begin{pmatrix} \cos\left(\frac{MT}{2}\right)\cos\left(\frac{YT}{2}\right) - \frac{M}{Y}\sin\left(\frac{MT}{2}\right)\sin\left(\frac{YT}{2}\right) & -i\frac{2\gamma}{Y}\cos\left(\frac{MT}{2}\right)\sin\left(\frac{YT}{2}\right) \\ -i\frac{2\gamma}{Y}\cos\left(\frac{MT}{2}\right)\sin\left(\frac{YT}{2}\right) & \cos\left(\frac{MT}{2}\right)\cos\left(\frac{YT}{2}\right) + \frac{M}{Y}\sin\left(\frac{MT}{2}\right)\sin\left(\frac{YT}{2}\right) \end{pmatrix}, \tag{3.20}$$

$$[M^+] = -i\begin{pmatrix} \sin\left(\frac{MT}{2}\right)\cos\left(\frac{YT}{2}\right) + \frac{M}{Y}\cos\left(\frac{MT}{2}\right)\sin\left(\frac{YT}{2}\right) & -i\frac{2\gamma}{Y}\sin\left(\frac{MT}{2}\right)\sin\left(\frac{YT}{2}\right) \\ -i\frac{2\gamma}{Y}\sin\left(\frac{MT}{2}\right)\sin\left(\frac{YT}{2}\right) & \sin\left(\frac{MT}{2}\right)\cos\left(\frac{YT}{2}\right) - \frac{M}{Y}\cos\left(\frac{MT}{2}\right)\sin\left(\frac{YT}{2}\right) \end{pmatrix}. \tag{3.21}$$

Post-measurement states along an arbitrary quantum trajectory can be calculated using Eq. (3.17) by applying the matrices and probabilities according to the sequence of outcomes specifying this trajectory. The matrices encompass joined chain-detector unitary time evolution and the projection of the detector. Note, that the mapping (3.17) is non-linear, due to the state dependent normalization factor $(P^{\pm})^{-1/2}$.

In the language of generalized measurements, our post-measurement matrices $[M^{\pm}]$ represent the *measurement operators* of our system [132], constructed out of unitary time evolution and projection. Accordingly, they fulfill a completeness relation

$$[M^+]^{\dagger}[M^+] + [M^-]^{\dagger}[M^-] = \mathbb{1} \tag{3.22}$$

which guarantees, that the probabilities of all possible measurement outcomes $(+)$, $(-)$ sum to one. All post-measurement states (and the initial state) are given by a normalized superposition of two orthogonal states $|b_2\rangle$ and $|b_4\rangle$. This suggests introducing a Bloch-sphere by parametrizing a generic post-measurement state as

$$|\Psi\rangle =: \cos\left(\theta/2\right)|b_2\rangle + e^{i\varphi}\sin\left(\theta/2\right)|b_4\rangle \quad \theta \in [0, \pi], \ \varphi \in [-\pi, \pi), \tag{3.23}$$

where the two angles θ and φ are interpreted as angular coordinates of a spherical coordinate system. In this way, the time evolution in terms of post-measurement states can be visualized on the surface of a three-dimensional sphere. The mappings $[M^{\pm}]$ can also be expressed on the surface Bloch sphere,
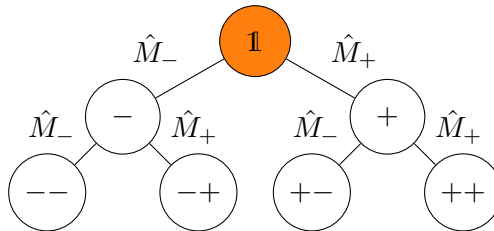
Figure 3.2: Exponential branching of states generated from the initial state (orange) by different combinations of post-measurement matrices $\hat{M}_\pm$ (the $j = 2$ trajectories are shown). After the j-th measurement, there are 2^j different endpoints (in principle, some endpoints can describe the same state). Each generated state (including all end-points) is labeled by the corresponding sequence of measurement outcomes.

as functions $(\theta, \varphi) \mapsto (\theta, \varphi)$.

A set of measurement outcomes $\mu_1, \mu_2, \ldots, \mu_{N_t}$ with $\mu_i \in \{+, -\}$ completely specifies a quantum trajectory in our system. If we perform time evolution according to our protocol for N_t steps, the system realizes one out of 2^{N_t} different quantum trajectories at random (according to the Born rule), see Fig. 3.2. Using the post-measurement mapping (3.17) all post-measurement states of a given quantum trajectory (we refer to this ordered set of states as the *post-measurement trajectory*), as well as the probability of that trajectory can be calculated. In this sense, the model is solved. However, we have not learned anything about the system yet. Our goal in the following is to make general statements about the evolution of a typical quantum trajectory represented by the corresponding post-measurement states.

3.2.3 The Grand Circle

In Fig. 3.3 we show an example of a trajectory of post-measurement states on the Bloch-sphere. We choose an initial state with $(\theta, \varphi) = (1.3, 2.5)$ and perform $3 \cdot 10^2$ steps of time evolution with parameters $\gamma = 1$, $M = 2.92$, $T = 1$ (choosing randomly between outcomes $(+)$ and $(-)$, according to the Born rule). States at early (late) instances of the time evolution are indicated by light (dark) markers on the sphere—see colorbar. We observe an interesting feature: All late states are located on a circle corresponding to the intersection of the Bloch-sphere with the $Y - Z$-plane, $\theta \in [0, \pi]$, $\varphi \in \pm\pi/2$. In the following we refer to this circle as the Grand Circle (GC). In fact, the attraction of our trajectory to the GC is not a coincidence but a general feature of quantum trajectories for almost all sets of parameters. To see this, we first notice, that the GC forms an invariant set for our $[M^\pm]$ maps. This can be checked by explicitly applying the maps to a GC state:

$$[M^+] \begin{pmatrix} \cos\left(\theta/2\right) \\ \pm \mathrm{i}\sin\left(\theta/2\right) \end{pmatrix} \propto \begin{pmatrix} \cos\left(\theta'/2\right) \\ s_\pm \mathrm{i}\sin\left(\theta'/2\right) \end{pmatrix} \quad s_\pm \in \{+, -\}, \ \theta' \in \mathbb{R}. \tag{3.24}$$

Analogously for $[M^-]$.

Secondly, it can be shown that for almost all sets of parameters (and initial states) there is a sequence of plus and minus matrices that attracts to the GC. For this we establish some properties of these
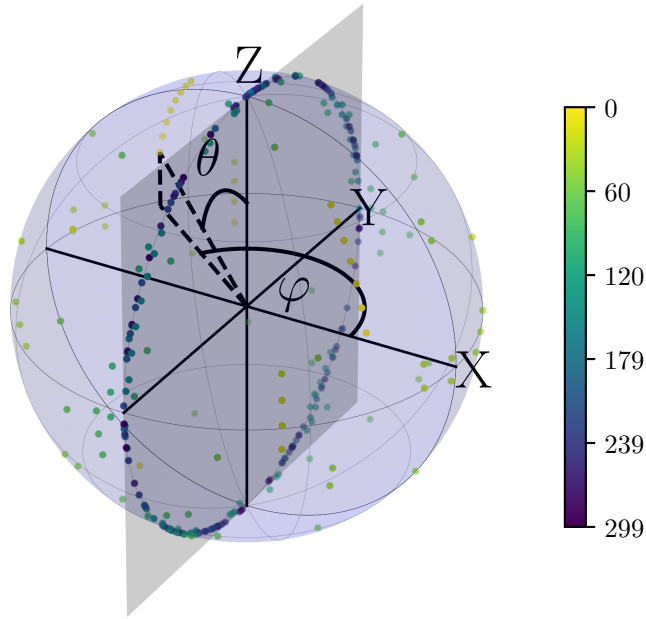
Figure 3.3: Example of a trajectory of post-measurement states (colorful markers) on the Bloch-sphere. The parameters are $\gamma = 1$, $M = 2.92$, and $T = 1$ and the trajectory is initialized at $(\theta, \varphi) = (1.3, 2.5)$. The time instance is color coded, with light (dark) markers corresponding to early (late) times, see colorbar.

matrices. Their eigenvectors and eigenvalues are

$$[V_{(\eta)}^-] = \begin{pmatrix} \frac{M/Y \sin\left(MT/2\right) + \eta\sqrt{(M/Y)^2 - \cos^2\left(MT/2\right)}}{2\gamma/Y \cos\left(MT/2\right)} \\ i \end{pmatrix} \tag{3.25}$$

$$[V_{(\eta)}^+] = \begin{pmatrix} \frac{M/Y \cos\left(MT/2\right) + \eta\sqrt{(M/Y)^2 - \sin^2\left(MT/2\right)}}{2\gamma/Y \sin\left(MT/2\right)} \\ -i \end{pmatrix} \tag{3.26}$$

$$\lambda_{(\eta)}^- = \cos\left(MT/2\right)\cos\left(YT/2\right) - \eta\sin\left(YT/2\right)\sqrt{(M/Y)^2 - \cos^2(MT/2)} \tag{3.27}$$

$$\lambda_{(\eta)}^+ = -i\left[\sin\left(MT/2\right)\cos\left(YT/2\right) + \eta\sin\left(YT/2\right)\sqrt{(M/Y)^2 - \sin^2(MT/2)}\right] \tag{3.28}$$

where $[V_{(\eta)}^\pm]$ and $\lambda_{(\eta)}^\pm$ are eigenvectors and eigenvalues of the $[M^\eta]$ matrix. We note, that the arguments of the square roots expressions in eigenvalues and eigenvectors can be either negative or positive
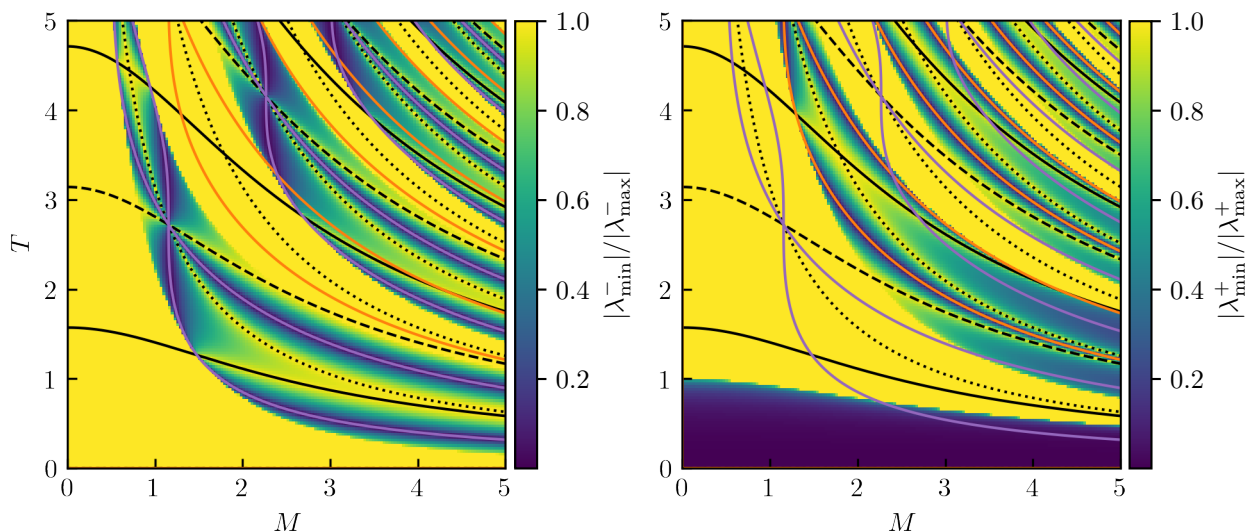
Figure 3.4: Ratio of eigenvalue moduli (smaller to larger) of $[M^-]$ (*left panel*, see Eq. (3.27)) and $[M^+]$ (*right panel*, see Eq. (3.27)) matrices. Solid lines correspond to period-2-cases $YT = (2k+1)\pi$ with $k \in \mathbb{N}_0$. Dashed lines correspond to the frozen cases $TY = 2k\pi$. Dotted lines correspond to the shift cases $MT = k\pi$. Purple (orange) lines correspond to the projective limits $\lambda_{\min}^- = 0$ ($\lambda_{\min}^+ = 0$). (See Secs. 3.2 and 3.4 for descriptions of these special cases.)

depending on the parameters. This gives conditions

$$c_+ : \quad \left| M/Y \right| > \left| \cos\left(MT/2 \right) \right| \tag{3.29}$$

$$c_- : \quad \left| M/Y \right| > \left| \sin\left(MT/2 \right) \right| \tag{3.30}$$

for the $(+)$ and $(-)$ matrices. If the respective condition is fulfilled, the corresponding matrix has two eigenvalues of different moduli, and both (normalized) eigenvectors point to the GC (the first component of Eq. (3.25) or (3.26) is real). If the condition is not fulfilled, it can be seen that the first components of the respective eigenvectors have modulus one, and the eigenvectors are thus of the form $(1, \mathrm{e}^{\mathrm{i}\varphi})^{\mathrm{T}}$ with some angle $\varphi \in [-\pi, \pi)$. In this case, the eigenvectors thus point to the equator of the Bloch-sphere, $\theta = \pi/2$. The eigenvalues in this case are complex conjugate to each other and have the same modulus. See Fig. 3.4 for plots of the eigenvalue ratios $|\lambda_{\min}^\pm|/|\lambda_{\max}^\pm|$ in the $M - T$ parameter plane (with $\gamma = 1$). Yellow regions correspond to ratio one (for example, if the respective condition (3.30) or (3.29) is not fulfilled). Purple (orange) lines correspond to the projective limit of $[M^-]$ ($[M^+]$), $\lambda_{\min}^- = 0$ ($\lambda_{\min}^+ = 0$).

To find general attraction to the GC, we need to consider three different cases:

1. The eigenvectors of both matrices point to the GC.

2. The eigenvectors of one of the matrices points to the GC, the other pair of eigenvectors points to the equator.
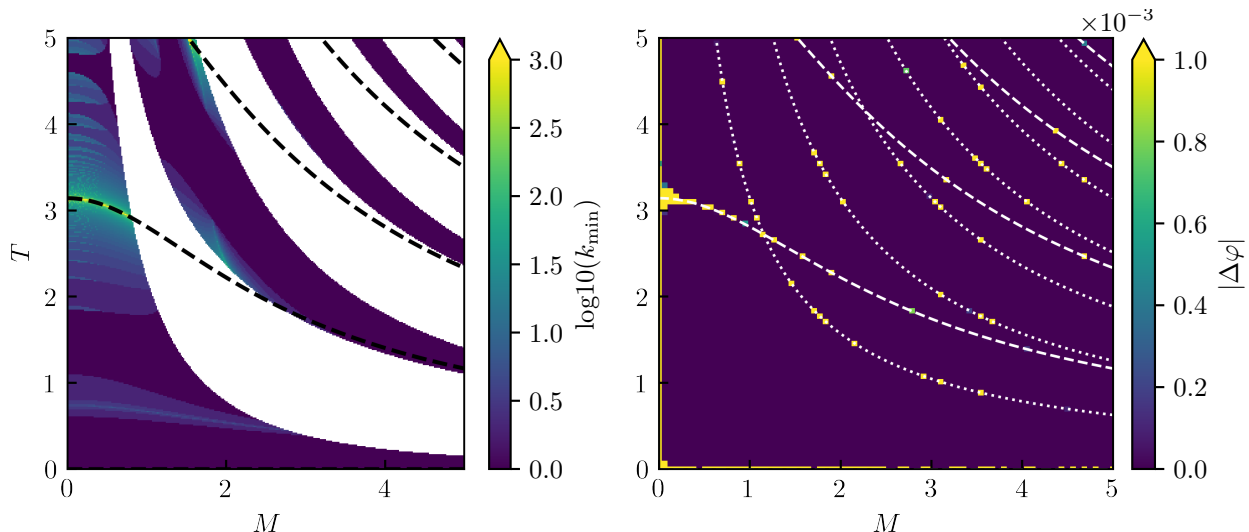
Figure 3.5: Convergence of generic post-measurement trajectories to the grand circle. *Left panel:* Minimal values of the power k, at which both eigenvectors of $[M^+]^k[M^-]$ point to the GC (up to errors of the order of the numerical precision). For this plot we consider $k \in [0, 10^3]$. White regions correspond to $k = 0$ (the eigenvectors of at least one of the matrices $[M^\pm]$ point to the GC). The general existence of such projective combinations facilitates attraction to the GC in the general case. *Right panel*: Phase difference $|\Delta\varphi| := \min(|\varphi - \pi/2|, |\varphi + \pi/2|)$ from the GC after 10^5 steps of time evolution with the MC method, starting from a random state on the Bloch sphere. Dashed lines correspond to the frozen commensurability $YT = 2l\pi$ with $l \in \mathbb{N}$, dotted lines correspond to the shift commensurability $MT = l\pi$ with $l \in \mathbb{N}$. For both commensurabilities, no convergence to the GC is expected as explained in Ref. 3.2.

3. The eigenvectors of both matrices point to the equator.

In the first two cases, we can just pick a matrix with eigenvectors on the GC, say $[M^+]$. Applying this matrix repeatedly to an arbitrary initial state leads to exponential convergence to its dominant eigenvector (the one corresponding to the eigenvalue with larger modulus), with the rate determined by the ratio of eigenvalues (*power-iteration* [140, 141]).

In the third case, there always exists a product of the form $[M^+]^k[M^-]^l$ with $k, l \in \mathbb{N}$, such that all eigenvectors of this product point to the GC, as we demonstrate numerically in the left panel of Fig. 3.5. In the limit $N_t \to \infty$ any typical trajectory thus realizes sequences of click- and no-click events, that attract to the GC, from which they can not escape [4]. In praxis, convergence to the GC happens quickly, as we show numerically below.

---

[4]Technically, the two statements "GC is an invariant manifold", and "attractive sequences of matrices always exist" make generic attraction to the GC plausible, but do not suffice to prove it. The matrices $[M^\pm]$ are generically invertible, and the GC is an invariant manifold for the inverse matrices as well. Consequentially, no trajectory that was not initialized on the GC can ever end up exactly on the GC. However, as long as the GC maps are smooth, a point from the vicinity of the GC is again mapped into the vicinity of the GC.

3.2.4 Freezing and Shifting

In the following we apply our single-step solution of the model discussed in the preceding section to discuss the dynamics on the Bloch sphere in two special parameter regimes in which the post-measurement mappings are particularly simple. These also form the only parameter sets for which the initial state is generally not attracted to the GC.

For our investigation we consider the post-measurement mapping matrices (3.20) and (3.21) along the following parameter lines (motivated by commensurabilites of the arguments of the trigonometric functions in the post-measurement mappings (3.17)):

YT = 2πl   with $l \in \mathbb{N}$ ("Freezing"). In this case, the matrices simplify to

$$[M^-] = \begin{pmatrix} -\cos\left(\frac{MT}{2}\right) & 0 \\ 0 & -\cos\left(\frac{MT}{2}\right) \end{pmatrix} \propto \mathbb{1}, \tag{3.31}$$

$$[M^+] = -\mathrm{i}\begin{pmatrix} -\sin\left(\frac{MT}{2}\right) & 0 \\ 0 & -\sin\left(\frac{MT}{2}\right) \end{pmatrix} \propto \mathbb{1}. \tag{3.32}$$

Therefore, both matrices act trivially on any state, which means that the post-measurement state does not change during time evolution, but remains "frozen". As a consequence, the state can not be attracted to the GC and remains at its initial position on the Bloch-sphere indefinitely.

MT = πl   with $l \in \mathbb{N}$ ("shifting"). (In the following we consider $MT = 2\pi l$, the case $MT = (2l+1)\pi$ can be treated analogously.)
For this choice of parameters, the matrices simplify to

$$[M^-] = \begin{pmatrix} (-1)^l \cos\left(\frac{YT}{2}\right) & \mathrm{i}\frac{2\gamma}{Y}\sin\left(\frac{YT}{2}\right) \\ \mathrm{i}\frac{2\gamma}{Y}\sin\left(\frac{YT}{2}\right) & (-1)^l \cos\left(\frac{YT}{2}\right) \end{pmatrix} = (-1)^l \left[\cos\left(\frac{YT}{2}\right)\mathbb{1} - \mathrm{i}\frac{2\gamma}{Y}\sin\left(\frac{YT}{2}\right)\sigma_1\right], \tag{3.33}$$

$$[M^+] = (-1)^{l+1}\mathrm{i}\begin{pmatrix} \frac{M}{Y}\sin\left(\frac{YT}{2}\right) & 0 \\ 0 & -\frac{M}{Y}\sin\left(\frac{YT}{2}\right) \end{pmatrix} = \mathrm{i}(-1)^{l+1}\sigma_3\frac{M}{Y}\sin\left(\frac{YT}{2}\right) \tag{3.34}$$

where σ_i, $i \in \{1,3\}$ are the Pauli-matrices.
The matrix $[M^+]$ introduces a relative phase shift of π in the state vector, $\varphi \to \varphi + \pi$. The matrix $[M^-]$ is of the form[5]

$$R_x(\theta_x) = \begin{pmatrix} \cos\left(\theta_x/2\right) & -\mathrm{i}\sin\left(\theta_x/2\right) \\ -\mathrm{i}\sin\left(\theta_x/2\right) & \cos\left(\theta_x/2\right) \end{pmatrix} \tag{3.35}$$

$$\theta_x = 2\mathrm{atan2}\left[2\frac{\gamma}{Y}\sin\left(YT/2\right), \cos\left(YT/2\right)\right]. \tag{3.36}$$

---

[5]The function atan2 returns by definition the polar angle, given the cartesian coordinates in a plane, for example $\mathrm{atan2}(\sin(\theta), \cos(\theta)) = \theta$. It can be written explicitly in terms of other trigonometric functions, but it is cumbersome, as one has to discriminate between different cases of the signs of Y- and Z-components.

$R_x(\theta_x)$ generates a rotation by θ_x on the Bloch-sphere around its X-axis. The outcome probabilities are state independent,

$$P^+ = 1 - P^- = \left(\frac{M}{Y}\right)^2 \sin^2(YT/2). \tag{3.37}$$

Using this, it is not difficult to characterize all possible post-measurement trajectories on the Bloch sphere. In the special shift-case, all post-measurement states are located on two circles parallel to the GC plane, and symmetric to each other with respect to the GC plane. The first circle is defined by the intersection of the Bloch sphere with the $Y-Z$ plane containing the initial condition. The matrix $[M_+]$ mediates jumps between these circles, while the matrix $[M_-]$ rotates the state along the circles. This can be described as a random walk between the circles. If the initial state is located on the GC, we obtain a GC distribution, which depends on the phase shift θ_x. In particular, if this phase shift is commensurate with π, the distribution has support only on a finite set of points, while it has support on an infinite number of points otherwise.

Attraction to the GC is broken in this case, because the eigenvectors of $[M^-]$ point to the equator, while the eigenvectors of $[M^+]$ do point to the GC, but the corresponding eigenvalues have the same modulus. This is why this special case is not visible in Fig. 3.5.

At this point we remark, that the action of the $[M^\pm]$ matrices can not generally be expressed as rotations on the Bloch-sphere. The problem is the necessary renormalization of the post-measurement state. Generally, the normalization constant (or outcome probability) depends on the previous post-measurement state, such that the action of the $[M^\pm]$ matrices cannot be represented by a rotation in three-dimensional space. In the shift case this is possible, because the probabilities $P^\pm$ are state independent.

In the right panel of Fig. 3.5, we demonstrate attraction to the GC in the generic parameter plane $M, T \in (0,5]$ (with $\gamma = 1$) using a Monte-Carlo method to simulate random post-measurement trajectories (explained in more detail in Sec. 3.3). For every data point, we choose random initial state anywhere on the Bloch sphere. This state is time evolved for 10^5 steps of the protocol, with random measurement outcomes, following the Born rule. The resulting states form a random post-measurement trajectory. The phase difference to the GC $|\Delta\varphi| := \min(|\varphi - \pi/2|, |\varphi + \pi/2|)$ after 10^5 steps of time evolution is color coded. For most parameter sets, the trajectories have converged to the GC and we obtain $|\Delta\varphi| = 0$ (to numerical accuracy). All exceptions are correlated either with frozen- or with shift-cases, associated with $TY = 2k\pi$ (dashed lines) or $TM = k\pi$ (dotted lines). Small M values correspond to a shift case, where the probability to apply the matrix $[M^+]$ vanishes (no detector-chain coupling means, that the detector can not time evolve and remains in the $(-)$ state), and the matrix $[M^-]$ induces a rotation as described above by an angle $2T\gamma$ (free Rabi-oscillations of the chain state). The limit $T \to 0$ corresponds to freezing of the initial state: The $(+)$-matrix is not applied for the same reason as in the limit $M \to 0$, and the $(-)$ matrix acts trivially on the state (as for the frozen commensurabilities).

Not all $|\Delta\varphi|$ are large around these special parameter lines because of the finite parameter grid resolution (80×80 $M-T$-values), due to which the special conditions are only met at some points with sufficient accuracy. Importantly, even small deviations from the non-GC conditions (at the order of the grid resolution) restore convergence to the GC.

With this, we numerically confirmed that GC convergence quickly happens in all but the described exceptional cases.

3.2.5 Information from measurement outcomes

To establish a connection to "conventional", projective measurements, one could ask, whether our model has a parameter regime, where a click (no-click) in the detector leads to a post-measurement state $|1,0\rangle|-\rangle/|0,1\rangle|-\rangle$—the north / south pole of the Bloch sphere. This would be the effect of projective density measurement on s_1—the site the detector is coupled to: A single measurement gives complete information about the post-measurement state of the chain (without having prior knowledge) and leads to a collapse of the chain wave function to a density eigenstate. In particular, one may naively expect this in the limit $M \to \infty$ (large coupling strength). However, this intuition is false: In the limit $M \to \infty$, if for example the freezing condition is fulfilled, the detector measurement outcome still has no effect on the system state, such that it is completely independent of the occupation on s_1.

In the limit $\gamma = 0$, our model reduces to the model discussed in the appendix of Ref. [30], with post-measurement matrices

$$[M^-] = \begin{pmatrix} \cos(MT) & 0 \\ 0 & 1 \end{pmatrix} \quad [M^+] = \begin{pmatrix} -\mathrm{i}\sin(MT) & 0 \\ 0 & 0 \end{pmatrix} \tag{3.38}$$

In this case, as noted in Ref. [30], there is a strong measurement limit in the aforementioned sense for $MT = (2n+1)\pi/2$ with $n \in \mathbb{N}_0$, as can be seen from above matrices, which become projectors on the second / first component of the state for this parameter relation. However, setting $\gamma = 0$ and fixing the chain to half-filling as in our setup trivializes the situation, since the particle then either is on site s_1—only the $(+)$ outcome is possible, the state does not change—or it is not—only the $(-)$ outcome is possible, the state does not change. If the filling is initially not fixed such that s_1 is in a superposition of occupied and not occupied, the first measurement fixes the occupation and all following measurements return the same result. Deviating from $MT = \pi/2$, the $[M^+]$ matrix can be seen to remain projective, while the $[M^-]$ matrix gradually changes the state. Physically, this can be understood as follows: The value $MT = \pi/2$ is fine-tuned to perfectly correlate the chain occupation with the measured detector state at $\gamma = 0$. Since transitions in the detector between its $(-)$ and $(+)$ states are only possible if s_1 is occupied, a $(+)$ outcome means, that the site must be occupied—thus $[M^+]$ always projects to the post-measurement state $|b_2\rangle$ at $\gamma = 0$ (regardless MT). A $(-)$ outcome can however generally also occur if the detector is in a superposition of occupied and unoccupied (facilitated by occupation of s_1) and we just happen to not measure the $(-)$ state. Choosing $MT = \pi/2$, the $(-)$ component is completely eliminated from the final state provided s_1 is occupied, since occupation of s_1 induces exactly half an oscillation period of the $(+)$ component in the final state, which starts off at 0. Due to this engineered correlation, a measurement of the detector gives complete information about the chain occupation, thus projecting the chain state to one of the occupation basis states.
Fixing $MT = \pi/2$ and expanding in $\gamma \to 0$, we obtain

$$[M^-] = \begin{pmatrix} 0 & -\frac{2\mathrm{i}T\gamma}{\pi} \\ -\frac{2\mathrm{i}T\gamma}{\pi} & 1 \end{pmatrix} \quad [M^+] = \begin{pmatrix} -\mathrm{i} & -\frac{2T\gamma}{\pi} \\ -\frac{2\mathrm{i}T\gamma}{\pi} & 0 \end{pmatrix}. \tag{3.39}$$

This allows us to approach the strong measurement limit by considering $\gamma T \to 0$, keeping $MT = \pi/2$ fixed. Physically, this limit corresponds to slowing the chain dynamics during a period of joint evolution (controlled by the tunneling γT), while keeping the detector dynamics (controlled by the coupling MT) fixed. For these parameters, we have an "imperfect quantum Zeno effect" in the chain: For $T \to 0$, the chain state is frozen by the ancilla measurements. However, the limit $T \to 0$ does not only control

the probability $p \to 1$ to find the same outcome in two successive (detector) measurements, but also the probability to actually (not) find the particle on s_1 immediately after a (no) click measurement on the detector.

For $\gamma \neq 0$, the situation becomes more complicated, since the chain changes its state during the joint time evolution not just due to detector coupling, but also due to its own tunneling dynamics. Regarding the ratios of eigenvalues $|\lambda_{\min}^{\pm}|/|\lambda_{\max}^{\pm}|$ (see Fig. 3.4), we see that there are some points in the parameter plane, where both matrices $[M^{\pm}]$ become projective (crossing of orange and purple lines). In such cases, both measurement outcomes in the detector lead to the projection of the chain state—however not generally to one of the occupation eigenstates. So what is special about projective matrices? In any case, using the $[M^{\pm}]$ matrices, we can determine the state of the chain after the measurement; not only if these matrices are projective. However, the case of two projecting matrices could be considered a "good detector" limit, where a single projective measurement on the detector determines the chain state even without prior knowledge. Generally, the post-measurement state of the chain is obtained by applying the matrices to the prior post-measurement state. If both matrices are projective, the result of this application is independent of the prior state. Such a double projective case however does not allow for measurement freezing like in the quantum Zeno effect, since there is no way to fix the next measurement outcome (like decreasing the time intervals in the Zeno effect). Instead, this case resembles a "quantum coin", where either one of two chain states is realized after a measurement, with fixed probabilites and no way to predict the outcome.

Moving away from the projective case, if one of the matrices has eigenvalues of different moduli, long sequences of the corresponding outcome drive the chain state to its dominant eigenstate, such that again information can be extracted from the readout *sequence* about the chain state. In this case, a single outcome is non-conclusive, but the sequence makes it more and more likely for the chain to be in the corresponding eigenstate—consequentially driving it there gradually via backaction. If none of the matrices has an eigenvalue hierarchy, we saw in Fig. 3.3 that chains of matrices have eigenvectors with projective eigenvalues, such that repeated sequences of the corresponding outcomes can be used for the determination of the chain state.

A short summary to conclude Sec. 3.2: We introduced our chain-detector model and the time evolution protocol, and solved the dynamics of the system between two successive measurements to show, how the states of the system immediately after a measurement (post-measurement states) are related to each other via the measurement operators (or post-measurement maps) $[M^{\pm}]$. We argued that typical post-measurement trajectories are typically attracted to a single circle $\varphi \in \{-\pi/2, \pi/2\}, \theta \in [0, \pi]$ (the "Grand Circle"), and presented the only two exceptions (frozen- and shift cases) that correspond to particularly simple behavior across different post-measurement trajectories. Having solved the model for a single time step, we need a way to characterize the exponentially (with N_t) growing ensemble of possible post-measurement trajectories, which we establish in the next section.

3.3 Distributions on the GC

As almost all post-measurement trajectories eventually converge to the GC, it is natural to wait for this convergence to happen and then describe time evolution on the GC. In order to describe time evolution on the GC, we introduce a polar angle in the $Y - Z$–plane as

$$\Phi = \text{atan2}[\sin(\theta)\sin(\varphi), \cos(\theta)] \quad \Phi \in [-\pi, \pi). \tag{3.40}$$

In terms of this angle, we define a probability distribution on the GC, given an initial GC angle Φ_0, as the limit

$$W(\Phi|\Phi_0) := \lim_{\Delta\Phi\to 0} W_{\Delta\Phi}(\Phi|\Phi_0), \quad \Phi \in [-\pi, \pi). \tag{3.41}$$

of the course-grained distribution

$$W_{\Delta\Phi}(\Phi|\Phi_0) := \frac{1}{\Delta\Phi} \int_{\Phi-\Delta\Phi/2}^{\Phi+\Delta\Phi/2} \mathrm{d}\Phi' \lim_{m\to\infty} \frac{\sum_{j=0}^{m} \left\langle \delta(\mathrm{angle}[\Psi_{\{o\}_j}(t_j^+)] - \Phi') \right\rangle_{\{o\}_j}}{m} \tag{3.42}$$

where $\{o\}_j := \{o_1, o_2, \ldots, o_j\}$ is the sequence of outcomes, and $\mathrm{angle}(\cdot)$ extracts the angle of a GC state. The outcome average

$$\langle\cdot\rangle_{\{o\}_j} := \sum_{o_1,\ldots,o_j\in\{-,+\}} (\cdot)\mathcal{P}(\{o\}_j) \tag{3.43}$$

is defined in terms of the conditional Born-rule probabilities $\mathcal{P}(\{o\}_j) := \mathcal{P}(o_1)\mathcal{P}(o_2|o_1)\ldots\mathcal{P}(o_j|\{o\}_{j-1})$.

The δ-function in Eq. (3.42) counts all post-measurement trajectories in the GC interval $[\Phi-\Delta\Phi, \Phi+\Delta\Phi]$. The initial state is encoded as $\mathrm{angle}[\Psi(t_0^+)]$ on the right hand side of Eq. (3.42). The notation $\Psi_{\{o\}_j}(t_j^+)$ provides a complete description of the post-measurement state at time t_j^+, by containing the sequence of outcomes $\{o\}_j$, that lead up to this state. After the j-th measurement, the outcome sequence has j elements, each $o_j \in \{-,+\}$. The outcome average of the state at time j is given by a sum over 2^j different outcome sequences (corresponding to potentially different quantum trajectories); each weighed by its respective Born rule probability.

Including a time average $\sum_{j=0}^{m}/m$ in the definition of the distribution (3.42) allows to attribute a unique distribution to a set of parameters and an initial angle, even if the process does not have a stationary state—think of a situation, where the measurements induce periodic switching between states on the GC.

Intuitively, $W(\Phi|\Phi_0)$ describes fractions of time spent in given subsets of the GC, averaged over the ensemble of post-measurement states. As a probability distribution, W is normalized

$$\int_{-\pi}^{\pi} \mathrm{d}\Phi \, W(\Phi|\Phi_0) = 1. \tag{3.44}$$

The definition of the distribution in terms of a limit of a coarse-grained distribution is important for the following reason: Even averaging over all possible post-measurement trajectories in the limit of infinitely many steps of the protocol ($m \to \infty$), the collection of all post-measurement states still comprises a at most countably infinite set, not allowing for a notion of a continuous distribution function. Without the limit definition, the distribution could only be defined in terms of a possibly infinite sum of weighted δ-peaks. With the limit definition (3.41), a dense set of points over the GC is converted into a continuous distribution by Eq. (3.41). Such a set emerges, if every point on the GC can be approached arbitrarily closely (with non-vanishing probabilities in the averages). On the other hand, if there is only a finite set of angles that are accessible to the post-measurement trajectory, the limit definition reproduces a sum of δ peaks as one would expect[6].

---

[6]The coarse-graining limit procedure is equivalent to introducing finite peak broadening for each delta-function and considering the distribution obtained by taking the peak widths to zero. This is done for the definition of the local density of states in disordered systems [68]. The coarse graining formulation is more convenient for our numerical

At this point we emphasize that at the level of the model there is no physical process that would introduce peak broadening. Every post-measurement trajectory occupies a single point on the GC at a given time instance. If we tried to determine the post-measurement state experimentally however, broadening could be introduced for instance by a finite detector resolution. If there is a cut-off to this resolution it becomes impossible to distinguish between a truly continuous distribution, and a distribution with points within each discretization cell. This problem exists also for our numerics.

In the following, we explore the definition (3.41) separately in terms of outcome average (stationary states that fulfil a Master-equation) and time average (individual trajectories from Monte-Carlo simulation).

3.3.1 Master equation

We start by considering the outcome average at fixed (possibly asymptotic) time.
For this purpose, we formulate a Master equation (ME), which governs a Markov process on the GC. This process is constructed from the two GC mappings $f_s^{-1} : \Phi \mapsto \Phi$ (with $s \in \{+, -\}$), defined by the actions of the click- and no-click maps $[M^{\pm}]$ on the corresponding state[7]

$$f_s^{-1}(\Phi) := \text{angle}([M^s]\text{state}(\Phi)). \tag{3.45}$$

Here, state$(\cdot)$ maps an angle on the GC to the corresponding state, and angle$(\cdot)$ maps a state on the GC to the corresponding angle.
Defining the probabilities of the two different measurement outcomes $P^{(\pm)}$ on the GC analogously, we obtain the following ME:

$$W_1(\Phi) = \sum_{s \in \{-, +\}} \int d\Phi' \, W_0(\Phi') P^{(s)}(\Phi') \delta(\Phi - f_s^{-1}(\Phi')) \tag{3.46}$$

$$=: \mathcal{M}[W_0](\Phi) \quad \Phi \in [-\pi, \pi). \tag{3.47}$$

The ME kernel $\mathcal{M}$ takes an initial distribution W_0 on the GC, and maps it to the new distribution W_1, assuming the Born rule weighted action of $(+)$ and $(-)$ maps. Physically, this should be understood in terms of an outcome average.

As an example, consider starting from an initial state on the GC—corresponding to the distribution $W_0(\Phi) = \delta(\Phi - \Phi_0)$—and applying the ME once:

$$W_1(\Phi) = \sum_{s \in \{-, +\}} P^{(s)}(\Phi_0) \delta(\Phi - f_s^{-1}(\Phi_0)). \tag{3.48}$$

W_1 has δ-peaks at the two different angles that can result from the actions of $[M^{\pm}]$-matrices. Physically, these are the two post-measurement states that can result after the first step of time evolution according to our protocol. Each peak has a weight corresponding to the probability that the corresponding outcome is realized. This is the outcome averaged distribution after one step. Since the ME is linear in the distribution, this argument can be iterated and after m applications of the ME, the outcome averaged distribution after m time steps is obtained, starting from state(Φ_0).

---

approaches.

[7] We define these maps suggestively of inverse functions f_s, which are introduced later. In the projective case, the functions f_s do not exist, but generically the matrices $[M^{\pm}]$ are invertible as can be seen from Fig. 3.4.

The ME preserves normalization of the distribution:

$$\int \mathrm{d}\Phi\, W_1(\Phi) = \sum_{s\in\{-,+\}} \int \mathrm{d}\Phi'\, W_0(\Phi') P^{(s)}(\Phi') \int \mathrm{d}\Phi\, \delta(\Phi - f_s^{-1}(\Phi')) \tag{3.49}$$

$$= \int \mathrm{d}\Phi'\, W_0(\Phi') \sum_s P^{(s)}(\Phi') \tag{3.50}$$

$$= \int \mathrm{d}\Phi'\, W_0(\Phi'), \tag{3.51}$$

where we used that the probability to obtain any of the two possible results is one.
In addition to the integral formulation (3.47) of the ME, we can also obtain an implicit functional equation by solving the integrals:

$$\mathcal{M}[W_0](\Phi) = \sum_{s\in\{+,-\}} |f_s'(\Phi)| P^{(s)}(f_s(\Phi)) W_0(f_s(\Phi)) \tag{3.52}$$

For both equations (3.47) and (3.52) it is important to keep in mind that they describe probability distributions, and probabilities are obtained by integrating over a finite interval. This implies in particular, that the application of the ME to a finite set of points $\{\Phi\}$ is not useful and can lead to contradictions as two probability distributions differing only on a set of measure zero are equivalent. In other words, a solution to the ME can *not* be found by solving a system of equations resulting from inserting a discrete set of angles into Eq. (3.47).

We define a *stationary distribution* $W(\Phi)$ in terms of the ME kernel as

$$\mathcal{M}[W] = W. \tag{3.53}$$

The solution to Eq. (3.53) is not necessarily unique: For example, if the GC is partitioned into two subsets I_1, I_2 such that $I_1 \cup I_2 = [-\pi, \pi)$, $I_1 \cap I_2 = \emptyset$ and without transitions between them

$$f_s^{-1}(I_1) \cap I_2 = \emptyset \tag{3.54}$$

$$f_s^{-1}(I_2) \cap I_1 = \emptyset, \tag{3.55}$$

where $f(I)$ is the image of I under f, each of these subsets may feature a stationary distribution, such that the GC stationary distribution is not unique.

Assuming an initial distribution W_0 on finite support, we can try to obtain a stationary state by repeatedly applying the ME to this distribution[8]:

$$W = \mathcal{M}[\mathcal{M}[\ldots [W_0]]]. \tag{3.56}$$

According to above reasoning, different initial distributions may result in different stationary states.

---

[8] This can be done explicitly to obtain a formal solution. However, this solution contains an infinite number of terms due to the infinite number of iterative applications of the ME which can be necessary for convergence. It is therefore not helpful to plot distributions for different parameter sets.

Discretized Master equation

Analytically solving the ME is generally difficult. Therefore, we discretize the ME, with the goal to solve it numerically. In Refs. [136, 139] the numerical solution of implicit equations on a circle where also discussed. If we consider only one of the maps $M^{\pm}$, our ME reduces to the type of equation that was considered in Ref. [136]. The circle equations from Ref. [139] can be brought to the same form as or ME but with constant instead of angle dependent probabilities.

To discretize the ME, we partition the GC into N equally sized subintervals c_i:

$$c_i := \left[\Phi_i - \Delta\Phi/2, \Phi_i + \Delta\Phi/2\right] \quad i \in [0, N-1] \tag{3.57}$$

$$\Phi_i := -\pi + (2i+1)\Delta\Phi/2 \qquad \Delta\Phi := \frac{2\pi}{N} \tag{3.58}$$

The stationary ME reduces to a set of N linear equations for the set of probabilities $\{\widetilde{\mathrm{Pr}}_i\}$:

$$\widetilde{\mathrm{Pr}}_i := \int_{c_i} \mathrm{d}\Phi\, W(\Phi) \approx \sum_{j=1}^{N} [\mathcal{M}_N]_{i,j} \widetilde{\mathrm{Pr}}_j, \tag{3.59}$$

$$[\mathcal{M}_N]_{i,j} := \frac{1}{\Delta\Phi} \sum_{s \in \{+,-\}} P^{(s)}(\Phi_j) |f_s(c_i) \cap c_j| \tag{3.60}$$

Here $f_s(c_i)$ is the image of c_i under f_s. f_s^{-1} is continuous on the periodic interval $[-\pi, \pi)$, and invertible for all sets of parameters besides the projective limit, in which one of the eigenvalues of the corresponding matrix vanishes. To obtain result (3.59), we used Eq. (3.52) and assumed, that $P^{(s)}$ barely changes on the scale of $\Delta\Phi$.

Eq. (3.59) is an approximate equation for the "true" probabilities $\{\widetilde{\mathrm{Pr}}_i\}$, resulting from an expansion in $\Delta\Phi$. With the discretized ME kernel $[\mathcal{M}_N]$ we define another set of probabilities $\{\mathrm{Pr}_i\}$ that exactly fulfills the *discretized master equation*

$$\mathrm{Pr}_i = \sum_{j=1}^{N} [\mathcal{M}_N]_{i,j} \mathrm{Pr}_j \quad i \in \{1, 2, \dots, N\}. \tag{3.61}$$

Its solution gives us an approximation of the coarse-grained stationary distribution

$$W_{\Delta\Phi}(\Phi) \overset{\Phi \in c_i}{\approx} \frac{\mathrm{Pr}_i}{\Delta\Phi}, \tag{3.62}$$

which we use to show numerical results for distributions with the ME (see for example Fig. 3.7).

We can estimate the number of cells that share overlap with $f_s(c_i)$ (equivalently, the number of non-zero matrix elements in row i) as $|f_s(c_i)|/\Delta\Phi = |f_s(\Phi_i + \Delta\Phi/2) - f_s(\Phi_i - \Delta\Phi/2)|/\Delta\Phi \approx |f_s'(\Phi_i)|$. As the f_s are invertible, this derivative is typically of the order of smaller than one[9]. This means in turn, that the matrix $[\mathcal{M}_N]_{i,j}$ is sparse.

See Fig. 3.6 for some examples of such matrices, for $N = 10^3$ and four different parameter sets. Finite matrix elements $[\mathcal{M}_N]_{i,j}$ are shown in orange and blue. Each matrix features two continuous "bands" of non-zero entries, corresponding to f_s, $s \in \{+,-\}$ (orange corresponds to the (+)-map,

---

[9]It can take arbitrarily large values on a small interval, but if it was for example 10 over an interval of $\pi/2$, the GC would be covered 2.5 times in contradiction to invertibility.
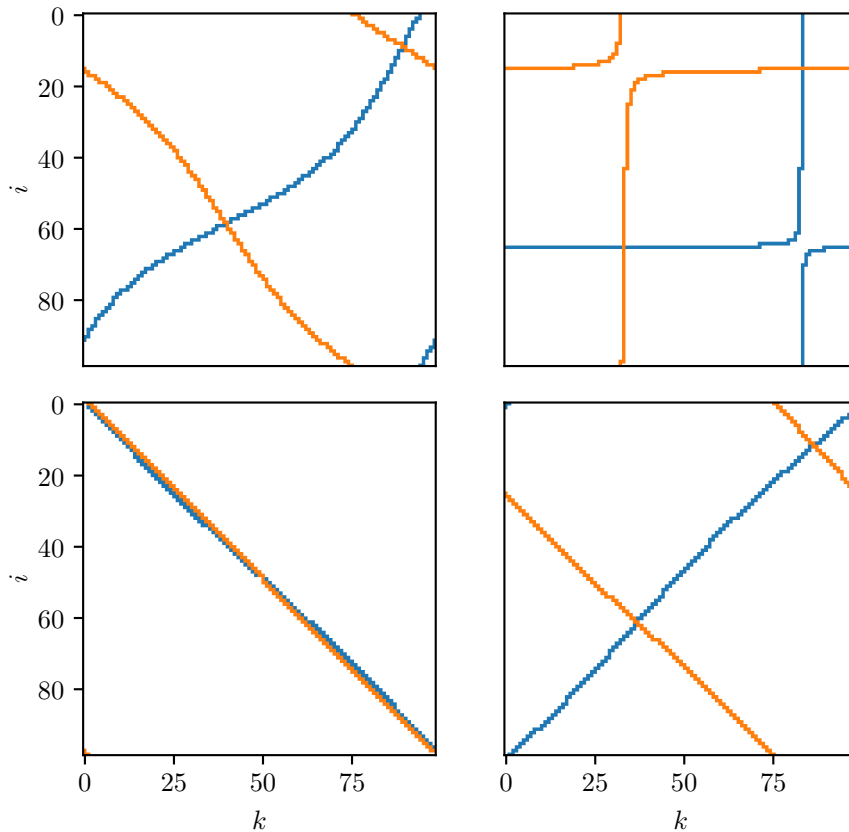
Figure 3.6: Structure of four different matrices $[\mathcal{M}_{10^3}]$, obtained from discretizing the master equation according to Eq. (3.59) for parameters ($M = 2.92, T = 3.0554$), ($M = 2.766, T = 2.840$), ($M = 1.979, T = 2.2663$), ($M = 2.258, T = 1.4369$) (γ is set to one). Non-zero matrix elements are indicated in orange (contributions from the $[M^+]$ matrix) and blue (contributions from the $[M^-]$ matrix). The *upper left* panel corresponds to generic parameters. In the *upper right* panel, both matrices $[M^\pm]$ have strong hierarchies between their eigenvalues ("almost projective"), such that a large interval of the GC is mapped to a close vicinity of the dominant eigenvalue—note the steep slopes of the "bands" near $j \approx 250, 750$. The parameters in the *lower left* panel are close to the frozen case, $YT \approx 2.03$. In the frozen case, we have $[M^\pm] \propto \mathbb{1}$, such that also $[\mathcal{M}_N] \propto \mathbb{1}$, since no transition away from a given bin exists. The lower right panel is close to the shift case, $MT \approx 1.03$. In the shift case, one of the matrices shifts $\Phi \to -\Phi$ on the GC (the anti-diagonal in the matrix plot). The other matrix causes a constant shift of Φ, that depends on the parameters. See Sec. 3.2 and 3.4 for more details on these special cases.

blue corresponds to the $(-)$-map). As the f_s are invertible, both bands are monotonous and cover all rows and columns. The bands have small widths, rendering $[\mathcal{M}_N]$ sparse. In the upper right panel, both matrices $[M^\pm]$ have strong hierarchies between their eigenvalues ("almost projective"), such that a large interval of the GC is mapped to a close vicinity of the dominant eigenvalue—note the steep slopes of the "bands" near $j \approx 250, 750$. The parameters in the lower left panel are close to the frozen

case, $YT \approx 2.03$. In the frozen case, we have $[M^{\pm}] \propto \mathbb{1}$, such that also $[\mathcal{M}_N] \propto \mathbb{1}$, since no transition away from a given bin exists. The lower right panel is close to the shift case, $MT \approx 1.03$. In the shift case, one of the matrices shifts $\Phi \to -\Phi$ on the GC. The other matrix causes a constant shift of Φ, that depends on the parameters. The upper left panel corresponds to generic parameters, but the matrix looks similar to the shift-case. In fact, all regions of the parameter plane are related more or less closely to the special cases, such that this is not an exception.

A stationary solution of the (discretized) ME corresponds to an eigenvector of $[\mathcal{M}_N]$ with eigenvalue 1. As can be seen from Eq. (3.59), all entries of $[\mathcal{M}_N]$ are positive. Furthermore, probability conservation is manifestly built into the ME,

$$\sum_{i=1}^{N} [\mathcal{M}_N]_{i,j} = 1. \tag{3.63}$$

For this reason, $[\mathcal{M}_N]$ is a positive Markov matrix and, as such, necessarily has an eigenvector corresponding to the eigenvalue 1 [97]: At least one stationary state of the ME always exists, regardless parameters and discretization. Such a state can be efficiently found for sparse $[\mathcal{M}_N]$ by repeatedly applying the matrix to an arbitrary initial state $\mathbf{Pr}^0$ until convergence is reached ("power iteration")—provided that the eigenvalue $\lambda = 1$ is not degenerate, and that there is no other eigenvalue of modulus one [140, 141].

Assuming a hierarchy between the eigenvalues of $[\mathcal{M}_N]$, convergence to the stationary state happens at an exponential rate, which is proportional to the difference $\Delta\lambda$ between the dominant and the second dominant eigenvalue (largest and second largest eigenvalues by modulus),

$$||\mathbf{Pr}^0 - [\mathcal{M}_N]^{n_{\mathrm{it}}} \mathbf{Pr}|| \propto \mathrm{e}^{-\frac{\Delta\lambda}{a_0} n_{\mathrm{it}}}. \tag{3.64}$$

a_0 is a positive number [140].

There are two cases where the ME method can run into problems: If the eigenvalue $\lambda = 1$ is degenerate, the converged state depends on the initial state. In this case we cannot make an immediate connection to the asymptotic behavior of quantum trajectories. If there is only one eigenvector corresponding to $\lambda = 1$, but other eigenvectors with $|\lambda'| = 1$ power iteration can converge to a state that does not correspond to a stationary solution of the ME.

As pointed out above, the stationary solution is not necessarily unique. In praxis however, we are able to find non-degenerate stationary states efficiently for most parameter sets, using power iteration[10]. There are two exceptions, corresponding to lines of special parameters:

- Frozen trajectories are maximally degenerate, as every basis state $\left[\hat{\mathbf{Pr}}^i\right]_j := \delta_{i,j}$ solves the ME.

- For certain "periodic" trajectories (see also Sec. 3.4) an iterative solution does not necessarily converge at all, as it can get stuck switching periodically between different angle bins. Say, if there is a periodic trajectory between two bins, occupation of one of these bins gives $[\mathcal{M}_N]^2[\mathbf{Pr}] = [\mathbf{Pr}]$, corresponding to $\lambda = -1$. The non-degenerate solution to the ME in this case corresponds to balanced occupation of the two peaks.

From the point of view of our definition of the GC distribution (3.41), a non-degenerate stationary state is equivalent to the fully averaged GC distribution at the same parameters for any initial angle

---

[10]A unique stationary state of the discrete ME can be an artifact of the discretization. To make exclude this possibility we checked the stability of our results with respect to the number of discretization cells.

Φ_0, assuming the discretization is valid (this can be proven by contradiction). This is, because the stationary solution to the ME is equivalent to an outcome average at asymptotic times and a stationary state dominates the behavior of the time average in Eq. (3.41) in the limit of long times:

$$\lim_{l \to \infty} \frac{1}{l} \sum_{i=0}^{l} [\mathcal{M}_N]^i \mathbf{Pr}^0 \approx \lim_{l \to \infty} \frac{1}{l} \left(\sum_{i=0}^{l_1} [\mathcal{M}_N]^i \mathbf{Pr}^0 + \sum_{i=l_1}^{l} \mathbf{Pr}^{\text{stat}} \right) \tag{3.65}$$

$$\to \mathbf{Pr}^{\text{stat}} \tag{3.66}$$

where we assumed, that the probability vector converges to the stationary distribution within l_1 applications of the Markov matrix. In terms of the discretized ME, we then expect

$$\lim_{\Delta\Phi \to 0} \frac{\mathbf{Pr}^{\text{stat}}_{\Delta\Phi}}{\Delta\Phi} \to W_{\Delta\Phi}(\Phi|\Phi_0). \tag{3.67}$$

However, the distribution W may always have features on a scale smaller than the histogram resolution, which are thus not captured by the coarse-grained $W_{\Delta\Phi}$. In the following numerical results, we ignore this fact in the notation, dropping the index $\Delta\Phi$ for convenience, assuming that the given discretization is sufficient to cover at least those features of the limit distribution which are visible in the plots.

Most of our numerical results are generated with the ME method, see Fig. 3.10 for a few examples of distributions obtained with the ME. Extensive numerical results are presented in Sec. 3.7.

3.3.2 Quantum trajectory approach and Monte-Carlo simulation

For any given quantum trajectory on the GC, the probability of a single-step transition $\Phi_j \to \Phi_{j+1}$ is determined by Born's rule and is equal to the corresponding probability $P^{(\pm)}(\Phi_j)$ in the ME. If the quantum trajectory visits the vicinity of every point Φ with $W_{\Delta\Phi}(\Phi|\Phi_0) > 0$ many times, all possible transitions between the coarse-grained angle intervals c_i are probed. The probability of any transition is then repeatedly sampled according to the Born rule, which means that the time-averaged distribution should converge to the fully averaged distribution. If this is the case, the GC distribution defined in (3.41) has a simple interpretation in terms of quantum trajectories: If a single trajectory is observed for a sufficiently long time, the fraction of time it spends in a certain interval of the GC is determined by the integral of $W(\theta|\theta_0)$ over that interval. The long-time behavior of almost any quantum trajectory is in this case completely described by the model parameters, being independent of outcome sequences.

If this is the case, it is natural to employ a Monte-Carlo (MC) approach similar to what was done in chapter 1: We simulate (at most) a few post-measurement trajectories for a given initial state Φ_0, by randomly drawing measurement outcomes according to the Born rule, and performing time evolution according to the maps $[M^{\pm}]$ corresponding to the chosen outcomes. The resulting post-measurement trajectories are then time averaged; a histogram of visited angles is obtained. This procedure provides information about the coarse-grained distribution $W_{\Delta\Phi}(\Phi|\Phi_0)$, if the outcome average is well described in terms of *typical* post-measurement trajectories. Consequentially, we may investigate a distribution

$$W_{\Delta\Phi}^{\{o\}m}(\Phi|\Phi_0) := \frac{1}{\Delta\Phi} \int_{\Phi-\Delta\Phi/2}^{\Phi+\Delta\Phi/2} \mathrm{d}\Phi' \, \frac{\sum_{j=0}^{m} \delta(\text{angle}[\Psi_{\{o\}_j}(t_j^+)] - \Phi')}{m} \tag{3.68}$$

without performing any explicit average over outcomes (or trajectories) that, in principle, depends on

the sequence of measurement outcomes $\{o\}_m$. This allows to approximate the distribution (3.41), if any typical path for sufficient m reproduces the distribution (3.41), as described above.

The simulation can be stopped, when the histogram of states has converged, i.e. when it does not change significantly anymore with additional time steps.

We use the MC method to

1. check, that post-measurement trajectories actually generically converge to the GC (see Fig. 3.5), and

2. compare the time average over a single trajectory to the ME result (see Fig. 3.9), relating to above discussion of time versus outcome average.

As discussed in the previous section probability conservation implies that a unique stationary state is accessible from any initial condition. This means that every typical post-measurement trajectory on the GC samples the stationary state corresponding to the given model parameters.

While the MC method is useful for above checks due to its simplicity, it converges slowly compared to the Markov method discussed above (in particular with decreasing $\Delta\Phi$).

To summarize this section, we started by defining a probability distribution on the GC, describing the ensemble of all possible time averaged post-measurement trajectories for a given set of parameters (3.41). We described the outcome average of a given initial distribution at a given post-measurement time in terms of a Master equation (3.47). This Master equation always features at least one stationary state, which is defined by Eq. (3.53). Discretizing the Master equation, we can efficiently look for such stationary states using numerical power iteration. Furthermore, the non-degeneracy of a stationary solution implies, that the stationary distribution is equivalent to the fully averaged distribution and independent on the initial state. If this is the case, we expect the stationary state to be universal across all sufficiently long (typical) post-measurement trajectories, and thus described in terms of a time-averaged distribution (3.68). Such time-averaged distributions can be found using a MC simulation scheme.

In Fig. 3.7 we show comparisons between GC distributions obtained from the ME stationary state (3.61) (solid blue lines) and MC time average (dotted orange lines) (3.68). The insets show smaller subintervals of the GC to facilitate a better comparison. As can be seen, the distributions agree with each other very accurately. This demonstrates, that both methods are suitable to obtain GC distributions [11].

In the following, we discuss two more cases of special parameters, where we can make strong statements about the GC distribution without relying entirely on numerics.

3.4 Solutions for two more special cases

Having introduced different kinds of distributions on the GC, we now discuss two special cases in which the GC distribution and the effect of different averages can be easily understood analytically.

3.4.1 Period-2-trajectories, $YT = (2l+1)\pi$

An interesting situation occurs along the lines $YT = (2l+1)\pi$ with $l \in \mathbb{N}$. These cases do not represent an exception to GC convergence, allowing us to investigate initial states on the GC exclusively.

---

[11]To get such an accurate agreement, we considered 10^8 time points of a random post-measurement trajectory in the MC method. We solved the ME on $N = 10^6$ grid cells. The distributions are shown on a grid with $\Delta\phi = 2\pi/(10**3)$. For other numerical distributions we often use a smaller resolution for the ME calculation, but the point is that very accurate agreement can be obtained which demonstrates the principal adequacy of the methods.
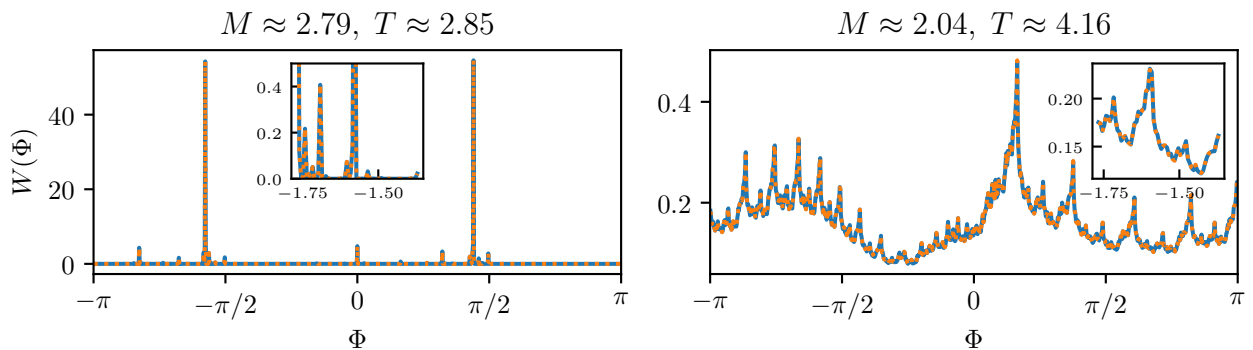
Figure 3.7: Examples for approximate GC distributions (3.41) obtained as the stationary state of the discrete master equation (3.61) (solid blue line) and the time average of a single Monte-Carlo post-measurement trajectory (3.68) (dotted orange line).

Furthermore, in these cases the square of the post-measurement matrices $[M^{\pm}]$ reduces to

$$[M^{\pm}]^2 \propto \mathbb{1}. \tag{3.69}$$

As a consequence, any sequence of post-measurement matrices can be collapsed to one of the forms

$$([M^+][M^-])^k \tag{3.70}$$

$$([M^-][M^+])^k \tag{3.71}$$

$$[M^-]([M^+][M^-])^k \tag{3.72}$$

$$[M^+]([M^-][M^+])^k \tag{3.73}$$

$$\tag{3.74}$$

with $k \in \mathbb{N}$. The eigenvectors of the products $[M^{\pm}][M^{\mp}]$ point to $\Phi_{\pm} := \pm\pi/2$ on the GC, and their eigenvalues are purely imaginary and have different moduli

$$\lambda^{\pm}_{(\eta)} = \lambda^{\mp}_{(\eta)} = \frac{\mathrm{i}}{2}(\eta 2M\gamma/Y + \sin(MT)/2) \quad \eta \in \{1, -1\}. \tag{3.75}$$

The angles $\Phi_{\pm}$ form an invariant set for the post-measurement maps,

$$f_{\pm}^{-1}(\Phi_{\pm}) = \Phi_{\mp}. \tag{3.76}$$

Due to the hierarchy of eigenvalues, long chains $([M^{\pm}][M^{\mp}])^k$ with $k \gg 1$ project to either point $\Phi_{\pm}$, depending on which one corresponds to the dominant eigenvalue. Once a state has been attracted to the vicinity of the invariant set, further applications of $(+)$ and $(-)$ maps lead to approximate switching between the two invariant points.

In the following, we reason that (the vicinity of) this invariant set also attracts typical post-measurement trajectories. For this, it is instructive think of all possible measurement paths as arranged in a tree structure. (See below for an example for $N_t = 4$ time steps.)
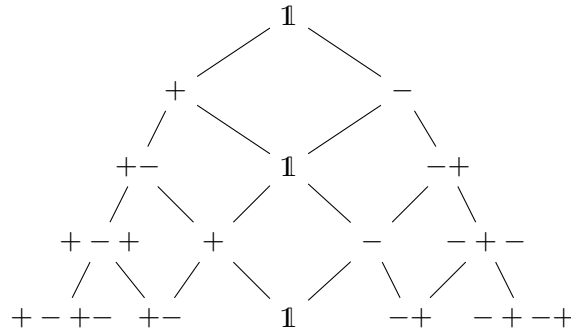
The set of all reachable states is given by applying the corresponding sequences of post-measurement maps to the initial state and renormalizing. The reduction $[M^{\pm}]^2 \propto \mathbb{1}$ means that this set grows linearly with N_t, instead of exponentially (compare to the generic state tree in Fig. 3.2). Still, at any level of the tree, there are "short chains" corresponding to small values of k. Since only long chains project to the vicinity of the invariant set, it is not immediately clear whether or not the invariant set is attractive.

Generally, the weight of each state in the distribution W has to be determined by summing up the probabilities corresponding to each path leading to this state. Since there are exponentially many different such paths, this seems like a difficult problem on first sight.

To tackle it, let us rearrange all states in the tree on a one-dimensional chain and think of the time evolution as a random walk between nearest neighbors on this chain, with the transition probabilities given by the respective probabilities of possible outcomes. See below for a schematic of the central region of the resulting chain.
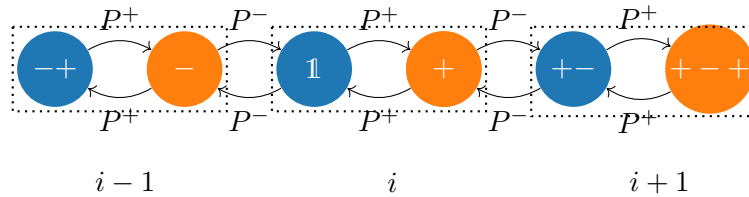
Considering a simplified situation $P^{\pm}(\Phi) = \frac{1}{2}$, every possible path at time step N_t has probability 2^{-N_t}. The problem of determining the probability corresponding to a certain state simplifies to counting the paths that lead to this state (instead of finding and summing all possibly different weights). This number of paths is given by a binomial coefficient, as can be seen by drawing Pascal's triangle on top of our tree-picture of states. The outcome-averaged distribution at even N_t is given by

$$W_{N_t}(\Phi|\Phi_0) = \frac{1}{2^{N_t}} \left[B[N_t, N_t/2]\delta(\Phi - \Phi_0) + \sum_{n=1}^{N_t/2} B[N_t, (N_t + 2n)/2] \right. \tag{3.77}$$

$$\left. \left[\delta\left(\Phi - \text{angle}[(M^+ M^-)^n \text{state}(\Phi_0)]\right) + (+ \leftrightarrow -) \right] \right], \tag{3.78}$$

(without coarse-graining), where $B[n, m]$ denotes the binomial distribution. The distribution for odd N_t can be obtained analogously. Due to the attractive nature of long $[M^{\pm}][M^{\mp}]$-chains, we can find

for any $\varepsilon \ll 1$ a number n_1 , such that

$$\forall l \geq n_1 : \text{ angle} \left[(M^\eta M^{-\eta})^l \text{state}(\Phi_0) \right] \in [\pi/2 - \varepsilon, \pi/2 + \varepsilon] \cup [-\pi/2 - \varepsilon, -\pi/2 + \varepsilon] =: I_\varepsilon \qquad (3.79)$$

We compare the probability within these ε-regions to the probability anywhere else on the GC:

$$\frac{\int_{[-\pi,\pi)\setminus I_\varepsilon} d\Phi \, W_{N_t}(\Phi|\Phi_0)}{\int_{I_\varepsilon} d\Phi \, W_{N_t}(\Phi|\Phi_0)} = \frac{B[N_t, N_t/2] + 2\sum_{n=1}^{n_1} B[N_t, (N_t + 2n)/2]}{2\sum_{n=n_1}^{N_t} B[N_t, (N_t + 2n)/2]} \qquad (3.80)$$

$$\leq \frac{(1 + 2n_1)B[N_t, N_t/2]}{2_t^N - (1 + 2n_1)B[N_t, N_t/2]} \qquad (3.81)$$

$$= \frac{\frac{\Gamma(N_t/2+1/2)}{\sqrt{\pi}\Gamma(N_t/2+1)}(1 + 2n_1)}{\left(1 - \frac{\Gamma(N_t/2+1/2)}{\sqrt{\pi}\Gamma(N_t/2+1)}(2n_1 + 1)\right)} \qquad (3.82)$$

$$\overset{N_t \to \infty}{\to} 0. \qquad (3.83)$$

This proves, that the distribution converges to arbitrarily narrow peaks around the angles $\Phi_\pm = \pm\pi/2$ for $N_t \to \infty$.

This consideration can be generalized to obtain the exact distribution for imbalanced $P^+(\Phi) = P = 1 - P^-(\Phi)$ by constructing a random walk across two-site unit-cells as indicated in above figure. Obtaining the exact distribution at given N_t is difficult for the general "realistic" case with angle-dependent probabilities. However, we can still make a prediction by realizing that above result for the balanced random walk is essentially a consequence of the diffusion law: The ensemble of all possible post-measurement trajectories spreads diffusively on the one-dimensional chain of states depicted above. According to the diffusion law in one dimension, the probability to find the particle in a central region of arbitrary size tends to zero as a function of time. As we saw in the first chapter, the diffusion law holds under quite general circumstances, and it is thus natural to expect that the probability in a central (short-chain) region becomes negligible in the limit of long trajectories as long as $P^\pm(\Phi) \neq 0$. Far away from the origin of the chain (the node labelled $\mathbb{1}$ in the picture) any state is projected to the vicinity of the central peaks. In this vicinity, all possible transitions correspond to switching between the peaks.

Based on this argument our prediction for the GC probability distribution in the *period-2 case* is

$$W(\Phi) = \frac{1}{2}[\delta(\Phi - \pi/2) + \delta(\Phi + \pi/2)]. \qquad (3.84)$$

It can be shown, that this distribution fulfills the stationary ME in the period-2 case. Because any typical quantum trajectory is eventually attracted to the peak regions, this behavior is expected to be observed in the time average as well.

While Eq. (3.84) is the only stationary state of the period-2 ME, it can be seen that it is not the only "eigenvector" of the discretized ME with modulus one: The distributions $W_\pm(\Phi) := \delta(\Phi \pm \pi/2)$ both correspond to eigenvectors with eigenvalue $\lambda = -1$, as described in Sec. 3.5. Therefore, power iteration of the matrix $[\mathcal{M}_N]$ can not be expected to produce this stationary state.

We confirm our result (3.84) numerically in the upper left panel of Fig. 3.8. This plot was obtained by finding the eigenstate with $\lambda = 1$ of the Markov matrix $[\mathcal{M}_{10^3}]$ via exact diagonalization. Slight peak broadening, as well as a slight imbalance between the peaks can be understood from the finite discretization, which introduces transitions out of the bins that contain the invariant points $\Phi_\pm$.

3.4.2 Projective case

If one of the matrices $[M^{\pm}]$ has a single non-zero eigenvalue it projects to its main eigenvector if applied. This means that any point on the GC is mapped to the angle corresponding to its dominant eigenvector (the *eigenangle*) The eigenangle is element of the GC because only on the GC there is a hierarchy between the moduli of eigenvalues.

By equating the eigenvalues (3.27) or (3.28) of the post-measurement matrices (3.27) or (3.28) to zero, we find the conditions

$$\lambda_{\min}^{-} = 0 \Rightarrow \left| \cos\left(MT/2\right) \right| = \frac{M}{Y} \left| \sin\left(YT/2\right) \right|, \tag{3.85}$$

$$\lambda_{\min}^{+} = 0 \Rightarrow \left| \sin\left(MT/2\right) \right| = \frac{M}{Y} \left| \sin\left(YT/2\right) \right|. \tag{3.86}$$

The conditions are visualized in Fig. 3.4 as purple / orange lines for $\lambda_{\min}^{-}$ / $\lambda_{\min}^{+}$.

For example, if the second condition is fulfilled, the $(+)$ map is

$$f_{+}^{-1}(\Phi) = \Phi_{\text{eig}} \tag{3.87}$$

where Φ_{eig} is the angle of the main eigenvector of the $+$ matrix on the Bloch-sphere. In this limit, the map is not invertible. The stationary ME is solved by the distribution

$$W(\Phi) = \mathcal{N} \left[\delta(\Phi - \Phi_{\text{eig}}) + \sum_{i=1}^{\infty} \delta\left(\Phi - \bar{F}_{\{i=-\}}^{i}(\Phi_{\text{eig}})\right) \prod_{j=1}^{i} P^{(-)}\left(\bar{F}_{\{i=-\}}^{j-1}(\Phi_{\text{eig}})\right) \right], \tag{3.88}$$

$$\mathcal{N}^{-1} = 1 + \sum_{i=1}^{\infty} \prod_{j=1}^{i} P^{(-)}\left(\bar{F}_{\{i=-\}}^{j-1}(\Phi_{\text{eig}})\right), \tag{3.89}$$

$$\bar{F}_{\{i\}}^{j}(\Phi) := \begin{cases} \Phi & j = 0 \\ f_{i_j}^{-1}\left(\bar{F}_{\{i\}}^{j-1}(\Phi)\right) & j > 0 \end{cases}. \tag{3.90}$$

While the $(+)$-map projects all points to its eigenangle, the $(-)$ map generates translations of this main peak to generate "satellites".

This mechanism is similar to the mechanism explained in Ref. [67], where the continuous measurement limit of a similar model was considered. In this limit, one of the matrices is always almost projecting, leading to a main peak, which is translated in infinitesimally small steps by the second matrix [67].

A good approximation for Eq. (3.88) can be obtained by truncating the sum after just a few terms, since higher-order terms are exponentially suppressed. The stationary state is non-degenerate and corresponds to the GC distribution and to the time-averaged distribution of a typical post-measurement trajectory.

See the upper right panel of Fig. 3.8 for an example of a GC distribution in the projective case. The leftmost peak corresponds to the eigenangle of the projecting matrix. The other peaks are quickly shrinking satellites produced by the other matrix. The blue curve was obtained by discretizing the time average over a single random Monte Carlo trajectory into 10^3 bins. The dotted curve are the first 20 terms of Eq. (3.88). The results agree perfectly.

The projective limit is approached, if there is a strong hierarchy of eigenvalues for one of the post-measurement matrices, for example

$$\frac{|\lambda_+^-|}{|\lambda_+^+|} \ll 1. \tag{3.91}$$

If the smaller eigenvalue does not exactly vanish, the matrix is invertible and the inverse of the post-measurement map can be defined. It can be proven, that

$$\left|\frac{\partial f_+}{\partial \Phi}(\Phi = \Phi_{\text{eig}})\right| = \frac{|\lambda_{\max}^+|}{|\lambda_{\min}^+|}. \tag{3.92}$$

Intuitively, a strong hierarchy between the eigenvalues means, that the main eigenvector strongly attracts, meaning that for small $\delta\Phi$

$$f_+([\Phi_{\text{eig}} - \delta\Phi, \Phi_{\text{eig}} + \delta\Phi]) \overset{\text{proj. limit}}{\rightarrow} [-\pi, \pi). \tag{3.93}$$

In the Markov matrix $[\mathcal{M}_N]$, this can be seen as steep slope in the "band" of matrix elements, which signifies, that probabilities from many different cells are mapped to a small region. In the upper right panel of Fig. 3.6, both matrices are close to projective—note the steep slopes around the two eigenangles (an eigenangle of one of the post-measurement maps on the GC corresponds to a finite diagonal element of the Markov matrix, $[\mathcal{M}_N]_{i,i} > 0$).

In the lower panel of Fig. 3.8, an almost projective case is shown with $M/\gamma \rightarrow \infty$ and $T\gamma \rightarrow 0$. These limits correspond to the continuous measurement limit, which was analyzed in Ref. [67]. In this work, the authors explain how one of the measurement outcomes ($[M^+]$ in our case, see Fig. 3.4) becomes almost projective, while the second matrix generates infinitesimal translations, leading to a smooth curve that decays from the main peak. They describe, that the onset of the quantum Zeno effect manifests for example in the opening of a "forbidden region" of states as measurements become strong. This region can be seen to the right of $\Phi = 0$ in the distribution plot. Instead of infinitesimal translations, the second matrix generates finite translations in our case, since we only approach the continuous limit. As a result, instead of a smooth curve, we obtain a series of shrinking peaks.

## 3.5 Comparison of stationary solution and time average

Having analyzed different kinds of probability distributions and their relation to the GC probability distribution (3.41) as well as special cases where we can understand these distributions without relying on numerics, we move on to a systematic numerical approach in the (M, T) parameter plane for fixed $\gamma = 1$. We consider the plane $M, T \in (0, 5]$ which turns out to include a broad range of different distributions. Our understanding of generic distributions is based on their respective vicinity to the four cases frozen, shift, period-2, and projective where the average is particularly simple.

As a first step, we need to investigate the validity of the MC and ME approaches for calculating the GC distribution (3.41). In the left panel of Fig. 3.9 we show the difference $|\Delta\lambda| = ||\lambda_1| - |\lambda_2||$ between the two dominant eigenvalues of the Markov matrix $[\mathcal{M}_{10^3}]$. λ_1 and λ_2 are eigenvalues of the Markov matrix with largest- and second largest modulus. While the largest eigenvalue always fulfills $\lambda = 1$, the difference between this eigenvalue and the second largest in modulus determines the validity of the power iteration procedure as described in Sec. 3.3.1. Regarding the figure, we note that generally
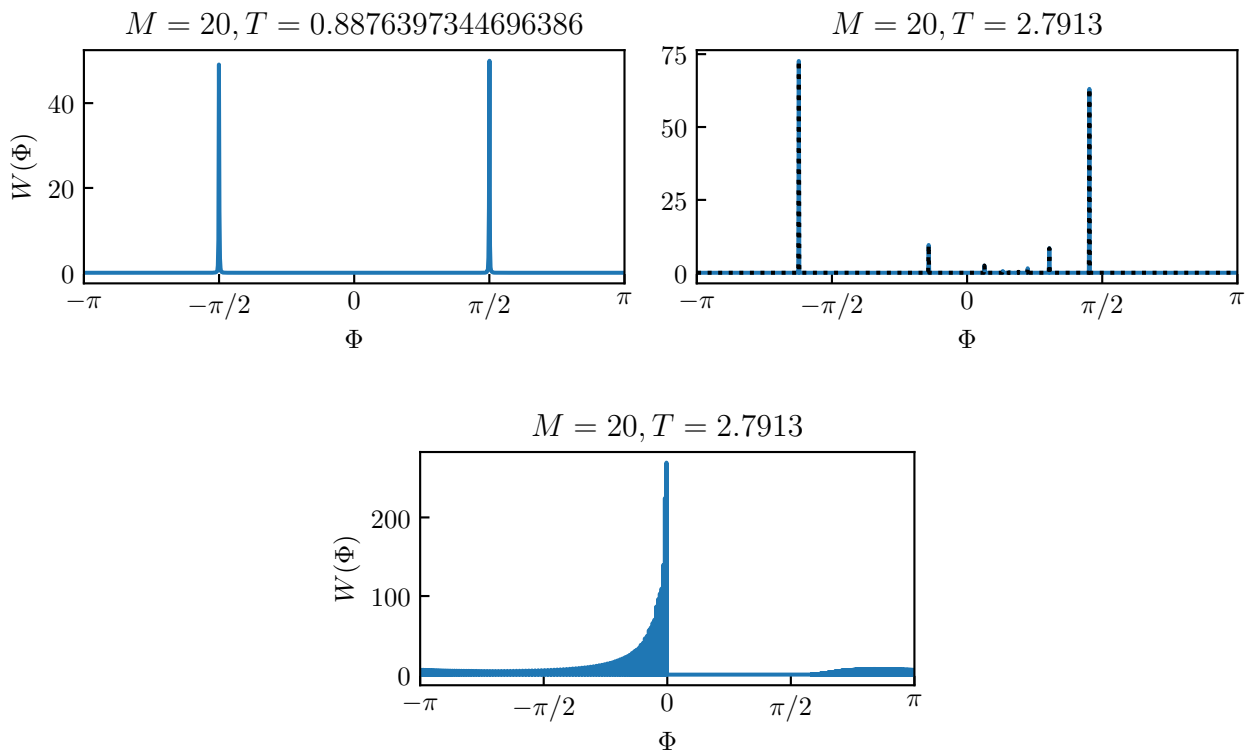
Figure 3.8: Examples for GC distributions in the special period-2 and projective cases (see Sec. 3.4). All panels were obtained for $\gamma = 1$ and with the M and T-values in plot titles. *Upper left panel*: Numerical result for the period-2-case, with $TY = \pi$. In agreement with our prediction (3.84), the distribution consists of two peaks of (approximately) equal height, at angles $\Phi = \pm\pi/2$. The distribution was generated by exact diagonalization of the GC Markov matrix $\mathcal{M}_{10^3}$ (defined in Eq. (3.59)) to find the eigenvector with eigenvalue $\lambda = 1$ (the stationary state). Slight peak broadening as well as a slight imbalance between the peaks are artifacts of the discretization (introducing transitions away from the bins that contain the invariant points). *Upper right panel*: Example for a projective case, where one of the matrices $M^\pm$ has a vanishing eigenvalue. In this case, the GC distribution is generated by projections to the main eigenangle (the leftmost peak) and translated by the non-singular matrix to produce the smaller peak-"satellites". The blue curve was obtained numerically by performing a time average over a single random Monte-Carlo post-measurement trajectory (discretizing into 10^3 grid cells). The dotted curve is the analytical prediction (3.88), truncated at just 20 terms. *Lower panel:* Almost projective case in the limit $M/\gamma \to \infty$ and $T\gamma \to 0$, where the matrix $[M^+]$ almost projects to $\Phi = 0$, while the $[M^-]$ matrix generates small translations of the main peak.

$|\Delta\lambda|$ approaches zero towards the frozen- and shift cases as well as the period-2-trajectory lines. This confirms the exceptions to the applicability of power-iteration discussed in Sec. 3.3.1—maximal degeneracy for the frozen- and shift cases, and the existence of a 2-periodic solution ($\lambda = -1$) in
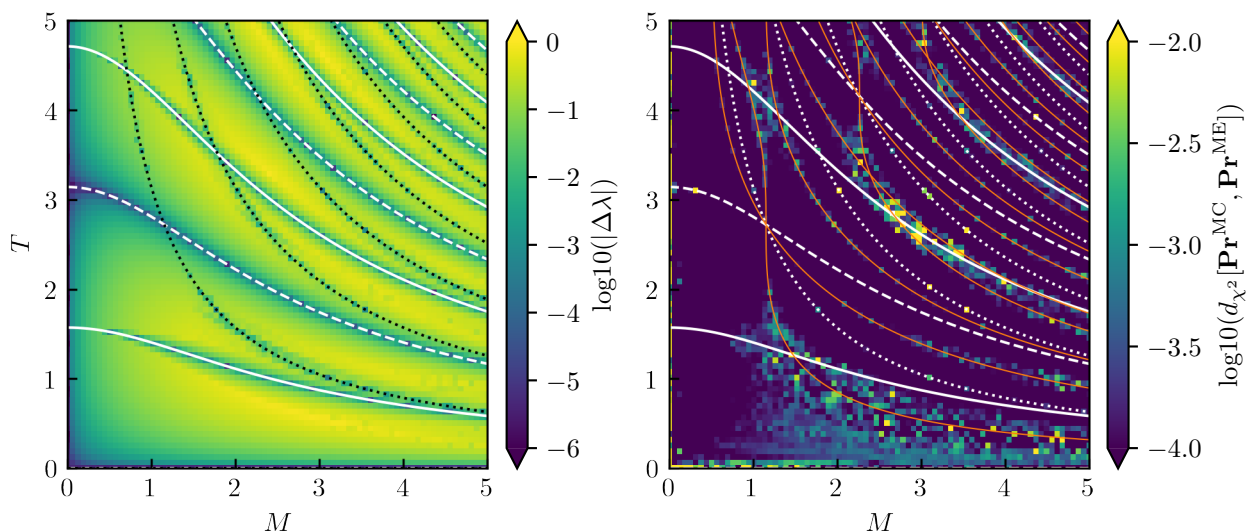
Figure 3.9: Characterization and comparison of discretized Master equation and Monte Carlo methods for obtaining Grand Circle distributions. *Left panel*: Difference of moduli between the first and second dominant eigenvalues of the ME matrix $[\mathcal{M}_{10^3}]$. The dominant eigenvalue is always equal to one. *Right panel*: χ^2-distance (3.94) between GC distributions with $N = 10^3$ grid cells, obtained from MC and ME method. For the MC simulation we start for each parameter tuple from a random state on the Bloch sphere and perform time evolution for 10^7 steps. We obtain the distribution from the last $6.9 \cdot 10^6$ states. The ME is solved starting from a uniform distribution on the GC on $N = 10^5$, iterating for up to 10^4 steps. The converged distribution is then coarse grained on $N = 10^3$ grid cells. Solid lines correspond to period-2-cases $YT = (2k+1)\pi$ with $k \in \mathbb{N}_0$. Dashed lines correspond to the frozen cases $TY = 2k\pi$. Dotted lines correspond to the shift cases $MT = k\pi$. Orange lines correspond to the projective limit, where an eigenvalue of one of the post-measurement matrices $[M^{\pm}]$ becomes zero.

the period-2-case. Deviating from these lines of special parameters, $|\Delta\lambda|$ increases rapidly (note the logarithmic scale). Away from these lines the finite gap between the dominant eigenvalues suggests that the discrete ME has a unique stationary solution which can be found efficiently using power iteration.

Next, we calculate distributions from both ME (power iteration) and MC simulation (time average over a single post-measurement trajectory) on $N = 10^3$ grid cells. For the MC simulation, starting from a random state on the Bloch sphere for every parameter set, we perform time evolution for 10^7 steps, using the last $9.9 \cdot 10^6$ steps to obtain the GC distribution; having checked that generic trajectories are converged to the GC after 10^5 steps, see Fig. 3.5.

Assuming, that a single MC trajectory captures the probability distribution $W_{\Delta\Phi}(\Phi)$, we can estimate the number of simulated time steps necessary for convergence. An approximate requirement for "qualitative" convergence of the MC distribution is to have a large number of sampling points per bin, $n_{GC}/N \gg 1$ where n_{GC} is the number of time steps on the GC from which the distribution is obtained. To get relative accuracy for every component of **Pr**, we need to require

$n_{\mathrm{GC}} \min_{i \in \{1,\ldots,N\}}(\mathrm{Pr}_i) = n_{\mathrm{GC}} \Delta\Phi \min_\Phi(W_{\Delta\Phi}(\Phi)) \gg 1$. We thus estimate, that we get accurate components if $\Delta\Phi W_{\Delta\Phi} \gtrsim 10^2/n_{\mathrm{GC}} \approx 10^{-5}$, which should give a good qualitative picture of the distributions. We compare the distributions obtained from MC simulation to results from the ME in the right panel of Fig. 3.9, thus comparing stationary states of the discretized ME to the time average of random quantum trajectories. We obtain the ME results from a uniform initial distribution on the GC, using 10^5 grid cells and up to 10^4 iteration steps. Using a uniform distribution as an initial state for power iteration, the iterated solution is guaranteed to contain components of all stationary states, in case the stationary state is degenerate. If this is the case, the iterated state can not be the same as the time-averaged state from a single post-measurement trajectory.

The iterated distribution is coarse grained to $N = 10^3$ cells. The distributions are compared by calculating the χ^2-distance between the probability vectors from ME and MC calculations,

$$d_{\chi^2}[\mathbf{Pr}^{\mathrm{MC}}, \mathbf{Pr}^{\mathrm{ME}}] := \frac{1}{2} \sum_{i=1}^{N} \frac{\left(\mathrm{Pr}_i^{\mathrm{MC}} - \mathrm{Pr}_i^{\mathrm{ME}}\right)^2}{\mathrm{Pr}_i^{\mathrm{MC}} + \mathrm{Pr}_i^{\mathrm{ME}}} \in [0,1] \qquad (3.94)$$

. In most cases we observe good agreement, $d_{\chi^2} < 10^{-2} \ll 1$. Some exceptions are related to the frozen- and shift cases (note bright markers exactly on dashed and dotted lines). If the freezing condition is perfectly fulfilled, both ME and MC methods preserve the initial state, which is localized at one point of the GC for MC evolution, and a uniform distribution on the GC for the ME calculation. In the numerical comparison we ignore the fact that the MC initial condition does not necessarily lie on the GC and just compare the distributions in Φ, keeping in mind that the frozen cases should be excluded from further analysis. This gives a large deviation $d_{\chi^2} \overset{N \to \infty}{\to} 1$ between the distributions. In the shift cases, there is again no convergence of the MC trajectory to the GC, while the ME calculation takes place entirely on the GC. Therefore, these cases must also be excluded from the comparison between MC and ME distributions.

Other points with large differences between MC and ME distributions are related to a strong eigenvalue hierarchy for $[M^+]$ or $[M^-]$. Vanishing $\lambda_{\min}^s$ for $s \in \{+, -\}$ corresponds to the orange lines in the plot, and for small M the eigenvalue ratio $\lambda_{\min}^+/\lambda_{\max}^+$ becomes small (see the dark blue region in Fig. 3.4, right panel). In the projective limit, the GC distribution can be calculated to high accuracy from a small number of terms in Eq. (3.88) and is independent of the initial angle. This distribution is also the unique stationary state of the ME (3.47). However, writing the ME as (3.52) or discretizing according to Eq. (3.59) are no longer valid, as the projective GC map is not invertible. This can also lead to inaccuracies on the projective lines.

Other inaccuracies with $d_{\chi^2} \sim 10^{-2}$ do not correspond to systematic problems with the methods but only to insufficient convergence (number of time points for the MC method, number of grid cells for the ME method). To demonstrate this, we show in the left panel of Fig. 3.7 a comparison between MC and ME distributions at one of the yellow parameter points with $d_{\chi^2} \sim 10^{-2}$, but increase the number of time steps in the MC simulation to 10^8, and the grid size for the ME to 10^6, coarse graining both results to $\Delta\Phi = 2\pi/10^3$ to approximate the corresponding $W_{\Delta\Phi}$. As the inset shows, the distributions agree perfectly. Note that $d_{\chi^2} \sim 10^{-2}$ is still good agreement between the distributions, sufficient for the following numerical investigations. In the discussed example distribution it corresponds to a slightly different weight distribution in the heavy right peak between the two methods.

In summary, we numerically confirmed convergence of generic post-measurement trajectories to the GC and found good agreement between the time-averaged distribution (3.68) and the power iterated solution of the ME (3.53). The stationary state of the discretized ME is non-degenerate and its eigen-

value $\lambda = 1$ always well separated by modulus from the other eigenstates of the Markov matrix (3.59), besides in the vicinity of frozen- and shift cases. This means, that the GC distribution (3.41) is independent on the initial state and can be obtained from the time average or stationary state equivalently.

The general independence of the GC distribution on the initial state allows us to drop the initial state argument Φ_0 from $W(\Phi|\Phi_0)$ and investigate the distributions $W(\Phi)$ within the chosen parameter range in the following. All following distributions are obtained with the established ME approach, allowing us to go to higher N- and parameter grid resolutions.

3.6 Characterization of distributions in the generic case

To first give an impression of different distributions for generic parameters, we fix (arbitrarily) $M = 2.92$ and present six different distributions from this cross-section, corresponding to different values of T in Fig. 3.10.

(De)Localization   Comparing several distributions, there is an immediate difference: For $T \in \{2.5, 2.7\}$, the distribution $W(\Phi)$ has heavy peaks around few points and is therefore close to zero at most angles. At $T = 3.0$ there are some peaks, but the distribution has small finite values at any angle. For $T \in \{3.0554, 3.1, 3.722\}$, the weight of the distributions is spread across the entire GC (note the scale of the y-axis). The distributions feature an intricate structure on smaller scale.

Based on the immediate visual difference between the distributions, it is tempting to refer to them as *localized* and *delocalized*. A distribution can be localized in the sense that there is a large chance to find the particle within a small subset of the GC within a short time interval on average (heavy peaks in $W(\Phi)$). If no such subset exists, the distribution is delocalized. To quantify this, we calculate a *participation ratio* (PR)

$$\mathcal{R}_N[W] := \left[\sum_{i=1}^{N} \mathrm{Pr}_i^2 \right]^{-1} = \frac{N^2}{(2\pi)^2} \left[\sum_{i=1}^{N} W_{\Delta\Phi}^2(\Phi_i) \right]^{-1} \tag{3.95}$$

where the Pr_i are probabilities obtained from integrating W over N equally sized discretization cells.

A perfectly localized distribution $W_{\mathrm{l}}(\Phi) = \delta(\Phi - \Phi_0)$ gives $\mathcal{R}_N[W_{\mathrm{l}}] = 1$, while a uniform distribution $W_{\mathrm{u}}(\Phi) = (2\pi)^{-1}$ gives $\mathcal{R}_N[W_{\mathrm{u}}] = N/(2\pi)$. Accordingly, large (small) values correspond to delocalized (localized) distributions. The scaling of the PR value with N can be attributed an exponent ζ as

$$\mathcal{R}_N[W] \propto N^\zeta \quad \zeta \in [0, 1]. \tag{3.96}$$

In the preceding chapters, we refer to (de)localization as a property of wave functions in site-space. In a one-dimensional Anderson localized system, the probability amplitude $|\psi_i|^2$ corresponding to an arbitrary eigenstate of the Hamiltonian falls off exponentially with the distance to the center site. In this case, a participation ratio is calculated as

$$\tilde{\mathcal{R}}_L[\psi] := \sum_{i=1}^{L} |\psi_i|^4 \tag{3.97}$$

where L is the system size. In a localized system, $\tilde{\mathcal{R}}_L$ becomes independent of the system size if L exceeds the localization length; while delocalization is defined by $\tilde{\mathcal{R}}_L \overset{L\to\infty}{\to} \infty$. Our model has a fixed
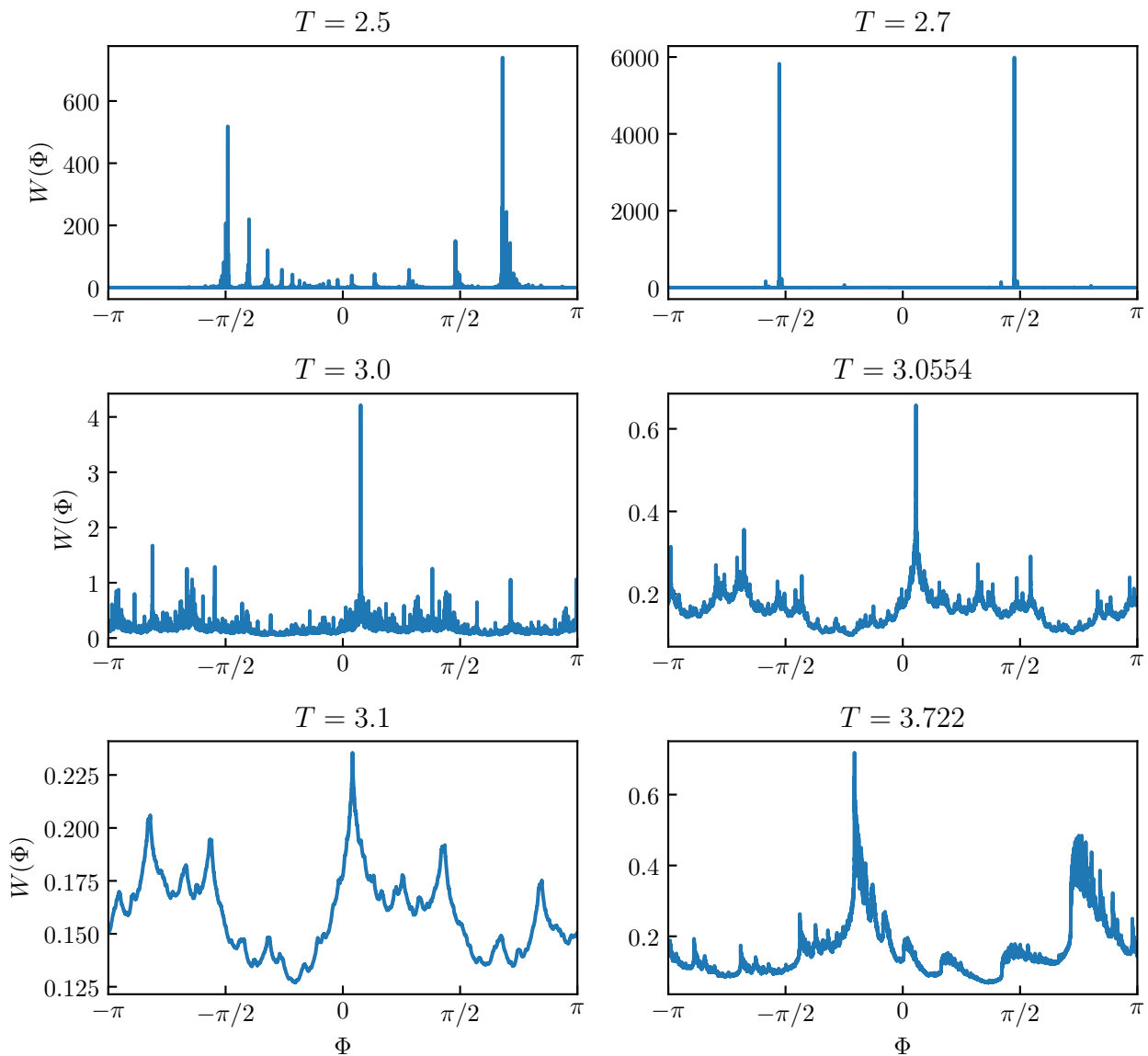
Figure 3.10: Different GC distributions obtained for $M = 2.92$ by solving the discretized Master equation ($N = 10^5$ grid cells) numerically for different values of T, starting from a homogeneous initial condition.

size, and localization does not refer to any spatial property, but to the spread over the GC. The role of the system size is played by the number of GC discretization grid cells N and the amplitude square of the wave function is replaced by the stationary probabilities on the GC. The scaling of the PR with N does not generally have an equivalent meaning as the scaling of the PR with L. For example, for a narrow box distribution which is non-zero on an interval I_1 with $|I_1| \ll 1$, we get $\mathcal{R}_N[W] \propto N$, as the fraction of the GC covered by the distribution is independent on N.

The situation is different, if the distribution is given by a sum of δ-peaks: In this case, the discretized

distribution $W_{\Delta\Phi}(\Phi)$ becomes narrower as $\Delta\Phi \to 0$, and the PR is constant as a function of N, similar to the PR scaling of a spatially localized distribution with system size. In this sense, a distribution would only be localized, if its support on the GC decreased with increasing resolution; and there can be situations where distributions are localized in the sense of a small PR value (narrow peaks), but delocalized in the sense that the support is independent of the discretization (if $\Delta\Phi$ is sufficiently small to resolve the distribution). Indeed, we know of two cases (period-2-trajectories, and the projective case), where the distribution $W(\Phi)$ is localized in the strict sense. Without analytical arguments, we are however always limited by the minimum resolution $\Delta\Phi$.

To further resolve the "localized-looking" characteristic in the distributions, we introduce another observable $\mathcal{S}_N^c$ which captures the minimum support N_c/N needed to cover a fraction $c \le 1$ of the total probability:

$$\mathcal{S}_N^c[W] := \frac{N_c}{N} \tag{3.98}$$

$$\sum_{i=0}^{N_c}[\text{sorted}(\{\text{Pr}\})]_i \ge c \tag{3.99}$$

where $\text{sorted}(\{\text{Pr}\})$ are descendingly sorted probabilities and N_c is the smallest integer, such that the inequality is fulfilled.

In the theory of Anderson transitions [10], the transition between insulating- and metallic phase manifests itself in the local density of states [10, 68, 142, 143]

$$\rho_i(\epsilon) = \sum_n \delta(\epsilon - \epsilon_n)|\langle i|\epsilon_n\rangle|^2. \tag{3.100}$$

On the localized side, at any given location, there is just a small number of wave functions contributing to the sum (3.100) at any given site i because most wave functions are localized away from i, and their contribution is exponentially suppressed. As a result, the typical value of the local density of states (essentially the value at the maximum of the distribution) vanishes [10, 68, 143]. On the metallic side close to the transition, many states contribute at any site, because the eigenfunctions $\langle i|\epsilon_n\rangle$ are spread out. The typical value assumes a finite value, and the distribution of values of ρ_i is spread around this value [142, 143].

Inspired by this "order parameter" of the Anderson transition, we introduce a third observable to capture localization, by counting the number of bins, where the GC probability distribution at given discretization lies within a given window of values (a "histogram of heights"). For this we introduce the height distribution

$$H(h_j) := \frac{\sum_{i \in \{1,\dots,N\}|W_{\Delta\Phi}(\Phi_i) \in [h_j - \Delta h, h_j + \Delta h]}}{N} \tag{3.101}$$

$$h_i := \min(W_{\Delta\Phi}) + (2i+1)\Delta h \qquad i \in [0, N_h - 1] \tag{3.102}$$

$$\Delta h := \frac{\max(W_{\Delta\Phi}) - \min(W_{\Delta\Phi})}{2N_h} \tag{3.103}$$

where $N_h \ll N$. Our GC distribution $W(\Phi)$ is an analogue of the local "density of states" (the local density of post-measurement trajectories on the GC). The height distribution $H(h_i)$ serves to analyze the distribution of values of $W(\theta)$ and in particular its typical value. Considering the discretized $W_{\Delta\Phi}(\Phi) \in [\min(W_{\Delta\Phi}), \max(W_{\Delta\Phi})]$, we discretize its values into N_h bins. $H(h_i)$ is the number of cells
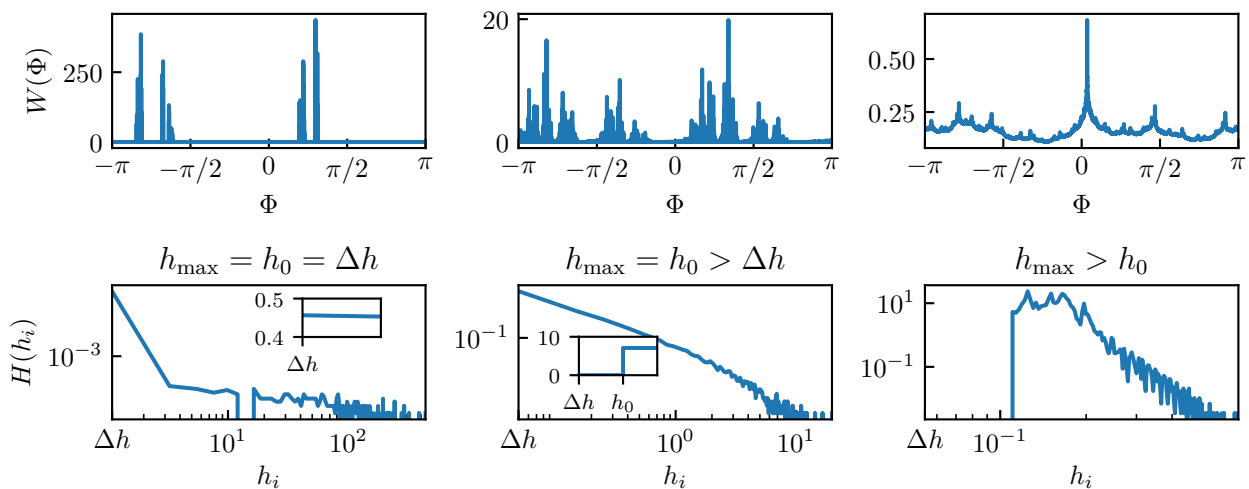
Figure 3.11: Examples of distributions and corresponding histograms of heights falling into the three different categories described in Sec. 3.6. *Upper panels:* Distributions obtained from the master equation with $N = 10^5$, at parameters $(M = 2.263, T = 3.498)$, $(M = 0.99, T = 1.811)$, $(M = 4.052, T = 3.768)$. *Lower panel:* The corresponding histograms of heights. From left to right categories 1 (localized, maximum at $h = \Delta h$), 2 (maximum $h_{\max}$ at the leftmost non-zero bin h_0 but at $h_0 > \Delta h$), and 3 (delocalized, maximum not at h_0).

$c_i = [\Phi_i - \Delta\Phi/2, \Phi_i + \Delta\Phi/2]$ with $W_{\Delta\Phi}(\Phi_i) \in [h_i - \Delta h, h_i + \Delta h]$. Each height bin has width $2\Delta h$, and the bin corresponding to the smallest height with $H(h_i) > 0$ is centered around $h_0 = \min(W_{\Delta\Phi}) + \Delta h$.

We analyze the typical value of $W_{\Delta\Phi}$ by considering the position of the histogram of heights maximum $h_{\max}$, such that $H(h_{\max}) = \max(H)$. Based on our numerical experience, we distinguish three different categories:

1. $h_{\max} = h_0 = \Delta h$,

2. $h_{\max} = h_0 > \Delta h/2$,

3. $h_{\max} > h_0$.

The first category means a vanishing[12] typical value in analogy to the insulating phase of a disordered system. The third category means a non-vanishing typical value in analogy to the metallic phase of a disordered system. The second value corresponds to a non-vanishing typical value, however at the left boundary of the distribution. This "transient regime" does not have an analogue in the Anderson transition. For examples of distributions in all three categories and the corresponding characterizations in terms of the histograms of heights see Fig. 3.11.

Fractality   Having introduced observables to quantify "localization", we now take a closer look at the apparent substructure in some of the distributions. As an example, we consider $M = 2.92$, $T \approx 3.729$ in Fig. 3.12 at high grid resolution $N = 10^7$. The upper left panel shows the entire distribution

---

[12]Note that the minimum value a height bin can be centered around is Δh.
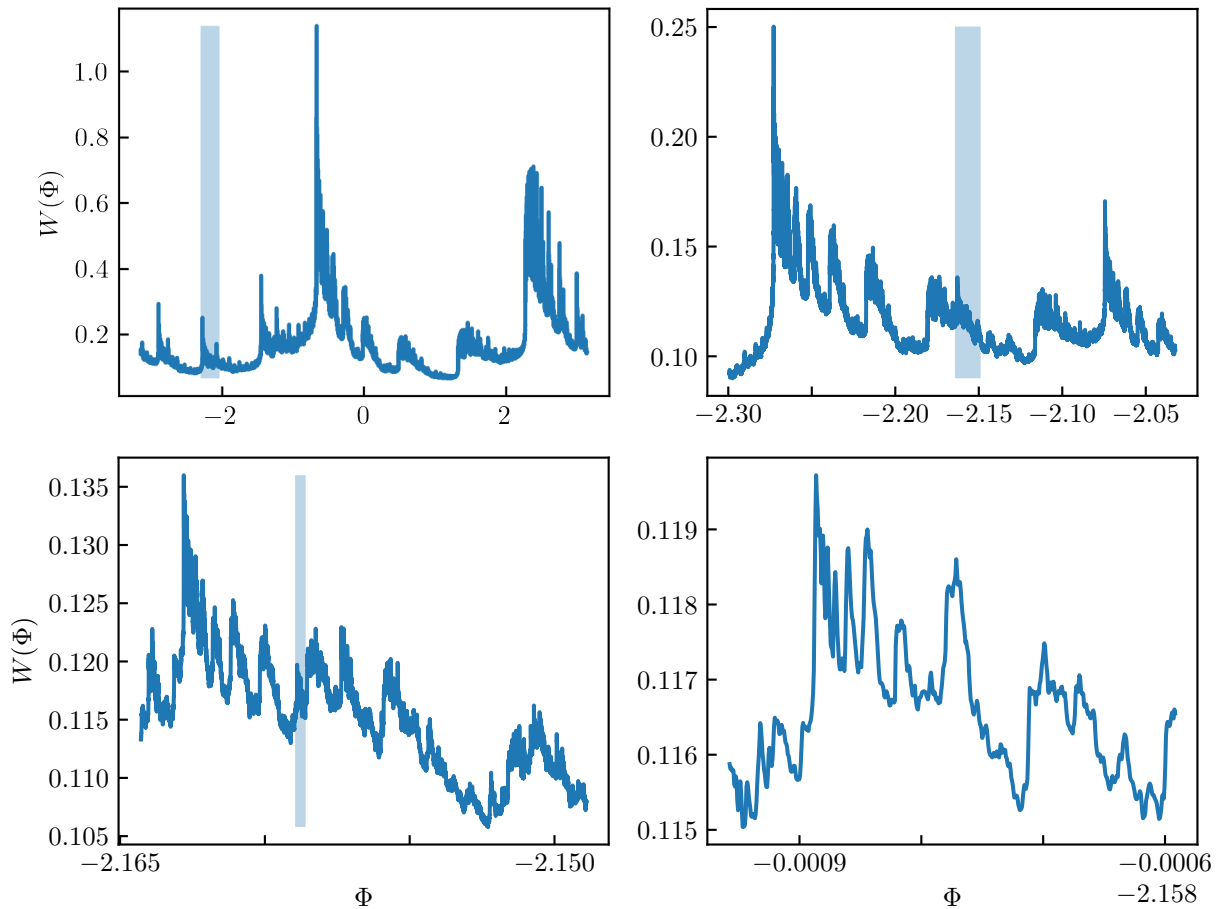
Figure 3.12: Fractal GC distribution corresponding to $M = 2.92$, $T \approx 3.729$, calculated with the ME at $N = 10^7$ grid cells, starting from a uniform initial condition. The upper panel shows $W(\Phi)$ on the entire GC, $\Phi \in [-\pi, \pi)$. The lower panels show progressively smaller sections of the GC, with the respective interval indicated by blue shading in the plot above.

$W(\Phi)$ with $\Phi \in [-\pi, \pi)$. The other panels show sections of the distribution taken from progressively smaller intervals on the GC. The blue shaded areas indicate the intervals which are displayed in the respective next panels. Remarkably, these four sections look similar to each other, suggesting that the distribution "repeats itself" as modulations on different scales, with the interval considered in the lower panel corresponding to a fraction of merely $5 \cdot 10^{-5}$ of the GC.

Numerically, we can not further resolve this pattern without going to larger N. A heuristic argument suggests however that this self-repetition can exist on any scale, rendering the distribution *fractal*. We quantify fractality of the distribution by calculating a fractal dimension d: Overlaying the curve corresponding to $W(\Phi)$ with a uniform grid of $m^{-1} \times m^{-1}$ cells, we count the number of cells $C(m)$

required to fully cover the curve[13]. The relation

$$C(m) \propto \left(\frac{1}{m}\right)^d \qquad m \to 0 \tag{3.104}$$

defines the *box counting dimension d* [144]. If the structure can be fully resolved at finite m, we get $d = 1$. $1 < d < 2$ corresponds to a fractal structure. Numerically calculating the fractal dimension we can not increase m above the number of grid cells N without trivializing the box counting dimension. Thus, any curve with $d > 1$ could turn out to scale trivially beyond our numerical resolution. However, this numerical evidence supports our heuristical argument suggesting fractal scaling (layed out in the next section).

The emergence of fractality is another parallel to the theory of Anderson transitions: At an Anderson transition, the wave function of the system becomes multifractal [10], which means that its self-similarity can be characterized by a whole set of non-trivial fractal dimensions by attributing a fractal dimension $f(\alpha)$ to a subset of points of the wave function that is characterized by scaling as $L^{-\alpha}$ with the system size [10, 145–147]. The function $f(\alpha)$ is called the singularity spectrum and can be extracted from the scaling of moments of the wave function (like the IPR) with the system size [10, 145]. In terms of these moments, fractality is associated, for example, with a fractal dimension $0 < \zeta < 1$ of the PR. The box-counting dimension $1 < d < 2$ of the entire wave function is closely related to the singularity spectrum but contains less information[14] [147].

(Non)ergodicity Finally, we ask about *ergodicity* of the Markov chain defined by $[\mathcal{M}_N]$. There exist several different notions of ergodicity for Markov processes in the literature [148, 149]. In the following, we call the system ergodic, if the Markov process is irreducible [15]. If this is the case, the time- and outcome averaged distribution is probed by any typical post-measurement trajectory implying ergodicity of the dynamical system [150]. Irreducibility means, that any state i (bin c_i) can be reached from every state j [148]. In our notation, for any i_0, j_0 there exists a natural number m such that

$$\left[[\mathcal{M}_N]^m\right]_{i_0,j} \delta_{j,j_0} > 0. \tag{3.105}$$

This is equivalent to ergodicity in the sense of a measure-preserving dynamical system, and the corresponding ergodic theorems hold true [150].

For our GC distributions, ergodicity implies:

1. Support of the GC distribution (3.41) on the entire GC.

2. A unique stationary state of the Markov matrix.

---

[13]We cover the curve resulting from connecting the data points, not the points themselves. A single spike of height h thus contributes h/m boxes, not one box.

[14]The reason we calculated the box-counting dimension of the curve is to describe the visible self-similarity in our GC distributions, see Fig. 3.12. An analysis of the singularity spectrum would be interesting to further establish the connection to the Anderson transition and is planned for future work.

[15]The apparently most common notion of ergodicity of a Markov chain requires aperiodicity as well [148]. This would exclude for example our period-2-trajectory case. Irreducibility and aperiodicity together imply a unique stationary distribution of the Markov process. However, including a time average in the definition of the GC distribution, we can define a universal distribution for a set of parameters without this requirement.

3. Equivalence of GC distribution, stationary state[16], and time average of a typical post-measurement trajectory.

4. Independence of the GC distribution on the initial condition.

To numerically check whether a given $[\mathcal{M}_N]$ corresponds to an ergodic system, we can regard $[\mathcal{M}_N]$ as the transition matrix of a directed graph

$$
\begin{aligned}
G_N &:= (V_N, E_N), \\
V_N &:= \{1, \ldots, N\}, \\
E_N &:= \{(j, i) \mid (j, i) \in V^2 \text{ and } [\mathcal{M}_N]_{i,j} > 0\},
\end{aligned}
\tag{3.106}
$$

where V_N is the set of nodes corresponding to the grid cells c_i and E is the set of edges corresponding to non-zero transitions $j \to i$ in the matrix $[\mathcal{M}_N]$. Ergodicity of the Markov process with transition matrix $[\mathcal{M}_N]$ is equivalent to G_N having a single strongly connected component (SCC) containing all N nodes (as an SCC is defined by every contained node being reachable by traversing exclusively edges within the SCC). The SCCs of a graph G_N can be calculated efficiently, within $\mathcal{O}(|V_N|+|E_N|)$ operations [151, 152] (we use the Python library networkx [153] to find SCCs). By calculating the SCCs of the graphs induced by our transition matrices, we decide whether or not the discrete process is ergodic. Whether or not this result at finite N can be used to make a statement about the continuous process, or the limit $N \to \infty$ is however not obvious and we do not prove (non)ergodicity for the continuous process for arbitrary parameters.

We know with certainty, that the frozen case is non-ergodic in the limit $N \to \infty$ because transitions away from the initial state are impossible. In the next section we present analytical arguments for non-ergodicity in an extended parameter regime.

From the numerical point of view calculating the number of SCCs gives a definite answer about (non)ergodicity of the discretized process characterized by $[\mathcal{M}_N]$. However, ergodicity can be an artifact of the discretization. As an extreme example, suppose we discretized the entire GC into a single cell $c_1 = [-\pi, \pi)$. This cell forms a single SCC, thus corresponding to an ergodic process. At a higher number of grid cells, sub-intervals of the GC may prove unreachable, rendering the process non-ergodic.

Importantly however, non-ergodicity of the process $[\mathcal{M}_N]$ at any discretization has definite physical implications for the continuous process. To see this, consider the *condensation* of the corresponding graph G_N. (The condensation is constructed as follows: Define one *supernode* for each SCC of G_N. Introduce a directed edge between two SCC nodes, if there exists a corresponding transition between the two represented sets of nodes [154].) The condensation is acyclic, such that we can define a partial order of the SCC supernodes in terms of reachability [155], where supernodes have a higher order, if they are reachable from a larger number of nodes. The SCC(s) at the highest order in this graph correspond to invariant subsets of the GC: By construction, transitioning out of a highest order node is impossible.

In this sense we refer to (non)ergodicity of the continuous process in the following: The process is non-ergodic, if the GC can be deconstructed into at least two invariant subspaces (corresponding to a non-ergodic discretization—not necessarily with uniform bins). Otherwise, the we call the process ergodic, implying that for any discretization transitions between any two bins exist. Note, that non-ergodicity does not imply degeneracy of the stationary state—as long as the condensation as an undirected graph

---

[16]Power-iteration does not necessarily work.

is fully connected, the stationary state is still non-degenerate.

Determining ergodicity with above method is numerically much favorable compared to, for example, calculating the stationary state to determine whether it has full support. For example, some components of the stationary distribution may be too small to be regarded finite in the numerical solution.

A summary of all our different characterization criteria:

- *Localization*: The GC distribution reduces to a sum of δ-functions. At any sufficient discretization the PR value (3.95) is $\mathcal{R}_N \sim 1$ and the support (3.98) $\mathcal{S}_N^1 \sim 1/N$. This is associated with category 1 of the histogram of heights indicator. Localization can not be proven using numerics, since it may always be a finite discretization artifact.

- *Delocalization*: The opposite of localization. It holds $\mathcal{R}_N \sim N$ and $\mathcal{S}_N^1 \approx const.$ Category 3 of the histogram of height indicator is associated with delocalization. Delocalization is also not provable numerically, since a continuous curve at given discretization may resolve as a set of δ-peaks at higher discretization. With this definition, delocalization also includes distributions which partly consist of δ peaks but also have extended regions.

- *Non-ergodicity*: This property is defined for the discrete process as featuring a number of strongly connected components of G_N greater than 1. Non-ergodicity of the discrete process implies non-ergodicity of the continuous process (invariant subsets on the GC). In this case the GC distribution may or may not depend on the initial angle. A priori, there are no further implications for the PR value, the support, or the histogram of heights.

- *Ergodicity*: The opposite of non-ergodicity. For the discrete process this property is defined by the number of strongly connected components of G_N being equal to 1. Ergodicity of the discrete process does *not* imply ergodicity of the continuous process. Ergodicity of the continuous process means that every point on the GC can be approach arbitrarily close by a post-measurement trajectory starting on an arbitrary point on the GC. It cannot be proven numerically. Ergodicity implies a unique stationary state of the discrete ME, support $\mathcal{S}_N^1 = 1$, delocalization, and equivalence of time-average, stationary state, and GC distribution.

- *Fractality*: The fractal box-counting dimension (3.104) fulfills $1 < d < 2$, implying a self-similar structure of the curve $W(\Phi)$. Since we can not take the limit $m \to 0$ numerically, this property cannot be proven numerically. However, as solutions for the functional stationary ME (3.53) fractal curves are a natural expectation. We expect the self-similarity of the curve to also manifest in the singularity spectrum in analogy to the Anderson transition [10, 145–147].

To summarize, we introduced three criteria for localization of the GC distribution (participation ratio, a support measure, and the typical value of the "histogram of heights") based on a loose analogy of the shape of our distributions (possibly at different discretizations) with localized and delocalized wave functions in a disordered system. To account for a possible fractal substructure of the distribution curves, we introduced a box-counting dimension. We can efficiently attribute ergodicity or non-ergodicity to the discrete Markov process corresponding to the transition matrix $[\mathcal{M}_N]$. This allows us to draw conclusions about the continuous process.

3.7 (De-)localization, (Non-)ergodicity, and fractality

3.7.1 Cross-section through the $M - T$ parameter plane

Using localization criteria, fractal dimension, and the ergodicity indicator of $[\mathcal{M}_N]$ we investigate a cross-section through the parameter space at $M = 2.92$, considering 640 equally spaced values of T in the interval $T \in [10^{-3}, 5]$, see Fig. 3.13. The distributions were obtained using the ME method with $N = 10^5$ grid cells, starting from uniform distributions and iterating for up to 10^4 steps. Different special conditions are indicated as black lines: Black solid lines correspond to period-2-trajectories, dotted lines correspond to the shift cases and dashed lines correspond to the frozen cases. Additionally, dash-dotted lines indicate the projective limit in either of the $[M^+]$, $[M^-]$ matrices.
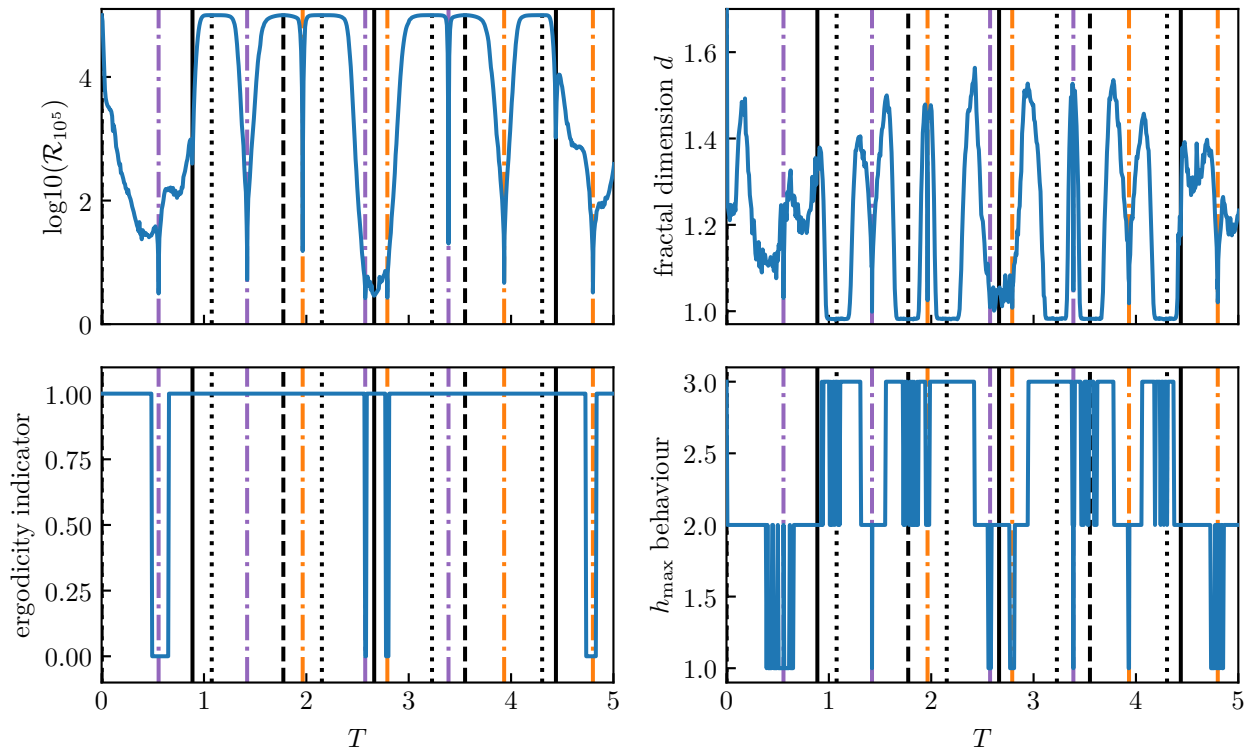
Localization and Delocalization

Let us first consider the upper panel, showing the PR $\mathcal{R}_{10^5}$. We note, that delocalization $\mathcal{R}_{10^5} \simeq 10^5$ occurs in the vicinity of the frozen- and shift commensurability conditions (dashed and dotted lines), while localization $\mathcal{R}_{10^5} \ll 10^5$ is observed in the vicinity of period-2-trajectories and the projective limit. Based on these conditions, all regions of the cross-section can be roughly distinguished. At $T = 0$ the PR indicates delocalization, but this is an artifact of the uniform initial condition. In this case the *detector* state is Zeno-frozen, since there is no (joint) unitary time evolution. Therefore, the detector state never changes, and the measurement outcome is always no-click, corresponding to the application of the $[M^-]$-matrix. Consequently, the $[M^-]$-matrix acts trivially on the chain state, such that it remains frozen as well (though not in an eigenstate of a projective density measurement).

Similarly, exactly along the frozen cases, both matrices act trivially and the chain state never changes, while the ME indicates a delocalized distribution. In these cases, any state is an eigenstate of the Markov matrix, and these degenerate stationary states do not correspond to the actual (frozen) GC distribution, which is given by the initial state. In the shift case, the ME also always has a uniformly delocalized stationary state, as every bin has exactly the same incoming contributions. The actual GC distribution depends on the shift angle ϕ: If this angle is commensurate with π, $n\phi = 2\pi$ for some $n \in \mathbb{N}$, the GC distribution only has support on a finite set of points. If the angle is non-commensurate with 2π, any point on the GC can be approached arbitrarily closely, and the GC distribution is delocalized. In any shift case, generic post-measurement quantum trajectories do not converge to the generic distribution, since the Bloch-angle θ is frozen.

The situation is different in the vicinity of the freezing and shift cases: The freezing of state and Bloch-angle is clearly broken away from the commensurabilities as we found that the trajectories converge to the GC if we slightly deviate from these conditions. The deviation lifts the exact degeneracy of eigenvalues in the frozen case, and the ME approach can be used—agreeing well with the MC time average. Around these commensurabilities the PR indicates regions of delocalization of width $\Delta T \approx 1/2$ with almost saturated PR values $\mathcal{R}_{10^5} \approx 10^5$. This means that the distributions are close to uniform.

Uniform distributions in the vicinity of the frozen cases can be understood based on the structure of the Markov matrix shown in the lower left panel of Fig. 3.6. The degenerate diagonal "band" of matrix elements splits into two separate bands which are slightly shifted from the main diagonal and bent towards opposite sites, crossing close to the middle and the ends. On the discretized level, it can be understood that a slight shift of the bands away from the main diagonal should lead to delocalization, since it essentially introduces transitions between neighboring grid cells. If the cells are smaller than the distance of the band to the diagonal at some point, then there is a next-nearest neighbor transition,

Figure 3.13: Cross-sections of different observables defined in Sec. 3.6 through the parameter plane, with $T \in [10^{-3}, 5]$ and $M = 2.92$. *Upper left panel*: PR values $\mathcal{R}_{10^5}$. Large (small) values correspond to delocalization (localization). *Upper right panel*: Fractal dimension d obtained from box counting. $1 < d < 2$ corresponds to a self-similar substructure, while $d = 1$ implies the absence of such substructure. *Lower left panel*: Ergodicity of the Markov process corresponding to $[\mathcal{M}_{10^5}]$. The plot indicates whether or not the corresponding graphs have a single strongly connected component. *Upper right panel*: Box counting dimension of the distribution curve. $d = 1$ corresponds to a fully resolvable curve, $1 < d < 2$ corresponds to a repeating (fractal) substructure to numerical resolution. *Lower right panel*: Different types of behavior of the maximum of the histogram of heights, defined in Sec. 3.6. Types 1 / 3 are defined in analogy to the behavior of the typical value of the local density of states in a disordered system in the localized / metallic phase. The distributions were obtained with the ME method; for 640 equally spaced values of $T \in [10^{-3}, 5]$, with $N = 10^5$ grid cells and a maximum of 10^4 iteration steps and starting from a uniform initial distribution. Solid lines correspond to period-2-cases $YT = (2k+1)\pi$ with $k \in \mathbb{N}_0$. Dashed lines correspond to the frozen cases $TY = 2k\pi$. Dotted lines correspond to the shift cases $MT = k\pi$. Dash-dotted lines correspond to the projective limit, where one of the eigenvalues $\lambda_{\min}^{\pm}$ vanishes.

but the other band can facilitate a back-transition to the cell in between and so on. At the same time, perturbing the parameters of the frozen case, the outcome probabilities $P^{\pm}$ are almost independent of

the state, such that the stationary state is almost translationally invariant. From the trajectory point of view, we can think of the state performing short-distance hops on the GC in a random direction, eventually covering many points on the GC in a diffusive fashion. Similarly, in the shift case, existing commensurabilities are broken by a perturbation.

Due to the above mechanism, the PR would reveal a sharp transition moving onto or off a frozen parameter line, if we had chosen a localized initial state. Dynamically, this transition is more of a crossover, since the distance from the commensurate line controls the "diffusion coefficient" in a post-measurement trajectory. Close to the frozen case the time average of a post-measurement trajectory converges slowly. Similarly, the difference between the two dominant eigenvalues of the Markov matrix is controlled by the distance to the frozen line, such that the convergence rate of power iteration goes to zero as the commensurability is approached.

Regions of localization can also be understood in terms of the corresponding special cases. The period-2-trajectory (solid lines) corresponds to perfect localization of the GC distribution. We see from the cross-section, that this localization can be destroyed by slight deviations from the commensurability. Perturbatively, we may expect naively that a product $[M^{\pm}][M^{\mp}]$ still has eigenstates close to the period-2-peaks. However, the attraction of the period-2-peaks depends on long chains of $[M^+][M^-]$ which emerge from the contraction argument $[M^{\pm}]^2 = \mathbb{1}$. If this contraction is not fulfilled exactly anymore, the deviations add up particularly in long chains. This means that the number of chains that project to the period-2-peaks becomes negligible and the peaks are immediately broadened.

The second special case related to small PR values is the projective limit (dash-dotted lines). In the projective limit, the solution of the ME is given by a discrete set of δ-peaks, which decay exponentially with the number of necessary transitions from the main projective peak, resulting in localization as well. From the cross-section we see that the stability of this projective localization to variation in T depends on the value of T. The first, fourth and fifth, and last projective lines are within regions of smaller PR values; first and second-to-last line lie within extended "valleys", and third and sixth lines are enclosed by shift and frozen lines and only lead to a sharp dip in the PR. As mentioned above, the vicinity of a projective case is special insofar, that a large interval of the GC is still mapped into a narrow region around the dominant eigenangle of the almost projecting map, if this map is applied. This may lead to a sharp peak at this eigenangle, which is translated by the second matrix. However, the stability of this localization mechanism depends on the probability to apply the projecting map as well as the stability of the strong eigenvalue hierarchy.

Interestingly, all broad regions of localization correspond to cases with a strong hierarchy in both post-measurement matrices (see Fig. 3.4).

The support measure $\mathcal{S}_{10^5}^{0.99}$ and the scaling of the PR value with the discretization which were also introduced in the previous section as indicators of localization show analogous behavior to the PR diagram just described, see appendix B.1. A small value of the support measure means, that only a small subset of the GC is needed to cover the support of the GC distribution which contains 0.99 of the total probability. A small PR exponent means, that the number of cells required to cover the distribution depends only weakly on the discretization. In summary, our loosely defined "localization" manifests in analogues of several common localization measures.

(Non-)Ergodicity and fractality

We move on to consider the ergodicity phase diagram in the lower left panel of Fig. 3.13. The plot shows, whether or not the Markov process corresponding to $[\mathcal{M}_{10^5}]$ is ergodic (whether or not G_{10^5} defined in Eq. (3.106) has a single SSC). Ergodicity does not necessarily imply delocalization in the

sense of a large PR value: As long as the stationary solution is finite everywhere, the process can be ergodic. For the same reason, non-ergodicity does not necessarily imply localization.

Most of the considered T interval is ergodic, but interestingly, we find extended non-ergodic regions in the vicinity of projective lines, where both post-measurement matrices have strong eigenvalue hierarchies (at small T, the $(+)$-matrix has a strong eigenvalue hierarchy, see Fig. 3.4). As argued in Sec. 3.6, non-ergodicity of the discrete process does imply non-ergodicity of the continuous process since there are invariant subspaces on the GC. The same conclusion does not hold true for ergodic regions, but the extent of these regions in the cross-sections suggests, that there is also genuine ergodicity in our parameter space.

The existence of extended regions of non-ergodicity can be understood if both post-measurement matrices have a strong (not necessarily singular) eigenvalue hierarchy. To understand this, consider two small but finite intervals around the two eigenangles $\Phi_\pm$; say $I_\pm := [\Phi_\pm - \delta_\pm, \Phi_\pm + \delta_\pm]$. These regions make up an invariant subspace on the GC, leading to non-ergodicity. We prove this, by considering the action of the post-measurement maps on these intervals. By definition, the eigenvalue is mapped onto itself by the corresponding map, $f_\pm^{-1}(\Phi_\pm) = \Phi_\pm$. A strong eigenvalue hierarchy means, that a large fraction of the GC (around this eigenangle) is mapped into the vicinity of the eigenangle by the corresponding map (see Sec. 3.4 and Fig. 3.6, upper right panel). In particular, a small vicinity of the eigenvalue is mapped back into itself,

$$f_\pm^{-1}(I_\pm) \subset I_\pm. \tag{3.107}$$

If these "attractive regions" of the intervals $I_\pm$ are sufficiently extended to include the respective other eigenangle as well, the condition

$$f_\pm^{-1}(I_\mp) \subset I_\pm \tag{3.108}$$

is fulfilled. In this case, neither measurement operator can facilitate escape from the intervals $I_\pm$ which thus form an invariant subset for the post-measurement state[17].

Below, we use this line of reasoning to estimate the stability of non-ergodicity around the projective cases due to this mechanism.

One may expect to find non-ergodicity also at least directly on the period-2-lines, since the period-2-case is associated with an invariant set on the GC as well. However, this set contains exactly two points and is never visible in a discretized picture.

Moving on to the fractal dimension displayed in the upper right panel of Fig. 3.13, we observe a trivial box counting dimension $d \approx 1$ around the frozen and shift cases. This is expected, since we learned from the PR values that these cases correspond to almost uniform distributions. The projective limit is also correlated with dips in the fractal dimension. Based on a series of exponentially shrinking peaks in this limit, we indeed expect trivial scaling $C(m) \propto 1/m$ in the exact projective limit. This is consistent with a low fractal dimension, even though our T-resolution is not sufficient to observe $d = 1$. Period-2-trajectories correspond to dips in d, since the period-2-case with just two peaks also corresponds to $d = 1$. All other cases have a non-trivial fractal dimension—this seems to be the generic case in our system. Fractality of the distributions can be understood heuristically from the following consideration. Suppose we are close to a projective case, such that the map f_+^{-1} maps a large fraction of the GC to a narrow interval around its main eigenangle, resulting in a slightly broadened peak. The

---

[17]The existence of such a region is constructively proven with analogous reasoning, if we find more than one SCC in G_N at any N. The maps $f_\pm$ are not approximated in the numerics.

($-$) map translates this peak to another angle interval, slightly "distorting" the peak shape (because f'_- and P^- are not constant). If we start from a peaked distribution around the main eigenangle, the translating map generates a set of decaying "peak clones" on the GC. Many of these peak clones are modulated back onto the main peak by the almost projecting map. Self-consistency requires those modulations to be translated to the secondary peaks as well. Recursively applying this argument suggests that the stationary limit is given by a fractal.

Generally, this mechanism is not limited to the projective cases. As soon as there is some back- and forth copying between two points, fractality can emerge. Quantifying when exactly this breaks down towards the uniform cases requires a more careful consideration, which we do not provide here.

To this point, we discussed "localization" in terms of the PR (and other localization indicators), and ergodicity in the discrete and continuous Markov processes. We explicitly pointed out that these are not necessarily correlated in any direction. A connection is established by the behavior of the maximum histogram of heights—introduced as an observable inspired by the typical value of local the density of states—which serves as an indicator for the Anderson (delocalization-localization) transition [10, 68], see Sec. 3.6. The behavior of this typical value according to the three categories introduced in the preceding section is shown in the lower right panel of Fig. 3.13. Interestingly, regions of non-ergodicity are correlated with the first category (analogous to the manifestation of the insulating phase in the local density of states). Around all of the non-ergodic projective cases, the maximum ventures into the first category. Additionally, around the projective case at $T \approx 4$, there is a small first-category dip, which is not present in the ergodicity cross-section. Also, the behavior of $h_{\max}$ fluctuates, which can be due to numerical inaccuracies[18]. The surrounding parameter regions of category-one behavior are "transitional" category two regions (which does not have an analogue in the Anderson transition). Delocalized regions (in PR terms) correspond to extended category three regions (delocalization in the Anderson-picture) with occasional fluctuations into the second region around special lines.

To summarize up to this point: In terms of PR, we found localized and delocalized phases, which can be qualitatively understood in terms of special cases. From the number of SCCs in the graph of the discretized Markov process, we found ergodic- and non-ergodic phases, which we can also understand based on the special cases. We established the existence of such non-ergodic phases also in the continuous process and have reason to believe, that the ergodic phases also partially survive. The behavior of $h_{\max}$ (inspired by the behavior of the typical local density of states around an Anderson transition) establishes a connection between (de)-localization and (non)-ergodicity. Also, fractal curves are rather generic as a solution of a continuous implicit equation of the form (3.52).

3.7.2 The $M - T$ parameter plane

Having investigated a fixed M cross-section the $M - T$-parameter plane, we move on to study localization, fractality, and ergodicity in the $M - T$ plane. See Fig. 3.15 for the same quantities as in Fig. 3.13, calculated for a 160×160 grid with $M, T \in [10^{-2}, 5]$. Consider first the PR values $\mathcal{R}_{10^4}$ in the upper left panel. Again, localized and delocalized phases can be distinguished based on the special cases in analogy to what was discussed before. Delocalized phases are found around frozen- and shift cases (dashed and dotted lines), while localization is related to the projective limit (orange and purple lines) and period-2-trajectories (solid lines). Again, the almost uniform delocalization around frozen and projective cases is remarkably stable with respect to change in parameters, manifesting in broad yellow "bands" around the commensurate parameters. On the other hand, the period-2-trajectory

---

[18]There are two discretization steps, one to find the stationary solution of the discretized Master-equation and another one to find the histogram of heights from which the maximum is extracted.

crosses these bands on narrow "bridges" bridges of localization (for example at $T = 0.3, M \approx 4.7$). For the projective lines, it depends on the exact parameters whether they are surrounded by a narrow or broad region of localization. Again, the case where both GC maps are almost projective is special in that such regions always correspond to extended localization. (Support measure and PR scaling phase diagrams are also visually very similar to the PR diagram, they are shown in the appendix B.2.)

Ergodicity regions where both matrices $[M^{\pm}]$ have a strong eigenvalue hierarchy are also special, due to the argument lined out above. As expected, we find extended regions of non-ergodicity embedded into the mostly ergodic phase diagrams; in the vicinity of strong hierarchies in both maps. To estimate the expected extension of these vicinities, consider the following simple criterion for a non-ergodic region, based on above argument:

1. Both matrices $[M^{\pm}]$ have eigenvectors on the GC (establishing the existence of a region according to relation (3.107).)

2. The respective opposite eigenangle lies within the attractive region of the map (to fulfill relation (3.108)). This corresponds to[19]

$$(f_{\pm}^{-1})'(\Phi_{\mp}) < 1. \tag{3.109}$$

In Fig. 3.14 we show the evaluation of above criterion in our parameter range. Comparing to the numerical data in Fig. 3.15 (lower left panel: ergodicity of the discrete process, lower right panel: $h_{\max}$ indicator) we note, that the positions of the non-ergodic regions are strongly correlated. The criterion covers all regions which we find to be non-ergodic at finite discretization (and which are category one of the indicator). Furthermore, it shows the regions of non-ergodicity to extend further in the parameter space. This could be either not true due to the inaccuracy of the estimation, or invisible in the numerics due to insufficient discretization.

Considering the fractal dimension as a function of M and T (upper right panel of Fig. 3.15) confirms again our conclusions from the cross-section. Extended regions of almost-uniform distributions around frozen and shift cases correspond to a trivial fractal dimension of one. Away from these regions, the fractal dimension is non-trivial (besides close to the projective cases, which are not drawn to avoid covering fine lines of $d \approx 1$).

Lastly, the behavior of $h_{\max}$ is displayed in the lower right panel. Again, there is astonishing agreement between category three and uniform delocalization as well as between category one and non-ergodicity. As before, the plot is somewhat noisy, probably due to discretization errors. Categories one and three are separated by the "transient" category two.

With our semi-analytical explanation of different regimes in the parameter space, we cannot understand every detail of the phase diagrams. One particularly prominent feature that we do not explain here is visible in the lower left corner of the $h_{\max}$, PR, and fractal dimension diagrams: Regions of delocalization are broken by almost horizontal lines of localization (category two for $h_{\max}$, $d \approx 1$ for the fractal dimension). This frequent change in behavior of the distributions may be attributed to crossings of other commensurabilities, which we did not uncover here.

---

[19]Technically, none of the discussed properties of the maps prevents the second derivative from becoming negative between those points (such that attraction at the "wrong" eigenangle does not imply attraction everywhere between the eigenangles). We ignore this in our estimation.
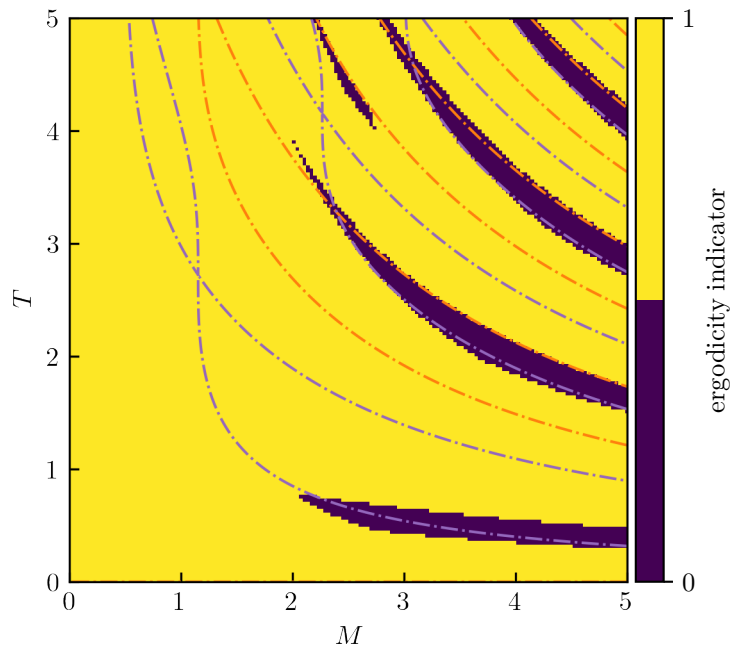
Figure 3.14: Evaluation of the analytical estimation for non-ergodicity in the continuous Markov
process on the grand circle (described in Sec. 3.7). This should be compared to
the numerical data in Fig. 3.15, lower panels. Purple / orange lines correspond to
projecting $[M^-]$ / $[M^+]$ matrix. Note, that the $[M^+]$ matrix has a strong eigenvalue
hierarchy in the region of the lower purple region as well, see Fig. 3.4.

3.8 Summary

We investigated a simple model of ancilla measurements where both the measured system (the "chain"),
as well as the detector only feature Hilbert spaces with two basis vectors each. In our time evolution
protocol, the detector is initialized in the $|-\rangle$ state at every step, evolves unitarily due to interaction
with the chain, and is projectively measured at the end of every step. This defines two measurement
operators, which map a post-measurement state onto one of two possible new post-measurement states,
depending on the measurement outcome. The time evolution of the post-measurement state is entirely
described by these measurement operators. We showed that the evolution generically takes place
on a one-dimensional circle on the Bloch sphere (the grand circle GC), see Figs. 3.3 and 3.3. We
characterized the evolution in terms of a distribution of states on the GC, which turned out to be
characteristic even for individual typical post-measurement trajectories, starting from an arbitrary
state on the Bloch-sphere. We described, how the evolution on the grand circle can be modeled as a
Markov process, which we discretized for numerical analysis. We described several special parametric
cases, their respective physical interpretations, and the corresponding behavior of the GC distribution.
Based on generic distributions for arbitrary points in the parameter plane of the model, we introduced
several observables to characterize the distributions. Depending on the parameters, the distributions
can "look" localized or delocalized on the GC. Even though there are fundamental differences between
apparent localization on the Bloch-sphere and Anderson localization, we defined some observables
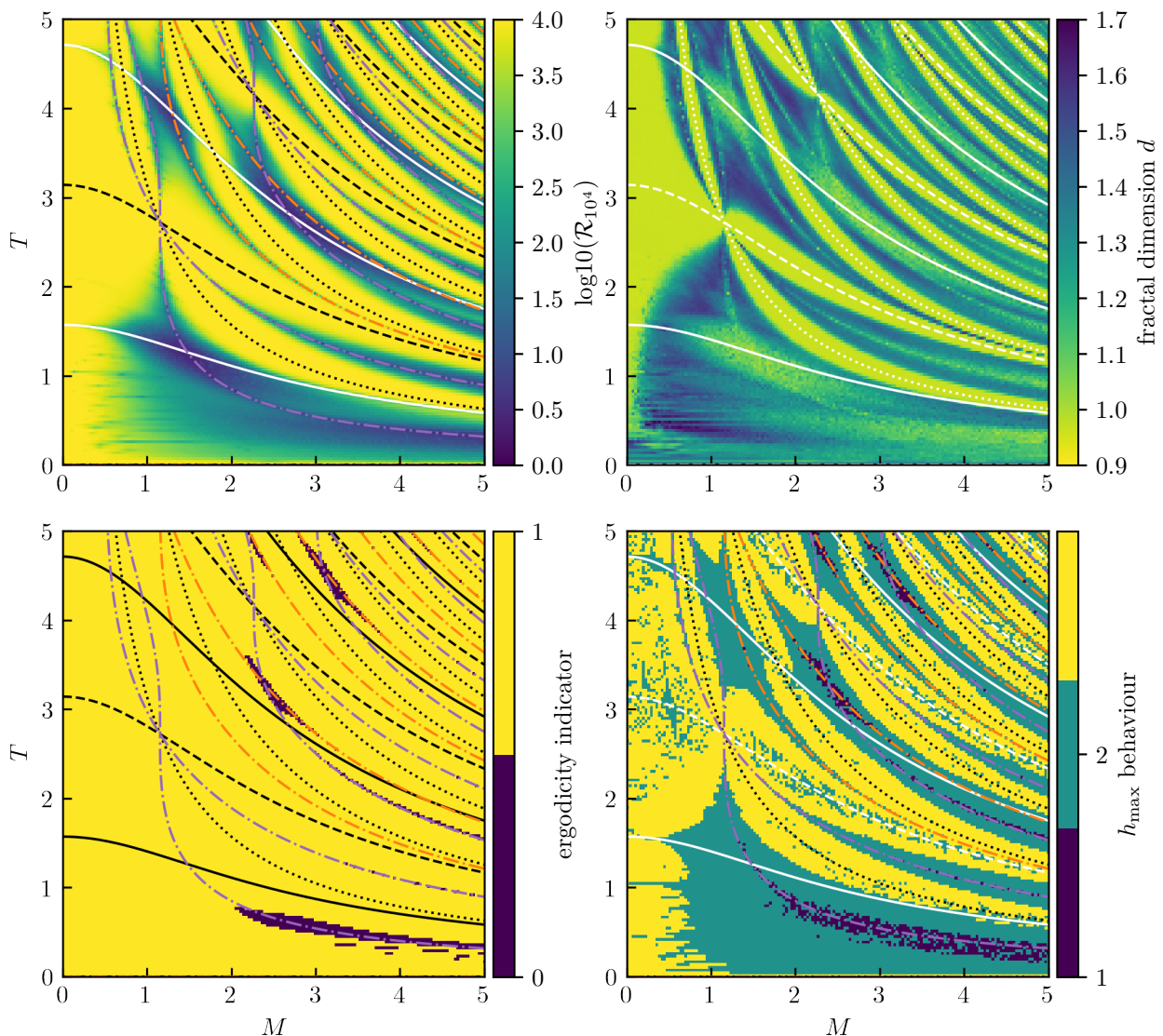
Figure 3.15: Diagrams of different observables defined in Sec. 3.6 in the $M - T$ parameter plane. *Upper left panel*: PR values $\mathcal{R}_{10^5}$. Large (small) values correspond to delocalization (localization). *Upper right panel*: Fractal dimension d obtained from box counting. *Lower left panel*: Ergodicity of the Markov process corresponding to $[\mathcal{M}_{10^5}]$ indicating whether or not the corresponding graphs have a single strongly connected component. *Lower right panel*: Behavior of the maximum of the histogram of heights, defined in Sec. 3.6. Types 1 and 3 are defined in analogy to the behavior of the typical value of the local density of states in a disordered system in the localized and metallic phase. The distributions were obtained with the ME method, with $N = 10^4$ grid cells and a maximum of 10^4 iteration steps, starting from a uniform initial distribution. Solid lines correspond to period-2-cases $YT = (2k + 1)\pi$ with $k \in \mathbb{N}_0$. Dashed lines correspond to the frozen cases $TY = 2k\pi$. Dotted lines correspond to the shift cases $MT = k\pi$. Dash-dotted lines correspond to the projective limit, where one of the eigenvalues $\lambda_{\min}^{\pm}$ vanishes.

based on counterparts from the analysis of the Anderson transition in a disordered material (the participation ratio, the support measure, the behavior of the maximum of the histogram of heights). Furthermore, due to remarkable self-similarity in some of our distributions (see Fig. 3.12), we analyzed the distributions in terms of a box-counting dimension. Borrowing from the mathematical theory of measure-preserving dynamical systems and Markov chains, we transferred a rigorous definition of ergodicity in discrete Markov chains that corresponds to the physical concept of ergodicity to our system.

Our main results are:

1. Our model provides a platform to consider non-trivial extensions of phenomena known from projective measurements. We can have situations where none, one, or both of the measurement maps leads to a collapse of the chain-state that is independent of the initial state. In the spirit of the generalization of the quantum Zeno effect in terms of a partially measured model, put forward by the authors of Ref. [67], this leads to a complex dynamical situation which manifests itself in the distribution of post-measurement states on the GC.

2. The accessible Hilbert space of only four basis states renders the solution of one time step in the model trivial. However, due to the randomness of the measurement outcomes, a complex Markov process emerges on the GC, which we were only able to analytically solve for some special cases (but analyzed numerically across a parameter plane). As was pointed out in Refs. [136–139] such processes can give rise to a plethora of different distributions, which can be spread out, localized around individual points, and even generically fractal (see Figs 3.10 and 3.12). Consequently, the study of these distributions proved fruitful in our investigation as well.

3. At a discretized level, cross-overs and transitions between localization and delocalization exist in the $M-T$ parameter plane, reflecting in indicators known from Anderson localization such as the participation ratio and support measures. These transitions and cross-overs can be understood qualitatively based on analytical statements about the distributions in certain special cases. At the same time, we found transitions between ergodicity and non-ergodicity in the discretized Markov process on the GC (see Figs. 3.13 and 3.15). We demonstrated analytically that non-ergodicity in extended parameter regions survives taking the limit to the continuous Markov process and reasoned that extended regions of ergodicity exist as well, based on their stability in all phase diagrams. This establishes transitions between ergodic- and non-ergodic behavior in the state space, which is explored by individual typical quantum trajectories. Cross-overs between localization and delocalization and transitions between ergodic and non-ergodic processes are brought together by the typical value in the "histogram of heights" of the distribution, which we constructed as an analogue of the typical value of the local density of states. This quantity is sensitive to an Anderson transition [10, 68] and similarly indicates the ergodicity transition in our system: In the non-ergodic phases, the "order parameter" indicates localization (in agreement with the PR), while delocalization in the sense of the PR corresponds to delocalization in the order parameter. In between, there is a transient phase that does not have any analogue in the Anderson transition. Dynamical transitions where also observed and characterized previously in a related model by the authors of Ref. [67].

Clearly, a lot can be learned from studying even the smallest non-trivial models of ancilla measurement evolution. This encompasses interesting mathematical properties of dynamical processes, physical implications of indirect measurements, and even the possibility of phase transitions in the dynamical behavior.

Regarding the model at hand, it may be interesting to understand better the mechanism of fractality, to see when it breaks down. Exploring the possibility of multifractal curves in the category two regions of the order parameter and analyzing fractality in terms of the singularity spectrum may establish an even closer connection to the theory of Anderson localization. The similarities between Anderson (de)localized wave functions and the distribution on the Bloch sphere could suggest a common mathematical origin—a connection between Anderson transitions in $D \geq 3$ dimensions and measurement induced transitions of free fermions in $D - 1$ dimensions was established in Refs. [38, 41] based on the mathematical descriptions of these transitions. The investigation of this connection in our system in particular is also left for further studies. Understanding delocalization in the continuous case based on the Master equation would rigorously establish the transition in the continuous model.

Introducing small variations to specifics of our model—for example imbalanced energy levels in the measured system, or a different kind of coupling—is expected to generate families of interesting dynamical system, possibly not described by a single angular variable but with the entire Bloch-sphere as the underlying manifold.

Slightly enlarging the measured system to permit for non-trivial evolution of two particles would allow to introduce and study an entanglement entropy, which is the usual subject of interest in measurement induced entanglement transitions.

Beyond such toy models, it would be interesting to see how and to what extent our results manifest in larger systems, for example if the chain size is increased, or a "crystal" of our chain-detector pieces is built. Ref. [39] considers both situations—ancilla measurements on a longer chain, and multiple ancillas on a chain. A principle difference to our model besides the size is the fact that the detectors are not reinitialized, allowing them to keep a memory of the measurement outcome. The authors describe the effect a single ancilla can have on the entanglement entropy (calling this a "Zeno-valve effect") [39]. Using multiple ancillas, a measurement-induced transition is found. Establishing parallels to our work requires further research.

4 Chapter 4
Conclusion and outlook

4.1 Summary

Over the course of this thesis, we considered different settings of disordered and measured systems, uncovering interesting dynamical effects emerging from these different sources of randomness.

In Chapter 1, we added projective onsite density measurements between long intervals of unitary time evolution to a one dimensional, strongly localized Anderson featuring a single particle. We found, that the introduction of measurements at randomly chosen locations restores transport in the chain, while typical quantum trajectories still propagate within exponential envelopes. We demonstrated, that the ensemble of particle trajectories—defined as the first moments of the quantum trajectories immediately before a measurement—can be described by a simple classical random walk, where a localized wave function is associated with a classical random walker. In this picture, the main influence of measurements on the wave function is a shift of the center site around which the particle is localized, thus inducing random jumps. The distribution of effective localization lengths at the given disorder strength is associated with a waiting time distribution in the random walk. Since it falls off quickly towards long waiting times, the ensemble of pre-measurement trajectories spreads asymptotically diffusively over the chain. This result holds true, even if only the measurement outcomes are random while the disorder realization and the sequence of measurement locations is kept fixed. We found that a not too large measurement frequency only impacts the diffusion constant, such that the system undergoes a dynamical transition from localized to diffusive from the transport point of view. The main effect of no-click measurements was found to be a slight modification of the effective localization length, which we calculated from the spread of a wave function around its center site. The effective localization length depends non-monotonously on the measurement frequency.
In above sense by combining measurements and disorder, we find coexisting localization (in the wave functions) and delocalization (due to the mobile centers).

Furthermore, we formulated measurement protocols, that can be used to spatially steer the particle to a designated target site within a polynomial number of measurements in the distance between initial location and target. Ballistic steering can be realized if the outcome of every measurement is known, by "dragging" the particle away from its last known location. Efficient steering is still possible without having access to the detector readout anywhere but on the target site, by performing measurements at random locations utilizing the diffusive spread.

In Chapter 2 was dedicated to the puzzlingly slow decay of large-wave vector initial states in the presence of disorder, even without localization. As an important motivation, in many studies of

many-body localization the density imbalance between neighboring sites is used as an indicator of the delocalization-localization transition. The imbalance is monitored after setting up a highly imbalanced state, which can not decay in a localized system, but is found to decay according to a power-law on the ergodic side of the transition [59–61]. Naively, one could expect this decay to happen exponentially fast due to the small distance each particle has to travel for the density to equilibrate. Using the diagrammatic technique for disorder averaging [126], we demonstrated, that the slow power-law decay of the imbalance is a universal property of disordered systems. It is related to so-called return processes, where a particle scatters twice on the same impurity, moving diffusively in between these two scattering events. In the diagrammatic picture this can be understood as the large external momentum being transmitted through the first impurity across the diffuson ladder, which thus acquires a small momentum leading to the diffusion pole. Consequently, the return probability enters the calculation of the asymptotic imbalance decay and contributes a long-time tail that depends on the number of spatial dimensions. This naturally leads to a relation between the imbalance- and mean-square displacement power-law exponents, which was previously observed numerically in Refs. [59, 117]. The imbalance exponent from our calculation coincides with numerical results in the diffusive phase of the many-body localization transition [60]. Interestingly, our arguments can be generalized to the pre-thermal, subdiffusive phase on the delocalized side of a system with a many-body localization transition, by assuming a modified diffusion propagator corresponding to a given subdiffusive exponent. Our analysis is also applicable to the transient regime of weak disorder in a two-dimensional system with $l \ll L \ll \xi$. In this situation, imbalance- and mean-square displacement exponents are slightly modified due to weak multifractality of the wave functions [124, 125]. We check our results numerically by exact diagonalization of a two-dimensional system in this parameter regime, confirming the imbalance exponent and the relation between imbalance and mean-square displacement. To substantiate our numerical results, we provide an additional analysis of the properties of transient weak localization in an intermediate-scale two dimensional system in Appendix A.1.

In Chapter 3, we considered a simple model for ancilla-measurement dynamics, consisting of a two-level system (one particle on a "chain" of two sites) and a two-level ancilla detector. During one period of time evolution, the detector is first initialized in the $(-)$ state, then evolved unitarily with the chain through an interaction coupling of strength M during a time interval T, and is finally projectively measured in its eigenbasis. This time evolution protocol defines two measurement operators, corresponding to the two possible outcomes of the detector measurement. The backaction of the measurement on the chain depends on the parameters M and T. We gave some intuitive explanations for the effect of a measurement, and demonstrated, that the chain state can generically be found on a one-dimensional submanifold of the Bloch sphere (the GC). To characterize a parameter tuple M, T we introduced a distribution function on the GC, by performing averages over time and measurement outcomes. We investigated this distribution by establishing connections to the time-averaged distribution of states in a typical post-measurement trajectory (accessible by Monte-Carlo simulation), and to the stationary state of a Markov-process on the GC, which can be approximated by solving a system of linear equations after discretization. Intriguingly, the distribution is found to behave localized, delocalized, and even fractal depending on the parameters. The discretized Markov process was shown to exhibit transitions between ergodic- and non-ergodic phases, which are argued to be genuine features of the continuous process. Using an analogue to an indicator which is used in the literature to pinpoint the Anderson transition, we demonstrated, that these phases manifest themselves in the localization properties of the distribution. We accompany our numerical results by discussions of the different dynamical regimes in the $M - T$ plane, being able to qualitatively explain the phase diagram based on different special cases for which the GC distribution can be understood analytically.

In summary, we considered three different settings with measurements and disorder, that feature non-trivial dynamical effects. In all three systems, we profited from analogies to classical Markov processes, which inherited from the quantum properties of the dynamics. The omnipresence of random walks in this context is a natural consequence of the central limit theorem for random numbers, which can enter either through the disorder distribution or through the random outcomes of measurements. The concept of localization is also somewhat common to disorder (due to Anderson localization) and measurements (due to local projections, and the quantum Zeno effect). Indeed, in Chapter 3 we found an interesting connection between a localization–delocalization (non-ergodic–ergodic) transition in the dynamics of post measurement states on the Bloch sphere, and the Anderson transition.

4.2 Outlook

Our results lay a basis for further studies, building on the intuition provided by the respective models. Possible directions include:

1. Further investigation of the applicability of our results from the second chapter numerically and experimentally, in particular the relation between imbalance and mean-square exponent on the ergodic side of the MBL transition. This could reveal details of the underlying process governing subdiffusion in such systems.

2. Adding more particles while keeping the same time evolution protocol and Hamiltonian for the measured Anderson chain. A continuously monitored, non-interacting Anderson-chain occupied by several fermions was investigated in Ref. [46] from the perspective of the measurement-induced entanglement transition. The entanglement transition in measured systems is a subject of debate even in for the clean measured free fermion chain [28, 32, 38], and thus certainly interesting in the presence of disorder as well. There are also other aspects of the dynamics that can be studied in such systems, for example the influence of measurements on the shape of the wave functions, as proposed in Ref. [46] (as we did for the wave function of a single particle). If several particles are present, more complex steering targets can be chosen; with the goal to introduce non-trivial correlations into the system that mimic the correlations in an interacting system.

3. Adding more particles and interaction effects to the measured Anderson chain. The possibility of a measurement induced entanglement transition in a many-body localized system was investigated in Ref. [47]. Clearly, the introduction of interactions adds a whole new element of complexity to the situation, since the relevant Hilbert space is exponentially large and can not generically be parametrized efficiently. Additionally, the interaction strength enters the consideration as another parameter.

4. Considering generalized (ancilla-) measurements instead of projective measurements on the Anderson chain. In Ref. [39] it was shown, that even a single ancilla on a clean, interacting chain can have an influence on the system dynamics. It is a natural extension to both Chapter 1 and 3 to take the more complex model of measurements from 3 and combine it with a larger (possibly disordered) chain.

5. As already shown in Ref. [67], studying small models of generalized measurements can be interesting in its own right, with the possibility of dynamical transitions that can not be observed in projectively measured systems. In the model investigated in Chapter 3, open questions remain

with regards to a possible connection to the Anderson transition, as well as to the solution of the Markov equation. An investigation of multifractality of the curves would be a logical first step. Even slight modifications of the model immediately complicate the situation, for example, the introduction of an imbalance of onsite energies of the two chain sites ("disorder") destroys GC convergence and thus leads to a dynamical process on the two-dimensional surface of the Bloch sphere.

Intriguingly, not even for the smallest systems (like our chain-detector setup) it is possible to accurately predict the future in the form of a single quantum trajectory, contrary to main statement from the initial quote by Laplace. This has been known for a long time and is owed to the nature of quantum mechanical measurements. However, as also seen in the preceding chapters, measurements do not make the field of dynamics less interesting but instead add a random element that leads to the emergence of new phenomena. Dealing with random numbers is a problem familiar from disordered systems, establishing a close connection between these two directions. The versatile effect of measurements further motivates the joint investigation; with the possibilities of creating localization effects in clean systems as well as establishing transport in otherwise localized systems. As outlined above, there are many natural generalizations of the models considered in this thesis which can be expected to be rich platforms for further studies.

A

Additional material for Chapter 2

The following sections were published in Ref. [54].

A.1 Additional numerical checks to Sec. 2.5: Fraction of localized states and energy dependence of the conductance in calculations of the imbalance

In Sec. 2.5, we numerically investigate memory effects in the (transient) diffusive regime of a 2D Anderson lattice. Our numerical results on the decay of the imbalance $I(t)$ in this regime are in agreement with the analytical prediction (Sec. 2.4.2) of the power law behavior $I(t) \propto t^{-\gamma_I}$, with exponent $\gamma_I = 1 - 1/(\pi g)$ for a non-interacting 2D system. Here, g is the conductance and the term $-1/(\pi g)$ in the exponent γ_I originates from a weak-localization correction to the classical memory effects ($\gamma_I = 1$).

It might come as a surprise that the imbalance numerics presented in Sec. 2.5 is described so well by a power law $I(t) \propto t^{-\gamma_I}$, for the following two reasons. First, even though we consider not too strong disorder, there is a fraction of localized states, with localization lengths smaller than the size of the system. Some of these localized states (in the tails of the band) are so strongly localized that their localization length is already probed on the time scales of our numerical simulations. Since the imbalanced initial condition for the numerics (for example, a checkerboard pattern in the density) encompasses the full range of energies, such strongly-localized states would also contribute to the imbalance. Their contribution is different from the power law that is characteristic for delocalized states: a strongly localized state is expected to give a time-independent contribution. Second, as the conductance $g(\varepsilon)$ is generically energy-dependent, the initial condition for the imbalance implies averaging of the corresponding power-law decay over energy [here $\nu(\varepsilon)$ is the density of states]:

$$I(t) \propto \int \mathrm{d}\varepsilon \, \nu(\varepsilon) \, t^{-\left(1 - \frac{1}{\pi g(\varepsilon)}\right)}. \tag{A.1}$$

In Sec. 2.5, we provide explanation on why the numerical data for the imbalance in the transient diffusive time window are described so well by a power law with a single power law exponent $\gamma_I = 1 - 1/(\pi g)$. First, the fraction of strongly localized states in band tails is very small, so that they do not play any essential role in the considered time regime. The dominant contribution to the imbalance in this time range comes from the broad central region of the band (encompassing nearly all states),
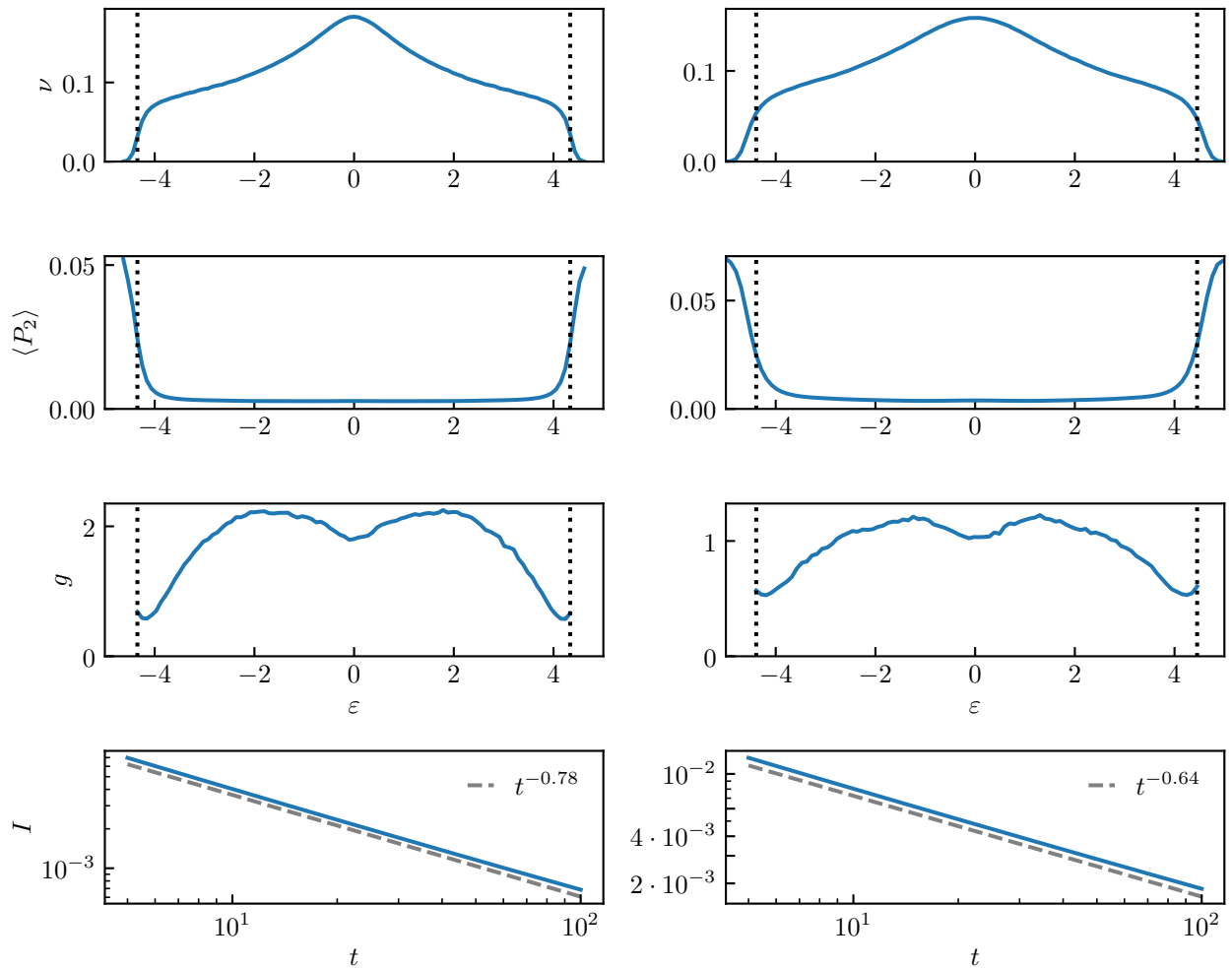
Figure A.1: Density of states ν (first row), inverse participation ratio P_2 (second row), and conductance g (third row) as functions of energy ε; imbalance I as a function of time on a double-logarithmic scale (fourth row). These results are obtained from exact diagonalization after averaging over 4000 disorder realizations of Hamiltonian (2.67) in a system of 40×40 sites at disorder $W = 1.5$ (left column) and $W = 2$ (right column). The vertical dotted lines separate the effectively delocalized states ($\xi \gg 10$) from the localized states ($\xi \lesssim 10$) in band tails. The imbalance was obtained (up to a constant prefactor) from $\nu(\varepsilon)$ and $g(\varepsilon)$ using Eq. (A.1). For convenience of comparison, the prefactors in the imbalance plots are chosen by fixing the values at time $t = 10$ to the direct results in Fig. 2.4. Dashed lines are power-law fits slightly shifted with respect to the imbalance curves (A.1) (solid) to make them easier to distinguish.

while the expected asymptotic saturation (due to strong localization) will set in at still longer times. Second, in this broad central part of the band, g is sufficiently large and depends only weakly on the energy, so that the average (A.1) is numerically almost indistinguishable from a simple power law. The

purpose of this appendix is to demonstrate these two statements explicitly by numerically evaluating $g(\varepsilon)$ and $\nu(\varepsilon)$ across the energy band.

To this end, we calculate the eigenstates and eigenvectors of Hamiltonian (2.67) for 4000 disorder realizations with $W = 1.5$ and $W = 2$, in a system of $N = 40 \times 40$ sites. From the eigenenergies we obtain the density of states $\nu(\varepsilon)$, and for each eigenstate $\psi(\varepsilon)$ at energy ε we determine the inverse participation ratio (IPR)

$$P_2(\varepsilon) = \sum_{i=1}^{N} \left| \psi_i(\varepsilon) \right|^4 . \tag{A.2}$$

Calculating the mean value $\langle P_2(\varepsilon) \rangle^2$ and the variance $\mathrm{var}[P_2(\varepsilon)]$ of $P_2(\varepsilon)$ (with respect to averaging over disorder realizations), we obtain information on the conductance $g(\varepsilon)$ and the localization length $\xi(\varepsilon)$, as we are now going to explain. For delocalized states (localization length much larger than the system size), the IPR is given by the random-matrix-theory value $\langle P_2 \rangle \approx 3/N$, with a weak-localization correction. On the other hand, for strongly localized states (with $\xi \ll L$), the IPR becomes much larger than this value. We can get an estimate of the localization length ξ of such a strongly localized state by assuming (for $1 \ll \xi \ll L$) that it spreads within the area ξ^2, resulting in $P_2 \sim 3/\xi^2$. This allows us to estimate the contribution of the localized states to the conductance. Further, we use IPR fluctuations to extract the conductance for the weakly localized states via [101]

$$g(\varepsilon) = \sqrt{\mathcal{A} \frac{\langle P_2(\varepsilon) \rangle^2}{\mathrm{var}[P_2(\varepsilon)]}}, \tag{A.3}$$

where $\mathcal{A}$ is a numerical factor that depends on the spatial dimensionality and boundary conditions; in our case $\mathcal{A} \approx 0.123$. Using the obtained conductance and density of states, we numerically verify that energy averaging (A.1) indeed does not lead to any essential deviations from a simple power law (in the considered time window).

Before presenting our numerical data, we point out that the localization length $\xi(\varepsilon)$ in the same 2D model was determined numerically by the transfer-matrix approach in Ref. [156] (see upper panel of Fig. 2 there). The disorder used in Ref. [156] was $W = 2.5$ in our units, i.e., somewhat stronger than in our simulations. The results of Ref. [156] show that, even for this stronger disorder, the fraction of strongly localized states with $\xi < 10$ (see below for the reason of the choice of this boundary) is very small. Furthermore, the conductance that can be estimated (from the one-loop formula) as $g \approx \pi^{-1} \ln \xi$ varies in a relatively narrow interval only, $1.3 \lesssim g \lesssim 1.7$, in the energy range $|\varepsilon| < 3.5$ comprising an overwhelming majority of all states. These results fully support the above two statements [formulated in the paragraph below Eq. (A.1)], in consistency with our numerics discussed below.

In Fig. A.1, we show the numerically obtained density of states (first row), average IPR (second row), conductance (third row), and imbalance decay obtained from Eq. (A.1) (fourth row) for $W = 1.5$ (left column) and $W = 2$ (right column). Inspecting the density of states, we observe that nearly all states lie within the energy band of the clean system, $|\varepsilon| < 4$. Already from this figure, one sees that almost the whole band is effectively delocalized, with only a small fraction of strongly localized states in the tails. From the IPR values, we find that states within $|\varepsilon| \lesssim 4$ are "delocalized" from the finite-size perspective of the system, with $\xi \gg L$ and thus $\langle P_2 \rangle \sim 3/N \sim 0.002$.

Diffusion with $D \sim 1$ over times $t \sim 100$ implies spreading over $\sim \sqrt{100} = 10$ sites in each direction. Therefore, states with $\xi \gtrsim 10$ still appear delocalized in the time window explored with our numerics in Sec. 2.5. Placing a cut-off at $\langle P_2 \rangle = 0.02 \lesssim 3/10^2$ on the density of states (dotted lines) to separate

the strongly localized states, we find that the fraction of strongly localized states is indeed very small: $\approx 99\%$ of all states at $W = 1.5$ and $\approx 97\%$ of the states at $W = 2$ are delocalized according to this criterion. Further, for the conductance within the energy window corresponding to delocalized states, we find values between approximately 0.6 and 2.3 (0.5 and 1.2) for $W = 1.5$ ($W = 2$). Note that the fact that $g(\varepsilon)$ has a local minimum at the band center is in full agreement with the results of Ref. [156].

Using the obtained results for $\nu(\varepsilon)$ and $g(\varepsilon)$, we numerically calculate the energy-averaged imbalance curves according to Eq. (A.1), which are shown in the fourth row in Fig. A.1. We find that the resulting curves for both values of disorder are virtually indistinguishable from power laws (dashed lines, slightly shifted for ease of comparing), with $\gamma_I = 0.78$ at $W = 1.5$ and $\gamma_I = 0.65$ at $W = 2$. These results are in good agreement with the values extracted from the direct imbalance simulations, $\gamma_I = 0.69$ for $W = 1.5$ and $\gamma_I = 0.61$ for $W = 2$, see Fig. 2.4.

The fact that, despite the energy averaging (A.1), the imbalance is described so well by a single-power law is fully consistent with the observation that, in most of the band, the conductance $g(\varepsilon)$ varies only weakly around its band-center value $g(0)$ (see the third row in Fig. A.1). Specifically, we find that for $\sim 85\%$ of states, the conductance $g(\varepsilon)$ is within $\approx 25\%$ from its band-center value $g(0)$.

The localized states are expected to give a time-independent contribution $\sim 1/\xi^2$ to the imbalance. Even for our stronger disorder, we thus get an estimated contribution on the level of 10^{-4}. This fully supports our interpretation of the numerics, as provided in Sec. 2.5. The power laws observed there are transient and will eventually saturate. However, the level at which saturation appears is very small ($\sim 10^{-4}$) and is not relevant in the considered time range (where the imbalance drops down only to $\sim 10^{-3}$).

A.2 Numerical calculation of the density response function

To calculate $\chi(q, t)$ in a 2D non-interacting system numerically, we start from the definition in the site space:

$$\hat{\chi}_{\mathbf{r},\mathbf{r}'}(t) = -\mathrm{i}\theta(t)\langle[\hat{n}_{\mathbf{r}}(t), \hat{n}_{\mathbf{r}'}(t)]\rangle. \tag{A.4}$$

Here $\mathbf{r}$ and $\mathbf{r}'$ label the sites on the two dimensional grid and $\hat{n}_{\mathbf{r}}(t)$ is the number operator in site space, with

$$\tilde{n}(q_x, q_y, t) = \sum_{\mathbf{r}} e^{-\mathrm{i}\mathbf{q}\mathbf{r}a}\hat{n}_{\mathbf{r}}(t). \tag{A.5}$$

Applying Wick's theorem, we find

$$\hat{\chi}_{\mathbf{r},\mathbf{r}'}(t) = -2\mathrm{Im}\left\{\langle c_{\mathbf{r}'}^{\dagger}(t)c_{\mathbf{r}}\rangle\langle c_{\mathbf{r}'}(t)c_{\mathbf{r}}^{\dagger}\rangle\right\} = -2\mathrm{Im}\left\{[G_{\mathbf{r}',\mathbf{r}}^{<}(t,0)]^{*}G_{\mathbf{r}',\mathbf{r}}^{>}(t,0)\right\}, \tag{A.6}$$

where we have identified the lesser and greater Green's functions $G^{<}$ and $G^{>}$. These Green's functions are time-evolved according to

$$G_{\mathbf{r},\mathbf{r}'}^{\lessgtr}(t,0) = \sum_{\mathbf{r}''} U_{\mathbf{r},\mathbf{r}''}(t)\, G_{\mathbf{r}'',\mathbf{r}'}^{\lessgtr}(0,0), \tag{A.7}$$

$$U_{\mathbf{r},\mathbf{r}'}(t) = \left[\exp(-\mathrm{i}Ht)\right]_{\mathbf{r},\mathbf{r}'}, \tag{A.8}$$

where H is the Hamiltonian in the site space.

We specify the initial condition in the eigenbasis of H (denoted with Greek indices), according to the Fermi distribution:

$$G_{\mathbf{r},\mathbf{r}'}^{\lessgtr}(0,0) = v_{\mathbf{r},\alpha} G_{\alpha,\beta}^{H,\lessgtr}(v^\dagger)_{\beta,\mathbf{r}'}, \tag{A.9}$$

$$G_{\alpha,\beta}^{H,<}(0,0) = \mathrm{i}\frac{\delta_{\alpha,\beta}}{\exp\left[\beta(\varepsilon_\alpha - \mu)\right] + 1}, \quad G_{\alpha,\beta}^{H,>}(0,0) = \delta_{\alpha,\beta}\left[-\mathrm{i} + G_{\alpha,\beta}^{H,<}(0,0)\right]. \tag{A.10}$$

Here, $\{\varepsilon_\alpha\}$ and $\{v_{\mathbf{r},\alpha}\}$ are the eigenenergies and eigenvectors of H. The chemical potential μ is chosen in the middle of the band, and the temperature $T = 1/\beta$ is of the order of the bandwidth. We obtain $\chi(q_x, q_y, t)$ by calculating the Fourier transform of $\hat{\chi}_{\mathbf{r}-\mathbf{r}'}(t)$ and performing the disorder average.

From $\chi(q_x, q_y, t)$, the imbalance tails are extracted by using the relations

$$I_{\mathrm{check}}(t) = \frac{1}{n_0 V}\langle\tilde{n}(q_x = \pi/a, q_y = \pi/a, t)\rangle, \qquad n_0 = \frac{1}{V}\langle\tilde{n}(q=0)\rangle, \tag{A.11}$$

$$\langle\tilde{n}(q_x, q_y, t)\rangle = \langle\tilde{n}(q_x, q_y, 0)\rangle\left[1 + \frac{1}{\nu}\int_0^t \mathrm{d}t'\,\chi(q_x, q_y, t-t')\right], \tag{A.12}$$

see Sec. 2.3. We then perform numerical integration of $\chi(q_x, q_y, t)$, and fit the time dependence of the result using Eq. (2.75). Comparing with the initial value of the imbalance, we find an estimate for the fit parameter f_1,

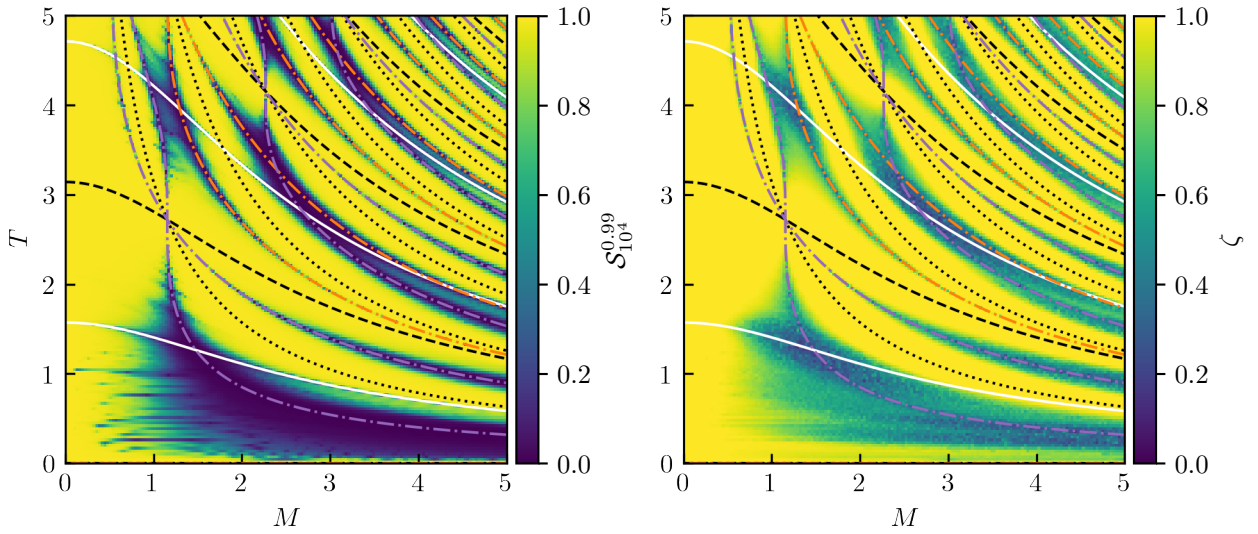$$f_1 \sim \frac{\langle\tilde{n}(q_x, q_y, 0)\rangle}{\langle\tilde{n}(q=0)\rangle\nu}. \tag{A.13}$$

B

Additional material for Chapter 3

B.1 Additional phase diagrams

The contents of this Appendix are also presented in Ref. [65]. In this Section we show additional indicators of localization: The support measure described in Eq. (3.98), and the exponent of PR values (see Eq. (3.95)) scaling with the discretization. The PR scaling allow to distinguish between localized peaks—becoming narrower with an increasing number of discretization cells—and narrow peaks that remain identical as a function the discretization in the limit $N \to \infty$. At finite N a scaling exponent $\zeta = 0$ is no more conclusive than the PR value at the highest resolution. The support measure provides additional information about whether or not a delocalized distribution spreads over the entire grand circle. The results are qualitatively similar to what was obtained for the PR values. Fig. B.1 shows results for the $T \in (0, 5]$ cross-section at $M = 2.92$ and should be compared to Fig. 3.13. Fig. B.2 shows results for the $M, T \in (0, 5]$ parameter plane and should be compared to Fig. 3.15.
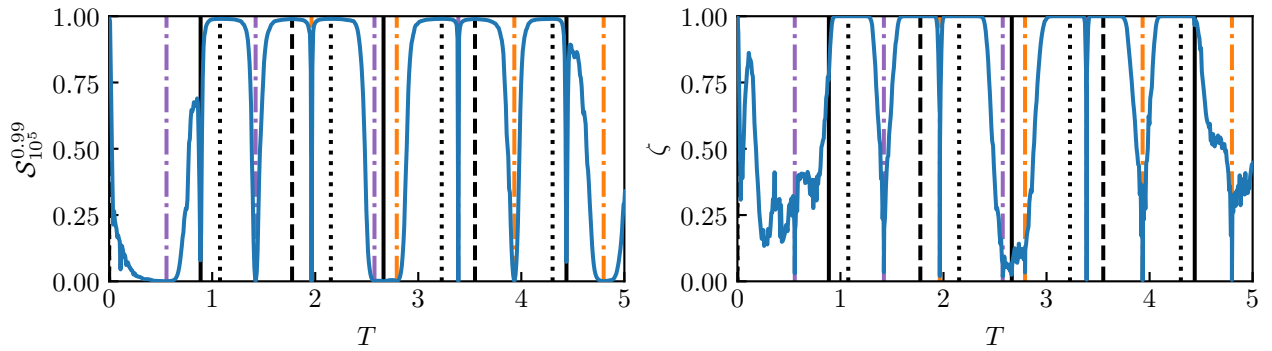
Figure B.1: Additional indicators of localization, calculated from the same distributions as Fig. 3.13. *Left panel:* Support $\mathcal{S}_{10^5}^{0.99}$, as defined in Eq. (3.98). *Right panel:* Scaling of the PR exponent with discretization $\Delta\Phi$ of the stationary distribution from Markov matrix power iteration. These values were obtained by calculating the distributions from $[\mathcal{M}_{10^4}]$, coarse graining these highly resolved distributions to lower resolution, calculating the PR value (Eq. (3.95)) at each discretization, and fitting the resulting values to a power law. Different lines show special parameter regimes described in Secs. 3.2 and 3.4. Solid lines correspond to period-2-cases $YT = (2k + 1)\pi$ with $k \in \mathbb{N}_0$. Dashed lines correspond to the frozen cases $TY = 2k\pi$. Dotted lines correspond to the shift cases $MT = k\pi$. Dash-dotted lines correspond to the projective limit, conditions (3.85) or (3.86).

Figure B.2: Additional indicators of localization, calculated from the same distributions as Fig. 3.15. *Left panel:* Support $\mathcal{S}_{10^5}^{0.99}$, as defined in Eq. (3.98). *Right panel:* Scaling of the PR exponent with discretization $\Delta\Phi$ of the stationary distribution from Markov matrix power iteration. These values were obtained by calculating the distributions from $[\mathcal{M}_{10^4}]$, coarse graining these highly resolved distributions to lower resolution, calculating the PR value (Eq. (3.95)) at each discretization, and fitting the resulting values to a power law. Different lines show special parameter regimes described in Secs. 3.2 and 3.4. Solid lines correspond to period-2-cases $YT = (2k + 1)\pi$ with $k \in \mathbb{N}_0$. Dashed lines correspond to the frozen cases $TY = 2k\pi$. Dotted lines correspond to the shift cases $MT = k\pi$. Dash-dotted lines correspond to the projective limit, conditions (3.85) or (3.86).

Bibliography

[1] P. S. Laplace, *A philosophical essay on probabilities* (Dover Publications, 1952).

[2] H. Bruus and K. Flensberg, *Many-body quantum theory in condensed matter physics - an introduction*, English (Oxford University Press, United States, 2004).

[3] T. Vojta, "Disorder in quantum many-body systems," Annual Review of Condensed Matter Physics **10**, 233–252 (2019).

[4] B. Misra and E. C. G. Sudarshan, "The Zenos paradox in quantum theory," Journal of Mathematical Physics **18**, 756–763 (1977).

[5] W. M. Itano, D. J. Heinzen, J. J. Bollinger, and D. J. Wineland, "Quantum zeno effect," Phys. Rev. A **41**, 2295–2300 (1990).

[6] M. C. Fischer, B. Gutiérrez-Medina, and M. G. Raizen, "Observation of the quantum zeno and anti-zeno effects in an unstable system," Phys. Rev. Lett. **87**, 040402 (2001).

[7] F. Schäfer, I. Herrera, S. Cherukattil, C. Lovecchio, F. Cataliotti, F. Caruso, and A. Smerzi, "Experimental realization of quantum zeno dynamics," Nature Communications **5**, `10.1038/ncomms4194` (2014).

[8] P. W. Anderson, "Absence of Diffusion in Certain Random Lattices," Phys. Rev. **109**, 1492–1505 (1958).

[9] E. Abrahams, P. W. Anderson, D. C. Licciardello, and T. V. Ramakrishnan, "Scaling theory of localization: Absence of quantum diffusion in two dimensions," Phys. Rev. Lett. **42**, 673–676 (1979).

[10] F. Evers and A. D. Mirlin, "Anderson transitions," Rev. Mod. Phys. **80**, 1355–1417 (2008).

[11] R. Nandkishore and D. A. Huse, "Many-Body Localization and Thermalization in Quantum Statistical Mechanics," Ann. Rev. Cond. Mat. Phys. **6**, 15–38 (2015).

[12] Y. Zhao, D. Feng, Y. Hu, S. Guo, and J. Sirker, "Entanglement dynamics in the three-dimensional anderson model," Phys. Rev. B **102**, 195132 (2020).

[13] L. Fleishman and P. W. Anderson, "Interactions and the anderson transition," Phys. Rev. B **21**, 2366–2377 (1980).

[14] I. V. Gornyi, A. D. Mirlin, and D. G. Polyakov, "Interacting Electrons in Disordered Wires: Anderson Localization and Low-T Transport," Phys. Rev. Lett. **95**, 206603 (2005).

[15] D. Basko, I. Aleiner, and B. Altshuler, "Metalinsulator transition in a weakly interacting many-electron system with localized single-particle states," Annals of Physics **321**, 11261205 (2006).

[16] E. Altman and R. Vosk, "Universal Dynamics and Renormalization in Many-Body-Localized Systems," Ann. Rev. Cond. Mat. Phys. **6**, 383–409 (2015).

[17] D. A. Abanin and Z. Papić, "Recent progress in many-body localization," Ann. Phys. (Berl.) **529**, 1700169 (2017).

[18]F. Alet and N. Laflorencie, "Many-body localization: an introduction and selected topics," Comptes Rendus Physique **19**, 498–525 (2018).

[19]D. A. Abanin, E. Altman, I. Bloch, and M. Serbyn, "Colloquium: many-body localization, thermalization, and entanglement," Rev. Mod. Phys. **91**, 021001 (2019).

[20]S. Dhar and S. Dasgupta, "Measurement-induced phase transition in a quantum spin system," Phys. Rev. A **93**, 050103 (2016).

[21]Y. Li, X. Chen, and M. P. A. Fisher, "Quantum Zeno effect and the many-body entanglement transition," Phys. Rev. B **98**, 205136 (2018).

[22]B. Skinner, J. Ruhman, and A. Nahum, "Measurement-induced phase transitions in the dynamics of entanglement," Phys. Rev. X **9**, 031009 (2019).

[23]Y. Li, X. Chen, and M. P. A. Fisher, "Measurement-driven entanglement transition in hybrid quantum circuits," Phys. Rev. B **100**, 134306 (2019).

[24]A. Chan, R. M. Nandkishore, M. Pretko, and G. Smith, "Unitary-projective entanglement dynamics," Phys. Rev. B **99**, 224307 (2019).

[25]Y. Bao, S. Choi, and E. Altman, "Theory of the phase transition in random unitary circuits with measurements," Phys. Rev. B **101**, 104301 (2020).

[26]M. Szyniszewski, A. Romito, and H. Schomerus, "Entanglement transition from variable-strength weak measurements," Phys. Rev. B **100**, 064204 (2019).

[27]M. P. Fisher, V. Khemani, A. Nahum, and S. Vijay, "Random quantum circuits," Annual Review of Condensed Matter Physics **14**, 335–379 (2023).

[28]O. Alberton, M. Buchhold, and S. Diehl, "Entanglement transition in a monitored free-fermion chain: From extended criticality to area law," Phys. Rev. Lett. **126**, 170602 (2021).

[29]M. Buchhold, Y. Minoguchi, A. Altland, and S. Diehl, "Effective theory for the measurement-induced phase transition of Dirac fermions," Phys. Rev. X **11**, 041004 (2021).

[30]E. V. H. Doggen, Y. Gefen, I. V. Gornyi, A. D. Mirlin, and D. G. Polyakov, "Generalized quantum measurements with matrix product states: Entanglement phase transition and clusterization," Phys. Rev. Research **4**, 023146 (2022).

[31]J. Merritt and L. Fidkowski, "Entanglement transitions with free fermions," Phys. Rev. B **107**, 064303 (2023).

[32]X. Cao, A. Tilloy, and A. D. Luca, "Entanglement in a fermion chain under continuous monitoring," SciPost Phys. **7**, 024 (2019).

[33]X. Turkeshi, M. Dalmonte, R. Fazio, and M. Schirò, "Entanglement transitions from stochastic resetting of non-Hermitian quasiparticles," Phys. Rev. B **105**, L241114 (2022).

[34]A. Altland, M. Buchhold, S. Diehl, and T. Micklitz, "Dynamics of measured many-body quantum chaotic systems," Phys. Rev. Research **4**, L022066 (2022).

[35]B. Ladewig, S. Diehl, and M. Buchhold, "Monitored open fermion dynamics: Exploring the interplay of measurement, decoherence, and free Hamiltonian evolution," Phys. Rev. Research **4**, 033001 (2022).

[36]Y. Minoguchi, P. Rabl, and M. Buchhold, "Continuous Gaussian measurements of the free boson CFT: A model for exactly solvable and detectable measurement-induced dynamics," SciPost Phys. **12**, 009 (2022).

[37]Q. Yang, Y. Zuo, and D. E. Liu, "Keldysh nonlinear sigma model for a free-fermion gas under continuous measurements," Phys. Rev. Res. **5**, 033174 (2023).

[38]I. Poboiko, P. Pöpperl, I. V. Gornyi, and A. D. Mirlin, *Theory of free fermions under random projective measurements*, arXiv:2304.03138, 2023.

[39]E. V. H. Doggen, Y. Gefen, I. V. Gornyi, A. D. Mirlin, and D. G. Polyakov, "Evolution of many-body systems under ancilla quantum measurements," Phys. Rev. B **107**, 214203 (2023).

[40]R. Vasseur, A. C. Potter, Y.-Z. You, and A. W. W. Ludwig, "Entanglement transitions from holographic random tensor networks," Phys. Rev. B **100**, 134203 (2019).

[41]I. Poboiko, I. V. Gornyi, and A. D. Mirlin, *Measurement-induced phase transition for free fermions above one dimension*, arXiv:2309.12405, 2023.

[42]M. Ippoliti, M. J. Gullans, S. Gopalakrishnan, D. A. Huse, and V. Khemani, "Entanglement phase transitions in measurement-only dynamics," Phys. Rev. X **11**, 011030 (2021).

[43]S. Roy, J. T. Chalker, I. V. Gornyi, and Y. Gefen, "Measurement-induced steering of quantum systems," Phys. Rev. Research **2**, 033347 (2020).

[44]E. Schrödinger, "Discussion of probability relations between separated systems," Mathematical Proceedings of the Cambridge Philosophical Society **31**, 555563 (1935).

[45]E. Schrödinger, "Probability relations between separated systems," Mathematical Proceedings of the Cambridge Philosophical Society **32**, 446452 (1936).

[46]M. Szyniszewski, O. Lunt, and A. Pal, *Disordered monitored free fermions*, arXiv:2211.02534, 2022.

[47]O. Lunt and A. Pal, "Measurement-induced entanglement transitions in many-body localized systems," Phys. Rev. Res. **2**, 043072 (2020).

[48]S. Gopalakrishnan, K. R. Islam, and M. Knap, "Noise-induced subdiffusion in strongly localized quantum systems," Phys. Rev. Lett. **119**, 046601 (2017).

[49]S. Dhar, S. Dasgupta, and A. Dhar, "Quantum time of arrival distribution in a simple lattice model," Journal of Physics A: Mathematical and Theoretical **48**, 115304 (2015).

[50]S. Dhar, S. Dasgupta, A. Dhar, and D. Sen, "Detection of a quantum particle on a lattice under repeated projective measurements," Phys. Rev. A **91**, 062115 (2015).

[51]A. Comtet, J. Desbois, and C. Texier, "Functionals of brownian motion, localization and metric graphs," Journal of Physics A: Mathematical and General **38**, R341 (2005).

[52]H. Perrin, J.-N. Fuchs, and R. Mosseri, "Robustness of Aharonov-Bohm cages in quantum walks," Phys. Rev. B **105**, 235404 (2022).

[53]P. Pöpperl, I. V. Gornyi, and Y. Gefen, "Measurements on an anderson chain," Phys. Rev. B **107**, 174203 (2023).

[54]P. Pöpperl, I. V. Gornyi, and A. D. Mirlin, "Memory effects in the density-wave imbalance in delocalized disordered systems," Phys. Rev. B **106**, 094201 (2022).

[55]M. Schreiber, S. S. Hodgman, P. Bordia, H. P. Lüschen, M. H. Fischer, R. Vosk, E. Altman, U. Schneider, and I. Bloch, "Observation of many-body localization of interacting fermions in a quasirandom optical lattice," Science **349**, 842–845 (2015).

[56] J. yoon Choi, S. Hild, J. Zeiher, P. SchauSS, A. Rubio-Abadal, T. Yefsah, V. Khemani, D. A. Huse, I. Bloch, and C. Gross, "Exploring the many-body localization transition in two dimensions," Science **352**, 1547–1552 (2016).

[57] E. V. H. Doggen, F. Schindler, K. S. Tikhonov, A. D. Mirlin, T. Neupert, D. G. Polyakov, and I. V. Gornyi, "Many-body localization and delocalization in large quantum chains," Phys. Rev. B **98**, 174202 (2018).

[58] E. V. H. Doggen, I. V. Gornyi, A. D. Mirlin, and D. G. Polyakov, "Slow many-body delocalization beyond one dimension," Phys. Rev. Lett. **125**, 155701 (2020).

[59] D. J. Luitz and Y. B. Lev, "The ergodic side of the many-body localization transition," Annalen der Physik **529**, 1600350 (2017).

[60] , A. Scardicchio, and V. K. Varma, "Diffusive and subdiffusive spin transport in the ergodic phase of a many-body localizable system," Phys. Rev. Lett. **117**, 040601 (2016).

[61] S. Gopalakrishnan and S. Parameswaran, "Dynamics and transport at the threshold of many-body localization," Physics Reports **862**, 1–62 (2020).

[62] A. D. Mirlin, J. Wilke, F. Evers, D. G. Polyakov, and P. Wölfle, "Strong magnetoresistance induced by long-range disorder," Phys. Rev. Lett. **83**, 2801–2804 (1999).

[63] J. Wilke, A. D. Mirlin, D. G. Polyakov, F. Evers, and P. Wölfle, "Zero-frequency anomaly in quasi-classical ac transport: memory effects in a two-dimensional metal with a long-range random potential or random magnetic field," Phys. Rev. B **61**, 13774–13784 (2000).

[64] J. Rammer, *Quantum transport theory*, Vol. 117 (CRC Press, May 2018), p. 040601.

[65] P. Pöpperl, I. V. Gornyi, D. B. Saakian, and O. M. Yevtushenko, *Localization, fractality, and ergodicity in a monitored qubit*, arXiv:2310.01997, 2023.

[66] M. A. Nielsen and I. L. Chuang, *Quantum computation and quantum information: 10th anniversary edition*, Vol. 117 (Cambridge University Press, 2010), p. 040601.

[67] K. Snizhko, P. Kumar, and A. Romito, "Quantum zeno effect appears in stages," Phys. Rev. Res. **2**, 033512 (2020).

[68] A. D. Mirlin and Y. V. Fyodorov, "Distribution of local densities of states, order parameter function, and critical behavior near the anderson transition," Phys. Rev. Lett. **72**, 526–529 (1994).

[69] M. Fava, L. Piroli, T. Swann, D. Bernard, and A. Nahum, *Nonlinear sigma models for monitored dynamics of free fermions*, arXiv:2302.12820, 2023.

[70] T. Swann, D. Bernard, and A. Nahum, *Spacetime picture for entanglement generation in noisy fermion chains*, arXiv:2302.12212, 2023.

[71] K. Chahine and M. Buchhold, *Entanglement phases, localization and multifractality of monitored free fermions in two dimensions*, arXiv:2309.12391, 2023.

[72] V. Alba, "Unbounded entanglement production via a dissipative impurity," SciPost Phys. **12**, 011 (2022).

[73] F. Caceffo and V. Alba, "Entanglement negativity in a fermionic chain with dissipative defects: exact results," Journal of Statistical Mechanics: Theory and Experiment **2023**, 023102 (2023).

[74] T. Jin, J. a. Ferreira, M. Bauer, M. Filippone, and T. Giamarchi, "Semiclassical theory of quantum stochastic resistors," Phys. Rev. Res. **5**, 013033 (2023).

[75] F. Evers and A. D. Mirlin, "Anderson transitions," Rev. Mod. Phys. **80**, 1355–1417 (2008).

[76] Y. Herasymenko, I. Gornyi, and Y. Gefen, "Measurement-driven navigation in many-body hilbert space: active-decision steering," PRX Quantum **4**, 020347 (2023).

[77] S. J. Garratt, Z. Weinstein, and E. Altman, "Measurements conspire nonlocally to restructure critical quantum states," Phys. Rev. X **13**, 021026 (2023).

[78] M. Wampler, B. J. J. Khor, G. Refael, and I. Klich, "Stirring by staring: Measurement-induced chirality," Phys. Rev. X **12**, 031031 (2022).

[79] A. Peres, "Zeno paradox in quantum theory," American Journal of Physics **48**, 931–932 (1980).

[80] A. Z. Chaudhry, "A general framework for the quantum Zeno and anti-Zeno effects," Scientific Reports **6**, 2045–2322 (2016).

[81] K. Snizhko, P. Kumar, and A. Romito, "Quantum Zeno effect appears in stages," Phys. Rev. Res. **2**, 033512 (2020).

[82] A. Didi and E. Barkai, "Measurement-induced quantum walks," Phys. Rev. E **105**, 054108 (2022).

[83] P. A. Lee and T. V. Ramakrishnan, "Disordered electronic systems," Rev. Mod. Phys. **57**, 287–337 (1985).

[84] P. Wölfle and D. Vollhardt, "Self-consistent theory of anderson localization: general formalism and applications," International Journal of Modern Physics B **24**, 1526–1554 (2010).

[85] B Kramer and A MacKinnon, "Localization: theory and experiment," Reports on Progress in Physics **56**, 1469 (1993).

[86] J. J. Sakurai and J. Napolitano, *Modern quantum mechanics*, 2nd ed., Vol. 117 (Cambridge University Press, 2017), p. 040601.

[87] H. Carmichael, *An open systems approach to quantum optics*, Vol. 117 (Springer Berlin Heidelberg, 1993), p. 040601.

[88] J. Surace and L. Tagliacozzo, "Fermionic Gaussian states: an introduction to numerical approaches," SciPost Phys. Lect. Notes **117**, 54 (2022).

[89] J. Eisert, M. Cramer, and M. B. Plenio, "Colloquium: area laws for the entanglement entropy," Rev. Mod. Phys. **82**, 277–306 (2010).

[90] Q. Tang and W. Zhu, "Measurement-induced phase transition: a case study in the nonintegrable model by density-matrix renormalization group calculations," Phys. Rev. Res. **2**, 013022 (2020).

[91] S. Goto and I. Danshita, "Measurement-induced transitions of the entanglement scaling law in ultracold gases with controllable dissipation," Phys. Rev. A **102**, 033316 (2020).

[92] Y. Fuji and Y. Ashida, "Measurement-induced quantum criticality under continuous monitoring," Phys. Rev. B **102**, 054302 (2020).

[93] M. Coppola, E. Tirrito, D. Karevski, and M. Collura, "Growth of entanglement entropy under local projective measurements," Phys. Rev. B **105**, 094303 (2022).

[94] A. M. Childs, R. Cleve, E. Deotto, E. Farhi, S. Gutmann, and D. A. Spielman, "Exponential algorithmic speedup by a quantum walk," in Proceedings of the thirty-fifth annual acm symposium on theory of computing, Vol. 117, STOC '03 (2003), pp. 5968.

[95] E. Farhi and S. Gutmann, "Quantum computation and decision trees," Phys. Rev. A **58**, 915–928 (1998).

[96]G. F. Lawler and V. Limic, *Random walk: a modern introduction*, Vol. 117, Cambridge Studies in Advanced Mathematics (Cambridge University Press, 2010), p. 040601.

[97]R. Serfozo, *Basics of applied stochastic processes*, Vol. 117 (Springer Berlin Heidelberg, 2009), p. 040601.

[98]R. Metzler and J. Klafter, "The random walk's guide to anomalous diffusion: a fractional dynamics approach," Physics Reports **339**, 1–77 (2000).

[99]R. Metzler, J.-H. Jeon, A. G. Cherstvy, and E. Barkai, "Anomalous diffusion models and their properties: non-stationarity, non-ergodicity, and ageing at the centenary of single particle tracking," Phys. Chem. Chem. Phys. **16**, 24128–24164 (2014).

[100]B. Wischmann and E. Müller-Hartmann, "Level statistics and localization: A study of the 1D Anderson model," Zeitschrift für Physik B Condensed Matter **79**, 91–99 (1990).

[101]A. D. Mirlin, "Statistics of energy levels and eigenfunctions in disordered systems," Physics Reports **326**, 259–382 (2000).

[102]C.-M. Jian, H. Shapourian, B. Bauer, and A. W. W. Ludwig, *Measurement-induced entanglement transitions in quantum circuits of non-interacting fermions: born-rule versus forced measurements*, arXiv:2302.09094, 2023.

[103]R. Yin and E. Barkai, "Restart expedites quantum walk hitting times," Phys. Rev. Lett. **130**, 050802 (2023).

[104]J. Kurkijärvi, "Hopping conductivity in one dimension," Phys. Rev. B **8**, 922–924 (1973).

[105]J Machta, "Random walks on site disordered lattices," Journal of Physics A: Mathematical and General **18**, L531 (1985).

[106]G. F. Lawler, "Expected hitting times for a random walk on a connected graph," Discrete Mathematics **61**, 85–92 (1986).

[107]J. M. Deutsch, "Quantum statistical mechanics in a closed system," Phys. Rev. A **43**, 2046–2049 (1991).

[108]M. Srednicki, "Chaos and quantum thermalization," Phys. Rev. E **50**, 888–901 (1994).

[109]A. Morningstar, L. Colmenarez, V. Khemani, D. J. Luitz, and D. A. Huse, "Avalanches and many-body resonances in many-body localized systems," Phys. Rev. B **105**, 174205 (2022).

[110]D. J. Luitz, N. Laflorencie, and F. Alet, "Many-body localization edge in the random-field heisenberg chain," Phys. Rev. B **91**, 081103 (2015).

[111]K. Agarwal, S. Gopalakrishnan, M. Knap, M. Müller, and E. Demler, "Anomalous diffusion and griffiths effects near the many-body localization transition," Phys. Rev. Lett. **114**, 160401 (2015).

[112]Y. Bar Lev, G. Cohen, and D. R. Reichman, "Absence of diffusion in an interacting system of spinless fermions on a one-dimensional disordered lattice," Phys. Rev. Lett. **114**, 100601 (2015).

[113]I. V. Gornyi, A. D. Mirlin, and D. G. Polyakov, "Electron transport in a disordered luttinger liquid," Phys. Rev. B **75**, 085421 (2007).

[114]G. Zala, B. N. Narozhny, and I. L. Aleiner, "Interaction corrections at intermediate temperatures: longitudinal conductivity and kinetic equation," Phys. Rev. B **64**, 214204 (2001).

[115]D. J. Luitz, N. Laflorencie, and F. Alet, "Extended slow dynamical regime close to the many-body localization transition," Phys. Rev. B **93**, 060201(R) (2016).

[116]S. A. Weidinger, S. Gopalakrishnan, and M. Knap, "Self-consistent hartree-fock approach to many-body localization," Phys. Rev. B **98**, 224205 (2018).

[117]P. Pöpperl, E. V. Doggen, J. F. Karcher, A. D. Mirlin, and K. S. Tikhonov, "Dynamics of many-body delocalization in the time-dependent hartreefock approximation," Annals of Physics **435**, Special Issue on Localisation 2020, 168486 (2021).

[118]P. Sierant and J. Zakrzewski, "Challenges to observation of many-body localization," Phys. Rev. B **105**, 224203 (2022).

[119]M. Ernst and A. Weyland, "Long time behaviour of the velocity auto-correlation function in a lorentz gas," Physics Letters A **34**, 39–40 (1971).

[120]M. H. Ernst, J. Machta, J. R. Dorfman, and H. van Beijeren, "Long time tails in stationary random media. i. theory," Journal of Statistical Physics **34**, 477–495 (1984).

[121]W. Götze, "The mobility of a quantum particle in a three-dimensional random potential," Philosophical Magazine B **43**, 219–250 (1981).

[122]I. S. Burmistrov, I. V. Gornyi, and A. D. Mirlin, "Tunneling into the localized phase near anderson transitions with coulomb interaction," Phys. Rev. B **89**, 035430 (2014).

[123]S. Gopalakrishnan, K. Agarwal, E. A. Demler, D. A. Huse, and M. Knap, "Griffiths effects and slow dynamics in nearly many-body localized systems," Phys. Rev. B **93**, 134206 (2016).

[124]J. F. Karcher, I. A. Gruzberg, and A. D. Mirlin, "Generalized multifractality at metal-insulator transitions and in metallic phases of two-dimensional disordered systems," Phys. Rev. B **106**, 104202 (2022).

[125]S. A. A. Ghorashi, J. F. Karcher, S. M. Davis, and M. S. Foster, "Criticality across the energy spectrum from random artificial gravitational lensing in two-dimensional dirac superconductors," Phys. Rev. B **101**, 214521 (2020).

[126]S. F. Edwards, "A new method for the evaluation of electric conductivity in metals," The Philosophical Magazine: A Journal of Theoretical Experimental and Applied Physics **3**, 1020–1031 (1958).

[127]D. Vollhardt and P. Wölfle, "Diagrammatic, self-consistent treatment of the anderson localization problem in $d \leq 2$ dimensions," Phys. Rev. B **22**, 4666–4679 (1980).

[128]A. I. Larkin and D. E. Khmel'nitski, "Anderson localization and anomalous magnetoresistance at low temperatures," Soviet Physics Uspekhi **25**, 185 (1982).

[129]S. Chakravarty and A. Schmid, "Weak localization: the quasiclassical theory of electrons in a random potential," Physics Reports **140**, 193–236 (1986).

[130]F. Wegner, "Inverse participation ratio in $2+\epsilon$ dimensions," Zeitschrift für Physik B Condensed Matter **36**, 209–214 (1980).

[131]V. I. Fal'ko and K. B. Efetov, "Statistics of prelocalized states in disordered conductors," Phys. Rev. B **52**, 17413–17429 (1995).

[132]H. M. Wiseman and G. J. Milburn, *Quantum measurement and control*, Vol. 117 (Cambridge University Press, 2009), p. 040601.

[133]R. E. Kastner, "Demystifying weak measurements," Foundations of Physics **47**, 697–707 (2017).

[134]K. Jacobs and D. A. Steck, "A straightforward introduction to continuous quantum measurement," Contemporary Physics **47**, 279–303 (2006).

[135] M. Szyniszewski, A. Romito, and H. Schomerus, "Universality of entanglement transitions from stroboscopic to continuous measurements," Phys. Rev. Lett. **125**, 210602 (2020).

[136] A. C. Morlet and J. Lorenz, "Numerical solution of a functional equation on a circle," SIAM Journal on Numerical Analysis **29**, 1741–1768 (1992).

[137] D. B. Saakian, "Exact solution of the hidden markov processes," Phys. Rev. E **96**, 052112 (2017).

[138] D. B. Saakian, "Semianalytical solution of the random-product problem of matrices and discrete-time random evolution," Phys. Rev. E **98**, 062115 (2018).

[139] H. Mineo, V. Suvorov, and D. B. Saakian, "Investigation of the product of random matrices and related evolution models," Mathematics **11**, 040601 (2023).

[140] R. V. Mises and H. Pollaczek-Geiringer, "Praktische verfahren der gleichungsauflösung .," ZAMM - Journal of Applied Mathematics and Mechanics / Zeitschrift für Angewandte Mathematik und Mechanik **9**, 152–164 (1929).

[141] R. Bronson, G. B. Costa, and J. T. Saccoman, "Chapter 4 - eigenvalues, eigenvectors, and differential equations," in *Linear algebra (third edition)*, Vol. 117, edited by R. Bronson, G. B. Costa, and J. T. Saccoman, Third Edition (Academic Press, 2014), pp. 237–288.

[142] K. Yakubo and S. Mizutaka, "Testing the order parameter of the anderson transition," Journal of the Physical Society of Japan **81**, 104707 (2012).

[143] V. Dobrosavljevi, A. A. Pastor, and B. K. Nikoli, "Typical medium theory of anderson localization: a local order parameter approach to strong-disorder effects," Europhysics Letters **62**, 76 (2003).

[144] K. Falconer, *Fractal geometry*, Vol. 117 (Wiley, Sept. 2003), p. 040601.

[145] A. Chhabra and R. V. Jensen, "Direct determination of the f(α) singularity spectrum," Phys. Rev. Lett. **62**, 1327–1330 (1989).

[146] T. C. Halsey, M. H. Jensen, L. P. Kadanoff, I. Procaccia, and B. I. Shraiman, "Fractal measures and their singularities: the characterization of strange sets," Phys. Rev. A **33**, 1141–1151 (1986).

[147] H. Hentschel and I. Procaccia, "The infinite number of generalized dimensions of fractals and strange attractors," Physica D: Nonlinear Phenomena **8**, 435–444 (1983).

[148] , A. Scardicchio, and V. K. Varma, "6. markov chains: discrete parameter," in *Stochastic processes*, Vol. 117 (American Physical Society, 2016), pp. 187–275.

[149] D. Isaacson, "A characterization of geometric ergodicity," Zeitschrift für Wahrscheinlichkeitstheorie und Verwandte Gebiete **49**, 267–273 (1979).

[150] P. Walters, *An introduction to ergodic theory*, Vol. 117, Graduate texts in mathematics ; 79 (Springer, New York, 1982), pp. 187–275.

[151] R. Tarjan, "Depth-first search and linear graph algorithms," SIAM Journal on Computing **1**, 146–160 (1972).

[152] E. Nuutila and E. Soisalon-Soininen, "On finding the strongly connected components in a directed graph," Information Processing Letters **49**, 9–14 (1994).

[153] A. A. Hagberg, D. A. Schult, and P. J. Swart, "Exploring network structure, dynamics, and function using networkx," in Proceedings of the 7th python in science conference, Vol. 117, edited by G. Varoquaux, T. Vaught, and J. Millman (2008), pp. 11 –15.

[154] B. A. Farbey, "Structural models: an introduction to the theory of directed graphs," Journal of the Operational Research Society **17**, 202–203 (1966).

[155] D. C. Kozen, *The design and analysis of algorithms*, Vol. 117 (Springer New York, 1992), pp. 187–275.

[156] A. D. Zdetsis, C. M. Soukoulis, E. N. Economou, and G. S. Grest, "Localization in two- and three-dimensional systems away from the band center," Phys. Rev. B **32**, 7811–7816 (1985).

[157] J. D. Brehm, P. Pöpperl, A. D. Mirlin, A. Shnirman, A. Stehli, H. Rotzinger, and A. V. Ustinov, "Tunable anderson localization of dark states," Phys. Rev. B **104**, 174202 (2021).

Publications

The publications I was involved in and their bibliography reference in this thesis are listed in the following:

- Ref. [117]: Paul Pöpperl, Elmer V.H. Doggen, Jonas F. Karcher, Alexander D. Mirlin and Konstantin S. Tikhonov, *Dynamics of many-body delocalization in the time-dependent Hartree-Fock approximation*, Annals of Physics, pp. 168486, 2021.

- Ref. [157]: Jan David Brehm, and Paul Pöpperl, and Alexander D. Mirlin, and Alexander Shnirman, and Alexander Stehli, and Hannes Rotzinger, and Alexey V. Ustinov, *Tunable Anderson localization of dark states* Physical Review B **104**, pp. 174202, 2021.

- Ref. [53]: Paul Pöpperl, Igor V. Gornyi, and Yuval Gefen, *Measurements on an Anderson chain* Physical Review B **107**, pp. 174203, 2023.

- Ref. [54]: Paul Pöpperl, Igor V. Gornyi, and Alexander D. Mirlin, *Memory effects in the density-wave imbalance in delocalized disordered systems* Physical Review B **106**, pp. 094201, 2022.

- Ref. [38]: Igor Poboiko, Paul Pöpperl, Igor V. Gornyi, Alexander D. Mirlin, *Theory of free fermions under random projective measurements*, arXiv:2304.03138, 2023.

- Ref. [65]: Paul Pöpperl, Igor V. Gornyi, David B. Saakian, and Oleg M. Yevtushenko, *Localization, fractality, and ergodicity in a monitored qubit*, arXiv:2310.01997, 2023.

Acknowledgments

First of all, many thanks to my advisors Igor V. Gornyi and Alexander D. Mirlin who gave me the opportunity to work on topics that were very interesting and motivating to me. They found an ideal balance between guiding my efforts and leaving me the freedom to find my own direction. I learned a lot throughout many discussions, and their office doors and mail inboxes have always been open for questions.

I am very grateful to Jonas F. Karcher, who spent a lot of time answering my questions and explaining things to me, in person at TKM as well as from the other side of the Atlantic. I profited a lot from his knowledge and insights.

I would also like to thank all of my other collaborators, in particular Elmer V. H. Doggen, Konstantin S. Tikhonov, Jan David Brehm, Alexander Shnirman, Yuval Gefen, Sthitadhi Roy, Igor Poboiko, and Oleg M. Yevtushenko, all of whom I enjoyed learning from as well as working and discussing with.

Thanks to Marcin Szyniszewski for very helpful and interesting discussions about the contents of Chapter 1, his work [46], and possible future directions regarding measured, disordered systems.

I am grateful to the members and organizers of KSQM, it was great meeting and discussing with other PhD students during KSQM events.

A big thank you to Matthias Linster for thoroughly proofreading parts of this thesis, providing many valuable suggestions (and harshly criticizing excessive use of parentheses).

Special thanks to Daniel Hauck for sharing a long tradition of regular exchanges about current projects on the way to the bakery.

Thanks to my current and former colleagues at TKM for providing a very pleasant and friendly working environment.

Lastly, I would like to thank my friends and family and in particular my partner Laura Schüber for their continuous support and also for enduring uncalled-for rambling on physics.